Developing fluorite as a geochemical pathfinder mineral using globally reported REE-Y contents

by

Sarah Makin

B.Sc., Stockton University, 2013

Thesis Submitted in Partial Fulfillment of the
Requirements for the Degree of
Master of Science

in the
Department of Earth Sciences
Faculty of Science

SIMON FRASER UNIVERSITY

Spring 2017

Approval

Name:	**Sarah Makin**
Degree:	**Master of Science (Earth Sciences)**
Title:	***Developing fluorite as a geochemical pathfinder mineral using globally reported REE-Y contents***
Examining Committee:	**Chair:** **Dr. Andrew Calvert** Professor **Dr. Daniel Marshall** Senior Supervisor Professor **Dr. Derek Thorkelson** Supervisor Professor **Dr. Gregory Dipple** External Examiner Professor Earth Ocean and Atmospheric Sciences University of British Columbia May 12, 2017
Date Defended/Approved:	June 19, 2017

Abstract

Discrimination diagrams have been created to begin development of fluorite as a geochemical pathfinder mineral based on a compilation of approximately 630 trace-element analyses (ICP-MS, ICP-AES, LA-ICP-MS, NAA, INAA) of fluorite from 183 deposits/localities from nearly 60 regions world-wide. A classification scheme of primary mineralization environments was determined to describe potentially economic deposits in which fluorite commonly occurs as listed here in order of representation quality: 1.) hydrothermal/epithermal vein/replacement in igneous hosts, 2.) MVT, 3.) vein/replacement in carbonate hosts, 4.) carbonatite-related, 5.) vein/replacement in metamorphic hosts 6.) SEDEX, 7.) skarn, 8.) greisen, 9.) intrusion-related Mo, 10.) cryolite, 11.) peralkaline silicate igneous rock, 12.) vein/replacement in sedimentary hosts, 13.) rare-metal pegmatite, 14.) granite-related U, and 15.) IOCG deposits.

Discrimination diagrams were created using 67th percentile contours of scatter datafields per primary mineralization environment generated using ratios of REE-Y data and equations created by discriminant projection analyses. These diagrams were tested using FUS-ICP/MS analyses of fluorite handsamples sourced from eight North American deposits with predetermined primary mineralization environments assigned from literature review. Correct assignations were confidently returned for half of eight sampled deposits using 11 analyses of samples and less confidently returned for another quarter.

Though the exact mechanisms controlling trace-element partitioning in fluorite are poorly understood, this study provides an improved method to discriminate between fluorite-bearing deposits.

Keywords: fluorite; rare earth elements; pathfinder minerals; exploration tool; indicator minerals; specialty metals

Dedication

To everyone who helped and believed in me along the way,

Thank you.

No one does anything truly alone.

To my parents, especially.

Acknowledgements

I would like to give thanks to my supervisor Dan Marshall for taking me on as a research assistant at Simon Fraser University and for giving me the opportunity to further my education. I would also like to thank him for his patience, though constant goading for a sense of urgency, and his support in times of difficulty. Also, for his remarkable approach to research which is unrelenting, uncompromising, and seemingly insatiable.

I would also like to acknowledge George Simandl at the British Columbia Geologic Survey Ministry of Energy, Mines, and Natural Gas and Responsibility tasked under the Targeted Geoscience Initiative 4, for the original collection of publications containing fluorite trace-element data, the initial idea for the project, and for the handsample collection analyzed in this study.

I would also like to thank Derek Thorkelson for allowing me to practice my skills in the field by taking me on as a student of his regional mapping field-course as this specific thesis project did not offer the opportunity for a field program. I would also like to thank him for his words of encouragement and for his commitment to educating his students. He truly wants his students to understand and learn.

Thanks should also be given to Dan Gibson for being a good teacher. Your efforts don't go unnoticed.

And finally, I would like to thank my family and friends, all of whom offered their support and advice while I navigated this chapter in my life to complete this thesis. Without all of your help and support, I could not have done this. Here, I would like to thank my parents, Brad, Lucia, Flavien, Jaap, Snowy, Chloé, James, Bob, Aaron, and Jen.

Table of Contents

List of Tables

List of Figures

List of Acronyms

BCGS	British Columbia Geologic Survey
CL	Cathodoluminescence
DPA	Discrimination Projection Analysis
FUS-ICP/MS	Fusion Inductively Coupled Plasma Mass Spectrometry
HREE	Heavy Rare Earth Elements (Dy-Lu)
ICP-AES	Inductively Coupled Plasma Atomic Emission Spectrometry
ICP-MS	Inductively Coupled Plasma Mass Spectrometry
INAA	Instrumental Neutron Activation Analysis
IOCG	Iron-Oxide-Copper-Gold
LA-ICP-MS	Laser Ablation Inductively Coupled Plasma Mass Spectrometry
LCT	Li-Cs-Ta (pegmatite type)
LREE	Light Rare Earth Elements (La-Sm)
MREE	Middle Rare Earth Elements (Sm-Dy)
MVT	Mississippi Valley Type (deposit)
NAA	Neutron Activation Analysis
NYF	Nb-Y-F (pegmatite type)
PAAS	Post-Archean Australian Shale
Q-Q plot	Quantile-Quantile plot
REE	Rare-Earth Elements
REE-Y	Rare-Earth Elements including Yttrium
SEDEX	Sedimentary Exhalative (deposit)
SM	Specialty Metal
S-W	Shapiro-Wilk test
TGI4	Targeted Geosciences Initiative 4
USGS	United States Geologic Survey
XRF	X-Ray Fluorescence

Glossary

Lanthanoids	Rare-earth elements La-Lu plus Y
Indicator minerals	Identifiable resistate minerals unique to a targetable deposit type that are accessory to and more abundant than the targeted mineral commodity. Used as an exploration tool.
Pathfinder minerals	Indicator minerals when several secondary or gangue minerals are identified in association
Geochemical pathfinder minerals	Minerals that are themselves not unique to a specific deposit type, but the trace-elemental signatures contained within are indicative of specific ore-associated mineralization types or lack thereof.

Chapter 1.

Introduction

Fluorite, CaF_2, is a widespread accessory and gangue mineral associated with diverse mineral and metallic deposits. Fluorite is easily identified due to chemical and physical properties promoting vibrant coloration and fluorescence. It is identifiable within mineral separates, with properties of low hardness, a high degree of cleavability, and high density when enriched in heavy trace-elements. Fluorine may play a key role in concentrating and depositing rare metals and thus, fluorite is commonly associated with these deposit types. It also appears that fluorite contains trace-element compositions representative of formational fluid chemistry in most mineralizing conditions (Cherniak et al., 2001) and if the assumption is made that formational processes and fluid chemistries are consistent enough to produce genetic economic deposit types, the compositions of associated fluorite should contain unique signatures per deposit type, allowing for the development of fluorite into a geochemical pathfinder (indicator) mineral. This methodology has been proven effective using a similar mineral, apatite, in which it's trace-element composition has been used to create discrimination diagrams based on apatite source mineralization.

In order to determine the utility of fluorite as a geochemical pathfinder mineral, a compilation of reported trace-element data analyzed from fluorite was examined. In this examination, a classification scheme for fluorite-containing deposits was established which led to the creation of discrimination diagrams using REE-Y data after chemical variability on the grain and deposit scales were assessed (Appendix D.). In this introductory chapter, indicator mineral methods will be introduced, as well as fluorite chemical and physical properties that could aid in, or prove detrimental to, determining discriminatory criteria for fluorites of specific genetic affinity. These properties include trace-element substitutions and behavior, causes of fluorite coloration and fluorescence, and crystal habit and morphology. Additionally, REE systematics in relation to fluorite will be discussed and previous works including trace-element discrimination diagrams for fluorite will be summarized.

1.1. Indicator mineral methods

Over the past three decades, indicator mineral methods have been developed as useful or theoretically useful exploration tools (McClenaghan et al., 2000; McClenaghan, 2005; Gent et al., 2011) for targeting deposits containing diamonds, gold, precious gems and industrial minerals (emeralds, corundum, chrysoberyl, spinel, topaz, zircon, tourmaline, garnet, titanite, and fluorite), base-metals to massive sulfides, Cu-Ni sulfides, molybdenum, tungsten, Sn±Cu±W, and most recently specialty metal deposits including rare earth element deposits (Belousova et al., 2002; Mao et al., 2016 a, b; Simandl et al., 2012). Indicator mineral methods are becoming increasingly necessary as the search for exposed deposits becomes more complete, as more deposits are targeted in extensively glaciated terrain, and as the sizes of targetable economic deposit types decreases (carbonatite and kimberlite deposits). Fluorite has potential as a geochemical pathfinder mineral for various economic deposit types, but most importantly could be utilized for the exploration of rare metal deposits such as peralkaline igneous silicate intrusions or carbonatites.

Indicator mineral methods include those using indicator, pathfinder, and geochemical pathfinder minerals. Traditionally, *indicator minerals* are defined as identifiable resistate minerals unique to a targetable deposit type that are accessory to and more abundant than the targeted mineral commodity. For example, Cr- and Mg-rich pyrope, Cr-rich diopside, Cr-rich spinel, chromite, or Mg-rich ilmenite have been used for diamond exploration, (Dredge et al., 1997; McClenaghan, 2005; McClenaghan et al., 2000; McClenaghan et al., 2002; Gent et al., 2011). *Pathfinder minerals* are also considered indicators of specific mineralization types when several secondary or gangue minerals are identified in association (Stendal and Theobald, 1994). For instance, fluorite found with topaz, tourmaline, wolframite, and/or cassiterite could indicate highly fractionated granites containing potential greisen deposits, while gahnite found with nigerite and hogbomite could indicate the presence of metamorphosed Zn-containing massive sulfide deposits.

The advancement of chemical analytical techniques has allowed for the development of *geochemical pathfinder minerals* allowing for far greater exploration potential when examining mineral concentrates. These techniques use minerals that are themselves not unique to a specific deposit-type, but the trace-elemental signatures contained within are indicative of specific ore-associated mineralization types or lack thereof. For example, in

already discovered deposits, gold content in barite can be traced to target ore zone proximity, and trace-elements in apatite have been used to determine porphyry copper deposit alteration haloes (Bouzari et al., 2016). Alternatively, trace-elements in tourmaline, apatite, fluorite, and pyrchlore/columbite-tantalite series minerals have been used to distinguish between various source rocks and economically significant genetic deposit varieties (Stendal and Theobald, 1994; Belousova et al., 2002; Mao et al., 2016 b; Eppinger and Closs, 1990; Makin et al., 2014; Mao et al., 2016 a; Mackay and Simandl, 2015). It is for the targeting of specialty metal deposits, which can be relatively small in volume, that geochemical indicator minerals may prove most useful, as these types of deposits contain unique minerals and concentrations of elements that hopefully influence the trace-element composition of common gangue minerals allowing for noteable distinction.

Rare earth elements and mineralogically related elements (coined "specialty metals" or “SM’s" by the British Columbia Geological Survey’s (BCGS) Targeted Geoscience Initiative v. four (TGI-4), Simandl et al., 2012) have become important commodities over the past decade and are found in relatively rare minerals and deposit types. Commonly, these deposits are small in volume, with pipe and alteration plan-views spanning less than a couple of kms in diameter, such as the carbonatite mined for Nb at Niobec, St. Honoré, Quebec (Fournier, 1993). Subsequently, researchers have been developing geochemical indicator mineral methods to target these deposits, and such has been the effort in using apatite (Belousova et al., 2002, Mao et al., 2015), pyrochlore and columbite-tantalite (Mackay & Simandl, 2015), and fluorite (Eppinger & Closs, 1990; Makin et al., 2014; Mao et al., 2016 b). Developing minerals such as apatite or fluorite as exploration tools are appealing since these minerals can be far more abundant in targeted deposit types than the desired ore minerals, they are easily identifiable due to coloration and potential fluorescence, they both contain Ca-sites within their crystalline structures allowing for significant ionic substitutions, and their presence can be easily detected using water or soil geochemical anomalies (phosphate or fluorine).

Fluorite is a common gangue or accessory mineral occurring in a wide range of deposit types forming in primary, high-temperature, magmatic to secondary, low-temperature, hydrothermal or epithermal phases. Fluorite forms in nearly as many environments as economic deposits, and can occur with or within alkaline to peralkaline silicate igneous rocks and associated deposits such as pegmatites, skarns, uranium deposits,

and greisens, with or within REE- and igneous carbonate-enriched deposit types such as carbonatites and iron-oxide-copper-gold (IOCG) deposits, and within F-enriched Mississippi Valley-type (MVT) deposits and other epithermal/hydrothermal vein or replacement bodies in carbonate-rich rocks, commonly containing barite and/or Pb/Zn mineralization (Hora, 1996; Černý, 1991; Pell, 1994; Fisher et al., 2013; Rakovan, 2007; Elliot et al., 1995, Porter, 2000; Cook, 2013). Because of fluorite's occurrence within many potentially economic deposit types, and because it is easily identifiable within its fraction of non-magnetic, density-separated mineral concentrates (3.01-3.25 g/cm^3, but up to 3.6 g/cm^3 when enriched in dense mineral inclusions or heavy trace-elements such as REE (Staebler et al., 2006)) due to its fluorescent properties, (Gent et al., 2011), and because fluorite contains trace-element signatures reflecting mineral-forming conditions, fluorite has potential as a geochemical pathfinder mineral.

1.2. Fluorite properties

The properties of fluorite make it an ideal candidate for pathfinder mineral studies as its low hardness and high degree of cleavabilty promote proximal deposition from source deposits. Additionally, fluorite displays a wide spectrum of colors and color patterns, fluorescence, and is receptive to the inclusion of fluids and minerals, suggesting fluorite provides a record of differing mineralzing conditions. With controlled study, it may be possible to correlate fluorite composition, coloration, fluorescence, and mineral and fluid inclusions to genetic deposit varieties, but it is the mission of this paper to provide a baseline study for the development of fluorite as an exploration tool. To this end, discrimination diagrams utilizing the trace-element composition of fluorite will be developed which could be further enhanced or supplemented by studies correlating alternative fluorite properties to genetic deposit varieties. Therefore, fluorite properties will be introduced here with a focus on trace-element composition and its role in affecting fluorite phenotypes including fluorite's structure, crystal habit, color, fluorescence, and zoning patterns, as well as considerations when utilizing a mineral's composition to draw genetic inferences.

In order to exploit fluorite's trace-elemental composition to discern mineralization sources from potentially economic deposits a few things must first be addressed. First, what elements can be found in fluorite of appreciable quantities to compare between samples from

specific deposits, and how are these elements incorporated into the fluorite crystal structure? Secondly, how do these trace-elements behave within fluorite post-mineralization and do final compositions of fluorites reflect those entrapped during mineralization? Thirdly, it is important to realize the effect of analytical scale on interpreting results. Fluorite commonly exhibits colorful or fluorescent distinctions between growth and sector zones resulting from unknown variations in formational conditions. When observed using cathodoluminescence imaging, fluorite often displays zonation patterns (concentric, indicating temporal variations during crystal growth, and sector, indicating chemical or structural variations during temporally equivalent crystal growth) and it is important to understand if fluorite chemical variability on the sample-scale or grain-scale is adequately deficient to make the distinction between fluorites on the deposit-scale possible. Authors (Gagnon et al., 2003; Schwinn & Markl, 2005; Baele et al., 2012; Smolyanski et al., 2009) utilizing point-precision geochemical analytical techniques such as laser ablation inductively coupled plasma mass spectrometry (LA-ICP-MS) as opposed to bulk-analytical methods such as digestion inductively coupled plasma mass spectrometry (ICP-MS), induced neutron activation analysis (INAA), or X-ray fluorescence (XRF) noted substantial trace-element chemical variability between fluorite samples and within single fluorite grains and samples. These authors warned against using bulk analytical methods for determining fluorite chemical variability as well as using too few point-analyses to draw deposit-wide conclusions. Mao et al., (2016 b), however, attempted to ease these concerns by demonstrating that the observed variation of the trace-element cmposition of fluorite from a single crystal was less than that exhibited for all fluorite from a single deposit. Questions that must be addressed include: does the identification of consistently reported trace-elements in fluorite provide deposit-scale distinction; do final fluorite chemistries reflect chemical signatures from entrapment during mineralization; and, does fluorite trace-element chemistry vary too greatly on the grain or sample scales to make distinction on the deposit scale impossible such as been investigated by Mao et al., (2016 b)?

Additionally, fluorite color and fluorescence could aid in the utilization of fluorite to identify source deposit genetic types. However, if consistent correlations cannot be drawn, this is only possible if the mechanisms producing these phenomena are well understood. Fluorite can exhibit nearly any color, though it very commonly displays shades of purple, green, yellow, and blue. Fluorescence in fluorite is also diverse, but commonly exhibits spectrums of blue, green, and less commonly yellow. Not only are fluorite colors and fluorescence spectrums diverse, but fluorite can also be complexly zoned indicating changing

conditions or structural differences at the crystal growth site. Zonation patterns are of two varieties as mentioned above; growth and sector. Growth zones are depicted as concentric bands propagating from the crystal nucleus, and can be displayed by changes in fluorite color, fluorescence, or cathodoluminescence. Since the true cause of coloration cannot always be identified for fluorite, it is difficult to determine exactly what conditions changed during crystal growth to produce the zonation pattern. Since fluorescence intensity is likely attributed to varying degrees of REE incorporation besides inclusions of manganese, uranium, crystal defects and organic incusions (Verbeek, 2006), it is possible that zonation patterns displayed in this manner are caused by differential REE or impurity concentrations on the crystal scale. Similarly, cathodoluminescece is a visual measure of elemental impurity concentration gradients, namely of the REE, and thusly, represents differential trace-element concentrations on the crystal scale. The possible mechanisms responsible for producing concentric compositional gradients however, are diverse ranging from chemical, such as temporally varied chemical concentration in the growth medium, or physical, affecting factors controlling growth rate allowing for variable development of growth defects allowing free REE or other trace elements to cluster in crystal voids. Sector zones more likely display structural differences in fluorite, affected by conditions controlling crystal growth. Sector zones are defined by Rakovan (2009) as "symmetrically non-equivalent sectors and form due to variations occurring on crystal growth surfaces." This topic of zonation in fluorite provides two queries: 1) do color/fluorescence/cathodoluminesence variations in fluorite crystals display chemical variations that would add complication to using trace-elements to distinguish between fluorite source deposits; and, 2) if the causes of these variations could be identified, could they be utilized for discriminatory purposes?

1.2.1. Fluorite structure and ionic substitutions

Fluorite is a halide mineral with the empirical formula CaF_2 for which calcium is readily replaced by trace-elements. Its stoichiometric ratio is consistent with the coordination of its ions with 8-fold, cubic coordination for Ca^{2+} and 4-fold, tetrahedral coordination for F^- (Figure 1-1 and Figure 1-2). Unlike for most ionic structures, Ca^{2+} in fluorite acts as the packing ion as its crystal radius is larger at 1.26 Å than that for the anion, F^-, at 1.17 Å, (Shannon, 1976). These ionic radii, however, are nearly equivalent with a ratio of r-/r+ = 0.929 which typically favors a cubic packing arrangement, and creates a relatively flexible ionic crystalline structure (Cherniak et al., 2001). Due to Ca's $^{+2}$ charge, it can only

occupy the centers of half of the cubes created by F^- to maintain electro-neutrality as seen in Figure 1-1 of the fluorite unit cell. It is likely that the adjacent vacant cubes can accommodate ions or electrons, in order to maintain electroneutrality when Ca^{2+} is replaced by ions of different charges. Concentrations of ions in these vacancies may also explain some cases of coloration in fluorite. The arrangement of Ca in fluorite's crystal structure may partially control the ease of ionic substitutions and may influence sector zoning, as Rakovan (2009) suggested that the incorporation of ions on crystal sector surfaces during growth appears to be strongly controlled by structural limitations.

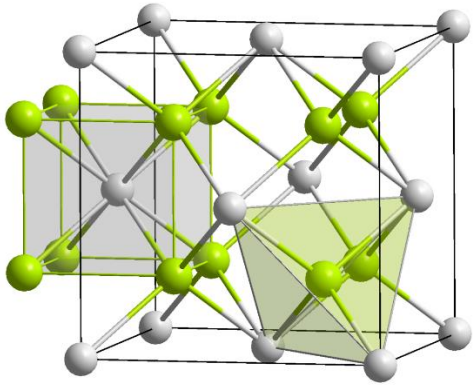

Figure 1-1

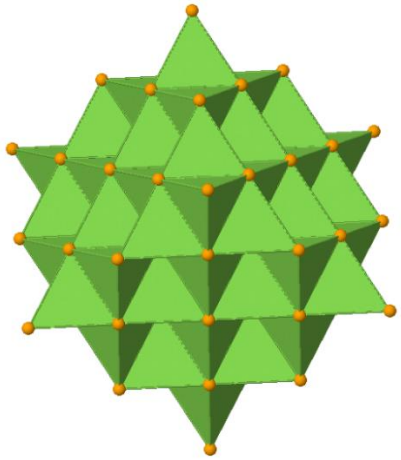

Figure 1-2

Figure 1-1 Fluorite unit cell, ball and stick model and demonstration of cubic (8-fold coordination of Ca^{2+} (grey) and tetrahedral (4-fold) coordination of F^- (green), (Solid State, 2014).
Note: If the cubic lattice was extended in the image, calcium would only occupy half of the cubic centers

Figure 1-2 Tetrahedral arrangement of fluorite. Ca^{2+} represented by orange spheres, with F^- (not visible) located at centers of tetrahedra, (Tem5psu, 2016).

The trace-element budget found in fluorite typically comes from replacement of the calcium cation by other elements of similar ionic charge ($^{2+}$) and effective ionic radius (1.26 Å) when in 8-fold coordination. Theoretically, substitutions for fluorine can also occur, and trace replacements by chlorine have been reported by Eppinger and Closs (1990). Figure 1-3 shows a comparison of effective cationic ($^{+2}$, $^{+3}$) radii that are similar to Ca^{2+} in 8-fold coordination, compiled from Shannon (1976). The elements of most similar size and charge, are the mostly likely to have favorable distribution coefficients in the mineral-forming environment to become trace-element substitutions for calcium. Trace elements found to replace Ca^{2+} recorded by Palache et al., (1951); Allen (1952); Deer et al., (1962); Greenwood

(1968); in Eppinger and Closs (1990), and by Eppinger and Closs (1990) include Al, Ag, Ba, Be, Cd, Cu, Fe, K, Mg, Mn, Na, Pb, Si, Th, U, Zr, and as mentioned above Cl can replace F. Gagnon et al., (2003) used the differences in Ba, Cu, K, Mg, Na, Nb, Pb, Rb, REE, Si, Sr, Th, U, Y, and Zn in varying phases of fluorite within several deposits to test if fluorite could be used to make paragenetical inferences about mineralizing fluids. Mao et al., (2016 a) determined that Y, Sr, and REE were essential for discriminating between fluorite formation sources while Ba, Th, and U could also prove useful. The ions listed here (Al, Ag, Be, Cu, K, Mn, Nb, Rb, Si, Th, U, and Zr) and in Figure 1-3 (Am, Ba, Bi, Cd, Co, Fe, Hd, Hg, In, Mg, Mn, Pb, Pm, Ra, Sc, Sr, Ti, Zn, and REE [La, Ce, Pr, Sm, Eu, Gd, Tb, Dy, Y, Ho, Er, Tm, Yb, Lu]) could be useful in developing fluorite as a geochemical indicator mineral, as they may assist in discerning between fluorite formation environments by comparison after trace-element analyses.

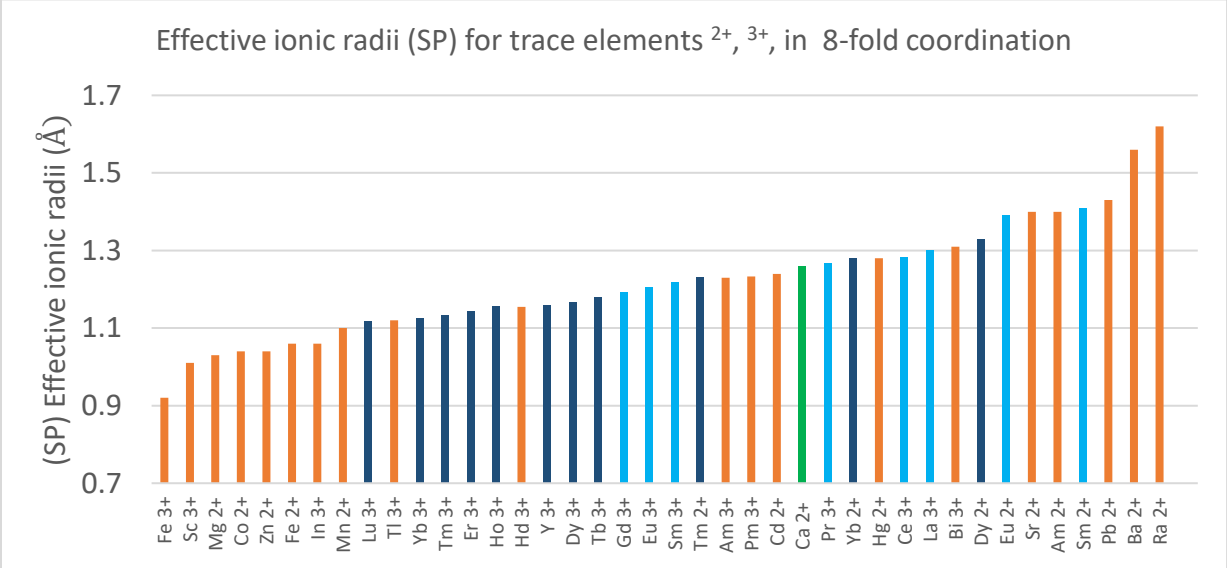

Figure 1-3 Effective ionic radii measured in Å for cations in 8-fold coordination of plus two and three charges compiled from Shannon (1976). "SP" refers to "SP 69," the author's original measurements for effective ionic radii that have been updated by their 1976 research. Data for Ca^{2+} is colored green, while data for HREE are colored dark-blue, LREE are colored light-blue, and all other trace elements are colored orange.

Considering the elements listed in Figure 1-3, one will notice oxidation states listed for REE include $^{2+}$ for Dy, Eu, Sm, Tm, and Yb and not listed here but compiled in Shannon (1976), $^{4+}$ for Ce, Pr, Sm, Tb, and Y, (also $^{5+}$ for Y). Concerning oxidation states of REE, Henderson (1984) stated that there are only evidences for the presence of Eu^{2+} and Ce^{4+} in natural systems manifested as significant anomalies in normalized REE patterns. Henderson (1984) explained that the presence of Yb^{2+} has been interpreted from negative Yb anomalies in natural systems, but the production of Yb^{2+} would require unrealistically reducing

conditions and its existence is unlikely. The production of Tb^{4+} is theoretically possible in natural systems, but its presence has not been observed, and the same claim was made by Goldschmidt, (1954) regarding Sm^{2+}, (Henderson, 1984). Finally, Henderson (1984) claimed that oxidation states could exist for other REE in manipulated chemistry, but it is unlikely that they exist in natural geochemical environments. According to this data, it is unclear why there is a discrepancy between Shannon (1976) and Henderson (1984) regarding the presence of reduced Dy, Sm and Tm as $^{2+}$ and oxidized Pr, Sm, Tb, and Y as $^{4+}$, where Shannon (1976) reported their effective ionic radius in mineralized systems implying potential existence in natural systems. It is possible that Shannon (1976) simply reported theorized calculations without considering the chemical limitations of natural systems as Henderson (1984) did, or that the presence of other cations within the fluorite structure can reduce ions post-mineralization as suggested by Zidarova (2003). Additionally, Zidarova (2003) reported the presence of Sm^{2+}, Eu^{2} and Yb^{2+} in fluorite using photoluminescence analyses and suggested a relationship between "donor and acceptor pairs" within the crystal between Dy, Sm, Yb, Y^{2+} and Ce^{4+}, and alternatively REE^{3+} and Fe^{2+} or Mg^{2+}, claiming these ions changed oxidation states post mineralization. From this data, it is possible that Dy, Eu, Sm, Yb, and Y^{2+}, and Ce, Tb, Y^{4+}, will be detectable in fluorite, and may be present in crystal structures due to oxidation states produced post mineralization.

REE replace Ca^{2+} by way of the following possible reactions: $2Ca^{2+} = REE^{3+} + Na^{+}$, $3Ca^{2+} = 2REE^{3+} + \boxdot$, or $Ca^{2+} = REE^{3+} + F^{-}$, (Möller et al., 1998 in Schwinn & Markl 2005), or $Ca^{2+} + 2F^{-} = REE^{3+} + O^{2-} + F^{-}$ (Vinokurov et al., 1963 from Sallet et al., 2005), and similarly charged cations can substitute for REE in these equations. Additionally, it is possible that trace elements could occupy lattice vacancies such as those present in half of the 8-fold coordinate cubic positions as noted in Figure 1-1. Charge compensation for these insertions are likely complex or varied.

A final condition that must be considered when using the trace element geochemistry of a mineral to assess genetic implications or conditions is whether or not the final composition reflects that which was entrapped during crystallization. In other words, could post-mineralization conditions effect the final trace-element geochemistry? One way the trace-element composition of a mineral could be altered after entrapment but before chemical analysis (besides secondary chemical processes like hydrothermal remobilization or alteration) is ionic diffusion. The diffusion of REE-Y and Sr in fluorite has been the focus of the work by Cherniak et al., (2001), and these authors demonstrate through analysis and

modeling that if fluorite resides at temperatures below ~650˚C in dry conditions at 1-atm, the trace-ionic content will remain stable for tens of millions to billions of years. "Fluorite grains of 1mm effective diffusion radius will retain initial Sr isotopic ratios when heated at 650˚C for times up to a few Ga, or at 750˚C for up to a few million years. REE isotope (or chemical) signatures (using Nd as an example) will be retained over about 100 Ma at 650˚C, and about 1 Ma at 750˚C," (Cherniak et al., 2001). The chemical signatures retained in fluorite should be those reflecting final mineralization processes such as mineralization, remobilization, or alteration, while ionic diffusion plays no role in fluorite chemical alteration at dry, near surface conditions, once the mineral cools from entrapment temperatures. However, if fluorite were to undergo metamorphism at similar temperatures at greater pressure conditions, ionic diffusion would be likely, if fluorite dissolution did not occur. Additionally, since Cherniak et al., (2001)'s study focused on measuring external to internal diffusion of ions into the mineral, the degree of mobility of ions already entrapped within fluorite is unclear.

1.2.2. Crystal habit

The arrangement of fluorite's ions as stacked cubes or tetrahedra (Figure 1-2) grants fluorite a high degree of symmetry allowing for modifications on crystal faces at many angles of many forms: cube, dodecahedron, hexoctahedron, tetrahexahedron, trapezohedron, trisoctahedron, (Offerman and Richards, 2006). This allows fluorite's crystal habit to form a continuum from cubes to spheres, such as the cubes, octahedrons, and dodecahedrons seen in Figure 1-3, to the "fluorite balls from hell" discovered in the Black Forest region of Teufelsgrund, modeled by Offerman and Richards, (2006) with 276 identified crystal faces. These rounded fluorite crystals can be seen in Figure 1-4 (a.) aside globally rare botryoidal fluorite, more common to the Deccan Traps of India Figure 1-4 (b.), (Richards, 2006). Crystal habit or morphology may indicate formational conditions, but a correlation of these causes would warrant further study. Additionally, final crystal morphology may not reflect internal growth structures, as Baele et al., (2012) demonstrated characteristically cubic crystals exhibited dodecahedral centers when examined by CL images of cleaved crystals.

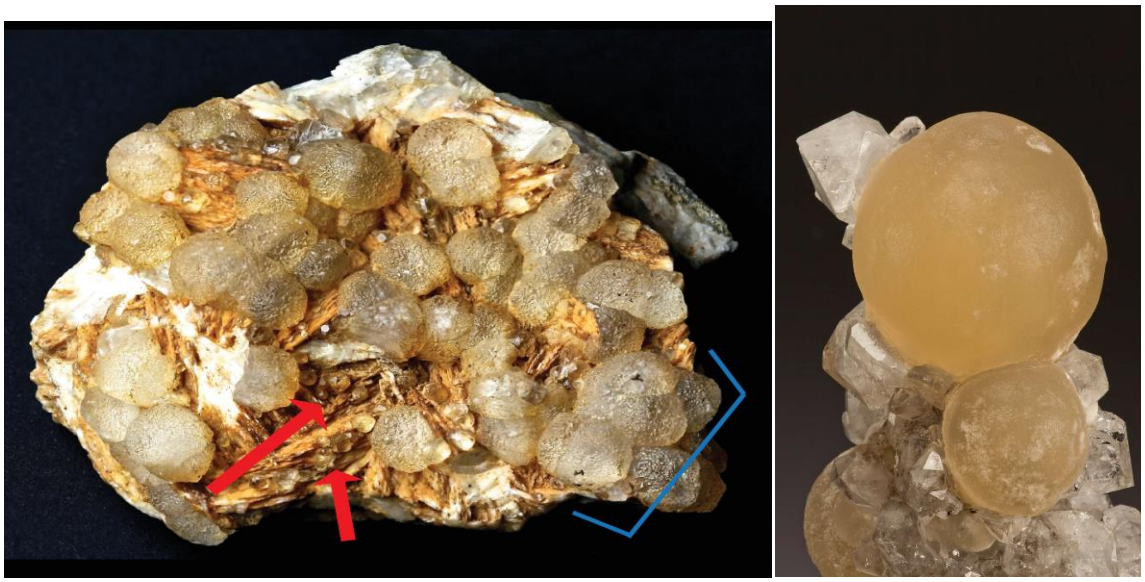

Figure 1-4 a.) Fluorite on barite from Teufelsgrund mine, Belchen, Münstertal, Black Forest, Baden-Württemberg, Germany, specimen dimensions: 7x5cm. Red arrows indicate "fluorite balls from hell" described by Offerman and Richards, 2006, as apparently spherical fluorite crystals composed of 276 faces. Blue bracket indicates botryoidal fluorite, (Klapproth, 2012).
b.) Yellow botryoidal fluorite sphere (3.5 cm diameter) on quartz from Mahodari, Nasik District, Maharashtra, India, (Budd, 2016).

1.2.3. Fluorite color and zoning

As mentioned above, fluorite exhibits a wide continuum of colors ranging from black to clear/colorless while commonly exhibiting complex patterns of growth and sector zonation (Rakovan, 2009). It is not clear what causes all colors in fluorite, but a combination of impurities/trace-element inclusions, mineral/fluid inclusions, interactions between contained ions, and factors affecting crystal structure such as structural/lattice defects are to cause (Allen, 1952; Braithwaite et al., 1973). It also appears that variables effecting emission of color or scattering by the lattice indicated by variations of refractive indices (Allen, 1952) may result in certain observations of fluorite color. Additionally, post-mineralization processes can impart color on fluorite such as radiation from sunlight or adjacent radioactive minerals or mineral inclusions, or from heating or compression of crystals. Therefore, final fluorite coloration may not always reflect initial formation conditions, but could reflect genetic deposit associative characteristics. Fluorite color has been investigated by many authors and some explanations are given below.

Staebler et al., (2006) outlined possible explanations for certain fluorite colors such as dark purple, purple, blue, light blue, green, pink, and yellow based on anecdotal studies. Some dark purple to nearly black fluorite can be explained by an excessive bombardment of

radiation, particularly when associated with uranium deposits, though radiation can be sourced from K, Gd, Lu, Nd, Sm, (Naldrett et al., 1987). According to Müller et al., (1960), some dark purple to blue fluorite can be explained by the presence of calcium colloids which are aggregates of neutral calcium ions that have diffused through the crystal after reduction by free electrons in fluorine vacancies. Wright (2003), explained green, blue, and purple coloration of fluorite by REE^{3+} substitution for calcium adjacent to a fluorine vacancy that houses two electrons. According to Staebler et al., (2006), light blue fluorite may be caused by Y^{2+} substitution and its interaction with a fluorine vacancy or by the presence of O^{2-} or OH^{-}. The latter of which would be unstable when exposed to ultraviolet radiation and therefore lightens in color when exposed to sunlight. According to Feofilov and Kapliansky (1962), irradiated and reduced Sm^{2+} in fluorite causes green coloration which is destroyed when heat oxidizes samarium back into a $^{3+}$ oxidation state, rendering the mineral colorless. Heat-stable green fluorite may be explained by the presence of Fe^{3+} adjacent to an F-vacancy according to Kempe et al., (2002). Pink fluorite from Mont-Blanc is caused by the presence of YO_2 according to Bill and Lacroix (1966), which is destroyed when heated in the presence of oxygen due to the release of O^{2-}. Finally, yellow fluorite can be explained by the replacement of two F^{-} by a single O^{2-} (Staebler et al., 2006). Trinkler et al., (2005) studied yellow fluorite and mostly determined low temperature formation with O_2 or O_3 with Na-. A study by Naldrett et al., (1987) determined REE patterns had no control on fluorite coloration, though increased total REE increased coloration intensity. The study by Braithwaite et al., (1973) determined that trace-element compositions were consist between colorless and blue to purple fluorite and that color was likely controlled by lattice defects which in turn could house calcium colloids.

Color combinations in fluorite can become more complex and therefore more desirable for collectors thanks to growth and sector zoning. These zonal patterns are observed not only as color changes but also via ultraviolet radiation and cathodoluminescent inspection. Zoning revealed by CL imaging suggests that the differences between zones are compositional, dominated by varied concentrations of major or trace-elements, including rare earth elements (a discussion of fluorescence in fluorite is yet to come). Variations in crystal growing conditions and rates lead to chemical and morphological differences observable as growth zones or gradients which follow the crystal faces concentrically. Variations observed between crystal sectors are potentially derived from differences in trace element incorporation between sectors mineralizing simultaneously. The latter can be

explained by preferential adsorption of impurities on specific growth faces and subsequently differing partitioning coefficients for certain trace elements for symmetrically non-equivalent sectors (Bosze and Rakovan, 2002; Rakovan, 2009), or alternatively by the uneven production of lattice defects on simultaneously growing faces. Partitioning coefficients for various ions are controlled by a variety of factors (growth rate, adsorption effects, fluid chemistry, temperature, and pressure) but the differences between specific ionic incorporation within the same mineralizing conditions is largely due to ionic charge and radius and the structure of the coordination site in which the ion is trying to enter (Bosze and Rakovan, 2002). Studies by Baele et al., (2012) and Smolyanski et al., (2009) seems to confirm these speculations where concentrations of the same trace elements vary across crystal sectors within equivalent growth zones, indicating variation of partitioning coefficients that must be correlated to strucutural differences between the crystal sectors. Alternatively, ionic diffusion into lattice defects whose abundance could vary between crystal sectors of equivalent growth zones could offer explanation to variable elemental concentrations.

The variety of color combinations in fluorite is not only appealing to collectors, but can offer suggestions and clues pertaining to mineralization history. These are complex systems with many controlling factors, but thanks to changes in fluorite color, we can quickly recognize that fluid conditions were either changing or favored the incorporation or formation of certain color centers along certain sectors. However, there are a lot of unknown variables involved in the attempt to offer explanation for changes in fluorite color. Therefore, systematic applications of various tests must be applied to deduce formational conditions across color changes including measurements of changes in chemical concentration, lattice damage, mineral inclusions, and fluid inclusions. Similar variations revealed by fluorescence and CL imaging suggesting changing conditions during mineral growth can be observed in fluorite or minerals of consistent color.

The causes of fluorite coloration are complex, sometimes varying between growth and sector zones and are occasionally capable of altering post-mineralization. Some color centers have been explained by concentrations of impurities and some color alterations have been explained by bombardment of radiation or the oxidation or release of ionic impurities. Furthermore, concentration differences of REE have been detected between growth sectors in the works of Baele et al., (2012), Smolyanski et al., (2009), and Bosze and Rakovan (2002), which in the latter two publications seemingly had no control over variable coloration

between sector zones whereas in the former publication, blue coloration was restricted to the cubic |100| sector. A study by Naldrette et al., (1987) determined that REE content had no control over fluorite coloration, though the overall concentration of REE seemingly affected coloration intensity. Since the mechanisms controlling fluorite coloration are complex, it is difficult to assess how much this mineral characteristic could contribute to genetic discriminatory efforts, if at all. Perhaps unique cases could contribute supplementary criteria to already developed discrimination procedures.

1.2.4. Fluorescence in fluorite and CL imaging

Just like coloration in fluorite, fluorescence and cathodoluminescence often display patterns of growth and sector zoning. Also like fluorite color, fluorescence produces a wide variety of colors. Cathodoluminescence is more limited in its typical color range, occurring most often as blue emissions caused by Eu, which overpowers spectra caused by other trace elements, but also displays ranges from whitish to pink to brownish (Baele et al., 2012). Fluorescence is often blue for the same reason, and both fluorescence and cathodoluminescence are commonly, but not exclusively, caused by the presence of trace REE (Verbeek, 2006). Fluorescence in fluorite as mentioned is most commonly blue, but can range from reddish, purple, pinkish, green, brown, yellow, and white. White-yellow fluorescence in fluorite can be influenced by hydrocarbon-containing inclusions such as those in samples from the Hastie Quarry deposit, Illinois, seen in Figure 1-5. Hydrocarbon-containing inclusions are typically limited to fluorite found in MVT and MVT-like deposits and thus, could provide a unique case of supplementary criteria for already developed discrimination procedures. However, like fluorite coloration, it is difficult to assess how much these characteristics could contribute to genetic discriminatory efforts without systematic study.

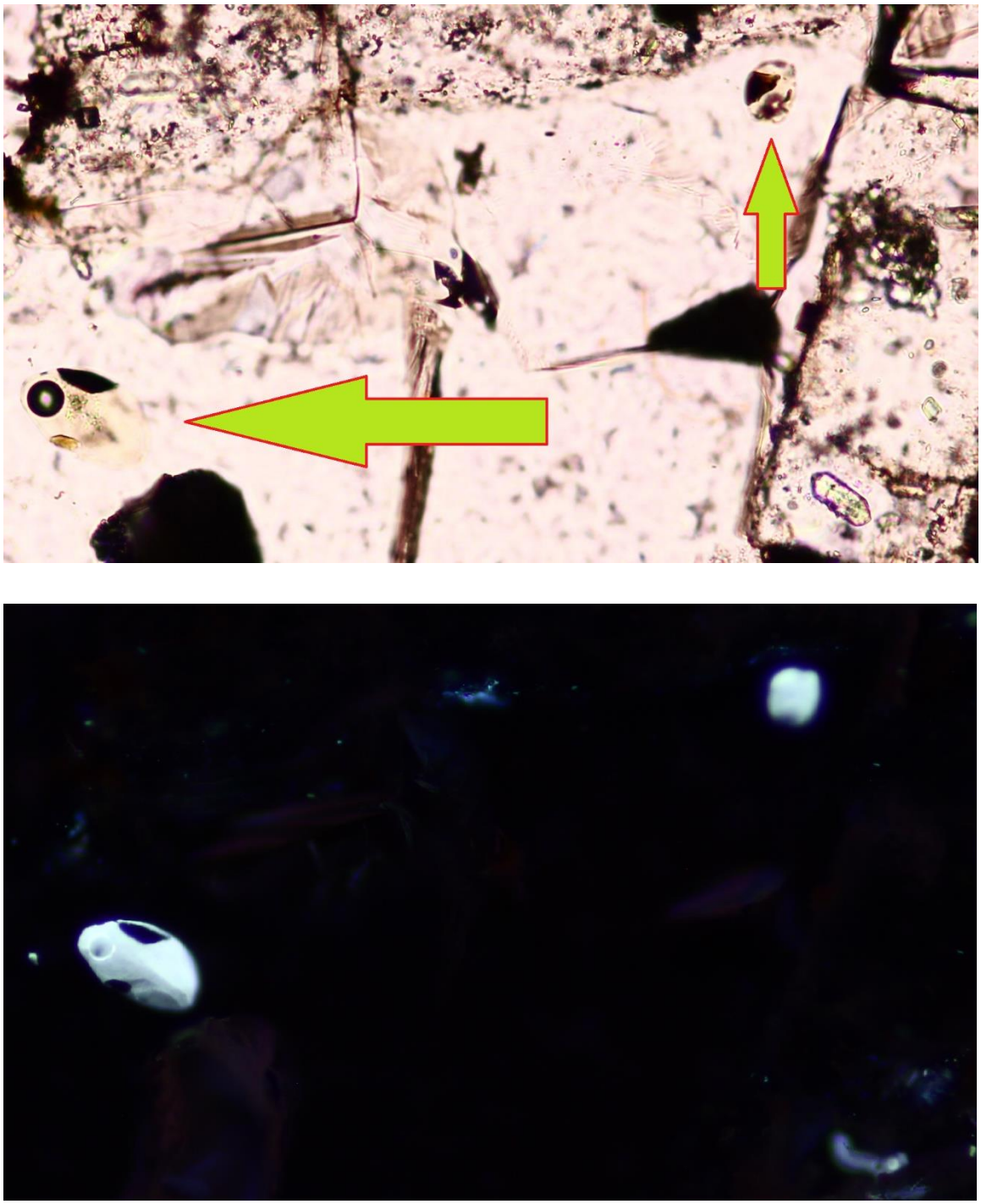

Figure 1-5 Microscope images of thick-section sample 3-12S-9E from Hastie Quarry deposit, Illinois in plain and shortwave UV light. Arrows point to two fluid inclusions containing hydrocarbons, dark bitumen (jagged black shapes), vapor bubbles, and other possible solids. Fluorescence of these inclusions appears bluish white to the naked eye.

1.3. REE and trace-element geochemistry

Since fluorite can mineralize in a wide variety of chemical environments and under highly variable physicochemical conditions, it is safe to assume that the fluid processes leading to fluorite growth are diverse. Fluorite can mineralize within igneous bodies via fluids derived from the mantle, and can also mineralize from the concentration of normal seawater in evaporitic environments at the surface of the Earth (Warren, 2006). From the included authors' works (ie: Gagnon et al., 2003; Hill et al., 2000; Schwinn & Markl, 2005; Zidarova, 2003), it is evident that complex hydrothermal processes often play roles in fluorite formation, sequestering trace elements from various rock and fluid sources via various chemical combinations and pathways.

This thesis is being completed under the assumption that dominantly, the trace-elemental contents of mineralizing fluids are unique to their definable genetic deposit types and that fluorite mineralizing in these environments records these chemical signatures. Additionally, this thesis concept is focused on creating a tool that could be useful for targeting specialty metal (REE) deposits apart from economic and non-economic deposit types containing fluorite within their respective mineral assemblages. Since many rare-earth minerals such as bastnäsite ($REECO_3F$) or fluocerite-(Ce) ($(Ce, La) F_3$) are fixed with fluorine, it has been suggested by Williams-Jones et al., (2012), and Migdisov and Williams-Jones (2014) that fluorine acts as binding ligand for these cations, evidenced by hydrothermal rare-earth deposits often containing significant fluorite (Metz et al., 1985; Williams-Jones et al., 2000; Xu et al., 2012). Because of this common association, coupled with fluorite's ability of REE (among other trace-elemental) uptake, it's seems reasonable that the REE (/trace-element) composition of fluorite may be a way to distinguish between these source deposit types.

Williams-Jones et al., (2012) and Migdisov and Williams-Jones (2014) demonstrated that the old interpretation of F^- behaving as a transport ligand for REE^{3+} based on theoretical interpretations of $REEF_3$ being more stable at ambient temperature than REE complexes with other ligands was outdated. These authors determined that the strong association of H^+ and F^- as HF and the low solubility of REE-F solids greatly limits the ability of fluoride complexes to transport REE in hydrothermal conditions. They showed that the more likely candidates for transport ligands are Cl^- in strongly acidic conditions, and SO_4^{2-} in weakly acidic conditions

(Migdisov and Williams-Jones, 2014). Additionally, through thermodynamic modelling Williams-Jones et al., (2012) showed that in a syenitic environment precipitating REE-bearing monazite, that initial deposition would produce monazite with heavy and light rare earth elements (HREE and LREE) of equal proportions. However, with continued fluid-rock interaction, LREEs would remobilize to be deposited in more distal portions of the deposit, while monazite of higher-temperature portions would become enriched in HREE. This remobilization of LREE is due to the heavier rare-earths forming more stable complexes than the LREE because of greater cation contraction and higher field strength. It seems possible that the same remobilization and recapture procedure outlined for monazite could be translated to fluorite deposited in different hydrothermal portions of deposits, and therefore REE-patterns in fluorite would prove variable for single deposits.

1.4. Previous discrimination diagrams

Attempts to sort fluorite mineralization sources from trace element patterns have been conducted since the late 1960's with increased interest due to innovations in analytical techniques, indicator mineral studies, and with increased interest in targeting rare-metal-containing deposits. The earliest discrimination diagrams between fluorite sources using trace-element content were created by Möller et al., (1976) distinguishing between fluorite formed in pegmatitic/pneumatolytic, hydrothermal, and sedimentary environments. This diagram used a comparison of La, Tb to determine the degree of fractionation of lanthanides, and stoichiometric values for Ca to determine the chemical environment in which fluorite mineralized. This work set the foundation for realizing fluorite's close association with enriched REE content, and sparked the initial interest in discriminating between mineralization environments using fluorite trace-element geochemistry that would later be investigated and adapted for the interest of economic targeting.

From then on, authors such as Eppinger and Closs (1990), Tümenbayar (1996), Hill et al., (2000), Zidarova (2003), and Mao et al., (2016 b) utilized the trace-element geochemistry in fluorite in attempts to distinguish between economic mineralization environments. Authors such as Gagnon et al., (2003), Schwinn and Markl (2005), and Vinokurov et al., (2014) used trace-element compositions of fluorite to draw other genetic inferences about fluorite formation environments, namely the resultant chemical differences

between fluorite phases and therefore potential differences between contributing fluids. Most success was achieved by authors seeking crystal chemical trends to represent fluorite genetic environments who utilized bulk analytical techniques such as Eppinger and Closs (1990), Hill et al., (2000), and Zidarova (2003). In contrast, authors utilizing analytical techniques with point precision (LA-ICP-MS) noticed differences in crystal chemical trends within the same fluorite crystal or sample and offered warning for caution when using the trace-element geochemistry as a tool for genetic implication including Gagnon et al., (2003), Schwinn and Markl (2005), Vinokurov et al., (2014). Baele et al., (2012) studied this problem exclusively and determined that partitioning coefficients for REE were different between fluorite |100| and |110| crystal growth sectors causing preferential enrichment of LREE in the |110| sector and subsequent HREE depletion. They noted that bulk analytical techniques would result in averaged REE patterns of sector-specific uptake. Additionally, Smolyanskii et al., (2009) determined similar results of preferential LREE enrichment of the |111| sector and comparatively HREE enrichment of the |100| sector. Finally, Mao et al., (2016 b) made two grain traverses using LA-ICP-MS analysis across a homogenous crystal of fluorite and determined three compositional zones. This crystal was cleaved "close to its |111| plane," however, the authors did not employ CL-imaging and it is unclear if these compositional zones represent different crystal sectors. Additionally, Mao et al., (2016 b) determined that the crystal chemical variability was less than that for all samples representing the same deposit, suggesting that chemical variability on the sample/grain-scale is less than that for the deposit, and the usefulness of this analytical tool is not compromised as such.

Much promise in using fluorite as a geochemical indicator of economic mineralization was introduced by the work of Eppinger and Closs (1990) in which the authors were able to differentiate between fluorite from barren veins, epithermal Au-Ag-Cu-Pb-Zn fissure veins, epithermal Ba-Pb fissure veins and W-Be-Fe skarn deposits within a single fluorine-rich, mineral-rich province in south-central New Mexico. Within this work, the authors even suggested that two of their vein localities initially described as "barren," exhibited fluorite compositions that could potentially indicate mineralization of economic interest at depth. The most effective comparison discovered by Eppinger and Closs (1990) was that of Eu anomalies and Sr, for which they explained is likely due to skarn and vein mineralization's relation to feldspar-rich intrusive bodies in which these elements preferentially incorporate. Other discrimination diagrams produced in this study include comparisons of Eu anomalies

to Ce anomalies and ratios indicating overall slope of chondrite-normalized REE patterns, as well as comparisons of Be to Ti, and U to Y.

Additional work in which fluorite trace-element content was used to describe economic association was included in the work by Tümenbayar (1996). This author, using 500 analyses on fluorite from deposits in Mongolia, distinguished between economic deposits of epithermal and hydrothermal fluorite from fluorite formed in non-economic pegmatite and magmatic-type deposits. The author accomplished these discriminations via logarithmic comparisons between Y and Yb content and the quantity of Gd in cubic or tetragonal coordination.

Gagnon et al., (2003) however, discovered fine-scale heterogeneity of trace-element compositions within optically homogenous fluorite crystals and between fluorite from different hydrothermal phases of the deposit when utilizing LA-ICP-MS analysis. Previous authors had all utilized bulk-method analyses to define discrimination diagrams correlating chemical variabily to genetic fluorite varieties. Gagnon et al., (2003) compared the compositions of magmatic and hydrothermal fluorite phases related to alkaline and granitic magmatism. They determined that chondrite-normalized patterns of REE from magmatic/primary fluorite were similar to those of the host alkaline magmatic rocks, whereas they differed slightly from host granitic rocks with differing Eu and Y anomalies. In contrast, hydrothermal fluorite exhibited more variable compositional trends, particularly between early- and late-stage mineralization, and these authors warned against utilizing fluorite trace-element abundances for identifying mineralization types without supplemental information regarding physico-chemical conditions for formation.

Schwinn and Markl (2005) also utilized LA-ICP-MS analyses across hydrothermal fluorite grain traverses to assess REE chemical variability. They analyzed samples from 63 post-Variscan hydrothermal veins containing varying assemblages of fluorite ±barite ±calcite ±quartz ±apatite and ±Cu ±Bi ±Ag ±Pb ±U ±Co ±Ni ±Fe ±Zn ±As ±Sb hosted in orthogneiss or paragneiss, Variscan granite, and a few in sedimentary rock. They identified two patterns on PAAS- (Post-Archean Australian Shale) normalized diagrams that dominated most sample analyses, which they linked to patterns exhibited by aquifer waters in either granitic or gneissic host rocks. The dominant patterns of REE in fluorite were identical to the patterns proposed for granitic or gneissic leachates, demonstrating a lack of fractionation of REE in

these hydrothermal conditions. They also compared their analyzed values using Tb/La vs. Tb/Ca proposed by Möller et al., (1976), to find that the two dominant groups either showed a fractionation trend or remobilization trend in their chemistries suggesting chemical links to granitic forming or metamorphic processes. Additionally, this work confirmed the fine-scale variability of trace-element chemistry in fluorite discovered by Gagnon et al., (2003) as fluorite exhibited either: a) homogenous distribution of REEs from core to rim, b) identical REE patterns with concentration gradients from core to rim, or c) variable concentrations and REE patterns from core to rim.

Vinokurov et al., (2014) warned against using geochemical data from single fluorite samples to infer genetic implications as the authors demonstrated substantial variability of the REE content in fluorite between different paragenetical zones distinguished initially by color and later by fluid inclusion analyses within single deposits. They demonstrated, however, that for two out of three deposits analyzed, the REE content found for all fluorite zones displayed identical chondrite-normalized patterns, but varied in concentration, while the REE chondrite-normalized pattern representing fluorite from one deposit displayed a concentration gradient for LREEs only (chondrite-normalized patterns of LREE displayed negative slopes in early fluorite phases and became positive for later phases). In addition, the concentration trends of deposits displaying consistent chondrite-normalized patterns for all fluorite phases mirrored each other where one deposit displayed progressive enrichment of REE concentration in later fluorite zones and the other, progressive depletion.

Hill et al., (2000) analyzed trace-element contents in fluorite from a variety of vein and replacement deposits across New Mexico, (and some of Arizona) using INAA methods. These authors expanded upon the work done by Eppinger and Closs (1990) by introducing microthermometric and isotopic analyses on fluid inclusions in fluorite in addition to trace-element analyses. These authors identified three groups of similarly formed fluorite through microthermometric analyses and determined that the majority of samples formed from "variably-exchanged" meteoric waters of either a) low-salinity (<8 eq. wt% NaCl) and low- to moderate-temperature (100-240℃), or b) low-moderate salinity (9-20 eq. wt% NaCl) and low- to moderate-temperature (120-200℃), or c) magmatic waters of high temperature and salinity. After determining these groups, the authors distinguished between fluorite from precious metal deposits formed by low-salinity epithermal processes using Sc/Eu, Sr content, and PAAS-normalized Tb/Yb and La/Yb ratios. The authors were not, however, able to

distinguish between fluorites formed by more moderately saline waters associated with base metals or W, V, or Mo. Finally, these authors recognized that fluorite geochemistry likely reflects fluid conditions, namely the composition of the mineralizing fluid.

Zidarova (2003) utilized the differences in contents of REE^{3+} and REE^{2+} determined by photoluminescence and X-ray luminescence analyses to assess chemical variability between different phases of fluorite between deposits. In addition to these methods, the author used optical and infrared spectroscopy to describe chemical centers and trace element contents as chemically related groups within the fluorite structure to specifically describe chemical substitutions and insertions which indicate definitively different mineralization conditions.

The work by Baele et al., (2012) revealed markedly different REE patterns in fluorite crystal sectors analyzed from single growth zones in fluorite crystals using LA-ICP-MS analysis. They noted that in crystals of fluorite from multiple deposits in Belgium, LREE preferentially partitioned into the |110| versus the |100| sector. This left the |100| more enriched in HREE, and the authors proposed that any resultant bulk analysis of crystals would represent an average value between included sectors. Similar results were founded by Smolyanski et al., (2012), where LREE seemingly partitioned preferentially into the |111| sector while the |100| sector contained greater concentrations of HREE. This concept is not new and work by Bosze and Rakovan (2002), assigned preferential partitioning for all REE into the |111| sector opposed to the |100| for samples from Long Lake, NY. However, they also reported that for fluorite crystals exhibiting up to four zones of sectors from Bingham, NM, that REE content varied less between sectors than between concentric growth zones.

Finally, Mao at al., (2016 b) published work in which they made important observations pertaining to useable trace elements in fluorite when analyzed with LA-ICP-MS methods and about trace-element variability between the grain and deposit scale. Out of 514 analyses on 38 samples, the authors found that 80% of the analyses returned detectable levels of Sr, Y, and all REE except Tm and Lu which were detected 70% of the time. Mg, Mn, Zr, Ba, W, Th, and U were detected in several analyses and show potential for discrimination between fluorites, and Fe was detected in nearly all samples, but showed little variation in concentration. Na, Ti, Nb, Mo, and Pb also showed little variation in concentration between analyses, while Sc, V, Cu, Zn, and Rb were rarely detected at all. Additionally, these authors

analyzed one optically homogenous sample along two grain traverses revealing three chemical zones out of 51 spot analyses. However, chemical variability across the single crystal grain was less than that found between all samples from the Rock Candy deposit for each of the elements analyzed listed in Figure 1-4. Chemical means and medians are nearly equivalent for each of these elements and the central half of data (Q1-Q3) for each group are nearly equivalent (Figure 1-4). Because the range of fluorite composition measured on the grain-scale was less than that measured between all samples from same deposit, grain-scale chemical heterogeneity of fluorite may not pose a problem in using the trace-element composition of fluorite to distinguish between source deposits. Furthermore, the overall patterns of chondrite-normalized trace-element compositions were relatively consistent despite overall concentration variability, suggesting diagrams employing elemental ratios could accommodate variability of fluorite composition on the grain- or sample-scales.

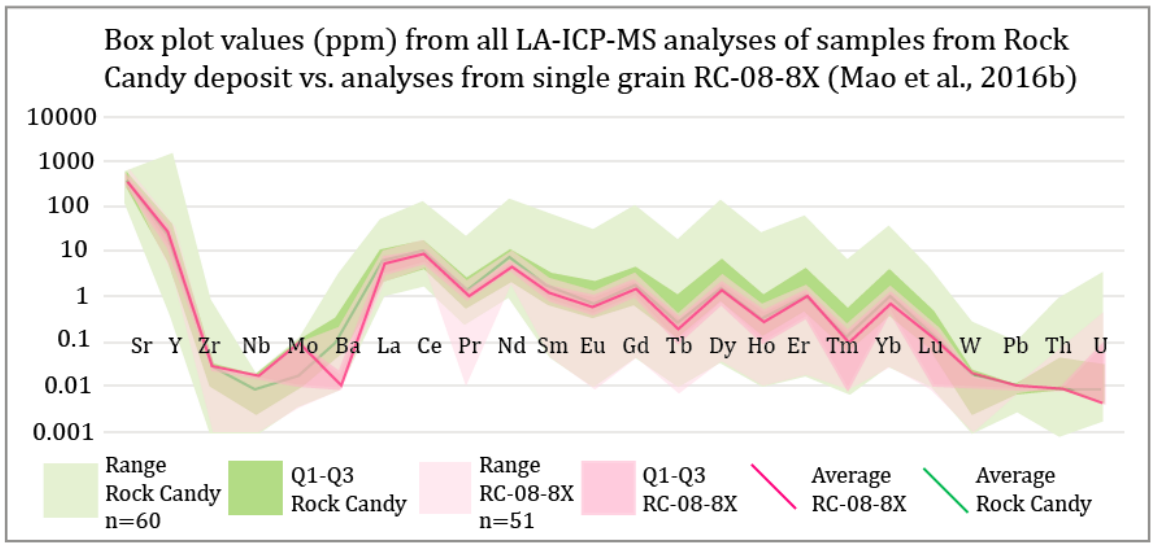

Figure 1-6 Trace element comparisons between all samples and multiple analyses of single crystal from Rock Candy deposit from Mao et al., 2016 b. Boundaries for minimum to maximum values and upper and lower bounds of 50% of analyses (Q3, Q1) and median values for 51 LA-ICP-MS analyses of sample RC-08-8X from the Rock Candy fluorospar deposit and 60 analyses from different samples from the Rock Candy deposit.

In summary, previous works revealed that the trace-element content of fluorite could potentially be utilized to identify genetic deposit types. Authors noted differences between multiple chemical analyses in single crystals and deemed bulk-method analytics as inadequate to describe the true nature of fluorite trace-element content. Baele et al., (2012) determined greater partitioning coefficients for LREE than HREE in the |110| growth sector relative to |100| and Smolyanskii et al., (2009) determined similar results for the |111| sector

relative to |100|. All of the samples from both of these works were collected from veins or replacement/karstic bodies hosted in carbonate rocks, so it is unclear if this partitioning behavior only operates in this type of mineral forming environment. If fluorite partitions REE unequally between growing crystal sectors, then attention must be made when employing analytical methods for their detection. It seems that the proper analytical procedure when analyzing fluorite grains would be to mount them in polished epoxy pucks, and employ CL-imaging in order to capture point-precise analyses in all represented crystal growth sectors. Mao et al., (2016 b) attempted to dispel concerns about fluorite chemical variability in single crystals by demonstrating the variability detected along two grain traverses was less than that detected for all samples from a single deposit. Not noted by Mao et al., (2016 b) however, was that the patterns of trace-element composition in fluorite were consistent on the crystal-scale and between samples, which suggests elemental ratios could be employed for discriminatory purposes.

1.5. Goals of this thesis

It is the objective of this thesis to compose a database of all reported trace-element compositions of fluorite, to sort these data into workable classified groups based on deposit geneses with economic implications, and to investigate the possibility of discrimination between these groups on scatter diagrams that could prove useful to the exploration community. Grain-scale chemical heterogeneity will also be addressed as will sample-scale chemical variability. The possible trace elements that could be implemented for this purpose are outlined above and include Al, Ag, Am, Ba, Be, Bi, Cd, Cl, Co, Cu, Fe, Hd, Hg, In, K, Mg, Mn, Nb, Pb, Pm, Ra, Rb, Sc, Si, Sr, Th, Ti, U, Zn, and REE (La, Ce, Pr, Sm, Eu, Gd, Tb, Dy, Y, Ho, Er, Tm, Yb, Lu). Mao et al., (2016 b) determined that Y, Sr, and REE were essential for discriminating between fluorite formation sources while Ba, Th, and U could also prove useful. There are additional properties of fluorite that could potentially be utilized for discriminatory purposes, as these properties originate (mostly) during fluorite formation and could therefore represent genetic characteristics. These properties include: fluorite color or fluorescence, mineral inclusions, and parameters that could be assessed from studies on fluid inclusions. Correlating these properties to genetic fluorite types could improve the precision of diagrams created herein, a topic that will be discussed in the conclusion as a proposal of future work.

1.6. References

1. Allen, R.D., 1952. Variations in chemical and physical properties of fluorite; American Mineralogist, v. 37, (910-930).
2. Baele., J-M., Monin, L., Navez, J., André, L., 2012. Systematic REE partitioning in cubo-dodecahedral fluorite from Belgium revealed by cathodoluminescence spectral imaging and Laser Ablation-ICP-MS; 10th International Congress for Applied Mineralogy (ICAM), (23-30).
3. Belousova, E.A., Griffin, W.L., O'Reilly, S.Y., Fisher, N.I., 2002. Apatite as an indicator mineral for mineral exploration: trace-element compositions and their relationship to host rock type; Journal of Geochemical exploration, v. 76, (45-69).
4. Bill, H., Lacroix, R., 1966. E.P.R. of a centre in Y3+ doped and artificial CaF2 crystal; Physics Letters, v. 22, (250).
5. Bosze, S., and Rakovan, J., 2002. Surface structure controlled sectoral zoning of the rare-earth elements in fluorite from Long Lake, N.Y. and Bingham, N.M.; Geochimica et Cosmochimica Acta, v. 66, (997-1009).
6. Bouzari, F., Hart, C.J.R., Bissig, T., Barker, S., 2016. Hydrothermal alteration revealed by apatite luminescence and chemistry: a potential indicator mineral for exploring covered porphyry copper deposits; Economic Geology, v. 111, (1397-1410).
7. Braithwaite, R.S.W., Flowers, W.T., Haszeldine, R.N., Russell, M., 1973. The cause of the colour of Blue John and other purple fluorites; Mineralogical Magazine,
8. Budd, J., 2016. Fluorite on Quartz, specimen TUC14B-1279, on The Arkenstone at www.iRocks.com, last accessed 4 March 2017.
9. Černý, P., 1991. Rare-element granitic pegmatites. Part I: Anatomy and internal evolution of pegmatite deposits. Geoscience Canada, v. 18, n. 2, (49-67).
10. Cherniak, D.J., Zhang, X.Y., Wayne, N.K., Watson, E.B., 2001. Sr, Y, and REE diffusion in fluorite. Chemical Geology, v. 181, (99-111).
11. Deer, W.A., Howie, R.A., Zussman, J., 1962. Rock-forming minerals, nonsilicates; New York, John Wiley Sons, v. 5, (347-356)
12. Dredge, L.A., Kerr, D.E., Kjarsgaard, L.M., Knight, R.D., Ward, B.C., 1997. Kimberlite indicator minerals in till, central Slave Province, Northwest Territories. Geological Survey of Canada, Open File 3426.
13. Elliot, J.E., Kamilli, R.J., Miller, W.R., Livo, K.E., 1995. Vein and greisen Sn and W deposits (Models 15a-c; Cox and Bagby, 1986; Reed, 1986a, b); Summary of relevant geologic, geoenvironmental, and geophysical information, (62-69).
14. Eppinger, R., Closs, L.G., 1990. Variation of trace elements and rare earth elements in fluorite: a possible tool for exploration; Economic Geology, v. 85, (1896-1907).
15. Feofilov, P.P., Kaplyanskii, A.A., 1962. Spectra of divalent rare-earth ions in crystals of alkaline-earth fluorides; Gpt. Spectr., USA, v. 12 (272).
16. Fisher, J., Lillie, R., Rakovan, J., 2013. Fluorite in Mississippi Valley-type deposits. Rocks and Minerals, v. 88, n. 1, (20-49).
17. Fournier, A., 1993. Magmatic and hydrothermal controls of LREE mineralization of the St. Honoré carbonatite, Québec. M.Sc. Thesis, Department of earth and planetary sciences, McGill University, Montreal, Canada, (95 pgs).
18. Friske, P.W.B., McCurdy, M.W., Day, S.J.A., McNeil, R.J., 2001. Evaluation of total, partial and selective leach data from humus, B horizon and till: a case study from the Clarence Stream gold property, southern New Brunswick. Carroll, B.M.W., (ed.) Current Research 2000. Mineral Resource Report, 2001-4. New Brunswick Department of Natural Resources and Energy, Minerals and Energy Division, (25-45).
19. Friske, P.W.B., Prior, G.J., McNeil, R.J., McCurdy, M.W., Day, S.J.A., 2003. National Geochemical Reconnaissance (NGR) stream sediment and water survey in the Buffalo Head Hills area, northern Alberta including analytical, mineralogical and kimberlite indicator mineral data from silts, heavy mineral concentrates and waters. Open File, 1790. Geological Survey of Canada.
20. Goldschmidt, V.M., 1954. Geochemistry, Clarendon Press, Oxford, (730 pgs).
21. Gagnon, J.E., Samson, I.M., Fryer, B.J., Williams-Jones, A.E., 2003. Compositional heterogeneity in fluorite and the genesis of fluorite deposits: insights from LA-ICP-MS analysis. The Canadian Mineralogist, v. 41, (365-382).
22. Gent, M., Menendez, M., Torañ̃o, J., Torno, S., 2011. A review of indicator minerals and sample processing methods for geochemical exploration. Journal of Geochemical Exploration, v. 110, (47-60).

23. Greenwood, N.N., 1968. Ionic crystals, lattice defects, and non-stoichiometry; Butterworths Co., London, (194 pgs).
24. Henderson, P, (ed.) 1984. Rare Earth Element Geochemistry in Developments in Geochemistry v. 2 Elsevier Science B.V., Amsterdam, Nederlands, (pp. 510). ISBN: 0-444-42148-3
25. Hill, G.T., Campbell, A.R., Kyle, P.R., 2000. Geochemistry of southwestern New Mexico fluorite occurrences implications for precious metals exploration in fluorite-bearing systems; Journal of Geochemical Exploration, v. 68, (1-20).
26. Hora, Z.D., 1996. Vein fluorite-barite, in Selected British Columbia mineral deposit profiles, (eds.) Lefebure, D.V., Höy, T.; British Columbia Ministry of Energy, Mines and Petroleum Resources, v. 2, (85-87).
27. Kempe, U, Plötze, M., Brachmann, A., Böttcher, R., 2002. Cathodoluminescence in the geosciences; Mineralogy and Petrology, v. 76, (213-234).
28. Klapproth, H., 2012. Fluorite, Baryte, Teufelsgrund mine, from mindat.org, last accessed 4 March 2017.
29. Mackay, D.A.R., Simandl, G.J., 2015. Pyrochlore and columbite-tantalite as indicator minerals for specialty metal deposits. Geochemistry: Exploration, Environment, Analysis, v. 15, (167-178).
30. Makin, S.A., Simandl, G.J., Marshal, D., 2014. Fluorite and its potential as an indicator mineral for carbonatite-related rare earth element deposits. Geological Fieldwork 2013, British Columbia Ministry of Energy and Mines Survey Paper 2014-1, (207-212).
31. Mao, M., Rukhlov, A.S., Rowins, S.M., Spence, J., Coogan, L.A., 2016b. Apatite trace element compositions: a robust tool for mineral exploration. Economic Geology, v. 111, (1187-1222).
32. Mao, M., Simandl, G.J., Spence, J., Neetz, M., Marshall, D., 2016a. Trace element composition of fluorite and its potential use as an indicator in mineral exploration. Geological Fieldwork, 2015, British Columbia Ministry of Energy and Mines, British Columbia Geological Survey Paper 2016-1, (181-206).
33. McClenaghan M.B., Ward, B.C., Kjarsgaard, I.M., Kjarsgaard, B.A., Kerr, D.E., Dredge, I.A., 2000. Indicator mineral and till geochemical dispersal patterns associated with the Ranch Lake kimberlite, Lac de Gras region, NWT, Canada. Geochemistry: Exploration, Environment, Analysis, v. 2, 299-320.
34. McClenaghan M.B., Kjarsgaard, B.A., Kjarsgaard, I.M., 2002. Kimberlite indicator mineral content and geochemistry of till around the Peddie kimberlite, Lake Timiskaming, Ontario. Open File, 4262. Geological Survey of Canada.
35. McClenaghan, B.M., 2005. Indicator mineral methods in mineral exploration. Geochemistry: Exploration, Environment, Analysis, v. 5, (233-245).
36. Metz, M.C., Brookins, D.G., Rosenberg, P.E., Zartman, R.E., 1985. Geology and geochemistry of the Snowbird deposit, Mineral County, Montana; Economic Geology, v. 80, 394-404.
37. Migdisov, A.A., Williams-Jones, A.E., 2014. Hydrothermal transport and deposition of the rare earth elements by fluorine-bearing aqueous liquids; Mineralium Deposita, v. 49, (987-997).
38. Möller, P., Bau, M., Dulski, P., Lüders, V., 1998. REE and Y fractionation in fluorite and their bearing on fluorite formation; Proceedings of the Ninth Quadrennial IAGOD Symposium. Schweizerbart, Stuttgart, (575-592).
39. Möller, P., Parekh, P.P., Schneider, H.-J., 1976. The application of Tb/Ca-Tb/La abundance ratios to problems of fluorspar genesis. Mineralium deposita, v. 11, (111-116).
40. Müller, G., Recke, W., Vera Mega, L., 1960. Interrelations between coloration, absorption spectra and radioactivaties of fluorites from diverse localities; Acta Crystallographica, v. 13, (1009).
41. Naldrett, D.L., Lachaine, A., Naldrett, S.N., 1987. Rare-earth elements, thermal history, and the colour of natural fluorites; Canadian Journal of Earth Sciences, v. 24, (2082-2088).
42. Offerman, E., Richards, R.P., 2006; in No. 9 Fluorite - the Collector's Choice; ed. Fisher, J., Jarnot, M., Neumeier, G., Pasto, A., Staebler, G., Wilson; publ. Lithographie, LLC, East Hampton, Connecticut, USA, (20-25).
43. Palache, C., Berman, H., Frondel, C., 1951. The system of mineralogy of James Dwight Dana and Edward Salisbury Dana; John Wiley and Sons, v. 2, ed. 7.
44. Pell, J., 1994. Carbonatites, nepheline syenites, kimberlites and related rocks in British Columbia; Province of British Columbia Ministry of Energy, Mines, and Petroleum Resources Bulletin 88, (136 pgs).
45. Porter, T.M., 2000. Hydrothermal iron-oxide copper-gold and related ore deposits; in Porter, T.M., (ed.); Hydrothermal iron-oxide copper-gold and related deposits a global perspective; PGC publishing, Adelaide, v. 1, (3-5).
46. Rakovan, J., 2007. Greisen; Word to the wise. Rocks and Minerals, v. 82, (157-159).
47. Rakovan, J., 2009. Sectoral Zoning; Word to the wise. Rocks and Minerals, v. 84, (171-176).

48. Richards, R.P., 2006. Botryoidal fluorite; in No. 9 Fluorite - the Collector's Choice; ed. Fisher, J., Jarnot, M., Neumeier, G., Pasto, A., Staebler, G., Wilson; publ. Lithographie, LLC, East Hampton, Connecticut, USA, (25).
49. Sallet, R., Moritz, R., Fontignie, D., 2005. The use of vein fluorite as probe for paleofluid REE and Sr-Nd isotope geochemistry: The Santa Catarina Fluorite District, Southern Brazil; Chemical Geology, v. 223, (227-248).
50. Schwinn, G., Markl, G., 2005. REE systematics in hydrothermal fluorite. Chemical Geology, v. 216, (225-248).
51. Shannon, R. D., 1976. Revised effective ionic radii and systematic studies of interatomic distances in halides and chalcogenides; Acta Crystallographica, A 32, (751-767).
52. Simandl, G.J., Prussin, E.A., Brown, N., 2012. Specialty Metals in Canada. British Columbia Geological Survey Open File 2012-7.
53. Solid State, 2014. CaF_2 polyhedra; Wikimedia Commons, 27 June 2014, last accessed 11 February 2017.
54. Smolyanskii, P.L., Proskurnin, V.F., Bogomolov, E.S., 2009. Growth dissymmetrization of rare earth element distribution and the Sm-Nd isotope system in fluorite crystals of the Nordvik Deposit (Taymyr). Doklady Earth Sciences (Geochemistry), v. 424, No. 1, (86-89).
55. Staebler, G., Deville, J., Verbeek, E., Richards, R.P., Cesbron, F., 2006. Fluorite: from Ancient Treasures to Modern Labs and Collections; in No. 9 Fluorite - the Collector's Choice; ed. Fisher, J., Jarnot, M., Neumeier, G., Pasto, A., Staebler, G., Wilson; publ. Lithographie, LLC, East Hampton, Connecticut, USA, (4-12).
56. Stendal, H., Theobald, P.K., 1994. Heavy-mineral concentrates in geochemical exploration. Hale, M., Plant, J.A., (eds.) Drainage Geochemistry. Handbook of Exploration Geochemistry, v. 6, (185-225).
57. Tem5psu, 2016. Polyhedral-fluorite; Wikimedia Commons, 27 November 2016, last accessed 11 February 2017.
58. Trinkler, M., Monecke, T., Thomas, R., 2005. Constraints on the genesis of yellow fluorite in hydrothermal barite-fluorite veins of the Erzgebirge, Eastern Germany: evidence from optical absorption spectroscopy, rare-element data, and fluid-inclusion investigations; The Canadian Mineralogists, v. 43, (883-898).
59. Tümenbayar, B., 1996. REE in different types of fluorites; 30th International Geological Congress, Beijing, China, 2, 685.
60. Verbeek, E., 2006. Fluorite Luminescence; in No. 9 Fluorite - the Collector's Choice; ed. Fisher, J., Jarnot, M., Neumeier, G., Pasto, A., Staebler, G., Wilson; publ. Lithographie, LLC, East Hampton, Connecticut, USA, (13-19).
61. Vinokurov, S.F., Golubev, V.N.., Krylova, T.L., Prokof'ev, V.Yu., 2014. REE and fluid inclusions in zoned fluorites from Eastern Transbaikalia: distribution and geochemical significance. Geochemistry International, v. 52, no. 8, (654-669).
62. Vinokurov, U.M., Zaripov, M.M., Polsky, Y.E., Stepanov, U.G., Chirkin, G.K., Shekun, L.Y., 1963. Electron paramagnetic resonance determination of trace amounts of Eu2+, Gd3+ and Nb4+, and their isomorphism in fluorite and zircon. Geochem. International, v. 11, (1041-1046).
63. Warren, J.K., 2006. Evaporite karst and indicator, in Evaporites: Sediments, Resources and Hydrocarbons. Springer, Berlin, Heidelberg, New York, (pp. 1036), ISBN: 3-540-26011-0
64. Williams-Jones, A.E., Migdisov, A.A., Samson, I.M., 2012. Hydrothermal mobilisation of the Rare Earth Elements – a tale of "ceria" and "yttria"; Elements, v. 8, (355-360).
65. Williams-Jones, A.E., Samson, I.M., Olivio, G.R., 2000. The genesis of hydrothermal fluorite-REE deposits in the Gallinas Mountains, New Mexico; Economic Geology, v. 95, 327-342.
66. Wright, C., 2003. Spectroscopic characterization of fluorite: Relationships between trace element zoning, defects and color. M.Sc. Thesis, Miami University, (189 pgs).
67. Xu, C., Taylor, R. N., Li, W., Kynicky, J., Chakhmouradian, A. R., Song, W., 2012. Fluorite geochemistry from REE deposits in the Panxi region and Bayan Obo China; Journal of Asian Earth Sciences, v. 57, (76-89).
68. Zidarova, B., 2003. Rare earth elements in natural fluorite as indicators of the mineral-forming environment. Geologie, Minéralogie, Comptes rendus de l'Académie bulgare des Sciences, t. 56, no. 11, (19-26).

Chapter 2.

Deposit classification and fluorite trace-element database

2.1. Introduction

In order to assess the potential of targeting economic deposits using discrimination diagrams based on the trace-element geochemistry of fluorite, a classification scheme describing fluorite-associated deposits must be established. The ideal application of these discrimination diagrams is to determine potential source deposits from detrital fluorite collected during stream sediment surveys. General "deposit-types" are an ideal classification criteria for discriminatory purposes as their descriptions include resultant mineralogy and metallogeny, the targeting of which is the proposed purpose of this exercise. Within this chapter, the classification scheme employed to describe fluorite occurrences of economic interest will be outlined and described, manipulation of compiled datasets and arguments for inclusion will be provided, representation quality of defined classification groups will be offered, and a summary of deposits for which the utility of created discrimination diagrams were tested with will be described.

The classification scheme designed herein includes "primary mineralization environments" and "secondary mineralization environments," though discrimination diagrams will only be generated using primary mineralization environment groups (e.g., MVT, carbonatite-related, greisen). Secondary mineralization environment classifications were provided to satisfy situations where deposits could be interpreted as more than one type (i.e., carbonatite-related and peralkaline silicate igneous deposits in a peralkaline intrusion/carbonatite complex). Additionally, information pertaining to commodities included within categorized "deposit-types" could be useful to the user and these classifications were also provided, though not utilized directly in creating discrimination diagrams. These groups include "metallic economic association" and "recovered/targeted/prospected commodity groups" and were described to provide the user of discrimination diagrams information about recoverable materials associated with deposit-type groups. For instance, certain deposit-types could be targeted for a variety of commodities and are not exclusively targeted for a specific suite of metals or elements such

as MVT's for fluorite and/or base metals, or carbonatite-related deposits for fluorite and/or specialty metals, opposed to greisens which are typically targeted for tin and/or tungsten exclusively.

The manipulation of data compiled within this study must also be described as the multiple publications from which data were extracted utilized a variety of analytical procedures and methods (ICP-MS, ICP-AES, INAA, LA-ICP-MS). Data must be managed accordingly to promote compatiblitiy between datasets, such as between point precision or bulk analytical methods, and the inclusion of data analyzed by several methods should be compared. Additionally, direct comparisons of trace-elements merely provide correlations, so calculations were made to maximize discrimination between primary mineralization environment groups and these calculations will therefore be described, including formulas created by discrimination projection analyses. Arguments for data inclusion and descriptions of data manipulation and calculations are described below.

Furthermore, representation of primary mineralization environment groups by compiled data should also be examined to offer a measure of credibility for the accuracy of generated datafields on discrimination diagrams. To this end, a hierarchy based on representation quality of deposit-type groups was determined by assessing sample sizes per group, data source diversity, and by examining univariate normality per REE-Y before and after logarithmic transformations, using histograms, Q-Q plots, and Shapiro-Wilk tests. This information is necessary for the user of discrimination diagrams, as all deposit-type groups are not equally represented and assigning primary mineralization environments to test data can be more accurately executed with knowledge of representation priority.

An evaluation of the utility of the discrimination diagrams produced herein is also necessary and these diagrams will be tested using analyses (FUS-ICP/MS) on a small collection of 11 fluorite samples from eight North American deposits. Results returned from discrimination diagrams for these North American deposits will be compared to primary mineralization environments assigned via literature review using the classification scheme determined herein. Brief summaries of test deposits and assigned primary mineralization environments are included within this chapter. Additionally, one crystal sample from Illinois that exhibited optically heterogeneous sector-zoning was analyzed using LA-ICP-MS analysis

to compare to FUS-ICP/MS analyses for the same sample and to determine grain-scale compositional consistency (Appendix D).

2.2. Classification scheme

In creating this classification scheme, previously published trace-element data for fluorite occurrences around the world were compiled and compared. These deposit descriptions and characterizations were based on this author's interpretation of the cited authors' interpretations. None of the deposits or mineralized bodies were visited by the writing author. All information summarized in this compilation is based on the assumption that the cited works and works therein are accurate and true. Primary and secondary mineralization environments were categorized to represent groups within the compiled dataset, though only primary mineralization environments were used to create discrimination diagrams. Additional categorization groups were assigned to indicate the economic interests of compiled deposits, particularly if the deposits were targeted for metals or industrial minerals (metallic economic association), and the specific commodities targeted, prospected, or recovered from compiled deposits. In theory, these additional groups could also be utilized for the creation of discrimination diagrams but that was not executed herein.

From 32 publications, 12 primary fluorite-containing deposit-types and four subtypes were determined to create user-friendly discrimination diagrams based on the REE content of their fluorite. Deposit-types were assigned to data sources according to ore deposit formation models familiar to the mineral exploration community (eg., MVT, skarn, greisen), as well as by using those invented by the author for specific descriptive purposes (eg., granite-related uranium, intrusion-related molybdenum). Deposit types with generally accepted phenotypic models include Mississippi Valley type (MVT) deposits, sedimentary exhalative (SEDEX) deposits, skarns, and greisens; while those having less conventional formation models include iron oxide copper gold (IOCG) deposits and carbonatites. Several compiled publication localities included economic targets in addition to fluorite associations but did not fit conventional models based on physical characteristics. These occurrences were therefore accommodated by describing like-characteristics and assigning "deposit types" invented by the author. Like-characteristics considered include host rocks and/or host

intrusions, mineral assemblages, and metallic or non-metallic commodities contained, or potentially contained therein. These invented primary mineralization environments include intrusion-related molybdenum, granite-related uranium, and cryolite deposits.

Primary mineralization environments characterized to produce discrimination diagrams include the following based on a representative hierarchy determined in the following sections: 1.) hydrothermal/epithermal vein/replacement deposits in igneous hosts, 2.) MVT deposits, 3.) hydrothermal/epithermal vein/replacement deposits in carbonate hosts, 4.) carbonatite-related deposits, 5.) hydrothermal/epithermal vein/replacement deposits in metamorphic hosts, 6.) SEDEX deposits, 7.) skarn deposits, 8.) greisen deposits, 9.) intrusion-related molybdenum deposits, 10.) cryolite deposits, 11.) peralkaline silicate igneous rock deposits 12.) hydrothermal/epithermal vein/replacement deposits hosted in sedimentary rock, 13.) rare-metal pegmatites, 14.) granite-related uranium deposits, and 15.) IOCG deposits.

Secondary mineralization environments were assigned to compiled data to accommodate localities where the composition of recovered fluorite could be interpreted as being influenced by rocks or processes related to more than one deposit type (ie., peralkaline silicate igneous rock and carbonatite-related deposits which are commonly found within the same igneous complexes). An additional deposit-type was also determined that was only represented in the secondary category; alkaline silicate igneous rock deposits. This group was established as a general descriptive type that would unify specific primary mineralization environment groups that are generated in relation to alkaline igneous activity such as greisen, granite-related uranium, rare-metal pegmatite, and some skarn deposits. Unfortunately, discrimination diagrams utilizing secondary mineralization environments were not created within this thesis due to time constraints.

Primary and secondary mineralization environment assignations are illustrated in Table A-11 and Table A-22 of Appendix A. Criteria for classifying these deposit types are listed below, while brief summaries based on source publications of the included deposits within each group are located in Appendix B.

Additionally, data were sorted into groups according to metallic economic association as primary, secondary, or none. If a deposit described in its respective publication(s) mentioned metallic commodities, the data were sorted according to how these metals were

targeted/mined as primary or secondary commodities. If there was no metallic target other than industrial minerals such as fluorospar or fluorite, the deposit and data were classified under "none." This information was provided for the user of discrimination diagrams to indicate economically interesting details about data included to generate datafields. As mentioned above, carbonatite-related deposits can be targeted for metals or industrial minerals exclusively and data from both producing varieties were compiled to represent that group such as carbonatites from the Panxi and Bayan Obo regions of China (Xu et al., 2012) and those at Okorusu, Namibia (Bühn et al., 2003) or Speewah, Australia (Alvin et al., 2003).

Finally, data were sorted into groups according to the types of commodities listed within source publications with preference given to primary commodities. These groups and qualifying targeted/mined commodities are as follows and are also listed in Table A-11: specialty metal (SM), fluorospar (F), base metal, precious metal, cryolite, Sn-W, U, Mo, and combinations of these, while specific commodities or lack thereof are clarified for vein/replacement deposits in Table A-22 (Appendix A.). Again, this information was provided mainly for the reader, to aid in understanding the details about deposits that were included within this study while discrimination diagrams were produced only using primary mineralization environment assignations for which these details are implied.

Fluorite occurrences associated with the above listed deposit types are varied and range from primary magmatic phases in peralkaline intrusions and granitoids, to metasomatic replacements in carbonates, to hydrothermal veins, replacements, and fluorspar deposits hosted in a variety of lithologies. Fluorite occurrences associated with these deposits also vary in volume from a primary commodity, to gangue, to accessory. Therefore, the REE data representing each economic deposit type within this study comes from fluorite without regard to paragenetic relationships and without regard to the volume of fluorite contained therein. This is also a realistic assessment for the purpose of implementing geochemical discrimination diagrams on REE analyses of fluorite sourced from stream sediment surveys, as detrital fluorite will likely represent that which formed from the most abundant phase within the source deposit, but should also reflect fluorite formed during any phase.

These listed deposit categories represent a colletion of available, published REE geochemical analyses of fluorite, but they in no way encompass all possible fluorite

occurrences and associations. Additionally, due to the nature of this classification system where priority was given to deposit models/formational models as well as conventionally undefined commodity occurrences, it is likely that certain deposits or fluorite found within certain publications could be described by more than one of the defined primary mineralization environment categories (i.e. carbonatite-related and peralkaline silicate igneous rock; rare metal pegmatite and peralkaline silicate igneous rock; cryolite deposit and alkaline igneous silicate rock; or skarn, rare metal pegmatite, and greisen mineralization). Therefore, publications involving fluorite mineralization for which multiple primary mineralization environments could have been assigned were assigned secondary mineralization environment classifications, though only primary mineralization environments were considered for the creation of discrimination diagrams. Classifications and groupings of compiled data based on commodities are also offered within this thesis, but distinctions between these groups were not attempted.

2.2.1. Primary deposit types

Brief summaries of primary mineralization environment categories are contained herein. These summaries include descriptions of defining criteria and the data compiled within this database. Primary mineralization environments (in order of appearance within section) include: 1.) peralkaline silicate igneous rock, 2.) carbonatite-related, 3.) Mississippi Valley type (MVT), 4.) sedimentary exhalative (SEDEX), 5.) iron oxide copper gold (IOCG), 6.) skarn, 7.) rare-metal pegmatite), 8.) granite-related uranium, 9.) greisen, 10.) cryolite, 11.) intrusion-related molybdenum, and 12.) hydrothermal/epithermal vein and/or replacement deposits (in carbonate, 13.) igneous, 14.) metamorphic, or 15.) sedimentary host rocks).

Peralkaline silicate igneous rocks are targeted for industrial minerals and semi-precious stones such as nepheline and sodalite or for metals such as REE, niobium, tantalum and titanium. REE-Y data from fluorite included within this category comes from magmatic, pegmatitic, and hydrothermal phases hosted in miaskitic and agpaitic rocks, augite syenite, and quartz syenite. Two publications are referenced herein and compiled REE-Y data from fluorite includes that of the high field-strength element, REE and Be deposits of the Gardar Province in South Greenland, (Schönenberger et al., 2008), and the F-REE deposits Gallinas Mountains alkaline complex in New Mexico, USA, (Gagnon et al., 2003).

Carbonatite-related mineralized bodies are often associated with ferrocarbonatites, calciocarbonatites, magnesiocarbonatites, ankeritic carbonatites and carbohydrothermal carbonatites/carbothermal residua-type bodies. Generally, carbonatites are targeted or mined for niobium ±tantalum ±rare earth elements ±phosphate, phosphate ±lime ±vermiculite ±phlogopite ±titanium ±iron, vermiculite, fluorite, titanium, lime, and rarely copper, iron, vanadium, olivine, uranium, or gold, (Woolley and Kjarsgaard, 2008). Woolley and Kjarsgaard (2008) noticed an apparent link between active carbonatite mines for phosphate, niobium, lime, and iron with those associated with nephilinite-ijolite and/or ultrabasic cumulate rock types. Carbonatites included within this study can be divided by commodity (REE±Fe±Ba±Nb; F±REE±Nb; F-REE; F) and consist of calciocarbonatite, magnesio-ankeritic carbonatite, carbohydrothermal carbonatite, and metasomatically replaced carbonate by proposed carbonatitic fluids. Carbonatite-related bodies mined for fluorite include the carbohydrothermal Speewah fluorite deposit in Western Australia (Alvin et al., 2003), the fluorite Okorusu calciocarbonatite in Namibia, (Bühn et al., 2003), the hydrothermal fluorite (±REE) Amba Dongar deposit hosted in sövite-ankerite, Baroda, India, (Palmer 1994) and the Mato Preto alkaline complex including magnesio-ankeritic carbonatite and calciocarbonatite fluorite±REE deposits in Brazil, (Ventura Santos et al., 1996). Carbonatite-related deposits targeted for REE include those of the Panxi Region, China, including the Maoniuping and Lizhuang REE deposits, and the REE±Ba Daluxiang deposit, (Xu et al., 2012), the world class replacement-style Bayan Obo REE±Fe±Nb deposit, Sichuan, China, (Xu et al., 2012), and the fluorite±REE±Nb Rock Canyon Creek/Deep Purple carbonate replacement deposit in British Columbia, Canada, (Gagnon et al., 2003).

Mississippi Valley type (MVT) deposits are epigenetic, predominantly stratabound, carbonate-hosted districts of sulfide (Zn, Pb, Fe) bodies that typically form in foreland thrust belt carbonate platforms and rarely in extensional environments, (Paradis et al., 2007). Typically targeted for lead and/or zinc, fluorite-rich varieties are a relatively rare subtype of MVT deposits hosting some of the world's prized fluorite hand-specimens like the Blue John fluorite from the Pennine Orefields, UK, or those from the Illinois/Kentucky fluorospar district, (Fisher et al., 2013). Fluorite data for MVT deposits compiled within this study include well-known fluorite MVT (F-Pb-Ag) deposits such as the Pennine Orefields, England, (Bau et al., 2003; Jones, 2006) and the Berbes, La Collada, and Villabona fluorite districts of Asturias, Spain, (Sánchez et al., 2010), as well as other MVT-style fluorite-(Ba-Pb-Zn) deposits such as Jebel Stah in north-eastern Tunisia, (Souissi et al., 2010), the MVT deposits of

Hansonburg, NW (Putnam III et al., 1983; Hill et al., 2000), the epigenetic fluorite deposit in a thrust zone in Çelikhan, Adiyaman, Eastern Turkey, (Sasmaz et al., 2005a), the fluorite deposits of MVT or manto origin at La Encantada, Mexico (González-Partida et al., 2002; Levresse et al., 2006), and the fluorite Portalet mines of the Valle de Tena region of the Spanish West Pyrenees of possible manto-style origin, (Subías, Fernández-Nieto, 1995).

Sedimentary exhalative (SEDEX) deposits are syngenetic, stratiform Pb-Zn sulfide deposits hosted within siliclastic and/or carbonate rocks that typically form in continental-rift environments, (Seal, 2004). Ore deposition typically occurs as fine-grained lenses and stratiform laminations of lateral extent (m to km), that are mm to few cm thick and are interbedded with clastic material. The main mineralogy of these deposits includes abundant pyrite and/or pyrrhotite, sphalerite, galena, barite, and lesser arsenopyrite, chalcopyrite, stibnite, tetrahedrite/tennantite, and secondary marcasite, barite, and anhydrite. These deposits can also be mineralogically zoned according to heat source proximity including a high Cu hydrothermal/stringer zone, with increasing Zn, Ba, Si upwards and outwards with decreasing temperature, (Seal, 2004). Seal (2004) makes no mention of fluorite association with SEDEX deposits, but it is likely that fluorite could form in evaporate, carbonate-rich sedimentary bodies by sedimentary or diagenetic means (Rude and Aller, 1991) or by the metamorphism of these SEDEX bodies. The fine-grained, sedimentary Pb-Zn deposits of the Nördliche Kalkalpen, hosted within the carbonate Austrian Alps (Schneider et al., 1975) is included in this compilation. This deposit, however, may represent an MVT deposit, and was assigned a secondary mineralization environment classification as such.

Iron oxide copper gold (IOCG) deposits encompass a wide range of sodic, potassic, or iron metasomatized mineralized bodies that share the common characteristics of low Ti-iron oxide ores (magnetite and/or hematite) that precede the deposition of other economic minerals, while varying considerably in specific mineralogy and deposit models (Porter, 2000). These deposits can be high-grade sources of copper and gold or sources of rare earth elements, fluorite, iron, or uranium, (Porter, 2000). These deposits are typically enriched in rare earth elements and carbonate with a fluid character resembling an oxidized carbonatite. Included within this compilation is data from the Lala Fe-Cu-REE deposit from the Kangdian region, China (Huang et al., 2014) where fluorite is an abundant gangue mineral.

Skarn deposits are one of the most chemically and mineralogically diversified groups of economic mineral deposits presented within this study. This is due to a great number of compositional combinations between parental igneous plutonic rocks and the (typically) sedimentary Ca-rich host rocks that they metasomatize. Since skarn composition can vary considerably between deposits, it may be reasonable to assume that the trace-element and REE-Y compositions of fluorite hosted by skarns may be highly variable or representative of mixing or re-equilibrating between the parental intrusion and host rocks. Additionally, a high degree of chemical variability means skarns can be targeted for an array of economic minerals/ores such as gold, garnet, scheelite, fluorite, copper, iron, or even for rare earth elements when the composition of the parental intrusion is peralkaline such as at the Ambohimirahavavy complex, Madagascar (Estrade et al., 2015). Included within this compilation, REE compositions of skarn fluorite were sourced from the El Pilote fluorite deposit, northern Mexico, (Levresse et al., 2006), the No. 19 vein of the Bailashui tin deposit, southern Hunan, China, (Yuan et al., 2008), the Perda Niedda deposit of the Sardinia fluorite district (Castorina et al., 2008), and the fluorite-scheelite deposits of Büyükçal Tepe and the fluorite-sulfide bodies related to the Akçakislan alkaline pluton of the Akdagmadeni region in Yozgat, Central Turkey, (Sasmaz et al., 2005 b).

Classes of **rare-metal pegmatites** are determined according to their bulk chemistry, trace element budget, and associated granitoids. This class of deposit is not to be confused with "pegmatitic" texture found in igneous or hydrothermal systems. Černý (1991), determined the following pegmatite varieties according to bulk compositions: NYF (Nb-Y-F), LCT (Li-Cs-Ta), and hybrid pegmatites. Sub-varieties have also been described by Černý, 1991, according to textural and morphological descriptions, as well as host metamorphic grade. Pegmatite bodies, despite their typically small size, can be particularly appealing exploration targets due to their coarse-grained nature of relatively pure minerals resulting from, but not always, final exsolution stages of cooling granitoids. Pegmatites formed by this mechanism are therefore enriched in incompatible elements making them useful targets for rare metals such as Li, Rb, Cs, Be, Ga, Sc, Y, REE, Sn, Nb, Ta, U, Th, Zr, and Hf, besides industrial minerals, and gemstones. Considering this mechanism of mineralization, it is likely that the REE signatures of fluorite sourced from differing pegmatites will be highly variable since highly fractionated rocks represent final products of innumerable mixing, segregating, and contaminating igneous processes and pathways. Included within this study are analyses on fluorite from the White Cloud and Oregon 3 (REE-F-Y-Nb-U) pegmatites, hosted within the

Pike's Peak granitic batholith of the South Platte District, Colorado, (Gagnon et al., 2003), and the barren skarn-contaminated pegmatites of the Vlastějovice area of the Bohemian Massif, Czech Republic, (Ackerman, 2005), with adjacent rare-element LCT, and U-Th-(Ti-Zr-Nb-Ta) pegmatites which were not sampled.

Granite-related uranium deposits is one of the categories created by the author to describe a class of uranium deposits that contain quantities of fluorite. Uranium deposits are not always associated with granitic intrusions, and are commonly associated with mafic rocks, instead. Mafic minerals such as biotite may trap available fluorine, and so uranium deposits that are also host to fluorite are typically associated with felsic to alkaline granitoids. Only two granite-related uranium deposits are included within this compilation, namely the No. 302 uranium deposit, China, (Zhang et al., 2007), and the U-F veins at Gabbal Gattar, Egypt, (Mahdy et al., 2014). Another similarity, though likely coincidental, shared between these two deposits is oblique tectonic motion as pivotal tensional faults at No. 302 and transtensional shearing at Gabbal Gattar.

Greisen deposits are commonly hosted along the upper contacts of, or within highly evolved, rare element plutonic rocks such as Li-F, S-type, or A-type granitoids, (Elliott et al., 1995). Greisenization occurs when final exsolution phases of highly-evolved granitoids release acidic, supercritical and/or condensed, fluorine-rich fluids that alter the host granitoid and/or surrounding country rocks resulting in the mineralization of quartz and mica (muscovite or lepidolite and lesser biotite or chlorite), with lesser topaz, fluorite, tourmaline, rutile, cassiterite, wolframite, huebnerite-ferberite, molybdenite, arsenopyrite, beryl, bismuthinite, scheelite, axinite, tetrahedrite, pyrite, stannite and apatite (Rakovan, 2007, Elliott et al., 1995). Greisen mineralization typically occurs as vein deposits exploited for Sn, W, Mo, and lesser Be. Greisen deposits containing fluorite compiled within this study are generally related to Li-F granites from the Hercynian metal province including: the Zinnwald tin deposits of the Erzgebirge region at the Germany-Czech Republic border, (Monecke et al., 2002), the Ehrenfriedersdorf Sn-W deposit, Erzgebirge, Germany, (Monecke et al., 2000), the Qaraoba tungsten district including the marble-hosted Solnechnoe tungsten ore field, central Kazakhstan (Monecke et al., 2002), the Aqshatau W-Mo-Be deposits, Kazakhstan, (Monecke et al., 2002), and the Nb-Zr-REE altered pegmatite deposits at Kent, Kazakhstan (Monecke et al., 2002).

As of 2008 only two economic **cryolite deposits** were globally exploited. These included the Ivigtut deposit in southwestern Greenland, (Schönenberger et al., 2008), where cryolite was first discovered, and the Pitinga mine in Amazon, Brazil, (Minuzzi et al., 2008) which was historically mined for tin. Cryolite (Na_3AlF_6) is a rare mineral that forms as a magmatic or magmato-hydrothermal/metasomatic phase in albite or A-type granitic deposits. Cryolite is exploited as an ore of aluminum and for its use in the extraction of aluminum from oxide ore such as bauxite. Synthetic cryolite, however, is manufactured from fluorite, an intimately associated mineral in crylolite deposits. Fluorite data from both Ivigtut (Schönenberger et al., 2008), and Pitinga (Minuzzi et al., 2008) are compiled within this study. This deposit type could also be split into peralkaline silicate igneous rock deposits and greisen deposits for the Ivigtut and Pitinga data, respectively.

Economic sources of molybdenum occur in a variety of deposit types from hydrothermal, to porphyry, to skarn, to Climax-type porphyry. **Intrusion-related molybdenum deposits** commonly occur, however, in accordance with highly evolved, rare-metal granites creating shared features with pegmatite, skarn, and greisen mineralizations. Two globally important regions of molybdenum mineralization exist today. One being the post-subduction, extensional belt of Climax-type porphyry molybdenum deposits of western North America, and the other being the post-subduction, collisional suture zone between the North China Craton and the Qinling Orogen forming the East Qinling Mo Belt (Ludington and Plumlee, 2009; Deng et al., 2014). Climax-type molybdenum porphyry deposits are strictly defined as quartz-molybdenite stockwork veins of calc-alkaline granitic cupolas and subvolcanic rhyolite-porhpyry bodies that are enriched in fluorine, rubidium, niobium, and tantalum while being depleted in strontium and zirconium, (Ludington and Plumlee, 2009). These deposits only occur in western North America of which, the Sweet Home Mo-Ag-rhodocrosite mine in Colorado is related to but not defined as a Climax-type deposit (Lüders et al., 2009). Geochemical fluorite data from this quartz-molybdenite-pyrite-topaz-muscovite-fluorite, sulfide-rhodochrosite deposit is included within this study. Additionally, fluorite data from the Tumen, molybdenite-fluorite skarn-porphyry deposit in eastern Qinling, China (Deng et al., 2014) is also compiled.

Fluorite-containing **hydrothermal/epithermal vein and replacement deposits** can be sources of base or precious metals or fluorspar. They're hosted in a variety of lithologies and dervied from various source fluids and trace elements from igneous,

metamorphic, and sedimentary rocks and processes. These deposits form due to tectonic or igneous activity, commonly following structural features, forming veins and occasionally replacement bodies when hosted in carbonates. This type of deposit typically consists of some combination of the following mineralogy fluorite-quartz±barite±calcite±sulfides, and occasionally containing chalcedony or tellurides. Fluorite REE data from hydrothermal/epithermal vein and replacement deposits were compiled from ten publications referencing 180 analyses on samples from 120 deposits from 22 regions (Table A-22 of Appendix A.). Hydrothermal/epithermal deposits containing fluorite were sorted according to host lithology including carbonate, igneous, metamorphic, and sedimentary rock, with occasional secondary classifications. Data included within this section are sourced from publications on the Valle de Tena region of Huesca, Spain (Subías, Fernández-Nieto, 1995), the Akdagmadeni region of Turkey (Sasmaz et al., 2005 b), Sardinia, Italy (Castorina et al., 2008), the Yixian deposits of Liaoning, China (Xiang et al., 2010), the deposits of New Mexico (Hill et al., 2000), the deposits of the Schwarzwald area of Eastern Germany (Schwinn and Markl, 2005), the El Hammam deposits of Morocco (Cheilletz et al., 2010), the veins of Santa Catarina, Brazil (Sallet et al., 2005), and the vein deposits of the Erzgebirge region, Germany (Trinkler et al., 2005).

2.2.2. Secondary deposit types

Secondary deposit types are summarized here including a new deposit type category not described above; alkaline igneous silicate rocks. Additionally, deposits that could have arguably been described by more than one of the primary mineralization environment groups listed above, were assigned with secondary mineralization environment descriptions. These are summarized here.

The assignment of secondary mineralization environments to the compiled deposits serves mainly as a display of the subjectivity of interpretation for primary assignations and shows the relatedness of primary mineralization environment groups. For example, carbonatite-related deposits and peralkaline silicate igneous rocks can often be found within the same peralkaline/carbonatite complexes and therefore deposits found within these suites can be related to both types of igneous processes or hydrothermal processes affected by both rock types seen in **Error! Reference source not found.**1 (Appendix A.). Another example of common association is alkaline igneous silicate rocks, skarns, greisen deposits,

granite-related uranium, cryolite and occasionally rare metal pegmatite deposits. Because of these similarities or common associations, chemical patterns found in fluorite sourced from these deposit types may prove similar and therefore their datafields on discrimination diagrams may often overlap. Datafields were not generated, however, based on secondary mineralization environment classifications.

The **alkaline igneous silicate rocks** group was determined as a secondary deposit type, as it can be formed by, or influenced by, alkaline igneous silicate rocks. These rocks, themselves, aren't necessarily economic producers or targets but contribute to the formation of other, somewhat similar deposit types such as greisens and rare-metal pegmatites. Within this compilation, alkaline silicate igneous rocks are related to the formation of peralkaline silicate igneous rock, skarn, pegmatite, greisen, granite related uranium, cryolite, and hydrothermal/epithermal vein deposits. These associations and possible chemical influences that secondarily qualify a deposit as an alkaline igneous silicate rock relative, include direct formation from alkaline magmatism, hydrothermal activity related to alkaline magmatism, and/or equilibration of formational fluids with alkaline igneous host rocks.

Characteristics that qualify deposits as this type include: alkali granites at the Ilímaussaq peralkaline igneous silicate deposit of the Gardar Province (Schönenberger et al., 2008), a proposed alkaline rock influence on MVT formation in the North Pennine Orefield (Bau et al., 2003), an alkaline granitoid contributing to garnet-epidote skarn formation at Akçakisla, Turkey (Sasmaz et al, 2005 b), unspecified granitoid (granite, quartz monzonite, quartz syenite, or syenite) forming epidote-skarn with fluorite and scheelite at Büyükçal Tepe, Turkey (Sasmaz et al., 2005 a), Li-F granites forming greisens at the Zinnwald tin deposit and Ehrenfriedersdorf Sn-W deposit of Eastern Germany, the tungsten deposit of Qaraoba, and the W-Mo-Be deposit of Aqshatau, Kazakhstan (Monecke et al., 2000; 2002), pegmatites hosted in anorogenic granite at the White Cloud and Oregon 3 deposits (Gagnon et al., 2003), porphyritic two mica and biotite granites hosting U-mineralization in a fault zone at No. 302 Uranium deposit of Guangdong, China (Zhang et al., 2007), U-F rich granite hosting U-mineralization in fracture fill of Gabbal Gattar, Egypt (Mahdy et al., 2014), metasomatized A-type granitic stock hosting cryolite mineralization at Ivigtut, South Greenland (Schönenberger et al., 2008).

Besides secondary classifications assigned to hydrothermal/epithermal vein and replacement deposits, and igneous intrusion-related deposits assigned secondary classifications of alkaline silicate affinity, deposits with characteristics that nearly, equally qualify under multiple deposit descriptions, were assigned secondary classifications. Secondary classifications includes *IOCG* for the Bayan Obo carbonatite deposit (Xu et al., 2012); *peralkaline silicate igneous rock* deposits for the carbonatite deposits of the Panxi region, China (Xu et al., 2012), the Mato Preto carbonatite complex of Amazon, Brazil (Ventura Santos et al., 1997), and the Mo-F deposit of Tumen, Qinling, China (Deng et al., 2014); *greisen* descriptions for the No. 19 Bailushui tin skarn of Hunan, China (Yuan et al., 2008), the Solnechnoe F-W skarn deposit of Qaraoba, Kazakhstan (Monecke et al., 2002), and the Pitinga cryolite deposit of Amazon, Brazil (Minuzzi et al., 2008); the Kent Nb-Zr-REE greisen was also classified as a *rare-metal pegmatite* deposit (Monecke et al., 2002); the Vlastějovice rare-metal pegmatite deposits were also classified as *skarn* deposits (Ackerman, 2005); and secondary classifications of *alkaline silicate igneous rock* association were attributed to the Akçakisla and Büyükçal Tepe skarns of the Akdagmadeni region, Turkey (Sasmaz et al, 2005 b), the Zinnwald, Ehrenfriedersdorf, Qaraoba, and Aqshatau greisens of Germany and Kazakhstan (Monecke et al., 2000 and 2002), the pegmatites of White Cloud and Oregon 3, Colorado (Gagnon et al., 2003), the No. 302, and Gabbal Gattar uranium deposits of Guangdong, China, and Egypt (Zhang et al., 2007; Mahdy et al., 2014), and the Ivigtut cryolite deposit of the Gardar Province, South Greenland (Schönenberger et al., 2008).

According to Hitzman et al., (1992)'s, description of IOCG deposits, as summarized by Porter et al., (2000), the Bayan Obo deposit is considered an IOCG deposit. The qualifying characteristics displayed by the Bayan Obo deposit are that it's a carbonate replacement deposit enriched in REE (particularly LREE), containing magnetite ores.

Deposits secondarily classified as peralkaline silicate igneous deposits includes carbonatite, syenite complexes of the Panxi Region, China, and Mato Preto, Brazil, as well as a replacement deposit associated with syenitic dikes at Tumen, China. The Daluxiang, Maoniuping, and Lizhuang deposits were first classified as carbonatite deposits and secondarily as peralkaline silicate igneous rock deposits (Xu et al., 2012). The REE±Ba Daluxiang deposit contains syenites within the carbonatite complex attributed to its formation. The REE deposit of Maoniuping are hosted in carbonatite sills, dykes and stocks intruded into syenites. And the REE deposits of Lizhuang are related to carbonatite and

syenite formation. The Mato Preto carbonatite complex of Amazon, Brazil (Ventura Santos et al., 1997), was first compiled as a carbonatite-related deposit and second as a peralkaline silicate igneous rock-related deposit. This deposit consists of lenses and veins of magnesio-ankeritic, and calciocarbonatite hosted in fenitized syenites and phonolites. Finally, the intrusion-related Mo-F deposit of Tumen, Qinling, China was secondarily classified as a peralkaline silicate igneous rock deposit, as its stratigraphically controlled vein and breccia-contained orebodies are located proximal to syenitic dikes (Deng et al., 2014).

Secondary classifications of greisen were established for tin bearing skarn deposits including those of Bailushui, Hunan, China, and Solnechoe, Qaraoba, Kazakhstan, as well as for ex-tin producing deposits of the Pitinga cryolite mine. The No. 19 Bailushui tin skarn deposit was also classified as a greisen deposit (Yuan et al., 2008). This is because endo-, exo-skarn, vein mineralization and metasomatism is similar in style to greisenization and the mineralogy produced includes cassiterite, quartz, and beryl. The Solnechnoe F-W skarn deposit was similarly classified as a greisen deposit to the No. 19 Bailushui tin deposit. In place of tin, this greisen-like mineralization contains tungsten in the form of wolframite (Monecke et al., 2000). The Pitinga cryolite deposit of Amazon, Brazil was also classified as a greisen deposit. This is because the Pitinga cryolite mine, was historically a major tin producer for Brazil, whose formation is due to the intrusion of multiple phases of an albite granite (Minuzzi et al., 2008). The location of the ore deposits within the cupolas of the albite granite, also suggests formation similar to greisenization.

Characteristics between greisens, skarns, and pegmatites can seem very similar within literature and often these types of deposits share many common features. Because of this, greisens at Kent, Kazakhstan were also described as altered pegmatites, and pegmatites at Vlastějovice were also described as skarns. The description of the Kent Nb-Zr-REE greisen offered by Monecke et al., (2002) is brief and makes mention that the deposit is a “rare metal, intensely altered pegmatite.” Because of this, this author decided to classify the deposit first as a greisen, since formation typically includes intense alteration by retrogressing cooling fluids, and second as a rare-meta; pegmatite since the deposit contains rare metals and an initial pegmatitic texture. The Vlastějovice pegmatite deposits of barren, LCT, and U-Th-(Ti-Zr-Nb-Ta) economic value are hosted within lenses of skarn found within a regional paragneiss (Ackerman, 2005). Due to this, it is very likely that these pegmatites are strongly

contaminated by the host skarn lenses and so, these deposits were also classified as skarn deposits.

Finally, multiple deposits were assigned a secondary classification as alkaline silicate igneous rock deposits as their formation or host rocks were igneous rocks of alkaline affinity. These include skarns of Turkey, greisens from various localities, alkaline pegmatites of Oregon, USA, U-deposits of Egypt and China, and cryolite deposits of Greenland. The Akçakisla and Büyükçal Tepe skarns of the Akdagmadeni region, Turkey have been classified as alkaline silicate igneous deposits after being classified as skarns. Both of these skarn deposits were generated by granitoids of alkaline composition. The Akçakisla skarn is related to an unspecified alkaline granitoid. The Büyükçal Tepe deposit was formed by granite, quartz monzonite, quartz syenite, and/or syenite (Sasmaz et al, 2005 b). The Zinnwald, Ehrenfriedersdorf, Qaraoba, and Aqshatau Sn, Sn-W, W, and W-Mo-Be greisen deposits were secondarily classified as alkaline igneous silicate deposits. All of these greisen deposits were formed by a Li-F granite compiled from Monecke et al., (2000 and 2002). The pegmatites of White Cloud and Oregon 3 containing REE-F-Y-Nb-U were also classified as alkaline igneous silicate rock deposits as the host intrusion was described by Gagnon et al., (2003) as an anorogenic granite. The No. 302, and Gabbal Gattar uranium deposits of Guangdong, China, and Egypt were secondarily classified as alkaline igneous silicate rock deposits due to their association with porphyritic two mica and biotite granites and U-F rich granite respectively (Zhang et al., 2007; Mahdy et al., 2014). The Ivigtut cryolite deposit of the Gardar Province, South Greenland was also classified as an alkaline igneous silicate rock deposit since its formation is attributed to phase separation of a metasomatized A-type granitic stock (Schönenberger et al., 2008).

2.2.3. Metallic economic association

Data were sorted into groups according to metallic economic association as primary, secondary, or none. Comparing REE signatures in fluorite according to these criteria could provide a means to test the basic usefulness of these discrimination diagrams if metallic commodities were the primary economic concern, though that was not accomplished within this thesis. Additionally, this information was provided in combination with commodity groups for each compiled deposit to offer more information about the data contained in diagram datafields. For an example, carbonatite-related deposits have been mined

exclusively for both industrial minerals or specialty metals, and so carbonatite-related deposits with primary and no metallic economic association were included within the study. This information may be useful for the reader or for someone intending to use the discrimination diagrams contained within this work and those interested are encouraged to examine Tables A-1 and A-2 in Appendix A.

If a deposit described in its respective publication(s) mentioned metallic commodities, the data was sorted according to how these metals were targeted/mined as primary or secondary commodities. If there were no metallic targets other than industrial minerals such as fluorospar or fluorite, the deposits and data were classified under "none." However, deposits where cryolite was listed as the primary commodity, were classified as having "primary" metallic economic associations, as cryolite is an ore for Al and for the processing of aluminum, (Minuzzi et al., 2008). Additionally, if the economic value of a given deposit was undetermined from the information provided in the source, the corresponding samples were labeled as "unknown" for this category. 347 fluorite samples were compiled from 29 deposits with primary metallic economic associations, 99 samples from 10 deposits were compiled with secondary metallic economic associations, 164 samples from 13 deposits and four regions were listed without metallic associations, and 24 samples were compiled from three deposits and one region where the economic metallic association was unknown.

2.2.4. Recovered/targeted/prospected commodity groups

Additionally, data were sorted into groups according to the commodities that were either recovered, targeted, or prospected from compiled deposits, with preference given to primary commodities. These groups and qualifying recovered/targeted/prospected commodities are listed in A-1 and A-2 (Appendix A.) as combinations of the following: specialty metal (SM), fluorospar (F), base metal, precious metal, cryolite, Sn-W, U, Mo.

Specialty metal deposits include peralkaline silicate igneous rock deposits of Greenland (Schönenberger et al., 2008) including the HFSE, REE, Be deposits of Motzfeldt and Ilímaussaq, carbonatite REE deposits of the Panxi Region, China (Xu et al., 2012) including Maoniuping and Lizhuang, the Nb-Zr-REE greisen deposits at Kent, Kazakhstan (Monecke et al., 2002), the barren, LCT, and U-Th-(Ti-Zr-Nb-Ta) pegmatite deposits at Vlastějovice, Czech Republic (Ackerman, 2005), and the Th-REE-containing vein deposits in alkaline igneous

rocks of the Capitan Mountains, New Mexico (Hill et al., 2000). SM-base metal deposits include the REE-Fe deposit of Bayan Obo, China (Xu et al., 2012) and the REE±Ba Daluxiang deposit of the Panxi Region, while base-SM-precious metal deposits consist of the Lala IOCG deposit of Kangding, China (Huang et al., 2014).

Specialty metal-fluorite deposits includes the REE-F-Y-Nb-U pegmatite deposits at White Cloud, and Oregon 3, Colorado (Gagnon et al., 2003). Fluorite-specialty metal deposits includes the F-REE peralkaline silicate igneous rock deposits at Pinatosa, Gallinas Mountains, New Mexico (Gagnon et al., 2003), the F±REE Mato Preto carbonatite, syenite complex, of Brazil (Ventura Santos et al., 1997), the F±REE±Nb carbonate replacement deposit of probable carbonatite origin at Deep Purple/Rock Canyon Creek, British Columbia, Canada (Gagnon et al., 2003), and the F±REE Amba Dongar deposit of Baroda, India (Palmer and Williams-Jones, 1994).

Base metal deposits include the Tebarray Zn-F-(Pb) veins hosted in carbonate of Valle de Tena, Huesca, Spain (Subías, Fernández-Nieto, 1995), Cu-Bi vein deposits of Schwarzwald, Germany (Schwinn and Markl, 2005), Ba-Sr, Bi-Co-Ni-As-Ag, Ge-Hg, Fe-Mn vein deposits of Erzgebirge, Eastern Germany, (Trinkler et al., 2005), Pb-Zn SEDEX deposits of Nördliche Kalkalpen (Schneider et al., 1975), and the Pb, Cu, W, V deposits of New Mexico (Hill et al., 2000). Base-precious and precious-base metal deposits include the Cu, Bi, Ag, Fe, Pb vein deposits of Schwarzwald, Germany (Schwinn and Markl, 2005), the Pb, Zn, Ag, Cu vein deposits of New Mexico (Hill et al., 2000), and the Pb-Zn-Ag MVT deposits of Hansonburg, NM, (Hill et al., 2000). F-base-precious metal deposits include the F-Pb-Ag MVT deposits of of the South and North Pennine Orefields (Bau et al., 2003), and F-Pb-Zn-Ag-(Cu) vein and skarn deposits of Tad Dere and Akçakisla, Akdagmadi, Turkey, (Sasmaz et al, 2005 b).

Cryolite deposits include those at Ivigtut, South Greenland, (Schönenberger et al., 2008) and the Pitinga Mine, Amazon, Brazil (Minuzzi et al., 2008). Uranium deposits include the No. 302 Uranium Vein, of the Changjiang uranium orefield, Guangdong, China, (Zhang et al., 2007), and Gabbal Gattar, Egypt, (Mahdy et al., 2014). Molybdenum deposits include the F-Mo deposit at Tumen, Qinling, China, (Deng et al., 2014), and the Mo-Ag-rhodochrosite Sweet Home Mine, Colorado, (Lüders et al., 2009). Deposits categorized under Sn-W include the Sn skarn deposit of No. 19 Skarn Vein, of the Tiepokeng-Wuchangping tin belt of Furong ore field, Hunan, China, (Yuan et al., 2008), the F-W skarn deposit of Büyükçal Tepe,

Akdagmadeni region, Turkey, (Sasmaz et al., 2005 b), the Sn greisen deposit at Zinnwald, and the Sn-W deposit at Ehrenfriedersdorf, Erzgebirge, Germany (Monecke et al., 2000; 2002; Trinkler et al., 2005), and the W and W-Mo-Be deposits at Qaraoba and Aqshatau, Kazakhstan (Monecke et al., 2002).

Fluorite deposits are plentiful and range from fluorospar deposits or deposits where fluorite hand-specimens have been extensively collected including: the Speewah and Okorusu fluorite carbonatite-related deposits of Australia and Namibia (Alvin et al., 2003; Bühn et al., 2003), the fluorite MVT deposits of Asturias, Spain (Sánchez et al., 2010), the Çelikhan MVT deposits of Turkey (Sasmaz et al., 2005a), the Portalet MVT deposits of Huesca, Spain (Subías, Fernández-Nieto, 1995), the Perda Niedda skarn deposit of Sardinia, Italy (Castorina et al., 2008), the fluorite vein deposits hosted in carbonate of Yixian, China (Xiang et al., 2010) and Sardinia, Italy (Castorina et al., 2008), as well as vein deposits hosted in sedimentary, metamorphic and igneous rocks of Sardinia, Italy (Castorina et al., 2008), vein deposits in metamorphic rocks of El Hamman, Morocco (Cheilletz et al., 2010), and vein deposits hosted in igneous rocks of St. Lawrence, Newfoundland (Gagnon et al., 2003), New Mexico (Hill et al., 2000), and Santa Catarina, Brazil (Sallet et al., 2005).

2.3. Data and Manipulation

Data were compiled from 32 publications, including 630 analyses of REE-Y in fluorite from 183 sample localities or mines, from about 60 regions worldwide. Publication years ranged from 1975 to 2014 (only 4 were from 1996 or earlier, with 13 from 2000-2005 and 15 from 2006-2014.) This of course, implies a variety of applied analytical procedures and methods to procured results of trace-elements and therefore occasionally required manipulation of data to induce compatibility. Compatibility was induced opposed to exclusion of a variety of analytical techniques or adherence to consistent techniques, to maximize representative datasets for each deposit-type group. One such manipulation involved averaging multiple point analyses performed on the same crystal/sample to create one representative sample, such as averaging LA-ICP-MS data. The analyses performed within each compiled publication within this dataset were not examined in detail, but the instrumental methods were noted where available. Applied analytical methods contained herein (listed in Table A-11 of Appendix A) have advantages and disadvantages, and include:

bulk sample techniques like inductively coupled plasma mass spectrometry (ICP-MS), instrumental neutron activation analysis (INAA/NAA), and inductively coupled plasma atomic emission spectroscopy (ICP-AES), and point or line analyses by laser ablation inductively coupled plasma mass spectrometry (LA-ICP-MS). Justifications for including INAA methods and modifying LA-ICP-MS data are included below. The majority of data collected were analyzed by ICP-MS methods, where 21 publications from the total 32 utilized this method. Otherwise, only two publications utilized ICP-AES analysis, four used INAA, and four used LA-ICP-MS. 399 compiled samples were analyzed by ICP-MS, 116 samples were analyzed by LA-ICP-MS, 15 by ICP-AES, 95 by INAA, and nine were analyzed by an unknown method (Huang et al., 2014).

Additionally, the trace-elements identified in fluorite within each publication are diverse. This was due to a number of reasons including variable physical presence or limitations of analytical techniques. Only trace-elements consistently reported in each of the compiled publications were utilized for comparison studies. The number of times an element was reported in fluorite per deposit type is listed in Table 2-1. As a result, the REE-Y contents reported in fluorite are the primary focus of comparison between determined deposit type groups within this study, and more specifically La, Ce, Sm, Eu, Yb, and Lu are the most well-represented elements in the dataset (each with over 600 recordings out of a possible 630, and with a minimum of 8 values representing each primary deposit group).

In determining this suite of trace-elements as useable for comparison, representation of determined primary-deposit type groups were examined which is critical in understanding the accuracy of produced datafields on discrimination diagrams and subsequently important for assigning primary mineralization environment sources to analyzed fluorite. Deposit-type representation was assessed by examining sample sizes per group, data source diversity, and univariate normality per REE-Y before and after logarithmic transformation using histograms, Q-Q plots, and the Shapiro-Wilk test. From these examinations, it was determined that primary mineralization environments were represented from best to worst in the following order and as seen in Table 2-3: 1.) hydrothermal/epithermal vein/replacement deposits in igneous hosts, 2.) MVT deposits, 3.) hydrothermal/epithermal vein/replacement deposits in carbonate hosts, 4.) carbonatite-related deposits, 5.) hydrothermal/epithermal vein/replacement deposits in metamorphic hosts, 6.) SEDEX deposits, 7.) skarn deposits, 8.) greisen deposits, 9.) intrusion-related molybdenum deposits, 10.) cryolite deposits, 11.)

peralkaline silicate igneous rock deposits 12.) hydrothermal/epithermal vein/replacement deposits hosted in sedimentary rock, 13.) rare-metal pegmatites, 14.) granite-related uranium deposits, and 15.) IOCG deposits.

Calculations were made on compiled data for comparison between determined primary-deposit type groups such as, averaged LA-ICP-MS data per sample, normalization to accepted geological schemes (carbonaceous chondrite from McDonough and Sun, 1995), logarithmic transformations, calculations of elemental anomalies normalized to chondrite ([Eu*/Eu]n, [Ce*/Ce]n, [Y*/Y]n), and calculations of select ratios for scatter diagram comparisons determined by previous work or current work. Ratios were determined as the best means of potential comparisons between primary mineralization environments as the patterns exhibited by REE-Y per deposit or group displayed highly varied concentrations but relative

consistency in overall patterns as outlined in Appendix D. The calculations performed are explained below.

Table 2-1 Tallies of reported trace-elements per deposit type included with total number of analyses per deposit type and true total. REE were the most consistently reported elements in fluorite given by publications, particularly La, Ce, Sm, Eu, Yb, and Lu and subsequently offer the best opportunity as variables for comparison between deposit type groups.

Primary deposit type	Peralkaline silicate igneous rock	Carbonatite-related	MVT	SEDEX	IOCG	Skarn	Rare-metal pegmatites	Granite-related U	Greisen	Cryolite	Intrusion-related Mo	Hydrothermal/epithermal veins and replacements in carbonate hosts	...in igneous hosts	...in metamorphic hosts	...in sedimentary hosts	Total
# of analyses	53	99	138	33	9	24	17	15	17	14	29	54	93	27	8	630
La	53	99	138	32	9	23	17	13	10	14	29	54	93	27	8	619
Ce	53	99	138	32	9	24	17	14	16	14	29	54	93	27	8	627
Pr	53	81	133	0	9	12	4	14	17	14	29	28	40	24	7	465
Nd	53	99	138	0	9	24	17	14	17	14	29	52	93	27	8	594
Sm	53	99	138	24	9	23	17	14	17	14	29	54	93	27	8	619
Eu	53	99	135	31	9	23	17	10	17	14	29	54	93	27	8	619
Gd	51	91	133	0	9	11	13	14	17	10	29	28	62	24	7	499
Tb	53	88	138	32	9	23	17	13	17	14	29	54	62	27	8	584
Dy	53	92	133	0	9	11	4	14	17	14	29	28	65	24	7	500
Y	53	92	72	0	0	12	4	7	14	14	29	19	37	17	2	372
Ho	53	92	133	0	9	11	14	14	17	14	29	28	62	24	7	507
Er	53	92	132	0	9	11	4	14	17	14	29	28	65	24	7	499
Tm	53	81	102	0	9	10	7	13	16	14	29	7	40	21	7	409
Yb	53	99	136	32	9	23	17	14	17	10	29	54	93	27	8	621
Lu	53	99	135	24	9	23	15	13	17	14	29	52	93	27	8	611
Sr	40	81	101	0	0	19	4	7	0	8	29	38	28	14	2	371
Th	39	74	86	32	0	10	4	3	0	8	29	12	3	0	0	300
U	39	74	80	32	0	10	4	7	0	8	29	12	2	0	0	297

Ba	2	81	114	0	0	10	4	2	0	0	29	28	7	1	1	279
Pb	39	74	76	0	0	0	4	4	0	8	29	12	18	2	1	267
Rb	39	39	76	0	0	9	4	2	0	8	29	14	21	14	2	257
Zr	0	72	45	0	0	10	0	5	0	0	29	36	16	3	1	217
Sc	0	8	43	28	0	10	0	2	0	0	17	36	21	3	1	169
Zn	2	1	44	0	0	10	4	0	0	0	17	23	18	2	1	122
Hf	0	73	0	0	0	0	0	0	0	0	29	0	0	0	0	102
Nb	2	52	0	0	0	0	4	6	0	0	17	0	2	0	0	83
Ta	0	51	0	0	0	0	0	2	0	0	17	0	0	0	0	70
V	0	0	23	0	0	0	0	2	0	0	17	12	0	0	0	54
Cr	0	0	24	0	0	0	0	0	0	0	17	12	0	0	0	53
Cs	0	22	0	0	0	0	0	2	0	0	29	0	0	0	0	53
Na	39	1	0	0	0	0	4	0	0	8	0	0	0	0	0	52
Cu	2	1	24	0	0	0	4	0	0	0	17	0	2	0	0	50
Ni	0	0	32	0	0	0	0	0	0	0	17	0	0	0	0	49
Sb	0	0	37	0	0	0	0	0	0	0	0	12	0	0	0	49
Co	0	0	23	0	0	0	0	2	0	0	17	0	0	0	0	42
Ga	0	0	21	0	0	0	0	0	0	0	17	0	0	0	0	38
Mn	2	0	23	0	0	0	0	0	0	0	0	0	0	0	0	25
Cd	0	0	23	0	0	0	0	0	0	0	0	0	0	0	0	23
Mo	0	0	22	0	0	0	0	0	0	0	0	0	0	0	0	22
W	0	0	0	0	0	10	0	0	0	0	0	12	0	0	0	22
Li	0	0	0	0	0	0	0	2	0	0	17	0	0	0	0	19
Ti	0	0	0	0	0	0	0	2	0	0	17	0	0	0	0	19
Bi	0	0	0	0	0	0	0	0	0	0	17	0	0	0	0	17
Be	0	0	0	0	0	0	0	0	0	0	17	0	0	0	0	17
As	0	0	15	0	0	0	0	0	0	0	0	0	0	0	0	15

Mg	2	1	0	0	0	0	4	0	0	0	0	0	2	0	0	9
Si	2	1	0	0	0	0	4	0	0	0	0	0	2	0	0	9
K	2	1	0	0	0	0	4	0	0	0	0	0	0	0	0	7
B	0	0	0	0	0	0	0	3	0	0	0	0	0	0	0	3

2.3.1. Averaged LA-ICP-MS data

Publications that reported results taken by LA-ICP-MS analysis did so by one of three ways: one point analysis per one sample per one locality (usually a specific mine within a region) (Schwinn and Markl, 2005), multiple reported analyses per one sample per each locality (Schönenberger et al., 2008; Mahdy et al., 2014), or multiple point analyses represented by an averaged value per locality (Gagnon et al., 2003). To induce compatibility between these results, either random values could be generated for each representative average from Gagnon et al., (2003) according to the number of analyses (n=#) depicted by each average, or values per sample could be averaged like those in Gagnon et al., (2003). The latter is a much simpler resolution, and averaged LA-ICP-MS analysis may provide representative values that more closely mimic those offered by bulk ICP-MS analysis without trace-element contamination introduced by inclusions within fluorite crystals (though this is conditional upon LA-ICP-MS procedure where spot or line analyses were implemented, and if careful observation of crystals preceded laser analysis). Therefore, the LA-ICP-MS data compiled from Schönenberger et al., (2008) and Mahdy et al., (2014) required averaging as described below.

LA-ICP-MS values of REE collected along grain traverses from fluorites from the Gardar Province, South Greenland (Schönenberger et al., 2008), included results representing peralkaline silicate deposits and cryolite deposits. These multiple analyses on single fluorites were averaged to create representative values to more closely mimic results collected from compiled ICP-MS analyses and LA-ICP-MS analyses that were averaged by the source authors. Averaging was performed before data were normalized for use in spider diagrams and prior to ratio calculations for discrimination diagrams, and therefore normalization values were applied to averaged sample values. This treatment of data reduces the amount of variability in total REE-Y values, and reduces the amount of noise on subsequent diagrams. As seen in Figure 2-1 for secondary fluorite sample, JS9A from the Motzfeldt deposit, total REE-Y concentrations vary over two orders of magnitude, while relative patterns remain consistent which can be represented by an average value. The data from Mahdy et al., (2014), though also analyzed by LA-ICP-MS analyses, were not averaged per sample, since the reduction of the already small dataset of seven analyses down to three is not ideal.

As mentioned above one of the compiled publications (Gagnon et al., 2003) included averaged LA-ICP-MS data to represent samples with the noted number (n = #) of analyses contained. These represent three fluorite samples from peralkaline silicate igneous rocks at Gallinas Mountains, New Mexico, two fluorite samples from the carbonatite-related replacement deposit at Rock Canyon Creek/Deep Purple, British Columbia, four samples from rare metal pegmatite associated with anorogenic granite in South Platte, Colorado, and three samples from fluorite veins related to granite from St. Lawrence, Newfoundland.

Data compiled herein analyzed by LA-ICP-MS methods includes the work of Gagnon et al., (2003) which were already averaged, and the analyses compiled from Schönenberger et al., (2008) were averaged per sample to induce compatibility between these sets and the remainder of the database which included analyses utilizing bulk methods. The analyses by Mahdy et al., (2014) were not reduced to averages per sample as to not minimize an already small dataset representing granite-related U deposits, and the work by Schwinn and Markl, (2005) could not be reduced as these results included single LA-ICP-MS analyses per sample.

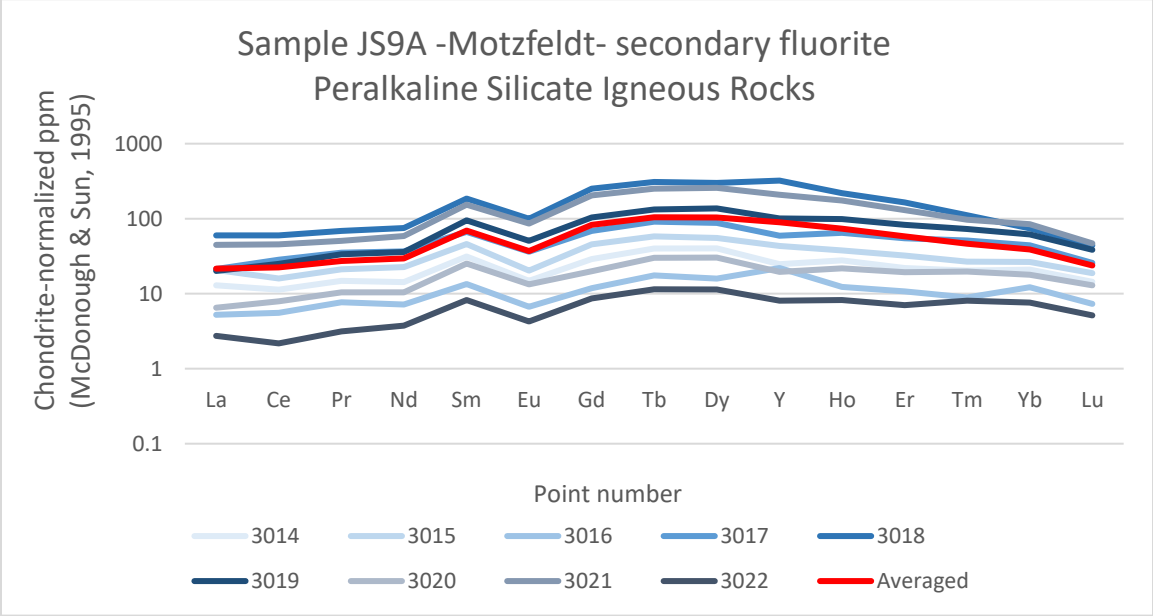

Figure 2-1 Chondrite-normalized (McDonough and Sun, 1995) REE (ppm) concentrations of nine points (3014-3022), and their representative, averaged value, in a secondary fluorite sample, JS9A, taken by LA-ICP-MS analysis from Motzfeldt, Gardar Province, South Greenland from Schönenberger et al., 2008. This value was averaged prior to chondrite normalization and any other calculations.

2.3.2. Including data analyzed by INAA

In the initial stages of data compilation, publications that utilized INAA were originally omitted on grounds that analyses for Pr, Gd, Dy, Ho, Er, and Tm were either always, or often not included. Because of these exclusions, calculations of estimated values and anomalous REE-Y values could not be determined from INAA data. Additionally, this method of analyses for determining REE content was one of the first to be historically implemented, after XRF analysis, and has been in use since the late 60's to early 70's, and it was the suspicion of this author that the method may be outdated. ICP-MS analyses also reach lower detection limits for REE. These facts, and the initial appearance that values found by INAA were slightly lower than values found by other analytical methods seen in Figure 2-2, caused this author to originally omit these publications from compilation.

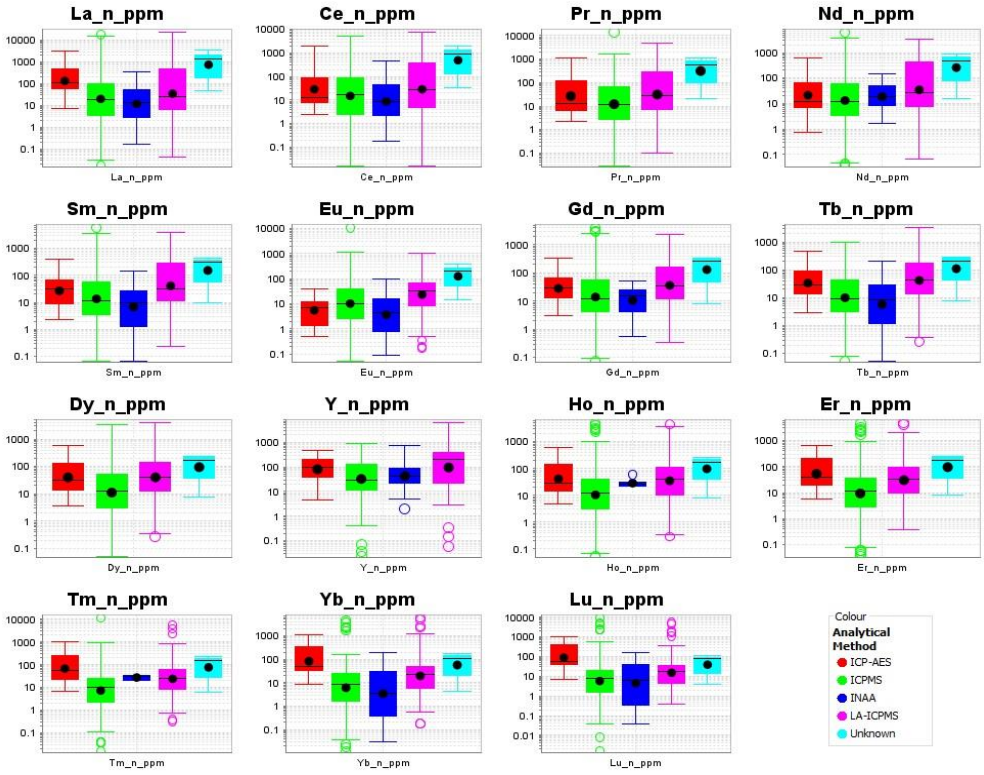

Figure 2-2 Tukey Box plots of all compiled data, normalized to chondrite (McDonough and Sun, 1995) sorted by analytical method. The maximum number of analyses included for each method type is as follows: 15 for ICP-AES, 399 for ICPMS, 95 for INAA, 166 for (averaged) LA-ICP-MS, and nine for Unknown methods. Notice values for INAA are slightly lower than other analytical methods. Boxes represent 50% of included data, black lines represent medians, black dots represent means, upper and lower whiskers represent maximum and minimum values respectively, excluding outliers which are represented by hollow circles calculated as exceeding 1.5 times the inner quartile range in either the positive or negative direction.

It was finally decided to include data analyzed by INAA, because it added a significant amount of data (95 analyses) to a project based on quantifying data, where the goal is to attempt to define genetic deposit types based on REE-Y signatures in fluorite, and a re-evaluation of the original premise that lower values collected by INAA was inaccurate. Jenner (1996) showed excellent correlation between Sm values analyzed by INAA and ICP-MS methods, determining that if elements are well above detection limits for both methods, the results are comparable. Pinte et al., (1998) also determined that the methods were generally in good agreement. In order to accurately represent any population of data to a degree that is statistically viable, one must attempt to use as many samples as possible to produce a normal distribution representing the population. Not only, did the addition of INAA data to the compilation add a significant portion of data to the set as a whole, it provided data for a fluorite-containing deposit type not described by any other analytical method, the SEDEX deposit from Nördliche Kalkalpen (Schneider et al., 1975), and also provided 13 additional analyses to the small sample size of only four analyses for rare metal pegmatites. Additionally, the original observation depicted in Figure 2-2 was found to be biased by the SEDEX dataset (33 of the 95 INAA measurements), for when a comparison of data for deposit types analyzed by INAA were compared to those of other methods, the values were found to be low to within range with data for carbonatite-related deposits (Figure 2-3), high to within range with data for MVT deposits (Figure 2-4), and in range with data for epithermal/hydrothermal vein and replacement deposits without regard to host lithology (Figure 2-5).

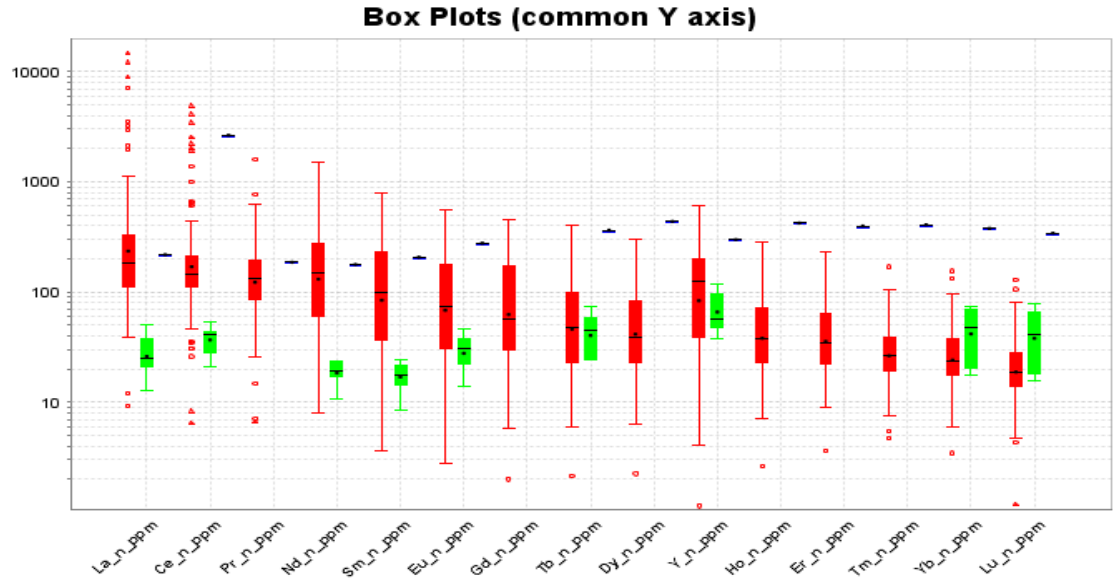

Figure 2-3 Box plots (Tukey) of data representing carbonatite-related deposits sorted by analytical method. Red boxes represent data analyzed by ICPMS methods, Green represents INAA, Blue represents LA-ICP-MS. ICPMS data includes 91 analyses from Daluxiang, Maoniuping, Lizhuang, Bayan Obo, Speewah Fluorite, Okorusu, and Mato Preto deposits, LA-ICP-MS data includes 1 averaged value from 44 analyses on a single sample from the Deep Purple/Rock Canyon Creek deposit, and INAA data includes 7 analyses from samples from the Amba Dongar deposit.

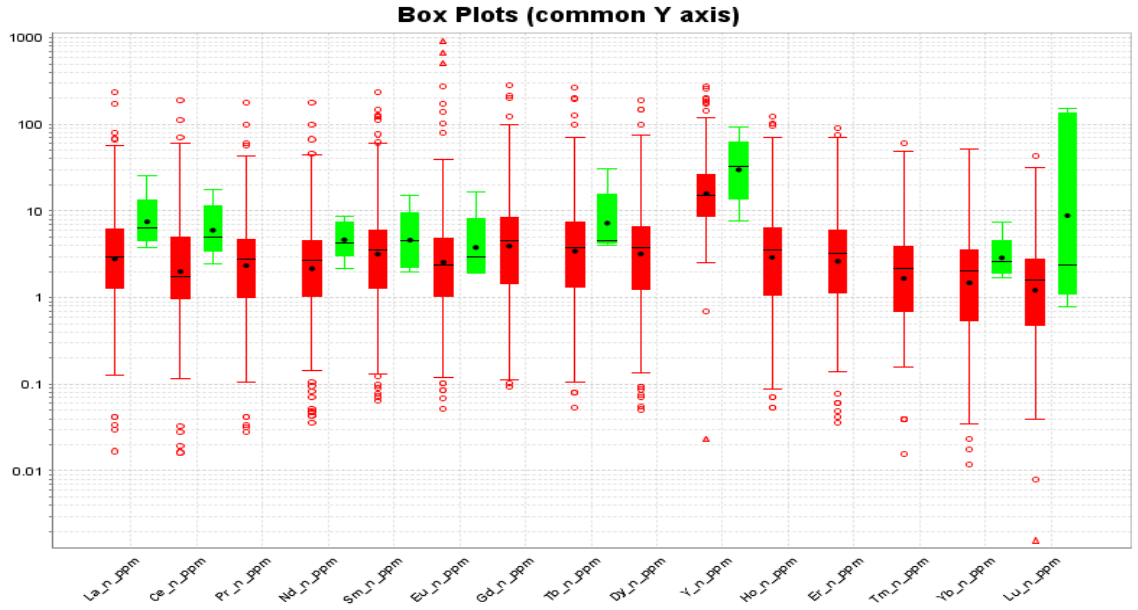

Figure 2-4 Box plots (Tukey) of data representing MVT deposits sorted by analytical method. Red boxes represent data analyzed by ICPMS methods and Green boxes represents INAA methods. INAA data includes 5 samples from one deposit, while ICP-MS data includes 126 samples from 15 deposits.

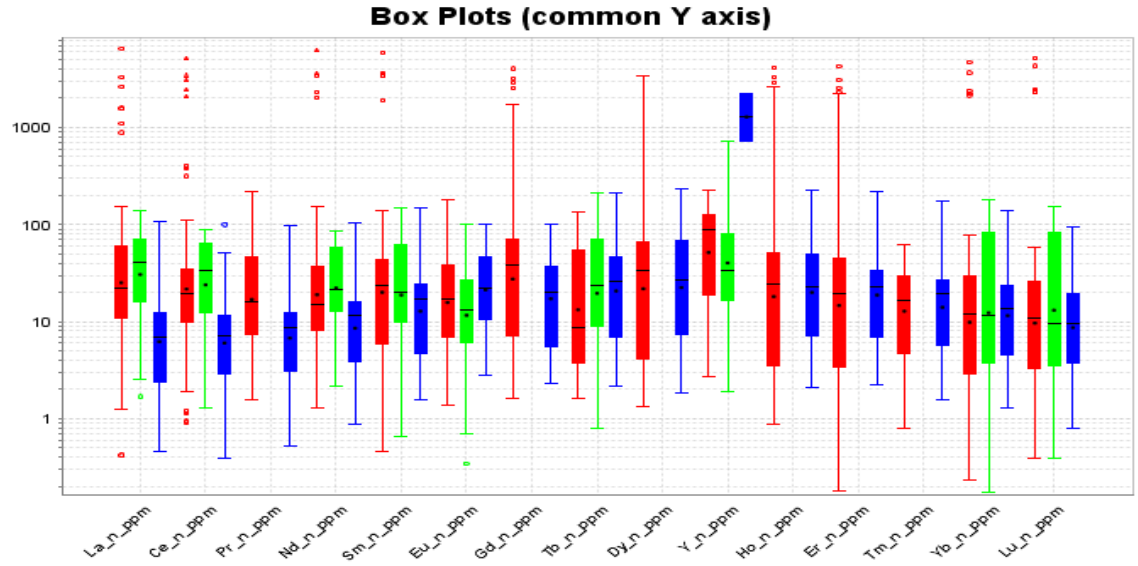

Figure 2-5 Box plots (Tukey) of data representing hydrothermal/epithermal vein and replacement deposit data in all hosts sorted by analytical method. Red boxes represent data analyzed by ICP-MS methods, data analyzed by INAA represented by Green boxes, and Blue boxes represents LA-ICP-MS data. 105 ICP-MS analyses are represented here, as well as 36 ICP-MS, and 38 neutron-activation analyses.

2.3.3. Representation of primary mineralization environments

As mentioned above, examining the representation quality of primary mineralization environments is useful in assigning confidence to created discrimination diagrams and their subsequent applications. Representation of primary mineralization environment groups was analyzed by assessing data sample sizes per group, data source diversity, and by examination of univariate normality per REE-Y before and after logarithmic transformation using histograms, Q-Q plots, and the Shapiro-Wilk test. Furthermore, investigation of the normality of data distributions representing primary mineralization environments can assign confidence to the translation of our samples of data to represented populations.

Sample sizes

First, it is prudent to question the number of samples representing each determined group and therefore each theoretical population. If the number of samples used is too low, distribution curves on histograms may not appear normal, and these groups cannot be represented with confidence. Powers and minimum sample sizes can be calculated and should be calculated prior to statistical testing as outlined by Noordzij et al., (2010) and Lenth (2001), but often an arbitrary number with no statistical significance is assigned as a minimum sample size, conventionally somewhere between 20-35. Since the experimental design of this project was limited to information that could be gathered from external sources and funding for the acquisition of more data, limited, the calculation of minimum sample size was not necessary, but every effort was made to collect the maximum amount of trace-element data reported from fluorite for the 15 determined primary mineralization environment groups. If the sample size is too small to adequately represent its respective population, the univariate distribution of that dataset will not achieve normality. Mindfulness of poorly represented deposit-type groups in utilization of discrimination diagrams may offer explanations for poor fit of applied data, and should be noted when applying certainty to identifying certain groups. A few deposit types were well-represented with the number of compiled samples approaching or exceeding 100 such as those for carbonatite-related deposits and MVT deposits, but others were severely limited at under 20 samples each, such as those for IOCG, greisen, rare-metal pegmatite, cryolite, and granite-related uranium deposits. The numbers of analyses compiled for primary mineralization environments are listed in Table A-11.

Of primary deposit types, the number of samples representing each are: peralkaline silicate igneous rocks – 52; carbonatite-related deposits – 99; MVT – 138; SEDEX – 33; IOCG – 9; skarn – 24; greisen – 17; pegmatite – 17; granite-related uranium – 15; cryolite – 14; intrusion-related molybdenum – 35; veins/replacements in carbonate hosts – 54; veins/replacements in igneous hosts 93; veins/replacements in metamorphic hosts – 27; veins/replacements in sedimentary hosts – 7. Of these groups, it is likely that peralkaline silicate igneous rock, carbonatite-related, MVT, SEDEX, intrusion-related molybdenum, hydrothermal/epithermal veins/replacements in carbonate hosts, and hydrothermal/epithermal veins/replacements in igneous hosts deposits will have sufficient sample sizes, will display favorable normality distributions therefore are sufficiently represented by data within this study to draw accurate conclusions. Skarn and hydrothermal/epithermal veins/replacements in metamorphic host rock deposits may have marginal success with tests of distribution normality due to samples sizes of less than 30, and it is likely that the sample sizes for IOCG, greisen, pegmatite, granite-related uranium, cryolite, and hydrothermal/epithermal veins/replacements in sedimentary rock deposits are too few for adequate representation of these groups.

Datasource diversity

Representation of primary mineralization environment groups improves if compiled data is sourced from an increasing number of deposits. The number of deposits from which REE-Y data in fluorite was compiled per primary mineralization environment is indicated in Table A-1. Primary deposit types that were adequately represented by several deposits from several regions includes: carbonatite-related, MVT, skarn, and hydrothermal/epithermal vein/replacement deposits hosted in carbonate, igneous, metamorphic, and sedimentary rock. Greisen deposit representation may have been adequately diversified using analyses from five deposits, however these deposits were located within the same expansive region. SEDEX deposits were also only represented by several deposits within the same district. The following deposit-types were represented only by one or two deposits from only one or two regions: peralkaline silicate igneous rock, IOCG, rare-metal pegmatite, granite-related uranium, rare-metal pegmatite, and intrusion-related molybdenum.

Carbonatite-related deposits are represented by information from nine deposits from seven regions, MVT's are represented by 18 deposits from eight districts, skarns are represented by six deposits from five regions, and hydrothermal/epithermal

vein/replacement deposits hosted in carbonates are represented by 20 deposits from eight regions, vein/replacement deposits hosted in igneous rocks are represented by 68 deposits in 15 regions, vein/replacement deposits hosted in metamorphic rocks are represented by 25 deposits in four regions, and those hosted in sedimentary rock are represented by eight deposits from four regions. Data included in the representation of greisen deposits consists of five deposits from one expansive region, and that which represents SEDEX deposits consists of 18 deposits within the same district. Finally, poorly represented groups include peralkaline silicate rocks for which representatitve data was only sourced from three deposits from two regions, IOCG deposits from a single deposit, rare-metal pegmatites from three deposits in two regions, granite-related uranium deposits from two deposits from two regions, cryolite deposits from two deposits in two regions, and intrusion-related molybdenum deposits from two deposits from two regions.

Normality of univariate REE-Y distributions

If a population of data is represented at random, with sufficient sample size, a histogram of the measurement representing this dataset should be normally distributed. A normal distribution of data implies that the sampled population has been sufficiently represented by the data, where the frequency of sample values is highest at the mean and median of the expected representative values and the frequency of higher or lower values are fewer. The extent of values deviated from the mean and median is otherwise known as variance. Additionally, if the distributions of the lanthanoids representing each respective group, such as primary deposit types, are normal, this implies that the selected sample of data is an effective representation of the population that can be identified. Nested within this logic is the point that opposing population assignations containing sample data that would satisfy the same normality curve, identifies a flaw in this representation scheme. In other words, if a dataset includes samples from two obviously different populations, but the overall distribution remains normal, there is likely a flaw in the classification scheme. Two population samples within the same dataset should display a distribution with two distinct peaks as seen in Figure 2-6. With the intention of testing our data groups' hypothesized population representations, the normality of the distributions of lanthanoids representing our determined groups (primary mineralization environments) were observed.

The normality of data distributions can be observed by three different methods. The first two, histogram distributions and quantile-quantile plots (Q-Q plots), are visual and

subsequently suffer from subjective interpretation. It may be possible to measure the correlation or R value for Q-Q plots for a less subjective interpretation, but this is beyond scope for this author. The third, the Shapiro-Wilk test, is a statistical method of testing normality with attached measures of significance, but is not without its shortcomings. Histograms were created using the IoGAS v.6.1 IoAnalytics software by REFLEX (and by using IBM's SPSS Statistics v. 23) where 20 bins were created along the x axis whose contained ranges were determined by sample size with counts on the y axis. Q-Q plots were generated by using the Blom's proportion estimation formula within IBM's SPSS software. Q-Q plots are created by comparing theoretically normally generated quantiles and the actual quantiles calculated from inputted sample values on an x-y diagram. Quantiles are fractions of data under a certain value and the ranges of the quantile values are determined by sample size and value. If the sample data observed via Q-Q plots are normally distributed, the data should plot in a straight line whose slope represents the standard deviation of the data distribution, (Thode, 2002). The Shapiro-Wilk test determines whether or not data is significantly normally distributed by assessing how closely the ratio (the p-value) of the theoretically normal estimate of the sample variance compared to the actual estimation of sample variance is equal to one. The range of p-values and interpretable levels of significance were determined empirically by Shapiro and Wilk, (Thode, 2002). Because of the manner in which the variance is compared, it would be difficult to use this test to reject normality if the sample sizes of data sets are small, or if the data sets include many equal values. Additionally, if the sample size of a given set is large, small deviations from normality are subject to stricter penalty and are often assigned a value of low significance, otherwise known as non-normal. Because of the subjective shortcomings of observed histograms and Q-Q plots and the foibles introduced through varying sample sizes with the Shapiro-Wilk test, each of these methods of distribution normality will be compared for assessment of our data groups.

Figure 2-6 Log-transformed histogram distributions of all analyses representing carbonatite-related deposits (purple) and MVT deposits (green) showing two distinct normality peaks representing each respective sample population. Minor secondary peaks may be observable for measurements of Gd, Tb, Dy, and Y for MVT and alternatively Y for carbonatite-related data that seem to mimic distribution curves of the opposing sample population, but it is unknown if these minor peaks would disappear with increased sample sizes, or if these are indicative of some conditional similarity between these deposit-type groups. Overall, these distributions seem to indicate adequate and accurate representation of these groups.

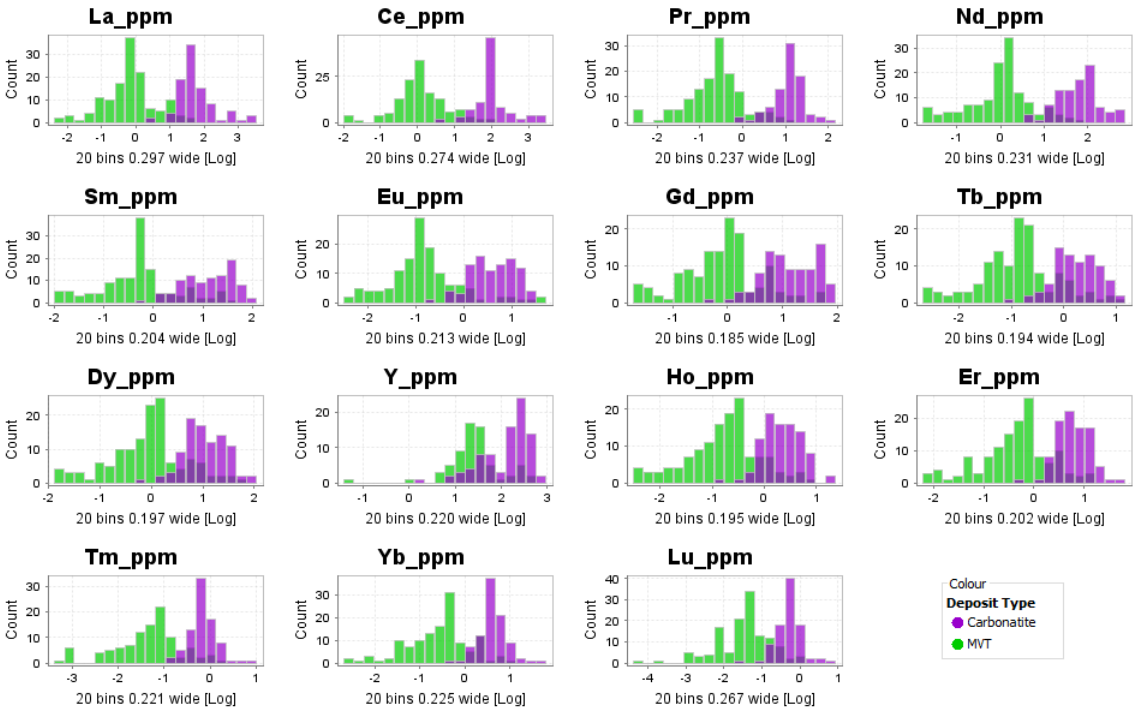

Alternatively, there are ways to test multivariate normality, (apparently 50 different ways), which is ideal for our situation as our data groups are represented by multiple elements simultaneously. However, there isn't a conventionally used test or any that have been proven most effective for any general application. Mecklin and Mundfrom, (2004), however, suggest using the Henze-Zirkler test-normality. It may be safe to assume that if the univariate distributions are normal going into a multivariate test of normality, that the result would indeed indicate normality. By this virtue, it may not be necessary to test multivariate normality separately (though it would save time if the investigator has the skills and means) if univariate normality has been proven for every variable considered.

The results of normality testing for primary-deposit type groups is outlined in Table 2-2. This table shows testing performed before and after logarithmic transformation of variables, and describes visually subjective results as a degree of skewness or a number of representative peaks in histograms. Additionally, the comparison of results for Q-Q plots between these tests is described as a degree of improvement toward normality, or alternatively toward a straighter trend line. The results of the Shapiro-Wilk test are measures of significance for normality. Any value over 0.05 is considered "significantly normal."

The results from Table 2-2 show that normality was achieved or at least improved by logarithmically transforming the data. This was true for all cases observed by comparing histogram distributions with the exceptions of measurements from the following primary mineralization environments where distribution normality was worsened: La from granite-related uranium deposits, Nd and Lu from hydrothermal/epithermal vein and replacement deposits hosted in sedimentary rocks, and there was no improvement for any measured elements for IOCG deposits, but the transformations had no negative effects on normality. For all transformations observed via Q-Q plots, normality was reached or improved upon except for the following elements where the transformations caused a further deviation from normality: Y from carbonatite-related deposits, La from granite-related deposits, Tb from hydrothermal/epithermal veins/replacements hosted in igneous rock, Y from hydrothermal/epithermal veins/replacements hosted in metamorphic rock, all elements from hydrothermal/epithermal veins/replacement deposits hosted in sedimentary rock except La and Er, and all elements from IOCG deposits except La and Ce. For the final four elements mentioned, no improvement nor detriment toward normality was caused by logarithmic transformation, which was also the case for measurements of Tb, Dy, Ho, and Tm from peralkaline silicate igneous deposits, Pr, Nd, and Sm from granite-related uranium deposits, and Gd from hydrothermal/epithermal vein/replacement deposits hosted in metamorphic rock. From these observations, it would appear that for most elements measured for most primary deposit types, logarithmic transformations improved the normality of dataset distributions. Results observed from Shapiro-Wilk tests are a bit more complicated and are discussed below.

Table 2-2 Results of normality testing by visual comparison of distribution histograms and quantile-quantile plots and of statistical normality testing by Shapiro-Wilk test for all lanthanoids representing primary mineralization environments before and after logarithmic transformations. The number of data points included in each test are represented by "n." Cells have been colored according to closeness to normality or relationally between results from the same test before and after logarithmic transformation of data points with red depicting "non-normal" and green depicting "normal" distributions.

Carbonatite-related								**Skarn**							
	Hist.	Log-hist.	Q-Q	Log- Q-Q	S-W	Log-S-W	n =		Hist.	Log-hist.	Q-Q	Log- Q-Q	S-W	Log-S-W	n =
La	Skew	Normal	Non-normal	Normal	0.000	0.000	92	La	Skew	Normal	Non-normal	Improved	0.505	0.068	8
Ce	Skew	Normal	Non-normal	Near-normal	0.000	0.000	92	Ce	Skew	Normal	Non-normal	Improved	0.627	0.034	8
Pr	Skew	Normal	Near-normal	Improved	0.000	0.001	81	Pr	Skew	2 Peaks	Non-normal	Improved	0.381	0.019	8
Nd	Skew	3-4 Peaks	Non-normal	Normal	0.000	0.246	92	Nd	Skew	2 Peaks	Non-normal	Normal	0.311	0.015	8
Sm	Skew	2 Peaks	Near-normal	Normal	0.000	0.057	92	Sm	Skew	Slightly skew	Non-normal	Improved	0.187	0.011	8
Eu	Skew	2 Peaks	Non-normal	Normal	0.000	0.092	92	Eu	Skew	Slightly skew	Non-normal	Improved	0.17	0.339	8
Gd	Skew	2 Peaks	Near-normal	Improved	0.000	0.023	91	Gd	Skew	2 Peaks	Non-normal	Improved	0.149	0.006	8
Tb	Skew	Normal	Near-normal	Normal	0.000	0.549	81	Tb	Skew	2 Peaks	Non-normal	Improved	0.542	0.037	8
Dy	Skew	2 Peaks	Near-normal	Normal	0.000	0.435	92	Dy	Skew	2 Peaks	Non-normal	Improved	0.381	0.022	8
Y	Skew	2 Peaks	Normal	Worse	0.000	0.000	85	Y	Skew	Normal	Non-normal	Improved	0.649	0.156	8
Ho	Skew	Normal	Near-normal	Normal	0.000	0.664	92	Ho	Skew	Slightly skew	Non-normal	Improved	0.261	0.021	8
Er	Skew	Normal	Non-normal	Normal	0.000	0.561	92	Er	Skew	Slightly skew	Non-normal	Improved	0.517	0.052	8
Tm	Skew	Normal	Non-normal	Normal	0.000	0.025	81	Tm	Skew	Slightly skew	Non-normal	Improved	0.65	0.074	8
Yb	Skew	Normal	Non-normal	Normal	0.000	0.012	92	Yb	Skew	Slightly skew	Non-normal	Improved	0.446	0.027	8

Lu	Skew	Normal	Non-normal	Normal	0.000	0.001	92

Peralkaline silicate igneous

	Hist.	Log-hist.	Q-Q	Log- Q-Q	S-W	Log-S-W	n =
La	Skew	2 Peaks	Non-normal	Improved	0.000	0.001	52
Ce	Skew	3 Peaks	Non-normal	Improved	0.000	0.001	52
Pr	Skew	2 Peaks	Non-normal	Improved	0.000	0.004	52
Nd	Skew	Slightly skew	Non-normal	Improved	0.000	0.000	52
Sm	Skew	Slightly skew	Non-normal	Improved	0.000	0.001	52
Eu	Skew	Slightly skew	Non-normal	Improved	0.000	0.001	52
Gd	Skew	Slightly skew	Non-normal	Improved	0.000	0.001	52
Tb	Skew	2 Peaks	Near-normal	Neutral	0.000	0.000	52
Dy	Skew	2 Peaks	Near-normal	Neutral	0.000	0.000	52
Y	2 Peaks	2 Peaks	Non-normal	Improved	0.000	0.000	52
Ho	2 Peaks	2 Peaks	Near-normal	Neutral	0.000	0.000	52
Er	2 Peaks	Slightly skew	Near-normal	Improved	0.000	0.000	52
Tm	2 Peaks	Slightly skew	Near-normal	Neutral	0.000	0.000	52
Yb	Skew	Slightly skew	Non-normal	Improved	0.000	0.000	52
Lu	Skew	2 Peaks	Non-normal	Improved	0.000	0.002	52

Lu	Skew	2 Peaks	Non-normal	Improved	0.179	0.015	8

Cryolite

	Hist.	Log-hist.	Q-Q	Log- Q-Q	S-W	Log-S-W	n =
La	Skew	2 Peaks	Non-normal	Normal	0.000	0.768	14
Ce	Skew	2 Peaks	Non-normal	Normal	0.000	0.398	14
Pr	Skew	Normal	Non-normal	Improved	0.000	0.554	14
Nd	Skew	Normal	Non-normal	Improved	0.000	0.532	14
Sm	Skew	2 Peaks	Non-normal	Improved	0.000	0.56	14
Eu	Skew	Slightly skew	Non-normal	Normal	0.000	0.357	14
Gd	Skew	Normal	Non-normal	Normal	0.000	0.907	10
Tb	Skew	Normal	Non-normal	Normal	0.000	0.534	14
Dy	Skew	2 Peaks	Non-normal	Normal	0.000	0.404	14
Y	Skew	Slightly skew	Non-normal	Improved	0.000	0.087	14
Ho	Skew	Normal	Non-normal	Improved	0.000	0.402	14
Er	Skew	Normal	Non-normal	Normal	0.000	0.387	14
Tm	Skew	Slightly skew	Non-normal	Improved	0.000	0.353	14
Yb	Skew	Normal	Non-normal	Improved	0.000	0.595	10
Lu	Skew	2 Peaks	Non-normal	Improved	0.000	0.383	14

MVT								Granite-related uranium							
	Hist.	Log-hist.	Q-Q	Log- Q-Q	S-W	Log-S-W	n =		Hist.	Log-hist.	Q-Q	Log- Q-Q	S-W	Log-S-W	n =
La	Skew	Normal	Non-normal	Improved	0.000	0.004	138	La	Normal	Slightly skew	Near-normal	Worse	0.817	0.000	13
Ce	Skew	Normal	Non-normal	Normal	0.000	0.001	138	Ce	Slightly skew	Normal	Non-normal	Improved	0.033	0.016	14
Pr	Skew	Normal	Non-normal	Normal	0.000	0.003	133	Pr	Slightly skew	Slightly skew	Near-normal	Neutral	0.083	0.092	14
Nd	Skew	Normal	Non-normal	Improved	0.000	0.000	138	Nd	Slightly skew	Slightly skew	Near-normal	Neutral	0.114	0.171	14
Sm	Skew	Normal	Non-normal	Improved	0.000	0.001	138	Sm	Skew	Normal	Near-normal	Neutral	0.008	0.392	14
Eu	Skew	Normal	Non-normal	Improved	0.000	0.000	135	Eu	Skew	Normal	Non-normal	Improved	0.015	0.747	10
Gd	Skew	Normal	Non-normal	Normal	0.000	0.057	133	Gd	Skew	2 Peaks	Non-normal	Improved	0.019	0.491	14
Tb	Skew	Normal	Non-normal	Normal	0.000	0.031	138	Tb	Skew	Normal	Near-normal	Improved	0.013	0.881	13
Dy	Skew	Normal	Non-normal	Normal	0.000	0.026	133	Dy	Skew	Normal	Non-normal	Improved	0.001	0.684	14
Y	Skew	Normal	Non-normal	Improved	0.000	0.000	72	Y	2 Peaks	Normal	Non-normal	Neutral	0.102	0.482	7
Ho	Skew	Normal	Non-normal	Normal	0.000	0.026	133	Ho	Skew	Normal	Non-normal	Normal	0.002	0.961	14
Er	Skew	Normal	Non-normal	Normal	0.000	0.006	132	Er	Skew	Normal	Non-normal	Normal	0.001	0.819	14
Tm	Skew	Normal	Non-normal	Normal	0.000	0.005	102	Tm	Skew	Normal	Non-normal	Improved	0.002	0.694	13
Yb	Skew	Normal	Non-normal	Normal	0.000	0.004	136	Yb	Skew	2 Peaks	Non-normal	Improved	0.001	0.119	14
Lu	Skew	Normal	Non-normal	Normal	0.000	0.001	135	Lu	Skew	Normal	Non-normal	Improved	0.001	0.225	13

Rare-metal pegmatite								Greisen							
	Hist.	Log-hist.	Q-Q	Log- Q-Q	S-W	Log-S-W	n =		Hist.	Log-hist.	Q-Q	Log- Q-Q	S-W	Log-S-W	n =
La	Skew	3 Peaks	Non-normal	Normal	0.000	0.705	17	La	Skew	Normal	Non-normal	Improved	0.000	0.549	10
Ce	Skew	Slightly skew	Non-normal	Normal	0.000	0.350	17	Ce	Skew	Slightly skew	Non-normal	Improved	0.000	0.428	16
Pr	2 Peaks	Normal	Non-normal	Normal	0.330	0.975	4	Pr	Skew	Normal	Non-normal	Normal	0.000	0.644	17
Nd	Skew	Slightly skew	Non-normal	Normal	0.000	0.746	17	Nd	Skew	Normal	Non-normal	Normal	0.000	0.989	17
Sm	Skew	Normal	Non-normal	Normal	0.000	0.372	17	Sm	Skew	2 Peaks	Non-normal	Normal	0.000	0.403	17
Eu	Skew	Slightly skew	Non-normal	Improved	0.000	0.011	17	Eu	Skew	Normal	Non-normal	Normal	0.000	0.862	17
Gd	Slightly skew	Slightly skew	Non-normal	Neutral	0.082	0.027	13	Gd	Skew	Normal	Non-normal	Normal	0.000	0.937	17
Tb	Skew	Normal	Non-normal	Improved	0.000	0.068	17	Tb	Skew	Slightly skew	Non-normal	Normal	0.000	0.912	17
Dy	2 Peaks	2 Peaks	Non-normal	Neutral	0.591	0.613	4	Dy	Skew	Slightly skew	Non-normal	Normal	0.000	0.937	17
Y	2 Peaks	2 Peaks	Non-normal	Neutral	0.317	0.417	4	Y	2 Peaks	Normal	Near-normal	Improved	0.015	0.981	14
Ho	Skew	Skew	Non-normal	Improved	0.000	0.000	14	Ho	Skew	2 Peaks	Non-normal	Improved	0.000	0.958	17
Er	2 Peaks	2 Peaks	Non-normal	Neutral	0.196	0.188	4	Er	Skew	Normal	Non-normal	Normal	0.000	0.984	17
Tm	Skew	Skew	Non-normal	Improved	0.010	0.242	7	Tm	Skew	Normal	Non-normal	Improved	0.000	0.983	16
Yb	Skew	Normal	Non-normal	Improved	0.000	0.025	17	Yb	Skew	Normal	Non-normal	Improved	0.000	0.932	17
Lu	Skew	Normal	Non-normal	Improved	0.000	0.018	17	Lu	Skew	Normal	Non-normal	Improved	0.000	0.744	17

Intrusion-related molybdenum							
	Hist.	Log-hist.	Q-Q	Log- Q-Q	S-W	Log-S-W	n =
La	Skew	Normal	Non-normal	Improved	0.000	0.045	29
Ce	Skew	2 Peaks	Non-normal	Improved	0.000	0.099	29
Pr	Skew	2 Peaks	Non-normal	Improved	0.000	0.307	29
Nd	Skew	Normal	Non-normal	Normal	0.000	0.647	29
Sm	Skew	Normal	Non-normal	Normal	0.000	0.002	29
Eu	Skew	2 Peaks	Non-normal	Improved	0.000	0.002	29
Gd	Skew	Slightly skew	Non-normal	Improved	0.000	0.036	29
Tb	Skew	Slightly skew	Non-normal	Improved	0.000	0.035	29
Dy	Skew	2 Peaks	Non-normal	Improved	0.000	0.055	29
Y	Skew	Normal	Non-normal	Improved	0.000	0.371	29
Ho	Skew	2 Peaks	Non-normal	Improved	0.000	0.071	29
Er	Skew	2 Peaks	Non-normal	Improved	0.000	0.104	29
Tm	Skew	2 Peaks	Non-normal	Improved	0.000	0.073	29
Yb	Skew	Normal	Non-normal	Improved	0.000	0.178	29
Lu	Skew	2 Peaks	Non-normal	Improved	0.000	0.136	29

Hydrothermal/epithermal vein/replacement in igneous host							
	Hist.	Log-hist.	Q-Q	Log- Q-Q	S-W	Log-S-W	n =
La	Skew	Slightly skew	Non-normal	Improved	0.000	0.000	93
Ce	Skew	Slightly skew	Non-normal	Improved	0.000	0.000	93
Pr	Skew	Slightly skew	Non-normal	Improved	0.000	0.176	40
Nd	Skew	Normal	Non-normal	Normal	0.000	0.000	93
Sm	Skew	Normal	Non-normal	Normal	0.000	0.000	93
Eu	Skew	2 Peaks	Non-normal	Normal	0.000	0.698	93
Gd	Skew	Slightly skew	Non-normal	Improved	0.000	0.000	62
Tb	Skew	Slightly skew	Near-normal	Worse	0.001	0.000	62
Dy	Skew	Normal	Non-normal	Improved	0.000	0.000	65
Y	Skew	Normal	Non-normal	Improved	0.000	0.017	37
Ho	Skew	Normal	Non-normal	Improved	0.000	0.000	62
Er	Skew	Normal	Non-normal	Improved	0.000	0.000	65
Tm	Skew	Normal	Non-normal	Improved	0.000	0.016	40
Yb	Skew	Normal	Non-normal	Improved	0.000	0.000	93
Lu	Skew	Normal	Non-normal	Improved	0.000	0.000	93

Hydrothermal/epithermal vein/replacement in carbonate host							
	Hist.	Log-hist.	Q-Q	Log- Q-Q	S-W	Log-S-W	n =
La	Skew	Slightly skew	Non-normal	Improved	0.000	0.011	53
Ce	Skew	Slightly skew	Non-normal	Improved	0.000	0.125	53
Pr	Skew	2 Peaks	Non-normal	Improved	0.000	0.077	32
Nd	Skew	2 Peaks	Non-normal	Normal	0.000	0.066	51
Sm	Skew	Normal	Non-normal	Normal	0.000	0.710	53
Eu	Skew	Normal	Non-normal	Normal	0.000	0.867	53
Gd	Skew	Normal	Non-normal	Normal	0.003	0.870	32
Tb	Skew	Slightly skew	Non-normal	Normal	0.000	0.124	53
Dy	Skew	Slightly skew	Non-normal	Improved	0.000	0.204	32
Y	Skew	Slightly skew	Non-normal	Improved	0.000	0.031	18
Ho	Skew	3-4 Peaks	Non-normal	Normal	0.001	0.634	32
Er	Skew	2 Peaks	Non-normal	Neutral	0.006	0.051	32
Tm	2 Peaks	Slightly skew	Non-normal	Improved	0.062	0.319	11
Yb	Skew	2 Peaks	Non-normal	Normal	0.000	0.167	46
Lu	Skew	Slightly skew	Non-normal	Normal	0.000	0.102	49

Hydrothermal/epithermal vein/replacement metamorphic host							
	Hist.	Log-hist.	Q-Q	Log- Q-Q	S-W	Log-S-W	n =
La	Skew	Normal	Non-normal	Improved	0.000	0.083	24
Ce	Skew	2 Peaks	Non-normal	Improved	0.000	0.406	24
Pr	Skew	2 Peaks	Non-normal	Improved	0.000	0.628	24
Nd	Skew	Slightly skew	Non-normal	Improved	0.000	0.545	24
Sm	Skew	Normal	Non-normal	Normal	0.000	0.922	24
Eu	Skew	Normal	Non-normal	Normal	0.000	0.529	24
Gd	Skew	Slightly skew	Near-normal	Neutral	0.007	0.252	24
Tb	Skew	Slightly skew	Near-normal	Improved	0.036	0.203	24
Dy	Skew	Slightly skew	Near-normal	Improved	0.008	0.956	24
Y	Skew	Slightly skew	Near-normal	Worse	0.652	0.010	24
Ho	Skew	Slightly skew	Non-normal	Improved	0.002	0.218	24
Er	Skew	Slightly skew	Non-normal	Improved	0.000	0.185	24
Tm	Skew	Normal	Non-normal	Improved	0.000	0.559	24
Yb	Skew	2 Peaks	Non-normal	Improved	0.000	0.781	24
Lu	Skew	2 Peaks	Non-normal	Improved	0.000	0.544	24

Hydrothermal/epithermal vein deposits in sedimentary host							
	Hist.	Log-hist.	Q-Q	Log- Q-Q	S-W	Log-S-W	n =
La	2 Peaks	Slightly skew	Non-normal	Neutral	0.016	0.002	7
Ce	2 Peaks	Normal	Non-normal	Worse	0.062	0.001	7
Pr	2 Peaks	Slightly skew	Non-normal	Worse	0.031	0.000	7
Nd	2 Peaks	Skew	Non-normal	Worse	0.000	0.000	7
Sm	2 Peaks	Slightly skew	Non-normal	Worse	0.072	0.000	7
Eu	2 Peaks	Slightly skew	Non-normal	Worse	0.020	0.001	7
Gd	2 Peaks	Slightly skew	Non-normal	Worse	0.032	0.008	7
Tb	2 Peaks	Slightly skew	Non-normal	Worse	0.034	0.007	7
Dy	2 Peaks	2 Peaks	Non-normal	Worse	0.019	0.000	7
Y	n/a	n/a	n/a	n/a	n/a	n/a	1
Ho	2 Peaks	2 Peaks	Non-normal	Worse	0.032	0.005	7
Er	2 Peaks	2 Peaks	Non-normal	Neutral	0.004	0.001	7
Tm	2 Peaks	2 Peaks	Non-normal	Worse	0.003	0.001	7
Yb	2 Peaks	2 Peaks	Non-normal	Worse	0.004	0.002	7
Lu	2 Peaks	Skew	Non-normal	Worse	0.007	0.003	7

IOCG							
	Hist.	Log-hist.	Q-Q	Log- Q-Q	S-W	Log-S-W	n =
La	2 Peaks	2 Peaks	Non-normal	Neutral	0.361	0.032	9
Ce	2 Peaks	2 Peaks	Non-normal	Neutral	0.528	0.021	9
Pr	2 Peaks	2 Peaks	Near-normal	Worse	0.489	0.007	9
Nd	2 Peaks	2 Peaks	Near-normal	Worse	0.554	0.003	9
Sm	2 Peaks	2 Peaks	Non-normal	Worse	0.159	0.001	9
Eu	2 Peaks	2 Peaks	Near-normal	Worse	0.761	0.019	9
Gd	2 Peaks	2 Peaks	Non-normal	Worse	0.055	0.001	9
Tb	2 Peaks	2 Peaks	Non-normal	Worse	0.046	0.000	9
Dy	2 Peaks	2 Peaks	Non-normal	Worse	0.063	0.001	9
Y	n/a	n/a	n/a	n/a	n/a	n/a	0
Ho	2 Peaks	2 Peaks	Non-normal	Worse	0.144	0.001	9
Er	Slightly skew	2 Peaks	Near-normal	Worse	0.228	0.002	9
Tm	Slightly skew	2 Peaks	Near-normal	Worse	0.405	0.004	9
Yb	Slightly skew	2 Peaks	Near-normal	Worse	0.393	0.005	9
Lu	2 Peaks	2 Peaks	Near-normal	Worse	0.353	0.006	9

SEDEX							
	Hist.	Log-hist.	Q-Q	Log- Q-Q	S-W	Log-S-W	n =

	Hist.	Log-hist.	Q-Q	Log- Q-Q	S-W	Log-S-W	n =	Tb	Skew	2 Peaks	Non-normal	Normal	0.000	0.337	32
La	Skew	Normal	Non-normal	Normal	0.000	0.029	32	Dy	n/a	n/a	n/a	n/a	n/a	n/a	0
Ce	Skew	2 Peaks	Non-normal	Normal	0.000	0.781	32	Y	n/a	n/a	n/a	n/a	n/a	n/a	0
Pr	n/a	n/a	n/a	n/a	n/a	n/a	n/a	Ho	n/a	n/a	n/a	n/a	n/a	n/a	0
Nd	n/a	n/a	n/a	n/a	n/a	n/a	n/a	Er	n/a	n/a	n/a	n/a	n/a	n/a	0
Sm	Skew	Normal	Non-normal	Improved	0.000	0.262	24	Tm	n/a	n/a	n/a	n/a	n/a	n/a	0
Eu	Skew	Normal	Non-normal	Normal	0.000	0.692	31	Yb	Skew	Normal	Non-normal	Improved	0.000	0.080	32
Gd	n/a	n/a	n/a	n/a	n/a	n/a	n/a	Lu	Skew	Normal	Non-normal	Improved	0.000	0.080	24

Results from the Shapiro-Wilk tests for normality are more sensitive to differences in sample sizes. When datasets are small, normality is easily achieved, and alternatively when datasets are large, normality is more difficult to prove. This is because any small deviation from normality is marked as an infraction and as the sample size increases, the number of chances for infraction also increases. The results of the Shapiro-Wilk tests show that only for cryolite and greisen deposits did all samples of analyses become normally distributed after logarithmic transformations, as well as for SEDEX deposits except for La which only improved after transformation but did not reach normality. Most of the remaining primary mineralization environments had representative datasets that either improved toward normality or became normally distributed after log-transformations with minor exceptions including: carbonatite-related deposits except La, Ce, Pr, Y and Lu; granite-related uranium except La and Ce; pegmatite deposits except Eu, Gd, Ho, Yb, and Lu; intrusion-related molybdenum deposits except Sm and Eu; hydrothermal/epithermal vein/replacement deposits hosted in carbonate rock except La and Y; and hydrothermal/epithermal vein/replacement deposits hosted in metamorphic rock where all sample sets reached normality after transformation except that for Y which was worsened. For some primary mineralization environments the representative sample sets never achieved normality before or after transformation such as those for peralkaline silicate igneous deposits, MVT deposits except for Gd, and hydrothermal/epithermal vein/replacement deposits in igneous host rocks except for Pr and Eu. A notable difference between representative sample sets for peralkaline silicate igneous deposits and those for MVT and hydrothermal/epithermal vein/replacement deposits in igneous hosts is that for distributions observed by histograms and Q-Q plots, the latter two deposit-types were generally observed as normally distributed while those for peralkaline silicate igneous rock deposits were consistently non-normal across all tests. For the cases of MVT deposits and hydrothermal/epithermal vein/replacement deposits hosted in igneous rock, failure of normality by the S-W test may be due to their large sample sizes, while results for peralkaline silicate igneous deposits represents true failure of normality distributions (possibly due to insufficient sample size as indicated by Figure 2-7Figure 2-7). Finally, for three deposit types where data distributions were tested for normality using the Shapiro-Wilk test, nearly all sample normality worsened after logarithmic transformations. This is true for data representing skarn deposits except for Eu, and for hydrothermal/epithermal vein/replacement deposits hosted in sedimentary rock and for IOCG deposits.

Summary of primary mineralization environments distribution normality

From using multiple methods to observe normality of univariate distributions of trace-elements to represent primary-deposit types, it can be concluded that these deposit-type groups are sufficiently and properly represented, with the exceptions of peralkaline silicate igneous deposits, IOCG deposits, and hydrothermal/epithermal vein/replacement deposits in sedimentary hosts. For the latter, half of the univariate dataset achieved normality (LREE), but the distributions of the HREE representing this group are non-normal. Regarding the former, it may be possible that additional data would smooth distribution toward normality as seen in Figure 2-7. For this set of data, it appears there may be multiple peaks in their distributions, but as can be seen, these peaks do not correlate to differences distinguished by source localities. Multiple apparent peaks in the distribution histogram uncorrelated to indivicual sources would indicate that the current criteria is adequate to describe the group but that the sample size may be insufficient to fully describe a random sampling of peralkaline silicate igneous deposits. Data representing IOCG deposits only reached normality using the Shapiro-Wilk test which is weak when sample sizes are small, prior to logarithmic transformation. For all other deposit types, normality or near-normality was observed or proven through statistical testing for elemental sample measurements, usually but not always, after logarithmic transformation of data. This widespread achievement of normality for primary mineralization environment groups indicates some validity to the representation of groups characterized by this scheme, but as seen in Table 2-2, it is not seamless.

Figure 2-7 Histograms of log-transformed trace-element distributions representing peralkaline silicate igneous deposits, distinguished by sample source deposits. Red represents sample analyses from the Ilímaussaq deposit, green from the Motzfeldt deposit, and blue from Pinatosa. Peaks in distributions cannot be correlated to source deposits and possibly represent gaps in data due to insufficient sample size or representation.

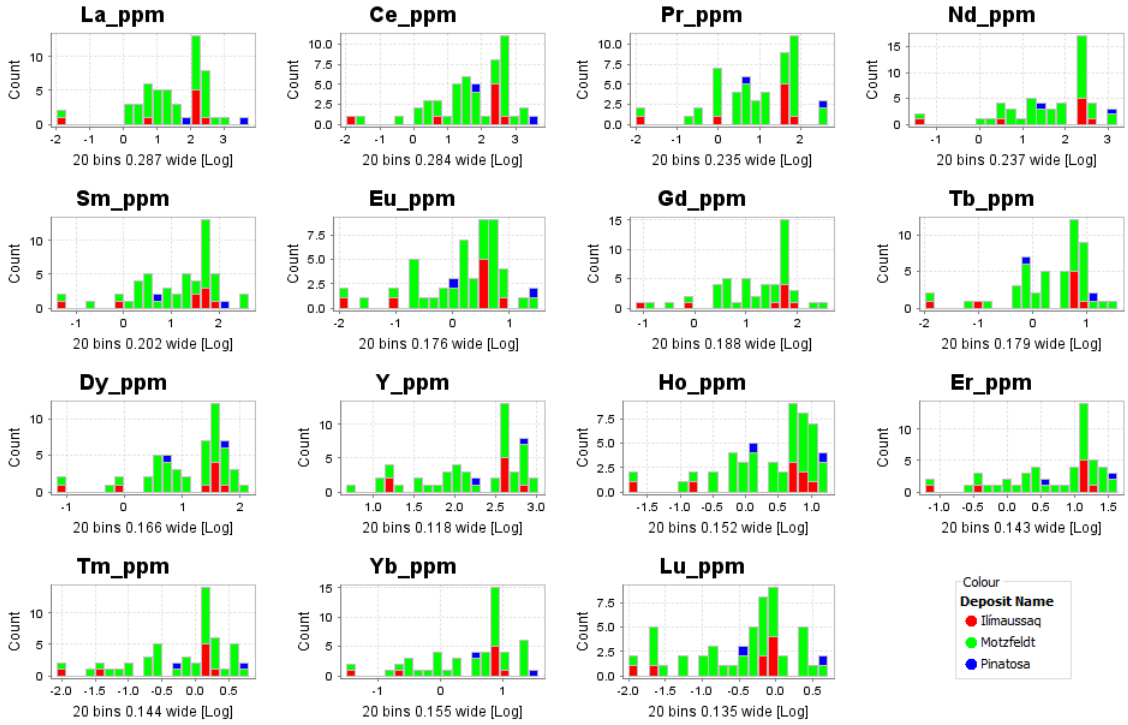

Conclusion of representation of primary mineralization environments

In condensing the representation quality of determined primary mineralization environment groups as established by considerations of sample sizes, datasource diversity, and normality distributions, the following heirarchial ranking was established (Table 2-3) listed from “best” to “worst.”

Table 2-3 Ranking order of quality of data representation for primary mineralization environments from #1, "best" to #15, "worst." Ranking criteria condensed from evaluations of sample sizes, diversity, and normality of univariate distributions of represented REE-Y data.

1.) Hydrothermal/epithermal vein/replacement deposits in igneous hosts	6.) Sedimentary Exhalative	11.) Peralkaline silicate igneous rock
2.) Mississippi Valley Type	7.) Skarn	12.) Hydrothermal/epithermal vein/replacement deposits hosted in sedimentary rocks
3.) Hydrothermal/epithermal vein/replacement deposits in carbonate hosts	8.) Greisen	13.) Rare-metal pegmatite
4.) Carbonatite-related	9.) Intrusion-related Mo	14.) Granite-related U
5.) Hydrothermal/epithermal vein/replacement deposits in metamorphic hosts	10.) Cryolite	15.) IOCG

2.3.4. Calculations

Several calculations were performed within this thesis including normalization of trace-elements to carbonaceous chondrite standards proposed by McDonough and Sun, 1995, anomalies of REE-Y with commonly observed oxidation states (Ce, Eu, Y), sums of REE-Y for comparison between small-scale chemical variability in fluorite as well as selected ratios, REE-Y ratios which were subsequently divided by sums of La, Ce, Lu for creation of elemental discrimination diagrams between primary mineralization environments, and four equations using select trace-elements via discriminant projection analysis were used to create two discrimination diagrams. These calculations are described below.

Anomalies were calculated after chondrite-normalization listed by McDonough and Sun, 1995. These were done by dividing the measured values of the anomalous elements in question by the average of their two neighboring elements according to atomic number. These calculations are as follows where values equal to one represent no anomaly, and values less than or greater than one represent negative or positive anomalies respectively: anomalous Ce = $\left[\frac{Ce}{(La+\mathrm{Pr})/2}\right]n$; anomalous Eu = $\left[\frac{Eu}{(Sm+Gd)/2}\right]n$; anomalous Y = $\left[\frac{Y}{(Dy+Ho)/2)}\right]n$.

Total REE-Y amounts were calculated per sample analyses to compare variability on the fluorite sample-scale and grain-scale examined in Appendix D. Y was reported for each of these analyses and therefore was included in all REE-Y sums. The ranges of logarithmic REE-Y sum values were calculated as the chemical variability of fluorite reported by these analyses and were visually compared on chondrite-normalized (McDonough and Sun, 1995) spider diagrams. Variability of chondrite-normalized patterns, and therefore elemental ratios were analyzed visually by comparing diagrams and were subsequently quantified.

All possible ratios were calculated using normalized REE and Y values which were then logarithmically transformed prior to visual comparison on scatter diagrams. Diagrams in which discrimination between primary mineralization environments were most effective were improved by dividing ratios by the sum of La, Ce, and Lu prior to logarithmic transformations (Figure 2-8). These values were then compared again on scatter diagrams resulting in the discrimination diagrams presented in the follwing chapter.

Logarithmic transformations were employed to data prior to comparisons for ease of display on diagrams with linear axes. Additionally, logarithmic transformations were necessary to give normality to dataset distributions per deposit type, a necessary check for statistically viable data comparison, and to assess the quality of data representation for each respective group (ie, primary mineralization environments). This was executed by creating diagrams with logarithmic scales or by taking the Log_{10}(REE-Y) prior to diagram assembly.

Discriminant projection analysis is increasingly being implemented by authors attempting to create schemes for geochemical pathfinder minerals such as for apatite in Mao et al., (2016) and Rukhlov et al., (2016). This type of analysis is conducted by taking multivariate datasets representing groups or populations and projecting these data into univariate space, allowing for two-dimensional comparison. This projection is done by creating one variable out of several by using a formula tailored to minimizing the spread of data for identified groups while maximizing the separation between groups. A limiting factor to the usefulness of DPA for our application was the requirement of consistently reported trace-elements to be input into formulas. Two discrimination diagrams were created using four formulas generated by discriminant projection analyses using the IoGAS software presented in the following chapter. The fomulas generated are listed here:

$$dpa\_1 = [-0.014587307\ (\mathrm{La} - 51.45401)] + [\ 0.00038982305\ (Ce - 104.44297)] + [0.09807781\ (\mathrm{Pr} - 14.978373)] + [-0.0190112\ (\mathrm{Nd} - 70.1237)] + [0.14552052\ (\mathrm{Sm} - 18.884602)] + [0.083552815(\mathrm{Eu} - 3.847108)] + [-0.04925609\ (\mathrm{Gd} - 20.097376)] + [-1.5955023\ (\mathrm{Tb} - 3.0827303)] + [0.206346\ (\mathrm{Dy} - 17.87891)] + [0.0012446165\ (\mathrm{Y} - 165.30759)] + [-0.8745967\ (\mathrm{Ho} - 3.2047267)] + [0.6408816\ (\mathrm{Er} - 8.1561365)] + [-5.050501\ (\mathrm{Tm} - 1.1139407)] + [\ -0.15283918\ (\mathrm{Yb} - 6.8972073)] + [4.8628035\ (\mathrm{Lu} - 0.8175968)]$$

$$dpa\_2 = [0.009889975\ (\mathrm{La} - 51.45401)] + [-0.0019889493\ (Ce - 104.44297)] + [-0.12261945\ (\mathrm{Pr} - 14.978373)] + [0.043564335\ (\mathrm{Nd} - 70.1237)] + [-0.33165836\ (\mathrm{Sm} - 18.884602)] + [-0.2652554\ (\mathrm{Eu} - 3.847108)] + [0.2139858\ (\mathrm{Gd} - 20.097376)] + [-0.8956324\ (\mathrm{Tb} - 3.0827303)] + [0.55675626\ (\mathrm{Dy} - 17.87891)] + [0.00047728742\ (\mathrm{Y} - 165.30759)] + [0.59947145\ (\mathrm{Ho} - 3.2047267)] + [-0.72905296\ (\mathrm{Er} - 8.1561365)] + [-5.830804\ (\mathrm{Tm} - 1.1139407)] + [0.0472436\ (\mathrm{Yb} - 6.8972073)] + [5.2921443\ (\mathrm{Lu} - 0.8175968)]$$

$$Dpa\_A = [-0.001114512(\mathrm{La} - 56.906017)] + [0.0024397313(\mathrm{Ce} - 96.19183)] + [-0.165863(\mathrm{Yb} - 11.786525)] + [1.194379(\mathrm{Lu} - 1.5306052)] + [-0.000037442944(\mathrm{Sr} - 1036.9337)]$$

$$Dpa\_B = [-0.0025800907(\mathrm{La} - 56.906017)] + [0.0032307461(\mathrm{Ce} - 96.19183)] + [-0.032677025(\mathrm{Yb} - 11.786525)] + [0.23692694(\mathrm{Lu} - 1.5306052)] + [0.00038603853(\mathrm{Sr} - 1036.9337)]$$

Another limiting factor in creating DPA calculations using the IoGAS software were returned errors when inputting logarithmically transformed lanthanoid data, thus calculations were performed on non-transformed data.

Principle component analyses were also considered for use in creating discrimination diagrams, but this user failed to create graphical representations of determined principle components from data analyses.

A process of linear programming was also considered but deemed impractical to discriminate between groups opposed to the method proposed within the next chapter, since overlap between discriminatory groups on diagrams was extensive.

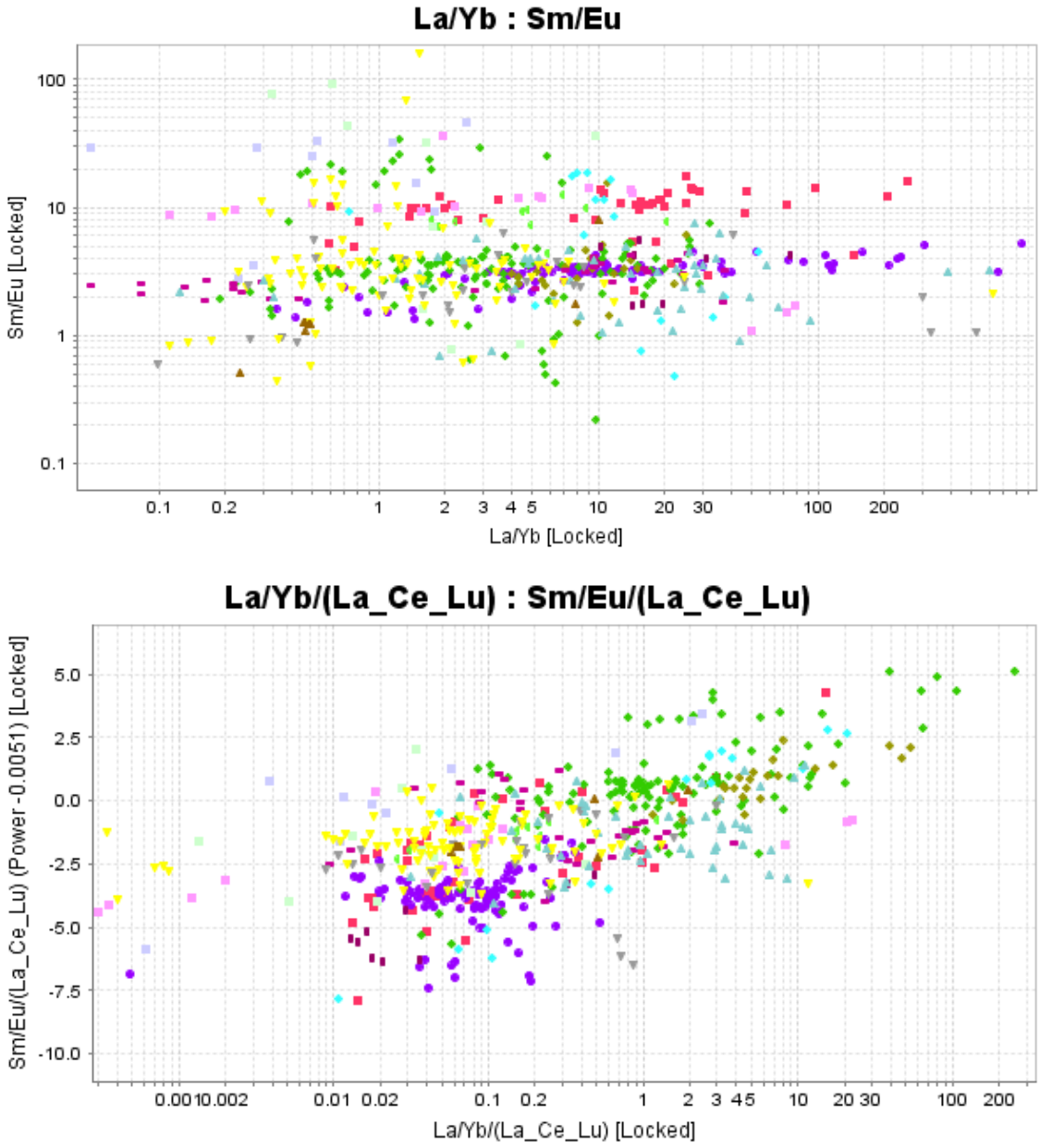

Figure 2-8. Comparison of scatter data before and after division of ratios by sum of La, Ce, Lu which are consistently reported in publications. Data becomes more well distributed when value of sums is applied.

2.4. Summary of hand samples used for test analyses

In addition to the compiled database of reported trace-elements in fluorite from global deposits, 11 samples from eight North American deposits provided by Geroge Simandl from the BCGS collection were analyzed by FUS-ICP/MS. In addition, one sample was analyzed 22 times by LA-ICP-MS analysis. These samples were analyzed and used to test

discrimination diagrams produced within this study, and to test color's correlation to compositional changes within fluorite of the same sample. Hand samples were sourced from four deposits located in British Columbia including the Liard fluorospar prospect, Rexspar fluorite-uranium prospect, Eaglet F-Mo-Sr prospect, and the Rock Candy fluorospar-silica past producer. Most information about these deposits were sourced from the British Columbia government's public minfile records as well as the United States Geologic Survey mining database. Other samples included within this study were sourced from two deposits in Quebec including Kipawa and Eldor, and two from Illinois including Hastie Quarry and Barnett Mine. Two samples were split from single samples for the Eaglet, Hastie Quarry, and Barnett Mine deposits according to color to total 11 samples from eight deposits, and an additional sample from Hastie Quarry was analyzed by LA-ICP-MS across two color zones in a single crystal. More detailed summaries of these deposits are provided in Appendix C.

2.4.1. Summaries of hand sample deposits

Primary mineralization environments determined for hand sample deposits are outlined in Table 2-4 and include Mississippi Valley Type for Liard Fluorospar, Hastie Quarry, and Barnett Mine, IOCG for Rexspar, intrusion-related molybdenum for Eaglet, peralkaline silicate igneous rock for Kipawa, carbonatite-related for Eldor, and hydrothermal/epithermal vein/replacement deposit hosted in igneous rocks for the Rock Candy past producer.

Secondary mineralization environments were also assigned for each deposit. The formation of the Hastie Quarry and Barnett Mine deposits may be related to carbonatite activity or rocks. Liard Fluorospar may also likely be a hydrothermal/epithermal deposit hosted in carbonate rocks or a skarn, but is more likely the former due to significant barium concentration. A secondary mineralization environment assigned to the Eaglet deposit is a hydrothermal/epithermal vein/replacement deposit hosted in igneous or metamorphic rocks. The Kipawa deposit is primarily related to peralkaline silicate igneous rocks, however extensive regional metamorphism and metasomatism has caused the formation of rare minerals as skarn deposits in structurally juxtaposed marble and therefore skarn deposit has been assigned as a secondary mineralization environment. The Eldor carbonatite complex includes intrusions of syenite and therefore the secondary mineralization environment assigned is peralkaline silicate igneous rock. The Rock Candy past producer has been assigned carbonatite-related as a secondary deposit type.

Table 2-4 Primary and secondary mineralization environments assigned to hand sample deposits. Deposit locality names and sample numbers included. Some third deposit-type assignations have been listed in the above text but are not listed here.

Deposit name	Primary mineralization environment	Secondary mineralization environment	Sample number(s)
Liard fluorospar	MVT	Hydrothermal/epithermal vein/replacement in carbonate host	LIARD-1
Hastie Quarry	MVT	Carbonatite-related	3-12-9EP 3-12-9EY
Barnett Mine	MVT	Carbonatite-related	28-12S-8EW 28-12S-8EP
Rexspar	IOCG	Hydrothermal/epithermal vein/replacement in igneous host	REXSPAR-82-C
Eaglet	Intrusion-related Mo	Hydrothermal/epithermal vein/replacement in igneous host	EAGLET-7 EAGLET-9
Kipawa	Peralkaline silicate igneous rock	Skarn	KIPAWA
Eldor	Carbonatite-related	Peralkaline silicate igneous rock	ELDOR-2
Rock Candy	Hydrothermal/epithermal vein/replacement in igneous host	Carbonatite-related	RC-1

2.4.2. Analytical methods

Analytical methods used in publication sources are diverse including bulk methods such as induced neutron activation analysis (INAA/NAA), digestion inductively coupled plasma mass spectroscopy and atomic emission spectroscopy (ICP-MS, ICP-AES), and point methods such as laser-ablation inductively coupled plasma mass spectroscopy (LA-ICP-MS). Hand samples sourced from North American deposits within this study were analyzed by bulk method lithium metaborate/tetraborate fusion ICP and ICP/MS (FUS-ICP/MS) analysis at Activation Laboratories, Ancaster, ON, and one sample was analyzed by LA-ICP-MS for comparison.

Fluorite samples were prepared for FUS-ICP/MS analyses by selective crushing of hand samples in a ceramic mortar and sieving to grain sizes between 0.088 and 4mm using stainless steel meshes. Select samples were sorted and split according to color and thusly 11 samples from 8 localities were hand-picked using a binocular microscope. Samples were picked to include at least 0.20 grams, then sent to Activation Laboratories in Ancanster, ON

for lithium metaborate/tetraborate fusion ICP/MS analyses to analyze for elemental oxides (Si, Al, Fe, Mn, Mg, Ca, Na, K, Ti, P) using ICP and trace elements (Sc, Be, V, Cr, Co, Ni, Cu, Zn, Ga, Ge, As, Rb, Sr, Y, Zr, Nb, Mo, Ag, In, Sn, Sb, Cs, Ba, Hf, Ta, W, Ti, Pb, Bi, Th, U, and REE) using MS. Samples were milled further into powders; robotic techniques were employed for the fusion process resulting in highly reproducible results. Fused samples were diluted and analyzed by Perkin Elmer Sciex ELAN 6000, 6100, or 9000 ICP/MS. Three blanks and five controls (three before and two after the sample group) were analyzed. Duplicates were fused and analyzed for error calculations resulting in the following root mean square deviations (ppm) for lanthanoids (La ±0.040; Ce ±0.144; Pr ±0.012; Nd ±0.017; Sm ±0.002; Eu ±1.92E-4; Gd ±0.011; Tb ±1.66E-4; Dy ±0.002; Y ±3.713; Ho ±3.22E-4; Er ±0.003; Tm ±1.27E-4; Yb ±8.66E-4; Lu ±9.63E-6).

Laser-ablation ICP-MS analyses were applied to a sample from Hastie Quarry, Illinois that exhibited colorful sector zoning. The cubic, yellow crystals are overgrown by later deep purple fluorite along octahedral (111) corners of the cubes and edges (Figure 2-9 Fluorite sample from Hastie Quarry exhibiting optically heterogeneous sector zoning between yellow cubes and purple octahedral corners. Smallest aggregate shown here is approx. 1 cm across.Figure 2-9A cleaved fluorite chip (~1cm across) was selected for a traverse analysis by LA-ICP-MS analyses and was sent to Perkin Elmer analytical test facility in Woodbridge, ON. 22 spots were analyzed using a 120 x 40µ rectangular spot at 5 Hz, 26 J/cm^2 using a Nexion NWR213 laser and Perkin Elmer mass spectrometer. Concentrations were calculated using NIST612, and using Ca as the internal standard.

Figure 2-9
Fluorite sample from Hastie Quarry exhibiting optically heterogeneous sector zoning between yellow cubes and purple octahedral corners. Smallest aggregate shown here is approx. 1 cm across.

2.5. References

1. Ackerman, L., 2005. Magmatic vs. hydrothermal origin of fluorites from Vlastějovice, Bohemian Massif; Journal of the Czech Geological Society, v. 50, (35-41).
2. Alvin, M. P., Dunphy, J. M., Groves, D. I., 2004. Nature and genesis of a carbonatite associated fluorite deposit at Speewah, East Kimberley region, Western Australia; Mineralogy and Petrology, v. 80, (127-153).
3. Bau, M., Romer, R. L., Lüders, V., Dulski, P., 2003. Tracing element sources of hydrothermal mineral deposits: REE and Y distribution and Sr-Nd-Pb isotopes in fluorite from MVT deposits in the Pennine Orefield, England; Mineralium Deposita, v. 38, (992-1008).
4. Bixel, F., Lucas, C., 1983. Magmatisme, tectonique et sedimentation dans les fossés stéphano-permiens des Pyrénées occidentales; Rev. Géol. Dyn. Géogr. Phys., v. 24, (329-342).
5. Bühn, B., Schneider, J., Dulski, P., Rankin, A. H., 2003. Fluid-rock interaction during progressive migration of carbonatitic fluids, derived from small-scale trace element and Sr, Pb isotope distribution in hydrothermal fluids; Geochimica et Cosmochimica Acta, v. 67, 23, (4577-4595).
6. Castorina, F., Masi, U., Padalino, G., Palomba, M., 2008. Trace-element and Sr-Nd isotopic evidence for the origin of the Sardinian fluorite mineralization (Italy); Applied Geochemistry, v. 23, (2906-2921).
7. Cheilletz, A., Gasquet, D., Filali, F., Archibald, D.A., Nespolo, M., 2010. A late Triassic $^{40}Ar/^{39}Ar$ age for the El Hammam high-REE fluorite deposit (Morocco): mineralization related to the Central Atlantic Magmatic Province?; Mineralium Deposita, v. 45, (323-329).
8. Černý, P., 1991. Rare-element granitic pegmatites. Part I: Anatomy and internal evolution of pegmatite deposits; Geoscience Canada Articles, v. 18, 2, (49-67).
9. Davis, J.C., 1973; 1986. Statistics and data analysis in geology, second edition. John Wiley & Sons, Inc., ISBN: 0-471-08079-9, (646 pgs).
10. Deng, X.-H., Chen, Y.-J., Yao, J.-M., Bagas, L., Tang, H.-S., 2014. Fluorite REE-Y (REY) geochemistry of the ca. 850 Ma Tumen molybdenite-fluorite deposit, eastern Qinling China: Constraints on ore genesis; Ore Geology Reviews, (1-12).
11. Doroshkevich, A.G., Viladkar, S.G., Ripp, G.S., Burtseva, M.V., 2009. Hydrothermal, REE mineralization in the Amba Dongar carbonatite complex, Gujarat, India: The Canadian Mineralogist, v. 47, (1105-1116).
12. Elliott, J. E., Kamilli, R. J., Miller, W. R., Livo, K., E., 1995. Vein and Greisen Sn and W deposits (Models 15a-c; Cox and Bagby, 1986; Reed, 1986); USGS Bulletin 0831, Ch. 9, (62-69).

13. Estrade, G., Salvi, S., Béziat, D., Williams-Jones, A. E., 2015. The origin of skarn-hosted rare-metal mineralization in the Ambohimirahavavy alkaline complex, Madagascar; Economic Geology, v. 110, 6, (1485-1513).
14. Fisher, J., Lillie, R., Rakovan, J., 2013. Fluorite in Mississippi Valley-Type deposits; Rocks and Minerals, v. 88, 1, (20-49).
15. Hitzman, M.W., 2000. Iron oxide Cu-Au deposits: What, where, when and why; Porter, T.M., ed., Hydrothermal Iron Oxide Copper-Gold and related deposits: A global perspective; PGC Publishing, Adelaide, v. 1, (9-25).
16. Gagnon, J. E., Samson, I. M., Fryer, B. J., Williams-Jones, A. E., 2003. Compositional heterogeneity in fluorite and the genesis of fluorite deposits: insights from LA-ICP-MS analysis; Canadian Mineralogist, v. 41, (365-382).
17. González-Partida, E., Carillo-Chávez, A., Grimmer, J.O., Pironon, J., 2002. Petroleum-rich fluid inclusions in fluorite, Purisima mine, Coahuila, Mexico; International Geology Review, v. 44, 8, (755-764).
18. Goodenough, K. M., Upton, B. G. J., Ellam, R. M., 2000. Geochemical evolution of the Ivigtut granite, South Greenland: a fluorine-rich "A-type" intrusion; Lithos, v. 51, (205-221).
19. Gwalani, L. G., Rogers, K. A., Demény, A., Groves, D. I., Ramsay, R., Beard, A., Downes, P. J., Eves, A., 2010. The Yungul carbonatite dykes associated with the epithermal fluorite deposit at Speewah, Kimberly, Australia: carbon and oxygen isotope constraints on their origin; Mineralogy Petrology, v. 98, (123-141).
20. Hill, G.T., Campbell, A.R., Kyle, P.R., 2000. Geochemistry of southwestern New Mexico fluorite occurrences implications for precious metals exploration in fluorite-bearing systems; Journal of Geochemical Exploration, v. 68, (1-20).
21. Huang, C., Wang, J., Li, Z., 2014. REE geochemistry of fluorite from the Lala IOCG Deposit and its geological implications, Kangdian Region, SW China; Acta Geologica Sinica (English Edition), v. 88, 2, (357-358).
22. Jenner, G.A., 1996. Trace element geochemistry of igneous rocks: geochemical nomenclature and analytical geochemistry, in Wyman, D.A., ed., Trace element geochemistry of volcanic rocks: Applications of rmassive sulphide exploration: geological association of Canada, Short course notes, v. 12, (51-77).
23. Jones, I., 2006. Old classics and new finds: Fluorite from the United Kingdom, in *No. 9 Fluorite - the Collector's Choice*; ed. Fisher, J., Jarnot, M., Neumeier, G., Pasto, A., Staebler, G., Wilson; publ. Lithographie, LLC, East Hampton, Connecticut, USA, 2006. pp. 28-37.
24. Kendrick, M. A., Burgess, R., Pattrick, R. A. D., Turner, G., 2002. Hydrothermal fluid origins in a fluorite-rich Mississippi Valley-type district: combined noble gas (He, Ar, Kr) and halogen (Cl, Br, I) analysis of fluid inclusions from the South Pennine Ore Field, United Kingdom; Economic Geology, v. 97, (435-451).
25. Lenth, R.V., 2001. Some practical guidelines for effective sample size determination; The American Statistician, v. 55, (187-193).
26. Levresse, G., Tritlla, J., Villareal, J., Gonzalez-Partida, E., 2006. The "El Pilote" fluorite skarn; A crucial deposit in the understanding and interpretation of the origin and mobilization of F from northern Mexico deposits; Journal of Geochemical Exploration, v. 89 (205-209).
27. Li, Z., Hu R., Wang, J., Liu, J., Li, C-y., Liu, Y., Ye, L., 2002. Lala Fe-oxide-Cu –Au-U-REE ore deposit, Sichuan China: an example of superimposed mineralization; Mineralogy Petrology Geochemistry (in Chinese with English abstract), v. 21, (258-260).
28. Lüders, V., Romer, R. L., Gilg, H. A., Bodnar, R. J., Pettke, T., Misantoni, D., 2009. A geochemical study of the Sweet Home Mine, Colorado Mineral Belt, USA: hydrothermal fluid evolution above a hypothesized granite cupola; Mineralium Deposita, v. 44, (415-434).
29. Ludington, S., Plumlee, G., 2009. Climax-Type porphyry molybdenum deposits; USGS Open file report 1215, (1-16).
30. Mahdy, N. M., Shalagy, M. H., Helmy, H. M., Osman, A. F., El Sawey, E. S. H., Zeid, E. K. A., 2014. Trace and REE element geochemistry of fluorite and its relation to uranium mineralizations, Gabal Gattar area, Northern Eastern Desert, Egypt; Arabian Journal of Geoscience, v. 7, (2573-2589).
31. Mao, M., Rukhlov, A.S., Rowins, S.M., Spence, J., Coogan, L.A., 2016b. Apatite trace element compositions: a robust tool for mineral exploration. Economic Geology, v. 111, (1187-1222).
32. McDonough, W.F., Sun, S.-s., 1995. The composition of the Earth; Chemical Geology, v. 120 (223-253).

33. Minuzzi, O. R. R., Bastos Neto, A. C., Formoso, M. L. L., Andrade, S., Janasi, V. A., Flores, J. A., 2008. Rare element and yttrium geochemistry applied to the genetic study of cryolite ore at the Pitinga Mine (Amazon, Brazil); Anais da Academia Brasileira de Ciências, v. 80, 4, (719-733).
34. Mecklin, C.J., Mundfrom, D.J., 2004. An appraisal and bibliography of tests for multivariate normality; International Statistics Review, v. 72, no. 1, (123-138).
35. Monecke, T., Kempe, U., Monecke, J., Sala, M., Wolf, D., 2002. Tetrad effect in rare earth element distribution patterns: a method of quantification with application to rock and mineral samples from granite-related rare metal deposits; Geochimica et Cosmochimica Acta, v. 66, 7, (1185-1196).
36. Monecke, T., Monecke, J., Mönch, W., Kempe, U., 2000. Mathematical analysis of rare earth element patterns of fluorites from the Ehrenfriedersdorf tin deposit, Germany: evidence for a hydrothermal mixing process of lanthanides from two different sources; Mineralogy and Petrology, v. 70, (235-256).
37. Noordzij, M., Tripepi, G., Dekker, F.W., Zoccali, C., Tanck, M.W., Jager, K.J., 2010. Sample size calculations: basic principles and common pitfalls; Nephrol Dial Transplant, v. 25, (1388-1393).
38. Palmer, D.A.S., 1994. Geology and geochemistry of the Amba Dongar carbonatite-hosted fluorite deposit, India: MSc Thesis, McGill University, Montreal, (150 pgs).
39. Paradis, S., Hannigan, P., Dewing, K., 2007. Mississippi Valley-Type lead-zinc deposits; Goodfellow, W.D., ed., Mineral Deposits of Canada: A synthesis of major deposit-types, district metallogeny, the evolution of geological provinces, and exploration methods: Geological Association of Canada, Mineral deposits division, Special Publication No. 5, (185-203).
40. Pauly, H., Bailey, J. C., 1999. Genesis and evolution of the Ivigtut cryolite depost, SW Greenland; Medd. Grønl., Geosci., v. 37, (60).
41. Pinte, G., Veado, M.A., Oliveira, A.H., Khalis, M., Ayrault, S., Revel, G., 1998. Comparison of Neutron Activation Analysis and ICP-MS used for river water pollution control. Hydrobiologia, v. 373, iss. 0, (61-73).
42. Porter, T. M., 2000. Hydrothermal Iron-Oxide Copper-Gold and related ore deposits; Porter, T. M., ed., Hydrothermal Iron Oxide Copper-Gold and related deposits: A global perspective; PGC Publishing, Adelaide, v. 1, (3-5).
43. Putnam III, B.R., Norman, D.I., Smith, R.W., 1983. Mississippi Valley-type lead-fluorite-barite deposits of the Hansonburg mining district, New Mexico: New Mexico Geological Society Fall Field Conference Guidebook, v. 34, (253-260).
44. Rakovan, J., 2007. Greisen; Word to the Wise in Rocks and Minerals, v. 82, (157-159).
45. Rude, P. D., Aller, R. C., 1991. Fluorine mobility during early diagenesis of carbonate sediment: an indicator of mineral transformations; Geochimica et Cosmochimica Acta, v. 55, 9, (2491-2509).
46. Rukhlov, A.S., Plouffe, A., Ferbey, T., Mao, M., and Spence, J., 2016. Application of trace-element compositions of detrital apatite to explore for porphyry deposits in central British Columbia. In: Geological Fieldwork 2015: British Columbia Ministry of Energy and Mines, British Columbia Geological Survey Paper 2016-1, pp. 145–179.
47. Sánchez, V., Cardellach, E., Corbella, M., Vindel, E., Martín-Crespo, T., Boyce, A. J., 2010. Variability in fluid sources in the fluorite deposits from Asturias (N Spain): Further evidences from REE, radiogenic (Sr, Sm, Nd) and stable (S, C, O) isotope data; Ore Geology Reviews, v. 37, (87-100).
48. Sallet, R., Moritz, R., Fontignie, D., 2005. The use of vein fluorite as a probe for paleofluid REE and Sr-Nd isotope geochemistry: The Santa Catarina Fluorite District, Southern Brazil; Chemical Geology, v. 223, (227-248).
49. Sasmaz, A., Önal, A., Sagiroglu, A., Önal, M., Akgul, B., 2005a. Origin and nature of the mineralizing fluids of thrust zone fluorites in Çelikhan (Adiyaman, Eastern Turkey): a geochemical approach; Geochemical Journal, v. 39, (131-139).
50. Sasmaz, A., Yavuz, F., Sagiroglu, A., Akgul, B., 2005b. Geochemical patterns of the Akdagmadeni (Yozgat, Central Turkey) fluorite deposits and implications; Journal of Asian Earth Sciences, v. 24, (469-479).
51. Schneider, H.-J., Möller, P., Parekh, P.P., 1975. Rare earth elements distribution in fluorites and carbonate sediments of the East-Alpine Mid-Triassic sequences in the Nördliche Kalkalpen; Mineralium Deposita (Berlin), v. 10, (330-344).
52. Schönenberger, J., Köhler, J., Markl, G., 2008. REE systematics of fluorides, calcite, and siderite in peralkaline plutonic rocks from the Gardar Province, South Greenland; Chemical Geology, v. 247, (16-35).
53. Schwinn, G., Markl, G., 2005. REE systematics in hydrothermal fluorite; Chemical Geology, v. 216, (225-248).

54. Seal II, R.R., 2004. Geoenvrionmental Models for Massive Sulphide Deposits with an emphasis on Sedimentary-Exhalative Lead-Zinc Deposits; Sediment-hosted Lead-Zinc Sulphide Deposits, Ed. Deb, M., Goodfellow, W.D., (191-221).
55. Sørensen, H., 1997. The agpaitic rocks-an overview*: Mineralogical Magazine, v. 61, (485-498).
56. Souissi, F., Souissi, R., Dandurand, J.-L., 2010. The Mississippi Valley-Type fluorite ore at Jebel Stah (Zaghouan district, north-eastern Tunisia): Contribution of REE and Sr isotope geochemistries to the genetic model; Ore Geology Reviews, v. 37, (15-30).
57. Subías, I., Fernández-Nieto, C., 1995. Hydrothermal events in the Valle de Tena (Spanish Western Pyrenees) as evidenced by fluid inclusions and trace-element distribution from fluorite deposits: Chemical Geology, v. 124, (267-282).
58. Sun, S.-s., McDonough, W.F., 1989. Chemical and isotopic systematics of oceanic basalts: implications for mantle composition and processes; Geological Society, London, Special Publications, v. 42, (313-345).
59. Thode, H.C., 2002. Testing for normality; Statistics, textbooks and monographs; Marcel Dekker, v. 164, (479 pgs). ISBN: 0824796136Th
60. Trinkler, M., Monecke, T., Thomas, R., 2005. Constraints on the genesis of yellow fluorite in hydrothermal barite-fluorite veins of the Erzgebirge, Eastern Germany: evidence from optical absorption spectroscopy, rare-element data, and fluid-inclusion investigations; The Canadian Mineralogists, v. 43, (883-898).
61. Ventura Santos, R., Dardenne, M. A., De Oliveira, C. G., 1996. Rare earth elements geochemistry of fluorite from the Mato Preto carbonatite complex, southern Brazil; Revista Brasileira de Geociêcias, v. 26, 2, (81-86).
62. Woolley, A. R., Kjarsgaard, B. A., 2008. Carbonatite occurrences of the world: map and database; Geological Survey of Canada – open file 5796 (Natural Resources Canada).
63. Xiang, S., Jun, D., Liqiang, Y., Qingfei, W., Zirong, Y., Qingjie, G., Changming, W., 2010. REE and Sr-Nd isotope geochemistry for Yixian Fluorite Deposit, Westerin Liaoning Province, China and its geological implications; Journal of Earth Science, v. 21, (227-235).
64. Xu, C., Taylor, R. N., Li, W., Kynicky, J., Chakhmouradian, A. R., Song, W., 2012. Fluorite geochemistry from REE deposits in the Panxi region and Bayan Obo China; Journal of Asian Earth Sciences, v. 57, (76-89).
65. Yuan, S., Peng, J., Hu, R., Bi, X., Qi, L., Li, Z., Li, X., Shuang, Y., 2008. Characteristics of rare-earth elements (REE), strontium and neodymium isotopes in hydrothermal fluorites from the Bailashui tin deposit in the Furong ore field, southern Hunan Province, China; Chinese Journal of Geochemistry, v. 27, (342-350).
66. Zhang, G., Hu, R., Bi, X., Feng, H., Shang, P., Tian, J., 2007. REE geochemical characteristics of the No. 302 uranium deposit in northern Guangdong, South China; Chinese Journal of Geochemistry, v. 26, 4, (425-433).

Chapter 3.

Results and discrimination diagrams

3.1. Introduction

The primary objective of this thesis was to create user-friendly, discrimination diagrams using globally reported trace-element compositions of natural fluorites for the purpose of developing fluorite as an industry-specific geochemical pathfinder mineral. To accomplish this, we needed to first determine consistently reported trace-elements in fluorite for comparison between determined economic groups, assess the representation of determined groups through sample sizes, datasource diversity, and normality distributions, and to test the trace-element chemical variability on scales smaller than deposit-wide comparisons (ie: sample-scale and grain-scale outlined in Appendix D.). After these considerations were met, discrimination diagrams were produced using REE-Y data and were tested using scatter data produced from FUS-ICP/MS analyses on samples from North American deposits.

Through these considerations, we discovered that in using publications as our primary source of data, the most consistently reported trace-elements available for comparison were the lanthanides including yttrium (the lanthanoid suite). Other trace elements reported included Sr, Th, U, Ba, Pb, Rb, Zr, Sc, Zn, Hf, Nb, but it is unknown why these elements were less consistently reported. Considering that a lack of detection of any given trace-element correlated to a determined deposit-type could also be utilized for discriminatory purposes, we note that this is only attainable through consistent testing analysis. Since this work utilized published trace-element data from multiple sources, the methods are not normalized in order to draw conclusions from a lack of reported trace-elements for any given deposit or type. Therefore, we could only make comparisons between elements that were consistently reported in fluorite, eliminating the speculation between presence and detection limits for less consistently reported trace-elements. In doing so, the trace-elements determined useful for comparison and subsequently used to create discrimination diagrams from a compilation of reported data were REE-Y.

From this compiled database (Table E-1, Appendix E), data were sorted into groups determined by fluorite origins of economic interest. For this purpose, a classification scheme was created which is outlined in Section 2.2, and explained in detail in Appendix B, where "primary" and "secondary" deposit types were assigned per mentioned deposit from the compiled publications. Additional classification groups were also assigned pertaining to economic interest including "metallic economic association" and "recovered/targeted commodity groups" indicating if metallic commodities were of primary, secondary, or no economic interest, and what major commodities were targeted or recovered from these deposits (i.e.: specialty metals (SM), or Sn-W). Discrimination diagrams were ultimately only created to assign primary mineralization environments, but secondary classifications were explained to illustrate alternate interpretations of literature. These secondary mineralization environment classifications or other economically interesting classification groups could be implemented for discrimination in further studies.

Next, the representation of these primary mineralization environment groups by the compiled dataset was assessed prior to the creation of discrimination diagrams through examination of sample sizes, data source diversity, and normality distributions. Primary mineralization environments listed in order of representation quality from best to worst is as follows: 1.) hydrothermal/epithermal vein/replacement deposits in igneous hosts, 2.) MVT deposits, 3.) hydrothermal/epithermal vein/replacement deposits in carbonate hosts, 4.) carbonatite-related deposits, 5.) hydrothermal/epithermal vein/replacement deposits in metamorphic hosts, 6.) SEDEX deposits, 7.) skarn deposits, 8.) greisen deposits, 9.) intrusion-related molybdenum deposits, 10.) cryolite deposits, 11.) peralkaline silicate igneous rock deposits 12.) hydrothermal/epithermal vein/replacement deposits hosted in sedimentary rock, 13.) rare-metal pegmatites, 14.) granite-related uranium deposits, and 15.) IOCG deposits. This information should be taken into consideration when utilizing the discrimination diagrams created herein.

Finally, authors such as Vikorunov et al., 2014, Gagnon et al., 2003, Schwinn and Markl, 2005, Baele et al., 2012, Smolyanski et al., 2009, and Bosze and Rakovan, 2002, had cautioned against using bulk geochemical analytical techniques for assessing trace-element concentrations in fluorite by identifying small-scale chemical heterogeneity within single samples of fluorite between different represented paragenetical phases, and grain-scale chemical heterogeneity between crystal sectors. Mao et al., 2016, however, suggested that

the grain-scale heterogeneity of fluorite may be less variable than that for the entire deposit by comparing multiple LA-ICP-MS analyses between samples representing the Rock Candy deposit in British Columbia, with two perpendicular LA-ICP-MS grain traverses of a single crystal. Within this study (Appendix D.), we concluded that on the sample-scale, fluorite chemical variability displayed significant concentration gradients (approaching or exceeding ranges of half of an order of magnitude) approximately 20% of the time, while on the grain-scale, this range of concentration gradient existed approximately 50% of the time. Even though concentration gradients existed between both smaller-scale analytical comparisons, the overall patterns displayed by chondrite-normalized (McDonough and Sun, 1995) REE-Y data were relatively consistent. Additionally, it could be speculated that differing normalized patterns displayed by lanthanoids between crystal sectors, could be accommodated by averaging results according to sector volume, which would mimic results taken by bulk analytical techniques. Because of relatively consistent REE-Y patterns in fluorite despite concentration gradients on the grain- and sample-scales, it was determined that ratios derived from REE-Y analyses of fluorite could be utilized to create effective discrimination diagrams between primary mineralization environments. REE-Y patterns and concentrations do vary, however, between samples representing the same deposits and therefore overlap among data fields occurred.

Satisfying these inquiries we discovered which trace-elements recorded in publications were useable for the purpose of creating discrimination diagrams, we created a classification scheme from publication data outlining deposits containing fluorite of economic interest, we evaluated the representation of these assigned groups by our compiled database, and discovered utilizing ratios minimizes effects of fluorite chemical variability caused by concentration gradients on analyses of single samples. Therefore, the majority of discrimination diagrams were created using ratios of chondrite-normalized (McDonough and Sun, 1995), logarithmically-transformed lanthanoids divided by the sum of La, Ce, and Lu from analyses of fluorite. All groups were distinguished from others on discrimination diagrams with the exceptions of MVT deposits from hydrothermal/epithermal vein/replacement deposits hosted in carbonate and metamorphic rocks, intrusion-related molybdenum deposits from vein/replacement deposits in carbonate rock, and no attempt was made to isolate hydrothermal/epithermal vein/replacement deposit groups.

3.2. Discrimination diagrams between primary mineralization environments

Discrimination diagrams were created primarily using ratios of REE-Y data (including ratios representing anomalous lanthanoids, and values created using formulas generated by discriminant projection analyses) divided by sums of consistently reported lanthanoids (La, Ce, Lu) to produce scatter diagrams and were selected based upon a procedure of minimizing the amount of overlap between primary mineralization environment groups while maximizing the amount of data represented for each distinguished group for each diagram. Scatter diagrams (Figure 3-1) were contoured per primary deposit type to contain 2/3^{rds} of the scatter data per diagram, which does not always represent 2/3^{rds} of the available dataset per group and this discrepancy is clarified in information tables following diagrams. Ten discrimination diagrams were chosen, outlined in Table 3-1, displayed in Figure 3-1. All primary mineralization environment groups were completely separated from all other groups using one or more of the discrimination diagrams included herein with the exceptions of SEDEX from Mississippi Valley type deposits, Mississippi Valley type deposits from hydrothermal/epithermal vein/replacement deposits in carbonate and metamorphic hosts, intrusion-related molybdenum deposits from hydrothermal/epithermal vein/replacement deposits hosted in carbonate rock, and hydrothermal/epithermal vein/replacement deposits. The latter group and included subgroups were not focused upon for discrimination. Table 3-1 outlines the step-wise fashion in which primary mineralization environment groups are distinguished from all other groups which can be used to assign a primary mineralization environment or types to a data point or dataset.

Table 3-1 Outlining discrimination of primary deposit types using diagrams listed in Figure 3-1. Initial diagrams listed for each primary deposit type exhibit the best separation of that type from all other groups. If overlap still exists between groups, the subsequently listed diagrams can be examined to discriminate between those groups.

Primary deposit type	**Discrimination diagrams and procedure**
SEDEX	(A.) $\log_{10}\left[\frac{(Ce/Tb)}{(\Sigma La,Ce,Lu)}\right]_n$ vs. $\log_{10}\left[\frac{(La/Eu)}{(\Sigma La,Ce,Lu)}\right]_n$ Separated from skarn and vein in carbonate in (E.) $\log_{10}\left[\frac{(Eu/Eu*)}{(\Sigma La,Ce,Lu)}\right]_n$ vs. $\log_{10}\left[\frac{(La/Sm)}{(\Sigma La,Ce,Lu)}\right]_n$
Rare-metal pegmatite	(B.) $\log_{10}\left[\frac{(Ce/Tb)}{(\Sigma La,Ce,Lu)}\right]_n$ vs. $\log_{10}\left[\frac{(Tb/Ho)}{(\Sigma La,Ce,Lu)}\right]_n$
IOCG	(C.) $\log_{10}\left[\frac{(Eu/Dy)}{(\Sigma La,Ce,Lu)}\right]_n$ vs. $\log_{10}\left[\frac{(Pr/Gd)}{(\Sigma La,Ce,Lu)}\right]_n$
Granite-related uranium	(C.) $\log_{10}\left[\frac{(Eu/Dy)}{(\Sigma La,Ce,Lu)}\right]_n$ vs. $\log_{10}\left[\frac{(Pr/Gd)}{(\Sigma La,Ce,Lu)}\right]_n$
	Separated from cyrolite in (D.) $\log_{10}\left[\frac{Eu}{Eu*}\right]_n$ vs. $\log_{10}[\Sigma La, Ce, Lu]_n$ Separated from carbonatite-related in (D.) $\log_{10}\left[\frac{Eu}{Eu*}\right]_n$ vs. $\log_{10}[\Sigma La, Ce, Lu]_n$ Separated from greisen in (G.) in $\log_{10}\left[\frac{(Nd/Yb)}{(\Sigma La,Ce,Lu)}\right]_n$ vs. $\log_{10}\left[\frac{(Nd/Eu)}{(\Sigma La,Ce,Lu)}\right]_n$ and (I.) dpa_2 vs. dpa_1
MVT	(C.) $\log_{10}\left[\frac{(Eu/Dy)}{(\Sigma La,Ce,Lu)}\right]_n$ vs. $\log_{10}\left[\frac{(Pr/Gd)}{(\Sigma La,Ce,Lu)}\right]_n$
	Separated from skarn in (E.) $\log_{10}\left[\frac{(Eu/Eu*)}{(\Sigma La,Ce,Lu)}\right]_n$ vs. $\log_{10}\left[\frac{(La/Sm)}{(\Sigma La,Ce,Lu)}\right]_n$ Separated from greisen in (G.) $\log_{10}\left[\frac{(Nd/Yb)}{(\Sigma La,Ce,Lu)}\right]_n$ vs. $\log_{10}\left[\frac{(Nd/Eu)}{(\Sigma La,Ce,Lu)}\right]_n$ Separated from hydrothermal/epithermal vein and replacements hosted in igneous rocks in (G.) $\log_{10}\left[\frac{(Nd/Yb)}{(\Sigma La,Ce,Lu)}\right]_n$ vs. $\log_{10}\left[\frac{(Nd/Eu)}{(\Sigma La,Ce,Lu)}\right]_n$ and (E.)

	$\log_{10}\left[\frac{(Eu/Eu*)}{(\Sigma La,Ce,Lu)}\right]_n$ vs. $\log_{10}\left[\frac{(La/Sm)}{(\Sigma La,Ce,Lu)}\right]_n$ Separated from intrusion-related molybdenum in (J.) Dpa_A vs. Dpa_B Not separable from hydrothermal/epithermal vein and replacements hosted in metamorphic rocks or carbonated rocks
Cryolite	(D.) $\log_{10}\left[\frac{Eu}{Eu*}\right]_n$ vs. $\log_{10}[\Sigma La, Ce, Lu]_n$ Separated from greisen deposits in (I.) dpa_2 vs. dpa_1
Carbonatite-related	(D.) $\log_{10}\left[\frac{Eu}{Eu*}\right]_n$ vs. $\log_{10}[\Sigma La, Ce, Lu]_n$
	Separated from skarn in (B.) $\log_{10}\left[\frac{(Ce/Tb)}{(\Sigma La,Ce,Lu)}\right]_n$ vs. $\log_{10}\left[\frac{(Tb/Ho)}{(\Sigma La,Ce,Lu)}\right]_n$ Separated from intrusion-related molybdenum in (B.) $\log_{10}\left[\frac{(Ce/Tb)}{(\Sigma La,Ce,Lu)}\right]_n$ vs. $\log_{10}\left[\frac{(Tb/Ho)}{(\Sigma La,Ce,Lu)}\right]_n$ Separated from hydrothermal/epithermal veins and replacements hosted in carbonate rocks in (G.) $\log_{10}\left[\frac{(Nd/Yb)}{(\Sigma La,Ce,Lu)}\right]_n$ vs. $\log_{10}\left[\frac{(Nd/Eu)}{(\Sigma La,Ce,Lu)}\right]_n$ "hosted in igneous rocks in (I.) dpa_2 vs. dpa_1 "hosted in metamorphic rocks in (J.) Dpa_A vs. Dpa_B
Skarn	(F.) $\log_{10}\left[\frac{(Nd/Lu)}{(\Sigma La,Ce,Lu)}\right]_n$ vs. $\log_{10}\left[\frac{(Ce/Tb)}{(\Sigma La,Ce,Lu)}\right]_n$
	Separated from MVT in (E.) $\log_{10}\left[\frac{(Eu/Eu*)}{(\Sigma La,Ce,Lu)}\right]_n$ vs. $\log_{10}\left[\frac{(La/Sm)}{(\Sigma La,Ce,Lu)}\right]_n$ Separated from greisen in (H.) $\log_{10}\left[\frac{(Pr/Dy)}{(\Sigma La,Ce,Lu)}\right]_n$ vs. $\log_{10}\left[\frac{(Pr/Eu)}{(\Sigma La,Ce,Lu)}\right]_n$ Separated from cryolite in (D.) $\log_{10}\left[\frac{Eu}{Eu*}\right]_n$ vs. $\log_{10}[\Sigma La, Ce, Lu]_n$ Separated (mostly) from hydrothermal/epithermal vein and replacements hosted in carbonate rock in (C.) $\log_{10}\left[\frac{(Eu/Dy)}{(\Sigma La,Ce,Lu)}\right]_n$ vs. $\log_{10}\left[\frac{(Pr/Gd)}{(\Sigma La,Ce,Lu)}\right]_n$

Greisen	(G.) $\log_{10}\left[\frac{(Nd/Yb)}{(\Sigma La,Ce,Lu)}\right]_n$ vs. $\log_{10}\left[\frac{(Nd/Eu)}{(\Sigma La,Ce,Lu)}\right]_n$
	Separated from rare metal pegmatite in (B.) $\log_{10}\left[\frac{(Ce/Tb)}{(\Sigma La,Ce,Lu)}\right]_n$ vs. $\log_{10}\left[\frac{(Tb/Ho)}{(\Sigma La,Ce,Lu)}\right]_n$ Separated from cryolite in (I.) dpa_2 vs. dpa_1
Peralkaline silicate igneous rock	(H.) $\log_{10}\left[\frac{(Pr/Dy)}{(\Sigma La,Ce,Lu)}\right]_n$ vs. $\log_{10}\left[\frac{(Pr/Eu)}{(\Sigma La,Ce,Lu)}\right]_n$
	Separated from rare metal pegmatite in (B.) $\log_{10}\left[\frac{(Ce/Tb)}{(\Sigma La,Ce,Lu)}\right]_n$ vs. $\log_{10}\left[\frac{(Tb/Ho)}{(\Sigma La,Ce,Lu)}\right]_n$ Separated from IOCG in (C.) $\log_{10}\left[\frac{(Eu/Dy)}{(\Sigma La,Ce,Lu)}\right]_n$ vs. $\log_{10}\left[\frac{(Pr/Gd)}{(\Sigma La,Ce,Lu)}\right]_n$ Separated from granite-related uranium in (C.) $\log_{10}\left[\frac{(Eu/Dy)}{(\Sigma La,Ce,Lu)}\right]_n$ vs. $\log_{10}\left[\frac{(Pr/Gd)}{(\Sigma La,Ce,Lu)}\right]_n$ Separated from greisen in (G.) $\log_{10}\left[\frac{(Nd/Yb)}{(\Sigma La,Ce,Lu)}\right]_n$ vs. $\log_{10}\left[\frac{(Nd/Eu)}{(\Sigma La,Ce,Lu)}\right]_n$ Separated from hydrothermal/epithermal veins and replacements hosted in igneous rock deposits in (I.) dpa_2 vs. dpa_1
Intrusion-related Mo	(J.) Dpa_A vs. Dpa_B
	Separated from rare metal pegmatite in (B.) $\log_{10}\left[\frac{(Ce/Tb)}{(\Sigma La,Ce,Lu)}\right]_n$ vs. $\log_{10}\left[\frac{(Tb/Ho)}{(\Sigma La,Ce,Lu)}\right]_n$ Separated from cryolite in (D.) $\log_{10}\left[\frac{Eu}{Eu*}\right]_n$ vs. $\log_{10}[\Sigma La, Ce, Lu]_n$ Separated from peralkaline silicate igneous rock in (D.) $\log_{10}\left[\frac{Eu}{Eu*}\right]_n$ vs. $\log_{10}[\Sigma La, Ce, Lu]_n$ Separated from carbonatite-related in (I.) dpa_1 vs. dpa_2

	Not separable from hydrothermal/epithermal veins and replacements in carbonate rocks

Figure 3-1 Discrimination diagrams of primary deposit types with 66.7% data contours for each diagram. Tables per diagram list the number of data points within contours (N-67%), the number of data points represented in each diagram (N diagram), the number of analyses represented in the entire dataset (N total), and the percentage of datapoints represented by contours for the entire dataset (% total). Deposit-type group cells were shaded with their respective legend colors where diagrams are determined as starting points in Table 3-1, and deposit-type groups were bolded and the font colored when secondary distinctions were made per diagram (Sep. from). The legend on the first diagram (A.) represents contours. The legend on the second diagram (B.) represents test analyses from fluorite from North American deposits.

A. $\log_{10}\left[\frac{(Ce/Tb)}{(\Sigma La,Ce,Lu)}\right]_n$ vs. $\log_{10}\left[\frac{(La/Eu)}{(\Sigma La,Ce,Lu)}\right]_n$

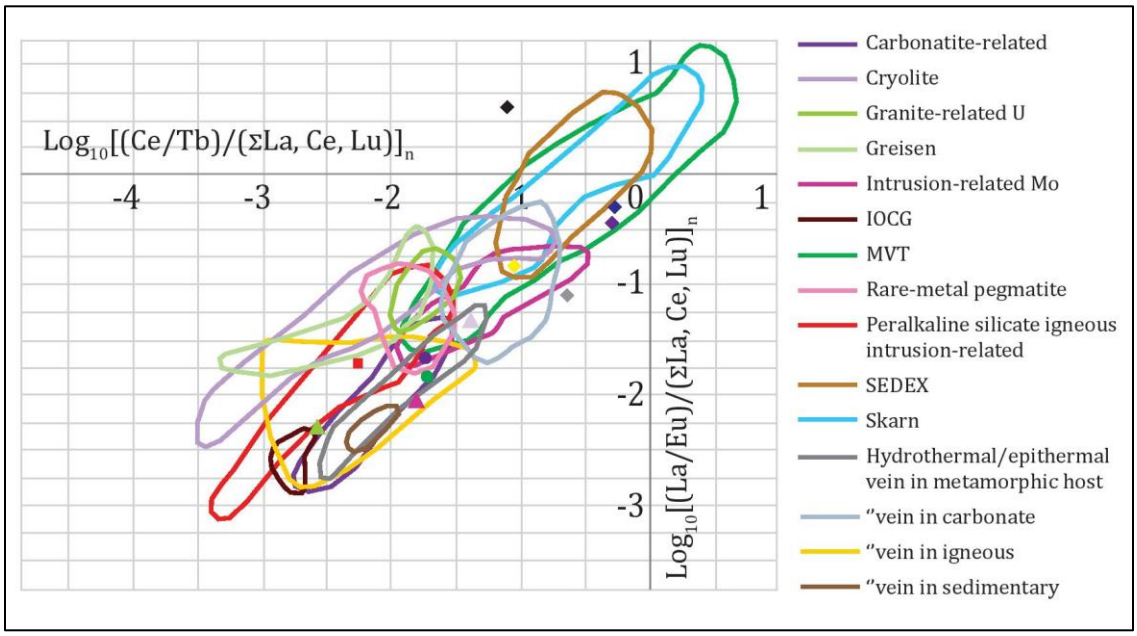

Deposit Type	N – 67%	N diagram	N total	% total
Peralkaline	31	47	48	65
Carbonatite	59	88	100	59
MVT	92	138	138	67
SEDEX	20	30	33	61
IOCG	6	9	9	67
Skarn	15	22	24	63
Pegmatite	11	17	17	65
Granite-U	7	10	15	47
Greisen	7	10	17	41
Cryolite	9	14	14	64
Intrusion-Mo	19	29	29	66
Vein - Igneous	42	62	93	45
Vein – Carb.	36	54	54	67
Vein – Met.	18	27	27	67
Vein – Sed.	5	7	8	63

B. $\log_{10}\left[\frac{(Ce/Tb)}{(\Sigma La,Ce,Lu)}\right]_n$ vs. $\log_{10}\left[\frac{(Tb/Ho)}{(\Sigma La,Ce,Lu)}\right]_n$

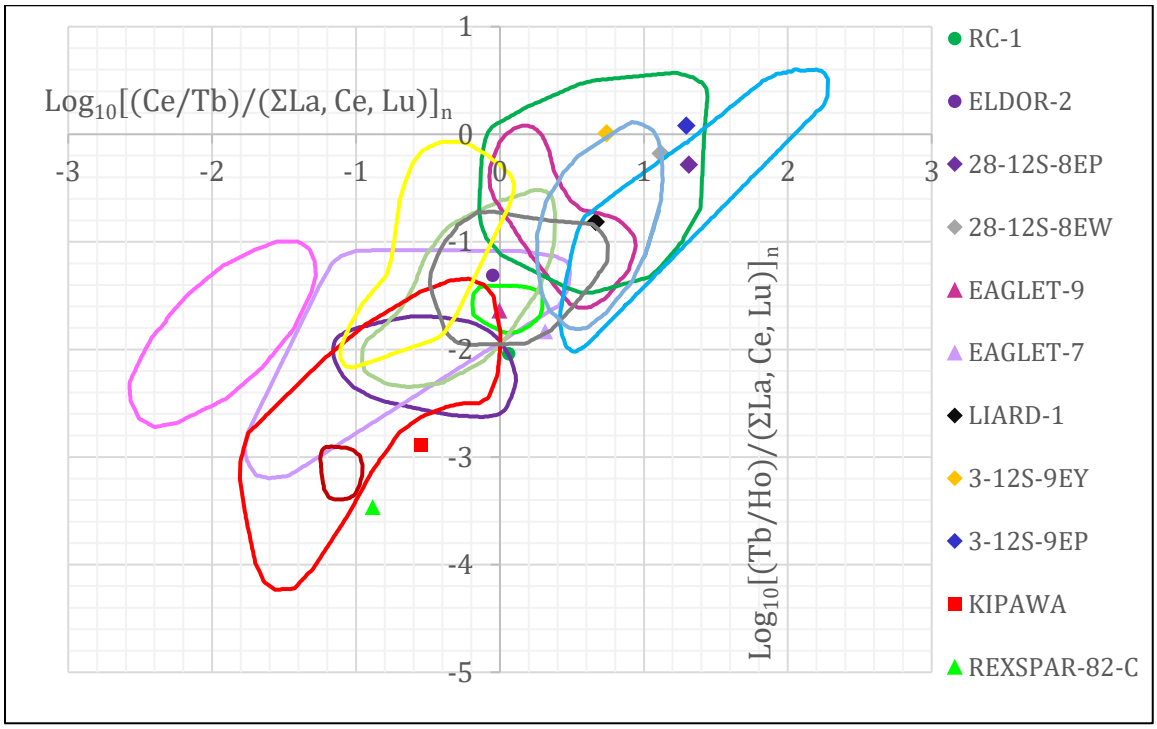

Deposit Type	N – 67%	N diagram	N total	% total	Sep. from
Peralkaline	**31**	**47**	**48**	**65**	Pegmatite
Carbonatite	**54**	**81**	**100**	**54**	Skarn, I-Mo
MVT	89	133	138	64	
SEDEX	0	0	33	0	
IOCG	6	9	9	67	
Skarn	11	17	24	46	
Pegmatite	9	14	17	53	
Granite-U	9	13	15	60	
Greisen	**11**	**16**	**17**	**65**	Pegmatite
Cryolite	9	14	14	64	
Intrusion-Mo	**19**	**29**	**29**	**66**	Pegmatite
Vein - Igneous	27	40	93	29	
Vein – Carb.	22	33	54	41	
Vein – Met.	11	17	27	41	
Vein – Sed.	5	7	8	63	

C. $\log_{10}\left[\frac{(Eu/Dy)}{(\Sigma La,Ce,Lu)}\right]_n$ vs. $\log_{10}\left[\frac{(Pr/Gd)}{(\Sigma La,Ce,Lu)}\right]_n$

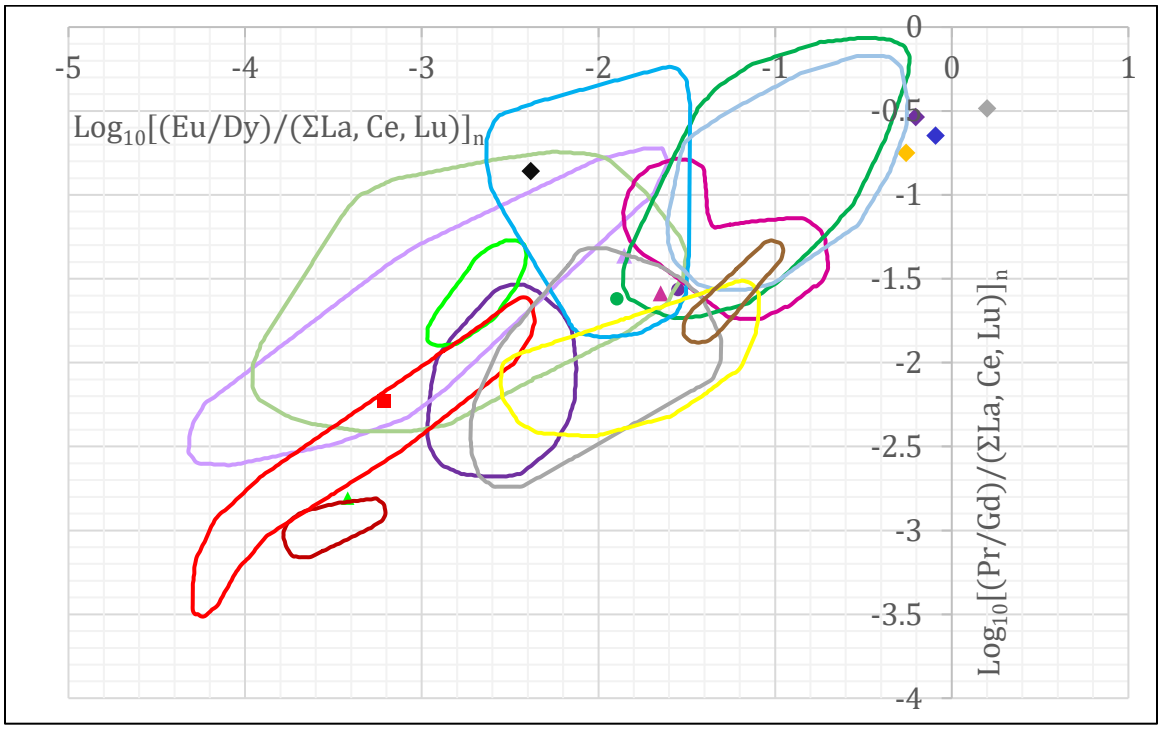

Deposit Type	N – 67%	N diagram	N total	% total	Sep. from
Peralkaline	**30**	**45**	**48**	**63**	IOCG, Granite-U
Carbonatite	54	80	100	54	
MVT	87	130	138	63	
SEDEX	0	0	33	0	
IOCG	6	9	9	67	
Skarn	**11**	**17**	**24**	**46**	Vein – Carb. (nearly)
Pegmatite	0	0	17	0	
Granite-U	7	10	15	47	
Greisen	11	17	17	65	
Cryolite	7	10	14	50	
Intrusion-Mo	19	29	29	66	
Vein - Igneous	25	37	93	27	
Vein – Carb.	22	33	54	41	
Vein – Met.	16	24	27	59	
Vein – Sed.	5	7	8	63	

D. $\log_{10}\left[\frac{Eu}{Eu*}\right]_n$ vs. $\log_{10}[\Sigma La, Ce, Lu]_n$; Eu* = $\left[\frac{Sm+Gd}{2}\right]_n$ (otherwise known as the average between normalized Sm and Gd)

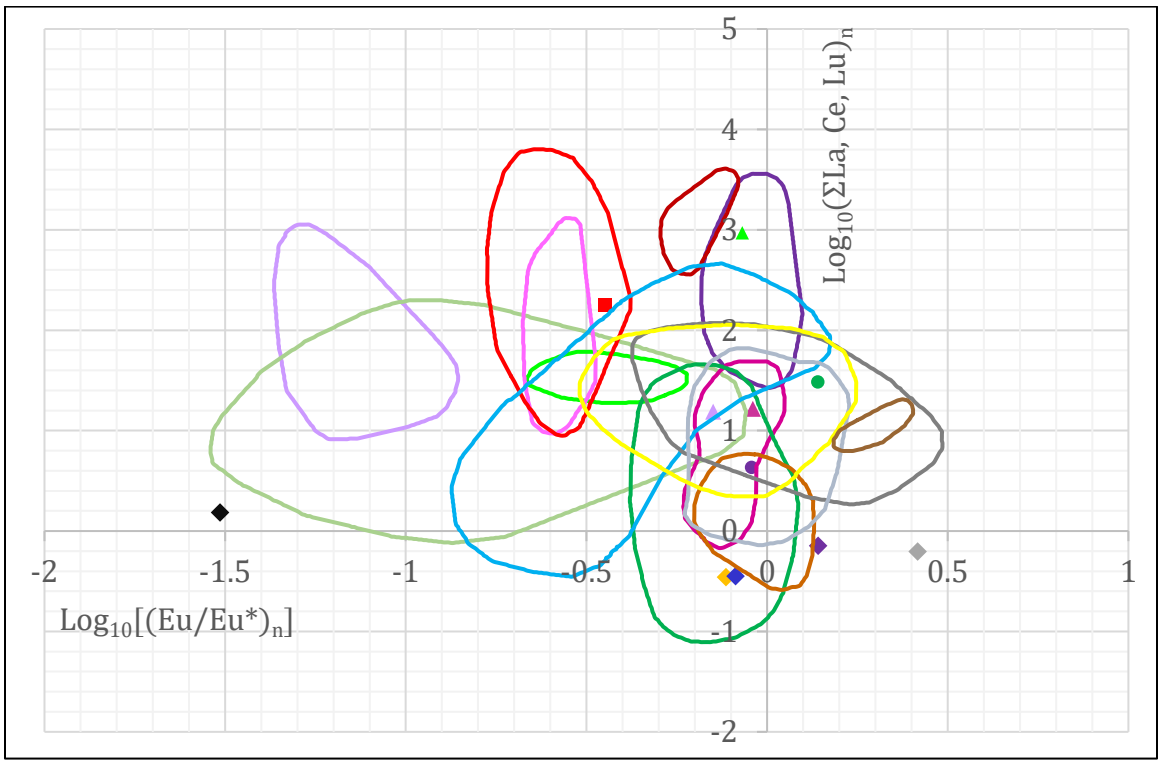

Deposit Type	N – 67%	N diagram	N total	% total	Sep. from
Peralkaline	31	47	48	65	
Carbonatite	66	99	100	66	
MVT	90	135	138	65	
SEDEX	15	23	33	45	
IOCG	6	9	9	67	
Skarn	**15**	**23**	**24**	**63**	Cryolite
Pegmatite	11	17	17	65	
Granite-U	**7**	**10**	**15**	**47**	Cryolite, Carbonatite
Greisen	11	17	17	54	
Cryolite	9	14	14	64	
Intrusion-Mo	**19**	**29**	**29**	**66**	Cryolite, Peralkaline
Vein - Igneous	62	93	93	67	
Vein – Carb.	36	54	54	67	
Vein – Met.	18	27	27	67	
Vein – Sed.	5	7	8	63	

E. $\log_{10}\left[\frac{(Eu/Eu*)}{(\Sigma La,Ce,Lu)}\right]_n$ vs. $\log_{10}\left[\frac{(La/Sm)}{(\Sigma La,Ce,Lu)}\right]_n$; Eu* = $\left[\frac{Sm+Gd}{2}\right]_n$ (otherwise known as the average between normalized Sm and Gd)

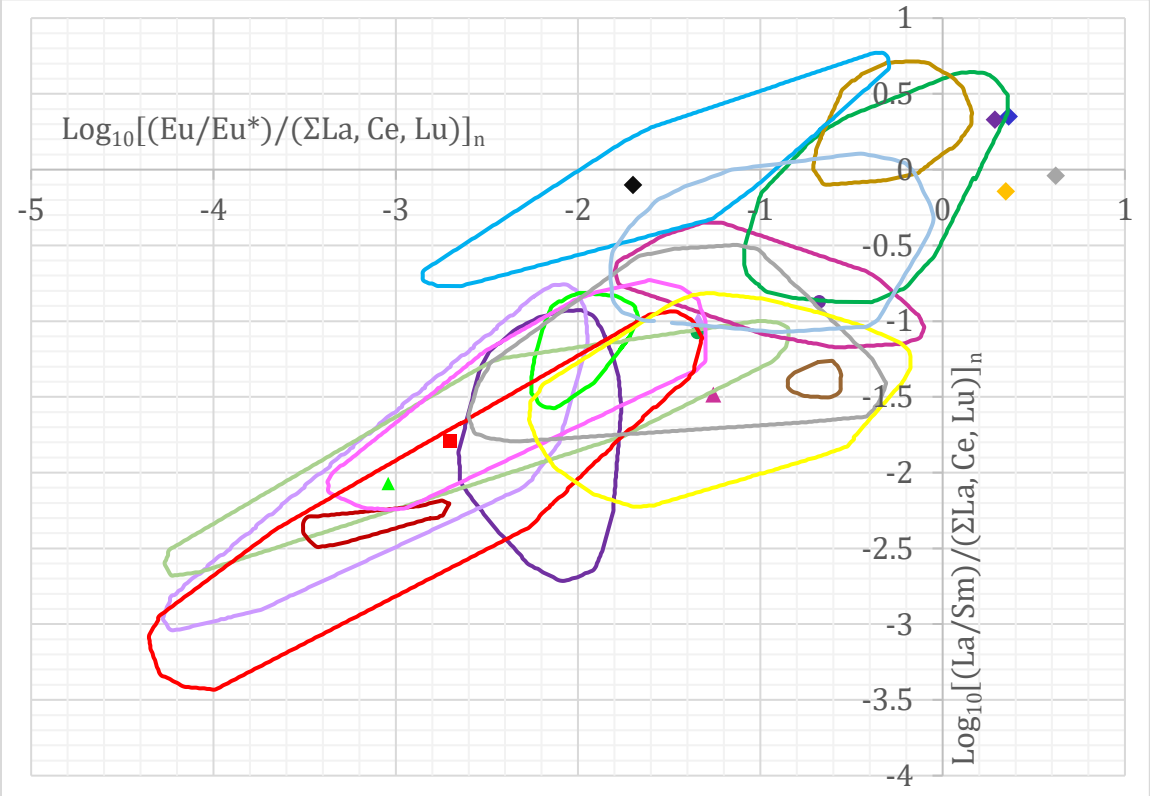

Deposit Type	N – 67%	N diagram	N total	% total	Sep. from
Peralkaline	31	47	48	65	
Carbonatite	66	99	100	66	
MVT	**90**	**135**	**138**	**65**	Skarn, Vein - Igneous
SEDEX	**15**	**23**	**33**	**45**	Skarn, Vein - carbonate
IOCG	6	9	9	67	
Skarn	**15**	**22**	**24**	**63**	MVT
Pegmatite	11	17	17	65	
Granite-U	7	10	15	47	
Greisen	7	10	17	41	
Cryolite	9	14	14	64	
Intrusion-Mo	19	29	29	66	
Vein - Igneous	62	93	93	67	
Vein – Carb.	36	54	54	67	
Vein – Met.	18	27	27	67	
Vein – Sed.	5	7	8	63	

F. $\log_{10}\left[\frac{(Nd/Lu)}{(\Sigma La,Ce,Lu)}\right]_n$ vs. $\log_{10}\left[\frac{(Ce/Tb)}{(\Sigma La,Ce,Lu)}\right]_n$

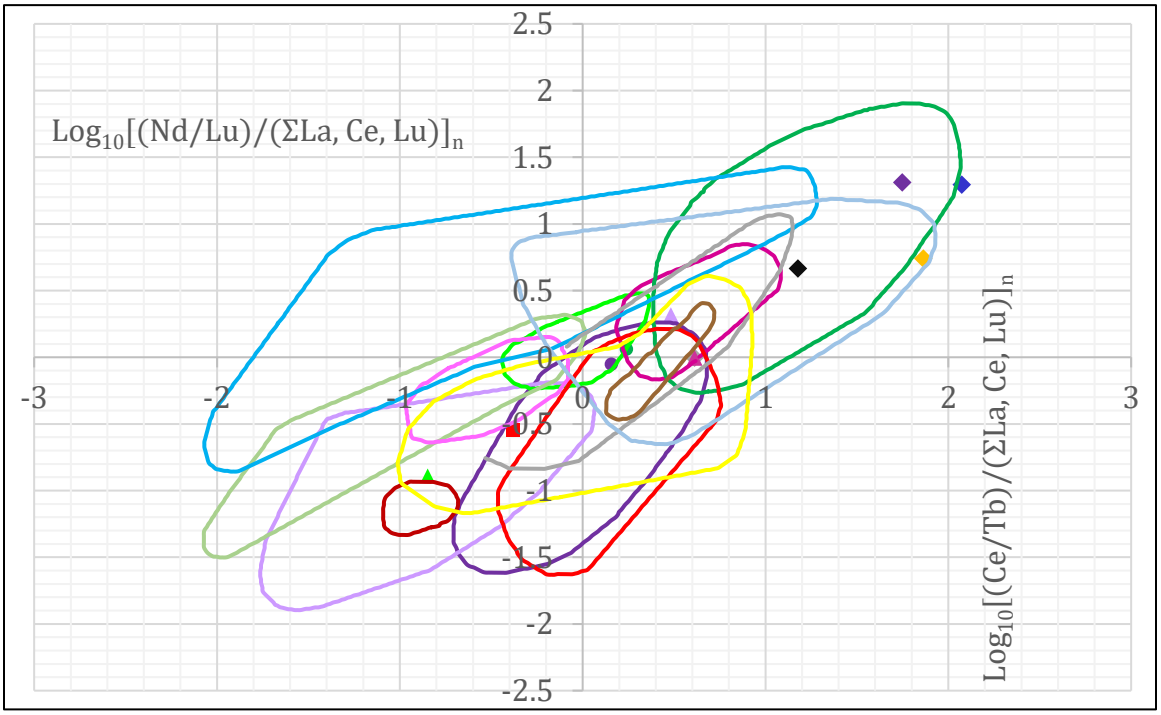

Deposit Type	N – 67%	N diagram	N total	% total
Peralkaline	31	47	48	65
Carbonatite	59	88	100	59
MVT	90	134	138	65
SEDEX	0	0	33	0
IOCG	6	9	9	67
Skarn	15	23	24	63
Pegmatite	10	15	17	59
Granite-U	9	13	15	60
Greisen	11	16	17	65
Cryolite	9	14	14	64
Intrusion-Mo	19	29	29	66
Vein - Igneous	42	62	93	45
Vein – Carb.	33	49	54	61
Vein – Met.	18	27	27	67
Vein – Sed.	5	7	8	63

G. $\log_{10}\left[\frac{(Nd/Yb)}{(\Sigma La,Ce,Lu)}\right]_n$ vs. $\log_{10}\left[\frac{(Nd/Eu)}{(\Sigma La,Ce,Lu)}\right]_n$

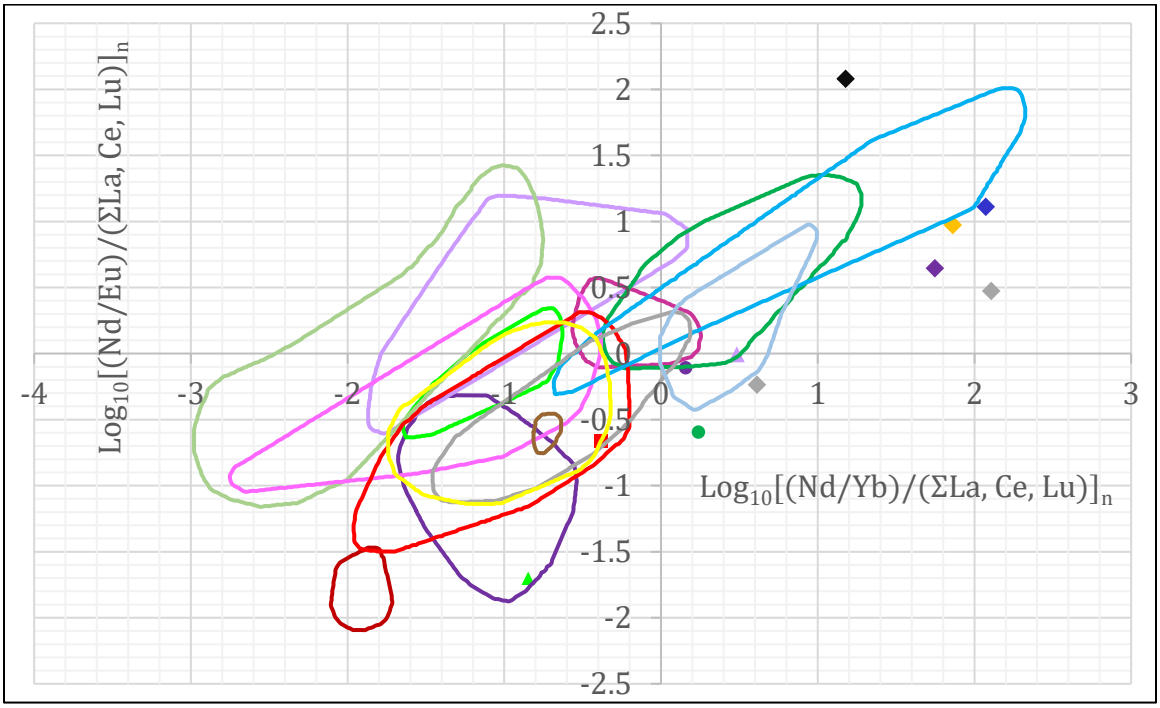

Deposit Type	N – 67%	N diagram	N total	% total	Sep. from
Peralkaline	**31**	**47**	**48**	**65**	Greisen
Carbonatite	**62**	**92**	**100**	**62**	Vein – Carb.
MVT	**84**	**126**	**138**	**61**	Greisen, Vein - Igneous
SEDEX	0	0	33	0	
IOCG	6	9	9	67	
Skarn	12	17	24	50	
Pegmatite	11	16	17	65	
Granite-U	**9**	**14**	**15**	**60**	Greisen
Greisen	12	17	17	71	
Cryolite	7	10	14	50	
Intrusion-Mo	19	29	29	66	
Vein - Igneous	52	78	93	56	
Vein – Carb.	22	33	54	41	
Vein – Met.	16	24	27	59	
Vein – Sed.	5	7	8	63	

H. $\log_{10}\left[\frac{(Pr/Dy)}{(\Sigma La,Ce,Lu)}\right]_n$ vs. $\log_{10}\left[\frac{(Pr/Eu)}{(\Sigma La,Ce,Lu)}\right]_n$

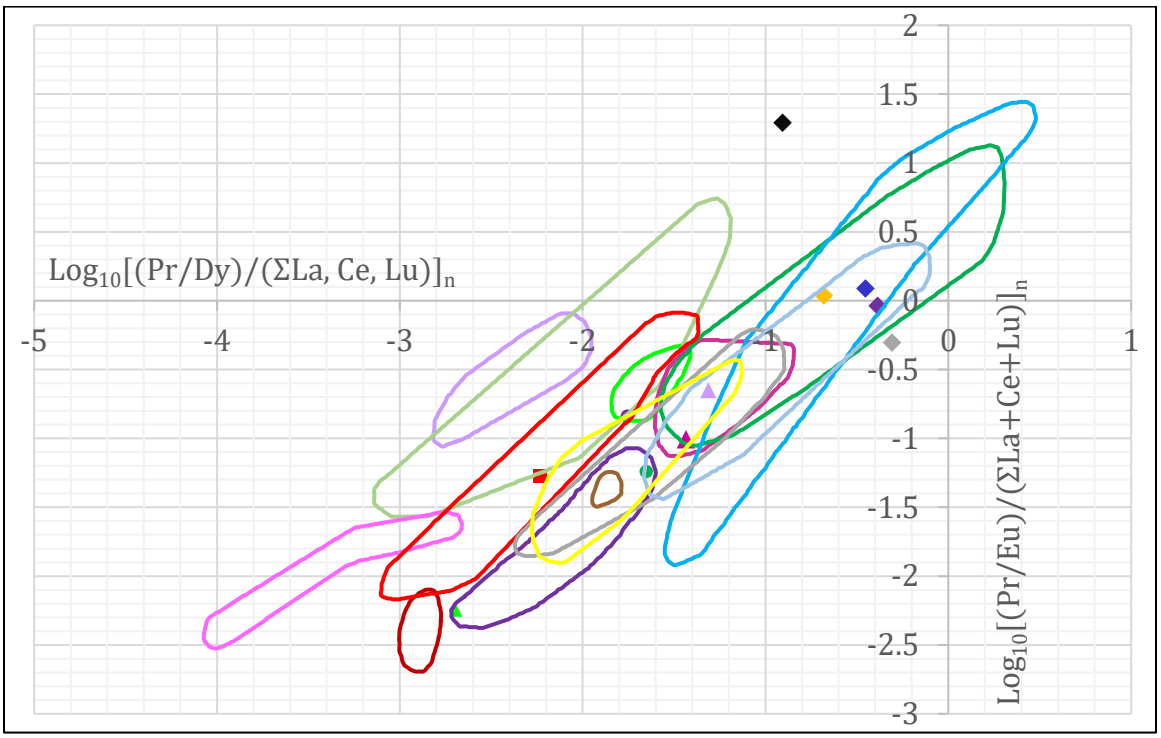

Deposit Type	N – 67%	N diagram	N total	% total	Sep. from
Peralkaline	31	47	48	65	
Carbonatite	54	81	100	54	
MVT	87	130	138	63	
SEDEX	0	0	33	0	
IOCG	6	9	9	67	
Skarn	**11**	**17**	**24**	**46**	Greisen
Pegmatite	3	4	17	18	
Granite-U	7	10	15	47	
Greisen	11	17	17	65	
Cryolite	9	14	14	64	
Intrusion-Mo	19	29	29	66	
Vein - Igneous	27	40	93	29	
Vein – Carb.	22	33	54	41	
Vein – Met.	16	24	27	59	
Vein – Sed.	5	7	8	63	

I. dpa_2 vs. dpa_1; input variables are not normalized to any scheme

$dpa\_2 = [0.009889975\ (\mathrm{La} - 51.45401)] + [-0.0019889493\ (Ce - 104.44297)] + [-0.12261945\ (\mathrm{Pr} - 14.978373)] + [0.043564335\ (\mathrm{Nd} - 70.1237)] + [-0.33165836\ (\mathrm{Sm} - 18.884602)] + [-0.2652554\ (\mathrm{Eu} - 3.847108)] + [0.2139858\ (\mathrm{Gd} - 20.097376)] + [-0.8956324\ (\mathrm{Tb} - 3.0827303)] + [0.55675626\ (\mathrm{Dy} - 17.87891)] + [0.00047728742\ (\mathrm{Y} - 165.30759)] + [0.59947145\ (\mathrm{Ho} - 3.2047267)] + [-0.72905296\ (\mathrm{Er} - 8.1561365)] + [-5.830804\ (\mathrm{Tm} - 1.1139407)] + [0.0472436\ (\mathrm{Yb} - 6.8972073)] + [5.2921443\ (\mathrm{Lu} - 0.8175968)]$

$dpa\_1 = [-0.014587307\ (\mathrm{La} - 51.45401)] + [\ 0.00038982305\ (Ce - 104.44297)] + [0.09807781\ (\mathrm{Pr} - 14.978373)] + [-0.0190112\ (\mathrm{Nd} - 70.1237)] + [0.14552052\ (\mathrm{Sm} - 18.884602)] + [0.083552815(\mathrm{Eu} - 3.847108)] + [-0.04925609\ (\mathrm{Gd} - 20.097376)] + [-1.5955023\ (\mathrm{Tb} - 3.0827303)] + [0.206346\ (\mathrm{Dy} - 17.87891)] + [0.0012446165\ (\mathrm{Y} - 165.30759)] + [-0.8745967\ (\mathrm{Ho} - 3.2047267)] + [0.6408816\ (\mathrm{Er} - 8.1561365)] + [-5.050501\ (\mathrm{Tm} - 1.1139407)] + [\ -0.15283918\ (\mathrm{Yb} - 6.8972073)] + [4.8628035\ (\mathrm{Lu} - 0.8175968)]$

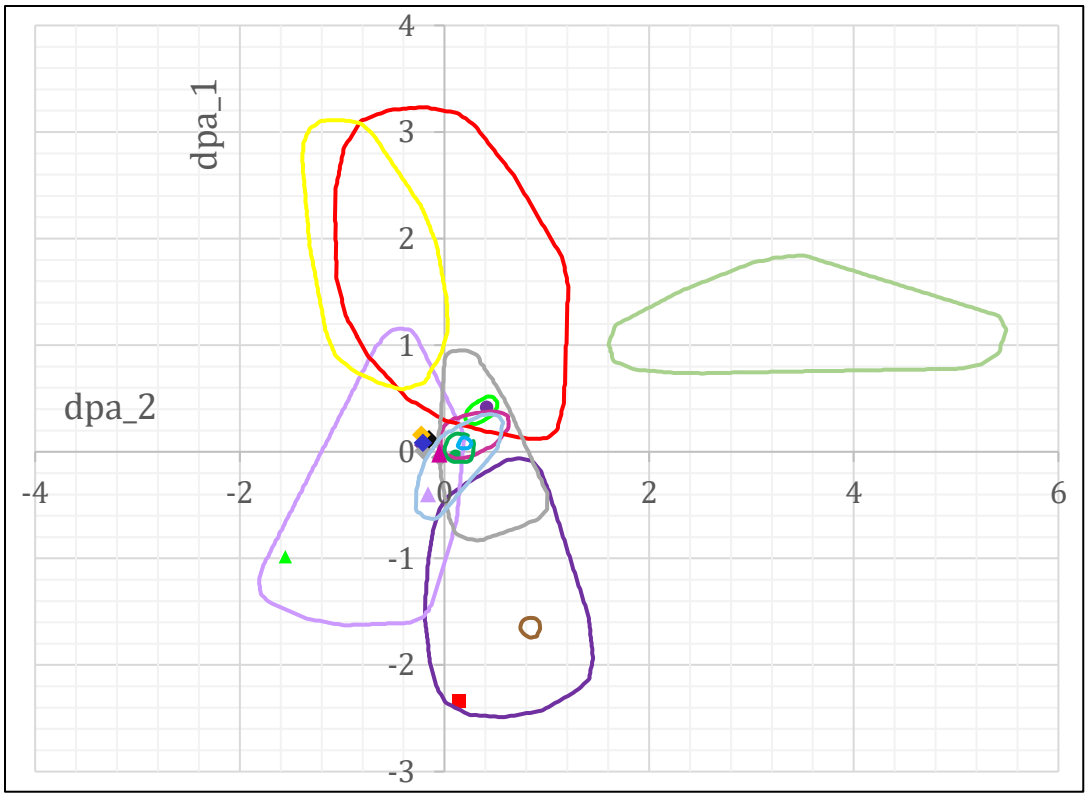

Deposit Type	N – 67%	N diagram	N total	% total	Sep. from
Peralkaline	**31**	**46**	**48**	**65**	Vein - Igneous
Carbonatite	**49**	**73**	**100**	**49**	Vein - Igneous
MVT	29	44	138	21	
SEDEX	0	0	33	0	
IOCG	0	0	9	0	
Skarn	6	9	24	25	
Pegmatite	0	0	17	0	

Granite-U	**2**	**2**	**15**	**13**	Greisen
Greisen	**3**	**5**	**17**	**18**	Cryolite
Cryolite	**7**	**10**	**14**	**50**	Greisen
Intrusion-Mo	**19**	**29**	**29**	**66**	Carbonatite
Vein - Igneous	12	18	93	13	
Vein – Carb.	5	7	54	9	
Vein – Met.	7	11	27	26	
Vein – Sed.	1	1	8	13	

J. Dpa_A vs. Dpa_B ; input variables are not normalized to any scheme

$$Dpa\_A = [-0.001114512(\text{La} - 56.906017)] + [0.0024397313(\text{Ce} - 96.19183)] + [-0.165863(\text{Yb} - 11.786525)] + [1.194379(\text{Lu} - 1.5306052)] + [-0.000037442944(\text{Sr} - 1036.9337)]$$

$$Dpa\_B = [-0.0025800907(\text{La} - 56.906017)] + [0.0032307461(\text{Ce} - 96.19183)] + [-0.032677025(\text{Yb} - 11.786525)] + [0.23692694(\text{Lu} - 1.5306052)] + [0.00038603853(\text{Sr} - 1036.9337)]$$

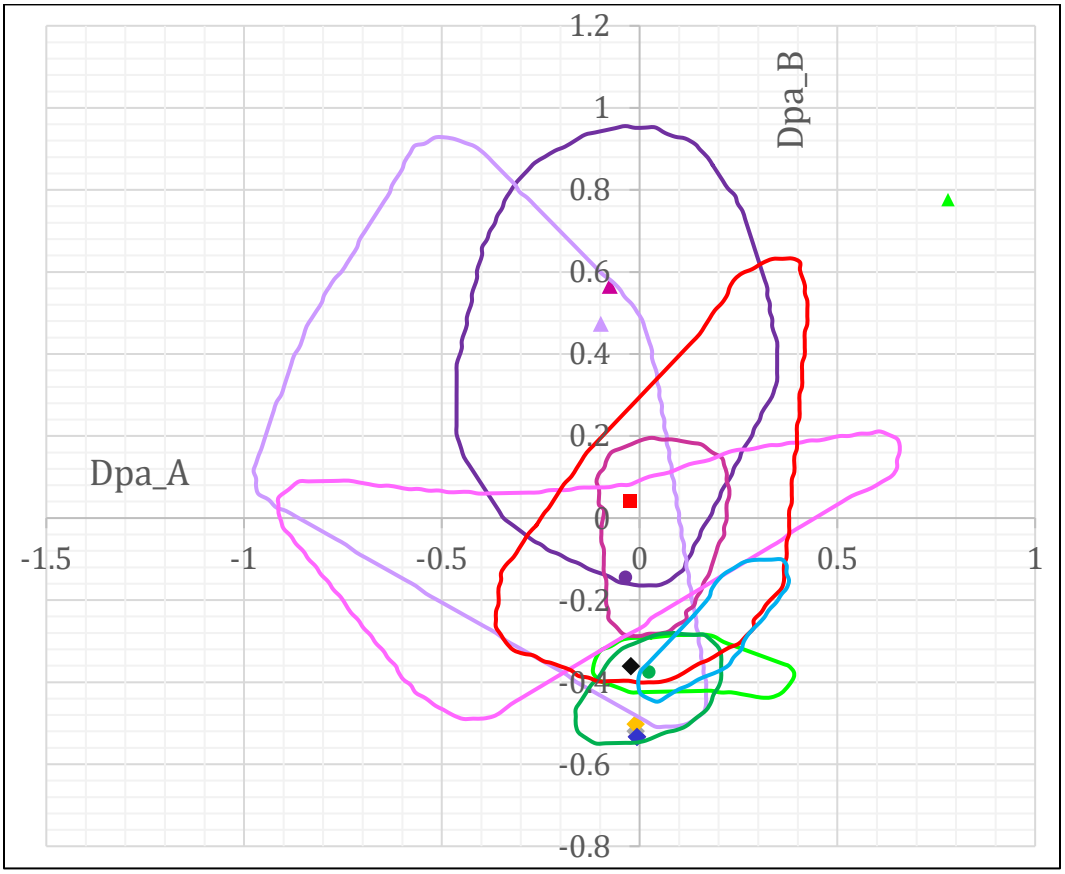

Deposit Type	N – 67%	N diagram	N total	% total	Sep. from
Peralkaline	26	39	48	54	
Carbonatite	**54**	**81**	**100**	**54**	Vein – Met.
MVT	**68**	**101**	**138**	**50**	Intr - Mo
SEDEX	0	0	33	0	
IOCG	0	0	9	0	

Skarn	11	19	24	46	
Pegmatite	3	4	17	18	
Granite-U	5	7	15	33	
Greisen	0	0	17	0	
Cryolite	5	8	14	36	
Intrusion-Mo	23	35	29	79	
Vein - Igneous	19	28	93	20	
Vein – Carb.	25	38	54	46	
Vein – Met.	9	14	27	33	
Vein – Sed.	1	2	8	13	

As can be observed in Figure 3-1Figure 3-1, there is a significant amount of overlap between primary mineralization environment fields even when generated using only ~2/3^{rds} of data contoured to greatest concentration. This overlap was mostly mitigated using the procedure of isolating data fields outlined in Table 2-1Table 3-1. Overlap of data fields is unavoidable when using lanthanoids as the sole basis for systematics since these elements chemically behave very similarly and their partitioning into fluorite appears to be consistent except between crystal sectors (Baele et al., 2012; Smolyanski et al., 2009; Bosze and Rakovan, 2002). Overlap is also inevitable without distinguishing between fluorites of different parageneses within single deposits, as chondrite-normalized (McDonough and Sun, 1995) patterns of REE-Y in fluorite, though consistent on grain- and sample- scales, are quite variable between samples from a single deposit. Several solutions could be proposed to remedy the large amount of overlap between groups: 1.) utilizing trace-elements in fluorite other than REE-Y which would require further research and analysis; 2.) an alternative classification scheme, possibly one more specific to deposit paragenesis, which would require an overhaul of this project concept and would require significantly more research; 3.) alternative data manipulation or equations to produce alternate discrimination diagrams, though discriminant projection analysis should remove speculation for possible improvement of data field separation. However, DPA was limited by inconsistent trace-element reporting in publications and it's possible that this method could be improved upon. Additionally, classification groups could alternately be described or identified using a simple analysis of trace-element data using methods such as hierarchical clustering, or simply by working backwards by identifying similar REE-Y patterns and attempting to identify similarities between the samples or deposit location descriptions.

3.3. Method verification with test data

The usability of these discrimination diagrams was tested by applying scatter data generated from FUS-ICP/MS analyses of fluorite from North American deposits with assigned primary-deposit types determined by literature review. Deposit-types were assigned by simply counting how many times the data point plotted in any deposit-type field on all ten diagrams. Then, deposit types could be assigned on a hierarchical basis, where the greatest number of occurrences was given priority as a most probable assignation. For fields with equal numbers of occurrences, priority was given to deposit-type groups that were more "well represented" by our data compilation. A procedure of determining deposit types via linear programming based on isolotaion of datafields as outlined in Table 3-1 was considered but was not implemented. This is due in part that datafield overlap remained extensive with only 67% of data encompassed within fields per deposit-type and that the representation of deposit types was not equivalent. In other words, these diagrams when used in combination provide an accurate estimate for fluorite deposit-type assignations but single diagrams are not precise enough for the implementation of linear programming. Therefore, a majority rules approach with weighted consideration of deposit-type representation is the more accurate, and is likely the easiest method for assigning deposit-types for scatter data. Additionally, if multiple analyses representing single samples were used, or if it's assumed that fluorite collected from stream sediments or till were likely sourced from the same location, clustering of the datasets on these diagrams should indicate probable deposit-types from a simple visual investigation.

Eleven datapoints from samples sourced from the Rock Candy, Eldor, Barnett Mine, Eaglet, Liard Fluorospar, Hastie Quarry, Kipawa, and Rexspar deposits were applied to discrimination diagrams with returned results listed in Table 3-2. Primary mineralization environments were assigned based on a majority rules approach with weighted consideration of deposit-type representation as listed in Table 3-3.

Sample	H/E V/R in igneous	MVT	H/E V/R in carbonate	Carbonatite-related	H/E V/R in meta.	SEDEX	Skarn	Greisen	Intrusion-related Mo	Cryolite	Peralkaline silicate igneous rock	H/E V/R in sed.	Rare-metal pegmatite	Granite-related U	IOCG
RC-1	3	3	4	5	7		2	3	3	2	4			2	
ELDOR-2	4	5	3	2	6	1	1	4	5	2	4		1	3	
28-12-8EP		6	1			1	2			1					
28-12-8EW	1	3	2	1	1		1		1	1	1			1	
EAGLET-9	5	4	4	3	6		1	3	4	2	2				
EAGLET-7	4	6	6	1	5		2	4	4				1	1	
LIARD-1		2	2		1		3	1	1	1	1				
3-12S-9EY		5	4				3			1					
3-12S-9EP		6	1				2			1					
KIPAWA	3			3	2			3		2	7		3	1	
REXSPAR-82-C	2			3				2		1	1				2

Table 3-2 Results of test analyses of fluorite handsamples plotted on discrimination diagrams. The number of occurrences scatter data enter primary mineralization environment fields on all ten discrimination diagrams (Figure 3-1) is listed here. Deposit-type groups are listed from most "well represented" to "worst" based on the database used to create discrimination diagrams so confidence can be weighted from highest to lowest from left to right.

Based on these results listed in Table 3-2Table 3-2, where the plotting of test analyses was counted from each discrimination diagram, the following primary deposit types could be assigned as follows and are listed in Table 3-3:

Rock Candy (RC-1): Hydrothermal/epithermal vein/replacement hosted in metamorphic rock, carbonatite-related, hydrothermal/epithermal vein/replacement in carbonate rock, or peralkaline silicate-igneous rock.

Eldor (ELDOR-2): Hydrothermal/epithermal vein/replacement hosted in metamorphic rock, MVT, intrusion-related molybdenum, hydrothermal/epithermal vein/replacement in igneous rock, greisen, or peralkaline silicate igneous rock

Barnett Mine (28-12-8EP; -8EW): MVT; MVT, hydrothermal/epithermal vein/replacement in carbonate rock

Eaglet (EAGLET-9; -7): Hydrothermal/epithermal vein/replacement in metamorphic rock, in igneous rock, MVT, in carbonate rock, intrusion-related Mo; MVT, hydrothermal/epithermal vein/replacement in carbonate rock, in metamorphic rock, in igneous rock, greisen, intrusion-related Mo

Liard fluorospar (LIARD-1): Skarn, MVT, hydrothermal/epithermal vein/replacement in carbonate rock

Hastie Quarry (3-12S-9EY; -9EP): MVT, hydrothermal/epithermal vein/replacement in carbonate rock, skarn; MVT

Kipawa (KIPAWA): Peralkaline silicate igneous rock deposit

Rexspar (REXSPAR-82-C): Carbonatite-related, hydrothermal/epithermal vein/replacement in igneous rock, greisen, IOCG

Table 3-3 Returned deposit types based on results from discrimination diagrams and determinations from Table 3-2. Confident returns are bolded and semi-confident assignations are italicized.

Deposit name	Primary mineralization environment	Secondary mineralization environment	Third possible type
Liard fluorospar	**Skarn**	*MVT*	Hydrothermal/epithermal vein/replacement in carbonate host
Hastie Quarry	**MVT**	Hydrothermal/epithermal vein/replacement in carbonate host	Skarn
Barnett Mine	**MVT**	Hydrothermal/epithermal vein/replacement in carbonate host	n/a
Rexspar	*Carbonatite-related*	Hydrothermal/epithermal vein/replacement in igneous host	Greisen or *IOCG*
Eaglet	Hydrothermal/epithermal vein/replacement in metamorphic host or MVT	Hydrothermal/epithermal vein/replacement in igneous or carbonate host	Intrusion-related Mo
Kipawa	**Peralkaline silicate igneous rock**	n/a	n/a
Eldor	Hydrothermal/epithermal vein/replacement in metamorphic host	MVT	Intrusion-related Mo or hydrothermal/epithermal vein/replacement in igneous host
Rock Candy	Hydrothermal/epithermal vein/replacement in metamorphic host	*Carbonatite-related*	Hydrothermal/epithermal vein/replacement in carbonate

From the results in Table 3-2, only four out of eight deposits could be assigned primary-deposit types with confidence as seen in Table 3-3Table 3-3 where specific deposit-type scores far exceeded alternate scores. Using these discrimination diagrams, it was determined that Barnett Mine is likely an MVT deposit, as is Hastie Quarry, while Kipawa is likely a peralkaline silicate igneous rock deposit and Liard is probably a skarn, but it is definitely a deposit hosted in carbonate rock. This is all in agreeance with predicted primary mineralization environments determined by literature review outlined in Table 2-4. The most likely deposit type returned for the Rock Candy and Eldor deposits were hydrothermal/epithermal vein/replacement deposits hosted in metamorphic rock, but both also returned many other possibilities. The next likely deposit type for Rock Candy is carbonatite-related which is in agreeance with one of its predicted deposit types outlined in Table 2-4. The next likely deposit-types that can be assigned to the Eldor deposit were MVT

or intrusion-related molybdenum deposits, while this deposit was predicted by literature review as being a carbonatite-related deposit. Based on the data from two samples for the Eaglet deposit, the most likely deposit-type assignations were MVT or hydrothermal/epithermal vein/replacement deposit in metamorphic rock. These two samples scored high for several deposit-types and a confident assignation is not possible. Both predicted deposit types from literature review listed in Table 2-4 were returned however, for the Eaglet deposit including intrusion-related molybdenum and hydrothermal/epithermal vein/replacement deposit in igneous rocks, though these types did not score high in comparison to others. Finally, the Rexspar deposit likely represents a carbonatite-related deposit according to these results, though it nearly equally scored as a hydrothermal/epithermal vein/replacement deposit in igneous rock, a greisen, and an IOCG deposit. It was the only sample to score within the IOCG deposit data field, which may be more precise than we can determine since this data field was created using few analyses. Even though a deposit-type could not be assigned for the Rexspar deposit with confidence, it appears that the deposit is related to igneous rocks or activity in some way, and carbonatite-related could be an adequate assignation as the deposit hosts rare-earth resources.

Since the Eaglet and Eldor deposits returned deposit-types across the board, not much can be concluded from those test samples other than no specific deposit-type could be assigned for either deposit. This was expected for the Eaglet deposit as it was difficult to assign a possible deposit-type from Minfile records, however the Eldor deposit was confidently described as being a part of a carbonatite complex. It is not known why the trace-element geochemistry from fluorite for the Eldor deposit did not indicate that it was a carbonatite-related deposit as this deposit was confidently described as such in literature and this deposit-type was well-represented in creating discrimination diagrams.

There were numerous returns for hydrothermal/epithermal vein/replacement deposits in metamorphic rocks and it was the determined primary mineralization environment for three of the test deposits. This deposit-type data field was often centrally located in respect to all other data fields on every diagram, and therefore overlapped many other fields allowing for large returns. The speculative explanation for this, is that this dataset included deposits hosted in metamorphic rocks with both igneous and sedimentary or

carbonate protoliths, formed due to a wide variety of mineralizing mechanisms. Additionally, metamorphism can remobilize elements from all rock types, especially incompatible elements, and subsequently can salvage, a sort of, average value of trace-elements in fluids based on all rock types and fluids involved. For both of these reasons, this deposit-type data field will overlap many others on discrimination diagrams. Ignoring hydrothermal/epithermal vein/replacement deposits hosted in metamorphic rock as a primary mineralization environment, though poor practice, would return primary mineralization environments for the Eaglet and Eldor deposits as MVTs, and the Rock Candy deposit as carbonatite-related. The first two are also very unlikely based on the literature reviewed for these deposits, but the latter is indeed a likely assignation.

Generally, there seems to be some accuracy in using these discrimination diagrams to determine whether deposits are hosted in carbonate rocks or are related to igneous rocks or activity in some way. Each deposit-type returned for the Liard Fluorospar, Hastie Quarry, and Barnett Mine deposits were those hosted in carbonate rocks. The results for the Rexspar and Kipawa deposits only confidently returned deposit-types involving igneous activity or rocks. There is a bit of overlap however, regarding skarn and hydrothermal/epithermal vein/replacement deposits hosted in carbonate rock, as both of these deposit-types though hosted in carbonate rock can be produced through igneous activity. This general accuracy, or general trend in distinction seen on discrimination diagrams could possibly be attributed to general chemical or mineralizing environment endmembers. Meaning, the mineralizing environments of deposit-types where carbonate rocks are the primary host are typically very different than those involving igneous rocks or processes. Mainly, the host rock chemical sinks are very different, and more loosely, the dominant mineralizing fluids are contrasted allowing for a general distinction within trace-element patterns in fluorite creating notable differences in discrimination diagrams.

3.4. Summary

Ten discrimination diagrams were created distinguishing between primary mineralization environments using ratios and equations of REE-Y values analyzed in natural

fluorites from 183 deposits/sample localities from approximately 60 mineralizing regions worldwide. Primary mineralization environments determined from literature for use on discrimination diagrams include the following which are listed according to representation quality by the dataset: 1.) hydrothermal/epithermal vein/replacement deposits hosted in igneous rock, 2.) Mississippi Valley Type deposits, 3.) hydrothermal/epithermal vein/replacement deposits hosted in carbonate rock, 4.) carbonatite-related deposits, 5.) hydrothermal/epithermal vein/replacement deposits hosted in metamorphic rock, 6.) SEDEX deposits, 7.) skarns, 8.) greisens, 9.) intrusion-related Mo deposits, 10.) cryolite deposits, 11.) peralkaline silicate igneous rock deposits, 12.) hydrothermal/epithermal vein/replacement deposits hosted in sedimentary rock, 13.) rare-metal pegmatites, 14.) granite-related U deposits, 15.) IOCG deposits.

Overlap of data fields on these discrimination diagrams is extensive due to the nature of REE-Y systematics in fluorite, but the majority of data fields were isolated using the step-wise procedure outlined in Table 3-1. Using this procedure, all groups were distinguished from others with the exceptions of SEDEX deposits from MVT deposits, MVT deposits from hydrothermal/epithermal vein/replacement deposits hosted in carbonate and metamorphic rocks, intrusion-related molybdenum deposits from vein/replacement deposits in carbonate rock, and no attempt was made to isolate hydrothermal/epithermal vein/replacement deposit groups.

The usability of these discrimination diagrams was tested using FUS-ICP/MS analyses on samples of fluorite from North American deposits with pre-estimated primary mineralization environment assignations. This was done by applying test data to each discrimination diagram and by counting the number of times the test data returned primary mineralization environment groups as outlined in Table 3-2. Primary mineralization environments were then assigned to test sample source deposits according to these returns with preference given to highest values followed by confidence assigned to the most "well represented" deposit-type groups as outlined in Table 3-2. From this procedure, four out of eight deposits were assigned confident primary mineralization environments that were in agreeance the predicted primary mineralization environments determined for those deposits from literature review, Table 3-3. Two out of eight deposits could be assigned primary-

deposit types with a lower degree of confidence, while two could not be assigned a single deposit-type at all. Additionally, a general accuracy was determined for the use of these discrimination diagrams where correctly returned deposit types predicted whether the deposit was hosted in carbonate, or igneous rock or if its formation was related to igneous processes.

3.5. References

1) Baele., J-M., Monin, L., Navez, J., André, L., 2012. Systematic REE partitioning in cubo-dodecahedral fluorite from Belgium revealed by cathodoluminescence spectral imaging and Laser Ablation-ICP-MS; 10th International Congress for Applied Mineralogy (ICAM), (23-30).
2) Gagnon, J. E., Samson, I. M., Fryer, B. J., Williams-Jones, A. E., 2003. Compositional heterogeneity in fluorite and the genesis of fluorite deposits: insights from LA-ICP-MS analysis; Canadian Mineralogist, v. 41, (365-382).
3) Mao, M., Rukhlov, A.S., Rowins, S.M., Spence, J., Coogan, L.A., 2016. Apatite trace element compositions: a robust tool for mineral exploration. Economic Geology, v. 111, (1187-1222).
4) McDonough, W.F., Sun, S.-s., 1995. The composition of the Earth; Chemical Geology, v. 120 (223-253).
5) Schwinn, G., Markl, G., 2005. REE systematics in hydrothermal fluorite; Chemical Geology, v. 216, (225-248).
6) Smolyanskii, P.L., Proskurnin, V.F., Bogomolov, E.S., 2009. Growth dissymmetrization of rare earth element distribution and the Sm-Nd isotope system in fluorite crystals of the Nordvik Deposit (Taymyr). Doklady Earth Sciences (Geochemistry), v. 424, No. 1, (86-89).
7) Vinokurov, S.F., Golubev, V.N.., Krylova, T.L., Prokof'ev, V.Yu., 2014. REE and fluid inclusions in zoned fluorites from Eastern Transbaikalia: distribution and geochemical significance. Geochemistry International, v. 52, no. 8, (654-669).

Chapter 4.

Conclusions

With the development of indicator mineral methods and the need for effective targeting strategies for specialty metal deposits, fluorite was chosen as a possible candidate for its development as a geochemical pathfinder mineral. Fluorite occurs in abundance in a variety of economic deposit-types and contains trace-elements substituting primarily for Ca^{2+} within its crystal structure. The approach taken here is that (1) trace-element signatures found in fluorite reflect those of mineralizing fluids, (2) the fluids contain signatures that reflect the mineralizing environment, and (3) fluorite compositions can be used to identify the types of associated mineral deposits. Because of these factors, this thesis was conducted to assess the viability and to begin development of fluorite as a geochemical pathfinder mineral for economic deposits.

Within this thesis, the trace-element geochemistry of fluorite was compiled from literature sourcing over 630 analyses from 183 deposit localities from approximately 60 regions worldwide from 32 publications. Analyses were conducted using multiple methods including ICP-MS, LA-ICP-MS, ICP-AES, NAA, and INAA, and some measures were taken to enhance compatibility of datasets such as the averaging of LA-ICP-MS analyses per sample. The total ranges of analytical results using each method for similar deposit types were also compared and it was determined that the average values across analytical method types were comparable. Additionally, including analyses taken by INAA and NAA allowed for the comparison of specific deposit types (ie., SEDEX) for which no other analyses were found, and therefore would not have been included in this study.

From this data compilation, it was determined that the lanthanoid suite of elements (REE and Y) were the most consistently reported elements in fluorite for all deposit types and therefore were the best trace-element candidates for comparison on discrimination diagrams. It was determined however, that REE-Y systematics can vary widely in concentration within fluorite on the grain-, sample-, and deposit scales (Appendix D.) causing a significant amount of overlap between data fields on discrimination diagrams. It is

suggested by the author herein to utilize trace-elements supplementary to REE-Y signatures in fluorite to compare economic deposit sources in further studies using normalized analytical techniques on an extensive collection of fluorite samples. The diagrams created in this study relied exclusively on compiled publication data, and subsequently could not effectively use trace-elements that were not consistently reported. If all samples were examined using consistent analytical methods, a lack of detection of certain trace-elements is a useful variable for discriminatory purposes.

Additionally, in examining REE-Y systematics in fluorite, authors such as Gagnon et al., 2003 and Schwinn & Markl, 2005 warned against chemical variability in single fluorite grains observable using point-ablation (LA-ICP-MS) analytical methods. Vinokurov et al., 2014 cautioned against drawing deposit-wide formational conclusions from chemical analyses using single fluorite samples. Baele et al., 2012, Smolyanski et al., 2009, and Bosze and Rakovan 2002, confirmed chondrite-normalized REE-Y pattern differences between temporally equivalent crystal sector zones. Mao et al., 2016 compared multiple fluorite analyses from a single deposit to multiple analyses from a single grain of fluorite and though, in determining three compositional zones in the fluorite grain, determined that the grain-scale chemical variability was less than that for the variability of all samples from the same deposit. In our investigation, we determined that total REE-Y concentrations were variable between analyses of single fluorite grains, between multiple analyses of single fluorite samples, and between analyses of single samples of different colors (Appendix D.). However, overall chondrite-normalized (McDonough & Sun, 1995) patterns remained relatively consistent on these scales of measurement. Because of this, we created fluorite discrimination diagrams utilizing ratios calculated from REE-Y data.

In creating discrimination diagrams, a classification scheme describing economic deposit-types was established. Each deposit from which data was sourced was assigned a primary and a secondary mineralization environment in order to offer subjective differences in interpretations of literature. These deposit-types were described using conventional deposit models as well as ones generated by the author to describe unconventional like deposits. Primary mineralization environments were the only classification group to be utilized on discrimination diagrams due to time constraints, but data were also sorted into

other economically interesting characterization groups to supplement the reader or user of discrimination diagrams with pertinent information about the data contained therein. These include metallic economic association (i.e., whether metals were the primary or secondary targeted or recovered commodity, or if industrial minerals were the only commodity of interest) and recovered/targeted/prospected commodity groups (i.e., the types of metals or materials that were targeted or recovered from these deposits). This classification scheme could be implemented in further studies to develop fluorite as a geochemical pathfinder mineral.

The representation of primary mineralization environment groups was then analyzed prior to creation of discrimination diagrams in order to assign confidence in generated discrimination fields. This representation was measured by considerations of sample sizes, data source diversity, and univariate distribution normality of REE-Y tested visually with histograms, quantile-quantile plots, and statistically with Shapiro-Wilks tests. From these considerations, a hierarchy of representation was determined from best to worst as follows (outlined in Table 2-3): 1.) hydrothermal/epithermal vein/replacement deposits hosted in igneous rocks, 2.) Mississippi Valley type, 3.) hydrothermal/epithermal vein/replacement deposits hosted in carbonate rocks, 4.) carbonatite-related, 5.) hydrothermal/epithermal vein/replacement in metamorphic hosts 6.) sedimentary exhalative (SEDEX), 7.) skarn, 8.) greisen, 9.) intrusion-related molybdenum, 10.) cryolite, 11.) peralkaline silicate igneous rock, 12.) hydrothermal/epithermal vein/replacement deposits in sedimentary hosts, 13.) rare-metal pegmatite, 14.) granite-related uranium, and 15.) iron oxide copper gold deposits (IOCG). This hierarchy should be considered when assigning deposit types to test data and gaps in representation should be recongnized for further studies.

Discrimination diagrams were then generated primarily by comparing REE-Y ratios on scatter diagrams, but values representing anomalous REE-Y and sum values were also generated, all divided by the sum of La, Ce, and Lu, the most consistently reported elements in the database. Additionally, discriminant projection analyses were used to create four equations to create two of the diagrams. Scatter data on diagrams were then contoured to a maximum interval of 2/3^{rds} of each data field per diagram. This eliminates the necessity of

determining outliers which is difficult to determine using a compiled database. A total of ten discrimination diagrams were selected to isolate primary mineralization environment groups from all others, accomplished in a step-wise matter as outlined in Table 3-1. All groups were distinguished from others with the exceptions of SEDEX from MVT deposits, MVT deposits from hydrothermal/epithermal vein/replacement deposits hosted in carbonate and metamorphic rocks, intrusion-related molybdenum deposits from vein/replacement deposits in carbonate rock, and no attempt was made to isolate hydrothermal/epithermal vein/replacement deposit groups.

Finally, these discrimination diagrams were tested using FUS-ICP/MS analyses of fluorite hand samples sourced from North American deposits. These deposits were assigned primary mineralization environments based on literature review according to the classification scheme created herein. Test data was then applied to discrimination diagrams and deposit-type assignations were determined according to the number of times sample data landed within those fields. As mentioned, linear programming was considered as a method of assigning deposit-types to applied scatter data on discrimination diagrams but it was determined that the diagrams when used in combination offer accurate assignations, though imprecise. If the number of returns were marked for a specific datafield, that deposit-type was assigned, but if single samples returned several primary mineralization environments equally, priority was assigned to deposit-types that were more "well represented." From this procedure, four out of eight deposits were confidently assigned primary mineralization environments that were in agreeance with predicted primary mineralization environments determined for those deposits from literature review. Two out of eight deposits could be assigned primary-deposit types with a lower degree of confidence, while two could not be assigned a single deposit-type at all. Additionally, a general accuracy was determined for the use of these discrimination diagrams where returned deposit types were correct at predicting whether the deposit was hosted in carbonate rock or hosted in igneous rock or if its formation was related to igneous processes.

These discrimination diagrams contribute to the development of fluorite as a geochemical pathfinder mineral, though the mechanisms controlling trace-element partitioning in fluorite is poorly understood. Their application worked confidently

approximately half of the time during our test assessment, and this accuracy would likely increase if test analyses were numerous allowing for distinct clustering into specific datafields. These diagrams however, merely represent a starting point for the development of this exploration tool and would only benefit from further study. It is the suggestion by this author that a widespread collection of samples representing a wide variety of mineralizing envrionments be analyzed under the same conditions to allow for a more comprehensive trace-element comparison. To this end, principle component analyses, discrimination projection analyses and linear programming could be more easily performed and implemented for robust development of fluorite as a geochemical pathfinder mineral. Perhaps during further analyses, trace element variability between fluorite sectors could be considered since LA-ICP-MS analyses is the ideal analytical method to be used in studies implementing these diagrams since this method would exclude contamination by fluid or mineral inclusions in crystals and is the most easily employed method for analyzing detrital fluorite grains. Additionally, it is not clear if fluorite color or fluorescence could contribute to discriminatory initiatives based on source deposit types, but could likely offer supplementary criteria for discrimination in specific cases. A study on fluid and mineral inclusions may provide more punctuated differences between fluorites sourced from varying deposit types, in which case a procedure of linear programming to determine deposit types could be implemented, which would offer great contribution to the diagrams created herein.

4.1. References

1) Baele., J-M., Monin, L., Navez, J., André, L., 2012. Systematic REE partitioning in cubo-dodecahedral fluorite from Belgium revealed by cathodoluminescence spectral imaging and Laser Ablation-ICP-MS; 10th International Congress for Applied Mineralogy (ICAM), (23-30).
2) Cherniak, D.J., Zhang, X.Y., Wayne, N.K., Watson, E.B., 2001. Sr, Y, and REE diffusion in fluorite. Chemical Geology, v. 181, (99-111).
3) Gagnon, J. E., Samson, I. M., Fryer, B. J., Williams-Jones, A. E., 2003. Compositional heterogeneity in fluorite and the genesis of fluorite deposits: insights from LA-ICP-MS analysis; Canadian Mineralogist, v. 41, (365-382).
4) Mao, M., Rukhlov, A.S., Rowins, S.M., Spence, J., Coogan, L.A., 2016. Apatite trace element compositions: a robust tool for mineral exploration. Economic Geology, v. 111, (1187-1222).
5) McDonough, W.F., Sun, S.-s., 1995. The composition of the Earth; Chemical Geology, v. 120 (223-253).
6) Schwinn, G., Markl, G., 2005. REE systematics in hydrothermal fluorite; Chemical Geology, v. 216, (225-248).
7) Smolyanskii, P.L., Proskurnin, V.F., Bogomolov, E.S., 2009. Growth dissymmetrization of rare earth element distribution and the Sm-Nd isotope system in fluorite crystals of the Nordvik Deposit (Taymyr). Doklady Earth Sciences (Geochemistry), v. 424, No. 1, (86-89).

8) Vinokurov, S.F., Golubev, V.N.., Krylova, T.L., Prokof'ev, V.Yu., 2014. REE and fluid inclusions in zoned fluorites from Eastern Transbaikalia: distribution and geochemical significance. Geochemistry International, v. 52, no. 8, (654-669).

Appendix A.

Tables representing data classification scheme

Table A.1

Table A-1 Table of classification scheme used to sort publication data for analysis. Data sorted by primary deposit types determined within this study, and secondary deposit types, metallic economic associations, and commodity groups are also identified. The number and methods of analyses are included for each deposit and publication and totals are provided for the numbers of deposits, regions, and publications compiled for each group. Where the number of analyses is listed as a number from another number, the first number is the resultant number of analyses after averaging LA-ICP-MS analyses per crystal/sample from the total number of analyses, the latter listed number as outlined in section 2.3.1.. Unnamed deposits condensed and labeled as "Multiple" are listed in **Table A-2***2 except for those at* Nördliche Kalkalpen***Error! Reference source not found.**.*

Primary deposit type	Deposit name	Region	Secondary deposit type	Metallic economic association	Commodity group	Analytical technique(s)	Number of analyses	Publication
Peralkaline silicate igneous rocks	Motzfeldt	Gardar Province	Peralkaline silicate igneous rocks	Primary	SM	LA-ICP-MS	41 from 131	Schönenberger et al., 2008
	Ilímaussaq	Gardar Province	Alkaline igneous silicate rocks	Primary	SM	LA-ICP-MS	8 from 28	Schönenberger et al., 2008
	Pinatosa	Gallinas Mountains	Peralkaline silicate igneous rocks	Secondary	F-SM	LA-ICP-MS	2 from 20	Gagnon et al., 2003
Total	3	2					51 from 179	2
Carbonatite-related	Daluxiang	Panxi Region	Peralkaline silicate igneous rocks	Primary	SM-base	ICP-MS	13	Xu et al., 2012
	Maoniuping	Panxi Region	Peralkaline silicate igneous rocks	Primary	SM	ICP-MS	20	Xu et al., 2012
	Lizhuang	Panxi Region	Peralkaline silicate igneous rocks	Primary	SM	ICP-MS	7	Xu et al., 2012

Primary deposit type	Deposit name	Region	Secondary deposit type	Metallic economic association	Commodity group	Analytical technique(s)	Number of analyses	Publication
	Bayan Obo	Bayan Obo	IOCG	Primary	SM-base	ICP-MS	11	Xu et al., 2012
	Speewah Fluorite	Yungul Carbonatite	Carbonatite-related	None	F	ICP-MS	7	Alvin et al., 2003
	Okorusu	Okorusu carbonatite complex	Carbonatite-related	None	F	ICP-MS	22	Bühn et al., 2003
	Mato Preto	Mato Preto alkaline complex	Peralkaline silicate igneous rocks	Secondary	F-SM	ICP-MS	11	Ventura Santos et al., 1996
	Deep Purple/Rock Canyon Creek	British Columbia	Hydrothermal/epithermal vein or replacement in carbonate	Secondary	F-SM	LA-ICP-MS	1 from 44	Gagnon et al., 2003
	Amba Dongar	Baroda	Carbonatite-related	Secondary	F-SM	INAA	7	Palmer, Williams-Jones, 1994
Total	9	7					99 from 142	6
Mississippi Valley Type	Treak Cliff Caverns	South Pennine Orefields	MVT	Primary	F-base-precious	ICP-MS	9	Bau et al., 2003
	Dirtlow open-pit	South Pennine Orefields	MVT	Primary	F-base-precious	ICP-MS	7	Bau et al., 2003
	Treak Cliff Castelton	South Pennine Orefields	MVT	Primary	F-base-precious	ICP-MS	8	Bau et al., 2003
	Smalldale	South Pennine Orefields	MVT	Primary	F-base-precious	ICP-MS	1	Bau et al., 2003
	Pindale	South Pennine Orefields	MVT	Primary	F-base-precious	ICP-MS	1	Bau et al., 2003
	Mitchell Bank	South Pennine Orefields	MVT	Primary	F-base-precious	ICP-MS	6	Bau et al., 2003

Primary deposit type	Deposit name	Region	Secondary deposit type	Metallic economic association	Commodity group	Analytical technique(s)	Number of analyses	Publication
	Lady Walsh Mine	South Pennine Orefields	MVT	Primary	F-base-precious	ICP-MS	6	Bau et al., 2003
	Frazer's Hush	North Pennine Orefield	Alkaline igneous silicate rocks	Primary	F-base-precious	ICP-MS	8	Bau et al., 2003
	Berbes	Asturias	MVT	None	F	ICP-MS	5	Sánchez et al., 2010
	La Collada	Asturias	MVT	None	F	ICP-MS	5	Sánchez et al., 2010
	Villabona	Asturias	MVT	None	F	ICP-MS	5	Sánchez et al., 2010
	Jebel Stah	Zaghouan	MVT	Secondary	F-base	ICP-MS	24	Souissi et al., 2010
	Çelikhan	Adiyaman	MVT	None	F	ICP-MS	15	Sasmaz et al., 2005a
	La Encantada	La Encantada	MVT (manto-style)	Unknown	Unknown	ICP-MS	2	Levresse et al., 2006
	Portalet	Valle de Tena	MVT	None	F	ICP-MS, NAA	30	Subías, Fernández-Nieto, 1995
	Ora	Hansonburg	MVT	Primary	Base-precious	INAA	3	Hill et al., 2000
	Royal Flush	Hansonburg	MVT	Primary	Base-precious	INAA	1	Hill et al., 2000
	MexTex	Hansonburg	MVT	Primary	Base-precious	INAA	1	Hill et al., 2000
Total	18	8					131	6
Sedimentary Exhalative	Multiple	Nördliche Kalkalpen	MVT	Primary	Base	INAA	33	Schneider et al., 1975

Primary deposit type	Deposit name	Region	Secondary deposit type	Metallic economic association	Commodity group	Analytical technique(s)	Number of analyses	Publication
Total	13	1					33	
IOCG	Lala	Kangding	IOCG	Primary	Base-SM-precious	unknown	9	Huang et al., 2014
Total	1	1					9	
Skarn	El-Pilote	La Encantada	Skarn	Unknown	Unknown	ICP-MS	2	Levresse et al., 2006
	No. 19 Skarn Vein	Tiepokeng-Wuchangping tin belt	Greisen	Primary	Sn-W	ICP-MS	8	Yuan et al., 2008
	Akçakisla	Akdagmadeni	Alkaline igneous silicate rocks	Secondary	F-base-precious	ICP-MS	4	Sasmaz et al, 2005b
	Büyükçal Tepe	Akdagmadeni	Alkaline igneous silicate rocks	Secondary	Sn-W	ICP-MS	8	Sasmaz et al, 2005b
	Solnechnoe	Qaraoba	Greisen	Primary	Sn-W	ICP-AES	1	Monecke et al., 2002
	Perda Niedda	Sardinia	Skarn	None	F	ICP-MS	1	Castorina et al., 2008
Total	6	5					24	5
Rare-metal pegmatites	White Cloud, Oregon 3	South Platte	Alkaline igneous silicate rocks	Primary	SM-F	LA-ICP-MS	4 from 26	Gagnon et al., 2003
	Bohemian Massif	Vlastějovice	Skarn	Primary	SM	INAA	13	Ackerman 2005
Total	3	2					17 from 39	2
Granite-related uranium	No. 302 Uranium Vein	Changjiang U orefield	Alkaline igneous silicate rocks	Primary	U	ICP-MS	8	Zhang et al., 2007

Primary deposit type	Deposit name	Region	Secondary deposit type	Metallic economic association	Commodity group	Analytical technique(s)	Number of analyses	Publication
	Gabbal Gattar	Gabbal Gattar	Alkaline igneous silicate rocks	Primary	U	LA-ICP-MS	7	Mahdy et al., 2014
Total	2	2					15	2
Greisen	Zinnwald Tin Deposit	Hercynian tin province	Alkaline igneous silicate rocks	Primary	Sn-W	ICP-AES	3	Monecke et al., 2002
	Ehrenfriedersdorf	Hercynian tin province	Alkaline igneous silicate rocks	Primary	Sn-W	ICP-MS	3	Monecke et al., 2000
	Qaraoba	Herzynian rare metal province	Alkaline igneous silicate rocks	Primary	Sn-W	ICP-AES	3	Monecke et al., 2002
	Aqshatau	Herzynian rare metal province	Alkaline igneous silicate rocks	Primary	Sn-W	ICP-AES	4	Monecke et al., 2002
	Kent	Herzynian rare metal province	Rare-metal pegmatite	Primary	SM	ICP-AES	4	Monecke et al., 2002
Total	5	2 (1?)					17	2
Cryolite	Ivigtut	Gardar Province	Alkaline igneous silicate rocks	Primary	Cryolite	LA-ICP-MS	8 from 64	Schönenberger et al., 2008
	Pitinga Mine	Pitinga	Greisen	Primary	Cryolite	ICP-MS	6	Minuzzi et al., 2008
Total	2	2					14 from 70	2
Intrusion-related molybdenum	Sweet Home Mine	Mosquito Range	Intrusion-related Mo	Primary	Mo	ICP-MS	12	Lüders et al., 2009
	Tumen	Qinling	Peralkaline silicate igneous rocks	Primary	Mo	ICP-MS	17	Deng et al., 2014
Total	2	2					29	2

Primary deposit type	Deposit name	Region	Secondary deposit type	Metallic economic association	Commodity group	Analytical technique(s)	Number of analyses	Publication
Hydrothermal/epithermal veins and replacements in carbonate rocks	Lanuza mine	Valle de Tena	Hydrothermal/epithermal veins and replacements in carbonate rocks	Secondary	F-base	ICP-MS, NAA	12	Subías, Fernández-Nieto, 1995
	Tebarray	Valle de Tena	Hydrothermal/epithermal veins and replacements in metamorphic rocks	Primary	Base	ICP-MS, NAA	11	Subías, Fernández-Nieto, 1995
	Tad Dere	Akdagmadeni	Hydrothermal/epithermal veins and replacements in metamorphic rocks	Secondary	F-base-precious	ICP-MS	12	Sasmaz et al., 2005b
	Monreale, Santa Lucia	Sardinia	Hydrothermal/epithermal veins and replacements in metamorphic rocks	None	F	ICP-MS	2	Castorina et al., 2008
	Multiple	Yixian F Deposit	Hydrothermal/epithermal veins and replacements in carbonate rocks	None	F	ICP-MS	5	Xiang et al., 2010
	Hanson, Chise	Chloride district	Hydrothermal/epithermal veins and replacements in carbonate rocks	Primary	Precious	INAA	2	Hill et al., 2000
	Multiple	New Mexico	Hydrothermal/epithermal veins and replacements in carbonate rocks	Primary	Base	INAA	7	Hill et al., 2000
	Hiebert, Grants	Bishop Cap	Hydrothermal/epithermal veins and replacements in carbonate rocks	Unknown	Unknown	INAA	2	Hill et al., 2000
	Ruby/Hayner	Organ Mountain	Hydrothermal/epithermal veins and replacements in carbonate rocks	Primary	Precious, Base	INAA	1	Hill et al., 2000
Total	20	8					54	5

Primary deposit type	Deposit name	Region	Secondary deposit type	Metallic economic association	Commodity group	Analytical technique(s)	Number of analyses	Publication
Hydrothermal/epithermal veins and replacements in igneous rocks	Santa Catarina	Santa Catarina	Alkaline igneous silicate rocks	None	F	ICP-MS	5	Sallet et al., 2005
	Garganta	Santa Catarina	Alkaline igneous silicate rocks	None	F	ICP-MS	13	Sallet et al., 2005
	Jaguaruna	Santa Catarina	Alkaline igneous silicate rocks	None	F	ICP-MS	2	Sallet et al., 2005
	Segunda Linha	Santa Catarina	Alkaline igneous silicate rocks	None	F	ICP-MS	3	Sallet et al., 2005
	Canela Grande	Santa Catarina	Alkaline igneous silicate rocks	None	F	ICP-MS	2	Sallet et al., 2005
	Canela Pequena	Santa Catarina	Alkaline igneous silicate rocks	None	F	ICP-MS	4	Sallet et al., 2005
	São Pedro	Santa Catarina	Alkaline igneous silicate rocks	None	F	ICP-MS	2	Sallet et al., 2005
	Multiple	Sardinia	Hydrothermal/epithermal veins and replacements in igneous rocks	None	F	ICP-MS	3	Castorina et al., 2008
	Multiple	Schwarzwald	Hydrothermal/epithermal veins and replacements in igneous rocks	Primary and None	F or base ± precious	LA-ICP-MS	19	Schwinn and Markl, 2005
	Multiple	Erzgebirge	Hydrothermal/epithermal veins and replacements in igneous rocks and greisen	Unknown and Primary	Base, Sn-W, U	ICP-MS	15	Trinkler et al., 2005
	Grebe's Nest, Iron Springs, Lawn Barite	St. Lawrence	Hydrothermal/epithermal veins and replacements in igneous rocks	None	F	LA-ICP-MS	3 from 73	Gagnon et al., 2003
	Multiple	New Mexico	Hydrothermal/epithermal veins and replacements in igneous rocks	Primary, unknown, none	Base ± precious	INAA	12	Hill et al., 2000

Primary deposit type	Deposit name	Region	Secondary deposit type	Metallic economic association	Commodity group	Analytical technique(s)	Number of analyses	Publication
	Multiple	New Mexico	Alkaline igneous silicate rocks	None	F	INAA	3	Hill et al., 2000
	Capitan Mountain	New Mexico	Alkaline igneous silicate rocks	Primary	SM	INAA	7	Hill et al., 2000
Total	68	15					93 from 163	6
Hydrothermal/epithermal veins and replacements in metamorphic rocks	Multiple	Sardinia	Hydrothermal/epithermal veins and replacements in metamorphic rocks	None	F	ICP-MS	11	Castorina et al., 2008
	Multiple	Schwarzwald	Hydrothermal/epithermal veins and replacements in metamorphic rocks	Primary and None	Base, F, Precious	LA-ICP-MS	10	Schwinn and Markl, 2005
	El Hammam	Central Variscan Massif	Hydrothermal/epithermal veins and replacements in sedimentary rocks	None	F	ICP-MS	3	Cheilletz et al., 2010
	Spruce Hill, Bonita, Long Lost Brother	Zuni Fluorospar	Hydrothermal/epithermal veins and replacements in metamorphic rocks	Unknown	Unknown	INAA	2	Hill et al., 2000
Total	25	4					27	4
Hydrothermal/epithermal veins and replacements in sedimentary rocks	Monte Cardiga	Sardinia	Hydrothermal/epithermal veins and replacements in sedimentary rocks	None	F	ICP-MS	1	Castorina et al., 2008
	Käfersteige, Dorothea	Southern Schwarzwald	Hydrothermal/epithermal veins and replacements in sedimentary rocks	Primary	Precious	LA-ICP-MS	2	Schwinn and Markl, 2005
	Clara	Southern Schwarzwald	Hydrothermal/epithermal veins and replacements in sedimentary rocks	Primary	Base	LA-ICP-MS	1	Schwinn and Markl, 2005

Primary deposit type	Deposit name	Region	Secondary deposit type	Metallic economic association	Commodity group	Analytical technique(s)	Number of analyses	Publication
	Heiligenwald, Wittenweiler, Zunsweier	Southern Schwarzwald	Hydrothermal/epithermal veins and replacements in sedimentary rocks	None	F, base-precious	LA-ICP-MS	3	Schwinn and Markl, 2005
	Gonzales East	Socorro Area	Hydrothermal/epithermal veins and replacements in sedimentary rocks	None	F	INAA	1	Hill et al., 2000
Total	8	3					8	3

Table A.2

Table A-2 Summary of hydrothermal/epithermal vein and replacement deposits hosted in carbonate, igneous, metamorphic, or sedimentary host rocks. Host rocks and potentially related heat/fluid sources or events are listed under "intrusion." Commodity lists the elements of economic interest at each deposit, while group represents the commodity groups used to characterize the deposits compiled within this study. N represents the number of compiled data analyses for each deposit and totals for deposits, regions, data analyses and publications are listed for each hydrothermal/epithermal vein and replacement deposit host rock group, as well as totals for all host rock types together.

Hydrothermal/epithermal veins and replacements hosted in…	Deposit Name(s)	Region	Secondary Deposit type	Host Rocks	Intrusion	Commodity/Group		Number of analyses	Publication
…carbonate host rocks	Lanuza Mine	Valle de Tena	…carbonate rocks	limestones with rare calcite and dolomite layers	diabase dikes	F-(Cu)	F-Base	12	Subías, Fernández-Nieto, 1995
	Tebarray	Valle de Tena	…metamorphic rocks	marbles with rare calcite and dolomite layers	Permian diabase dikes	Zn-F-(Pb)	Base	11	Subías, Fernández-Nieto, 1995
	Tad Dere	Akdagmadeni	…metamorphic rocks	marble, mica schist, and gneiss		F-Pb-Zn-Ag-(Cu)	F-Base	12	Sasmaz et al, 2005b

	Santa Lucia	Sardinia	…metamorphic rocks	limestones and dolomitic limestons, siliclastic metasedimentary rocks	Variscan uplift	F	F	1	Castorina et al., 2008
	Monreale	Sardinia	…metamorphic rocks	metalimestones, siliclastic metasedimentary rocks	Variscan uplift	F	F	1	Castorina et al., 2008
	Saobaotun, Liulongtai, Laohudong, Toadoahexiang	Yixian F Deposit	….carbonate rocks	carbonates	basalt, andesite, volcaniclastics, basanite, trachybasalt, basalt, basaltic andesite, andesite, rhyolite	F	F	5	Xiang et al., 2010
	Hanson, Chise	Chloride District	…carbonate rocks	limestone		Ag, Au	Precious	2	Hill et al., 2000
	Gonzales West	Socorro area	…igneous rocks	limestone, granite	granite	Pb	Base	1	Hill et al., 2000
	Marion	Sierra Caballo	…igneous rocks	limestone, granite	granite	Cu	Base	1	Hill et al., 2000
	Hardin, Cox	Sierra Caballo	…carbonate rocks	limestone		Pb, W, V	Base	2	Hill et al., 2000
	Nakaye, Esperanza	Sierra Caballo	…carbonate rocks	limestone		Pb, Zn, Ag, Cu	Base	2	Hill et al., 2000
	Hiebert, Grants	Bishop Cap	…carbonate rocks	limestone				2	Hill et al., 2000
(…carbonate rocks)	Ruby/Hayner	Organ Mountain	…carbonate rocks	limestone		Ag, Zn, Pb	Precious, Base	1	Hill et al., 2000
Total	20	8						54	5

…igneous host rocks	Santa Catarina	Santa Catarina	Alkaline igneous silicate rocks	granites, overlying coal-bearing sediments, and basaltic feeder dykes to Parana basin	leucocratic, alkaline, biotite-F granite	F	F	5	Sallet et al., 2005
	Garganta	Santa Catarina	Alkaline igneous silicate rocks	granites, overlying coal-bearing sediments, and basaltic feeder dykes to Parana basin	leucocratic biotite-hornblende, subalkaline-monzonitic granite	F	F	13	Sallet et al., 2005
	Jaguarana, Segunda Linha Torrens, Canela Grande, Canela Pequena, São Pedro	Santa Catarina	Alkaline igneous silicate rocks	granites, overlying coal-bearing sediments, and basaltic feeder dykes to Parana basin	leucocratic biotite-hornblende, subalkaline-monzonitic granite	F	F	13	Sallet et al., 2005
	Monte Grighini	Sardinia	…igneous rocks	rhyolite	Variscan uplift	F	F	1	Castorina et al., 2008
	Nuraghe Onigu	Sardinia	…igneous rocks	rhyolitic and basaltic (dacitic?) tuffs	Variscan uplift	F	F	1	Castorina et al., 2008
	Monte Genis	Sardinia	…igneous rocks	Multistage/remobilized deposit in leucogranite, originally hosted by metasedimentary rocks	Variscan uplift and granitoid emplacment	F	F	1	Castorina et al., 2008
	Friedenweiler, Hesselback, Ödsbach, Ilse i. Kaltbrunn, Daniel Gallen-back, Neubergmännisch Glück, Southern Reinerzau Valley, Johann	South and Central Schwarzwald	…igneous rocks	granite		Cu-Bi	Base	8	Schwinn and Markl, 2005

	Bleilersgrund, Burgfelsen, Ohlsback, Schlechthalde, Tennenbronn	S. Schwarzwald	…igneous rocks	granite		F	F	5	Schwinn and Markl, 2005
	König	Central Schwarzwald	…igneous rocks	granite		Cu-Bi-Co	Base	1	Schwinn and Markl, 2005
	Hilfe Gottes, Herzog Friedrich	Central and South Schwarzwald	…igneous rocks	granite		Co-U±Bi±Ag	Base	2	Schwinn and Markl, 2005
	Sophia, Neuglück	Central Schwarzwald	…igneous rocks	granite		Co-Ni-Ag-Bi-U	Base	2	Schwinn and Markl, 2005
	Hohberg	S. Schwarzwald	…igneous rocks	granite		Fe-(Pb)-(Ag)	Base	1	Schwinn and Markl, 2005
	Multiple	Erzgebirge	…igneous rocks	granite	Post Variscan (granites?)	Ba-Sr, Bi-Co-Ni-As-Ag, Ge-Hg, Fe-Mn	Base	12	Trinkler et al., 2005
	Ehrenfriedersdorf	Erzgebirge	…igneous rocks	granite	Post Variscan (granites?)	Sn	Sn-W	1	Trinkler et al., 2005
	Pöhla-Tellerhäuser U mine	Pöhla, near Schwarzenberg	…igneous rocks	granite	Post Variscan (granites?)	U	U	2	Trinkler et al., 2005
	Grebe's Nest	St. Lawerence	Alkaline?	porphyry dikes	St. Lawrence granite	F	F	1	Gagnon et al., 2003
	Iron Springs	St. Lawerence	Alkaline?	granite	St. Lawrence granite	F	F	1	Gagnon et al., 2003

	Lawn Barite	St. Lawerence	Alkaline?	"host rocks"	St. Lawrence granite	F	F	1	Gagnon et al., 2003
	Lemitar	Socorro area	…igneous rocks	granite		Pb, Zn, W	Base	1	Hill et al., 2000
	Independence	Sierra Caballo	…igneous rocks	granite		Cu	Base	1	Hill et al., 2000
	Greenleaf, Green Spar	Fluorite Ridge	…igneous rocks	granodiorite porphyry		F	F	2	Hill et al., 2000
	Sadler	Fluorite Ridge	Alkaline igneous silicate rocks	monzonite porhpyry		F	F	1	Hill et al., 2000
	Lucky, Gratten	Fluorite Ridge	…igneous rocks	andesite		F	F	2	Hill et al., 2000
	Animas	Animsas district	…igneous rocks	rhyolite porhpyry				1	Hill et al., 2000
	Fluorite Group	Lordsburg	…igneous rocks	basalt		Cu, Au	Base	1	Hill et al., 2000
	Lonestar	Lordsburg	…igneous rocks	granodiorite		Cu, Au	Base	1	Hill et al., 2000
	Spar Hill, Shrine	Big Burro Mountains	…igneous rocks	granite, rhyolite				2	Hill et al., 2000
	Foster, Clum	Gila Fluorospar	Alkaline igneous silicate rocks	trachitic latite		F	F	2	Hill et al., 2000
	Goat Camp Spring	Steeple Rock	…igneous rocks	andesite		Cu, Au, Ag	Base	1	Hill et al., 2000
(…igneous rocks)	Multiple	Capitan Mountains	Alkaline igneous silicate rocks	alkali granite		Th, REE	SM	7	Hill et al., 2000

Total	68	15						93	6
…metamorphic host rocks	Multiple	Sardinia	…sedimentary rocks	siliclastic metasedimentary rocks	Variscan uplift	F	F	6	Castorina et al., 2008
	Multiple	Sardinia	…igneous rocks	metavolcanites, siliclatic metasedimentary rocks	Variscan uplift	F	F	5	Castorina et al., 2008
	Drey	Central Schwarzwald	…metamorphic rocks	gneiss		F	F	1	Schwinn and Markl, 2005
	Erzengel Gabriel, Laßgrund	S. Schwarzwald	…metamorphic rocks	gneiss		Pb	Base	2	Schwinn and Markl, 2005
	Barbara, Segen Gottes, Fortuna Gelbach	Central Schwarzwald	…metamorphic rocks	gneiss		Pb±Zn± Ag	Base	3	Schwinn and Markl, 2005
	Artenberg quarry	Central Schwarzwald	…metamorphic rocks	gneiss		Cu-As	Base	1	Schwinn and Markl, 2005
	Wenzel	S. Schwarzwald	…metamorphic rocks	gneiss		Ag-Sb	Precious	1	Schwinn and Markl, 2005
	Ludwigs Trost	Central Schwarzwald	…metamorphic rocks	gneiss		Fe-(Pb)-(Ag)	Base	1	Schwinn and Markl, 2005
	El Hammam	Central Variscan Massif	…sedimentary rocks	limestones, schists and siltstones	evolved, peraluminous granite, dolerite, microgranite, rhyolite dikes	F	F	3	Gagnon et al., 2003

	Long Lost Brother	Big Burro Mountains	…metamorphic rocks	gneiss				1	Hill et al., 2000
(…metamorphic rocks)	Spruce Hill, Bonita	Zuni Fluorospar	…metamorphic rocks	granitic gneiss				2	Hill et al., 2000
Total	24	5						26	4
…sedimentary host rocks	Monte Cardiga	Sardinia	…sedimentary rocks	arkoses	Oligoceine-Miocene volcanism	F	F	1	Castorina et al., 2008
	Heiligenwald, Zunsweier, Wittenweiler	S. Schwarzwald	…sedimentary rocks	sandstone, sediments		F	F	4	Schwinn and Markl, 2005
	Dorothea, Käfersteige, Clara	South and Central Schwarzwald	…sedimentary rocks	sandstone, sediments		Ag-Cu±Bi	Precious, Base	3	Schwinn and Markl, 2005
(…sedimentary rocks)	Gonzales East	Socorro area	…sedimentary rocks	siliclastics		F	F	1	Schwinn and Markl, 2005
Total	8	3						8	3
Totals for all host rocks:	120	22						180	10

Appendix B.

Summaries of compiled primary mineralization environments

Summaries of deposits included within this study are provided here and are based primarily on information provided within source publications. These are sorted according to established primary deposit types. All compiled data herein is assumed to be accurate and true.

Peralkaline silicate igneous rocks

Fluorite data included in this category is sourced from the Gardar Province in South Greenland, (Schönenberger et al., 2008), and the Gallinas Mountains alkaline complex in New Mexico, USA, (Gagnon et al., 2003).

Fluorite data from the Gardar Province includes 167 LA-ICPMS analyses from two complexes that are enriched in HFSE, REE and Be. The Motzfeldt complex consists of five phases of peralkaline miaskitic rocks and one phase of agpaitic rock, which according to Sørensen, (1997), is peralkaline nepheline syenite or phonolite containing complex with Zr, Ti, and REE silicates and a high concentration of volatiles such as F and Cl. Within the Motzfeldt complex, fluorite occurs as a primary magmatic phase and as late- to post-magmatic fluorite±calcite veins. The Ilímaussaq complex consists of four magmatic batches of miaskitic augite syenite, alkali granite, and a succession of agpaitic rocks of roof cumulates (naujaites), and floor cumulates (kakortokites), where fluorite and villiaumite occur as primary magmatic phases and as late hydrothermal veins and pegmatites.

Data for fluorite from the Gallinas Mountains complex (Gagnon et al., 2003) includes three averaged samples from the Pinatosa deposit, a fluorite-matrix breccia hosted by quartz syenite, analyzed by LA-ICPMS. It's proposed by Williams-Jones et al., (2000) that progressive mixing of formational and magmatic waters caused this brecciation with three generations of fluorite occurring with bastnäsite, quartz, barite, calcite, pyrite and hematite.

Carbonatite related deposits

Data contained within this compilation for fluorite deposits related to carbonatites include the Speewah fluorite deposit in Western Australia (Alvin et al., 2003) of possible carbohydrothermal origin associated with the Yungul calciocarbonatite dike, the Okorusu calciocarbonatite in Namibia (Bühn et al., 2003), the Amba Dongar hydrothermal fluorite (±REE) deposit related to late stages of sövite-ankerite emplacement (Palmer 1994; Doroshkevich et al., 2009), and the Mato Preto alkaline complex in Brazil (Ventura Santos et al., 1996) consisting of magnesio-ankeritic carbonatite and calciocarbonatite with associated fenitized syenites, and phonolites. Carbonatites mined for REEs include those of the Panxi Region, China, (Xu et al., 2012) including the Maoniuping, Lizhuang, and Daluxiang (±Ba) deposits, as well as the carbonate-replacement style deposits at Bayan Obo (±Fe ±Nb), Sichuan, China, (Xu et al., 2012), and the possibly metasomatically replaced Rock Canyon Creek/Deep Purple (F±REE±Nb) deposit in British Columbia, Canada, (Gagnon et al., 2003).

The Speewah fluorite deposit in Western Australia (Alvin et al., 2003) of possible carbohydrothermal origin is associated with the Yungul calciocarbonatite dike that intruded the Hart Dolerite sill, which consists of tholeiitic dolerite, tholeiitic gabbro, and magnetite±olivine gabbro with granophyres and granitoids. Fluorite associated with this region is found in coarse-grained veins composed of quartz±adularia±fluorite±calcite that are related to siliceous, fluidized-breccia dikes containing lithic fragments of quartz and potassic-feldspar in a fine-grained matrix of quartz, potassic-feldspar, minor fluorite, calcite, barite, galena, and chalcopyrite. The main fluorite deposits however, are composed of epithermal veins of fluorite, bladed quartz, and adularia, (Gwalani et al., 2010). Seven analyses of REE in fluorite taken by ICPMS are from the Speewah deposit, presumably from the epithermal veins, (Alvin et al., 2003).

The Okorusu carbonatite complex consists of Cretaceous rift-related alkaline silicate igneous rocks and carbonatites emplaced into the Pan-African Damara System of schists, marbles, conglomerates, and micaceous and calcareous quartzites. Fluorite mineralization occurs within high-grade fenitization of the Damara marbles, calc-silicate rocks, and schists, producing alkali clinopyroxene, calcite, apatite, biotite, magnetite, titanite, sodic amphibole,

feldspar, and melanite, due to intrusion by a calciocarbonatite consisting of calcite, accessory apatite, quartz and feldspars. Fluorite occurs either as replacements and disseminations or as massive veins in the fenitized wallrocks, or as well-defined veins displaying comb textures and coarse banding. Data from this locality includes 35 analyses done by ICPMS, (Bühn et al., 2003).

The Amba Dongar fluorite±REE deposit of Baroda, India is intimately associated with the final stages of mineralization by a sövitic and ankeritic carbonatite ring complex hosted within Deccan flood basalts and Bagh sandstone-orthoquartzite (Doroshkevich et al., 2009; Palmer 1994). Doroshkevich et al., (2009) describes the formation of this deposit as: the intrusion of nephilinite and phonolite followed by brecciation by calcic-carbonatite which continued into multiple pulses of sövite intrusion followed by intrusion of plugs and dikes of siderite-containing ankerite, with final hydrothermal pulses of silica replacement and subsequent fluorite deposition. Fenitization is described by Viladkar (1986) as being sodic at depth and potassic at shallower levels, which occurred during the intrusion of sövite. Palmer (1994) describes fluorite formation as a result of the interaction between final orthomagmatic fluids of carbonatite formation with Ca-rich, meteoric fluids from the Bagh sandstone. Fluorite is the primary commodity at this deposit and occurs as early blue and purple, later white, and final yellow and clear subhedral to euhedral crystals in veins and vugs. Doroshkevich et al., 2009, however describes mineralization of REE minerals including fluoro-carbonates and others (florencite-(Ce), bastnäsite, parasite, synchysite, and monazite) during late-stage carbonatite mineralization and during minor to major hydrothermal overprinting. Final geologic activity in the area covered the central portion of the carbonatite ring complex in basalt in addition to the intrusion of basaltic and picritic dikes in the vicinity (Doroshkevich et al., 2009; Palmer 1994). Seven REE neutron activation analyses of fluorite samples from the Amba Dongar hydrothermal fluorite, carbonatite deposit were compiled in this study from Palmer (1994).

The Mato Preto alkaline complex is a part of the Arco de Ponta Grossa Alkaline province in Brazil occurring along the Moroo Agudo Fault Zone, which forms a contact between Açunguí metasedimentary rocks and Três Córregos granite. This complex consists of magnesio-ankeritic carbonatite and calciocarbonatite that occur as dikes, plugs, and

breccia matrix intruded into fenitized syenites, and phonolites. Fluorite at Mato Preto occurs in four lenses in four main generations consisting of black, purple, remobilized, and microcrystalline fluorite, hosted within fenitized phonolite and tinguaite dikes that are contained within carbonatite and breccia bodies. Twelve (ICPMS?) analyses on fluorite are included within this dataset, (Ventura Santos et al., 1996)

The Maoniuping and Lizhuang REE deposits consist of carbonatite sills, dykes and stocks intruded into syenites emplaced in Proterozoic crystalline basement and Paleozoic-Mesozoic metasedimentary sequences. Fluorite, the commonest gangue mineral at Maoniuping, occurs in NE-SW trending REE-vein and pegmatitic vein systems hosted by argillaceous clastic sediments, limestones, Tertiary talus, Cretaceous granite, syenite-carbonatite, and a Mesozoic rhyolite. According to the map provided in Xu et al., 2012, the REE-rich vein systems occur as structurally controlled late stage alteration features parallel to a carbonatite body, hosted dominantly within syenite. The carbonatite body as well as a late plug of syenite, cut ore veins. Ore veins consist of pegmatitic barite veins (pegmatitic bastnäsite-aegirine augite-fluorite-barite), pegmatitic calcite veins (pegmatitic bastnäsite-fluorite-barite-calcite), and thread veins (bastnäsite-aegirine augite-barite-calcite-fluorite). Fluorite data from Maoniuping includes 20 analyses, (Xu et al., 2012).

Four types of ore are recognized in the Lizhuang deposit expressed as small lenses and veins within syenite and carbonatite that intruded low to medium grade metamorphosed carbonate and arenaceous-pelitic sediments. Fluorite occurs in disseminated, banded, and stockwork orebodies consisting of fluorite-barite-bastnäsite±calcite±biotite±quartz. The map pattern offered by Xu et al., 2012 suggests REE ore mineralization preceded intrusion of the carbonatite hosted within syenite, and continued post carbonatitic intrusion cutting carbonatite. Fluorite data from Lizhuang includes 7 analyses, (Xu et al., 2012).

REE±Ba orebodies at Daluxiang occur as lentoid veins, thread veins and stockworks primarily within syenite, and within breccia pipes hosted within a syenite-carbonatite complex that intruded a Proterozoic quartz diorite. Fluorite occurs within pegmatitic or thread veins consisting of bastnäsite-aegirine augite-fluorite-(strontio)barite ±celestine ±calcite and 13 ICPMS analyses of REE contents in samples of fluorite are included within this

study, (Xu et al., 2012). Based on the map patterns offered by Xu et al., 2012, the lentoid REE deposits at Daluxiang are free of any structural controls hosted dominantly within syenite. The syenite also hosts a minor plug of carbonatite approximately 200 m away from the main orebodies. Though the orebodies at Daluxiang are hosted primarily within syenite, they share a similar cross-cutting relationship following a weak orientation with the associated carbonatite, offering the best candidate as an intrusive relative. For this reason, the orebodies at Daluxiang have been classified as carbonatite-related. Fluorite data from Daluxiang includes 13 analyses, (Xu et al., 2012).

The Bayan Obo deposit is located approximately 1000 km NE of the Panxi Region, located near the border with Mongolia. This deposit consists of nine categories of orebodies, none of which are associated with syenite and only two of which include fluorite: massive and banded fluorite-magnetite-REE ore, and banded fluorite-magnetite-bastnäsite ore. Ore bodies without fluorite include disseminated aegirine-magnetite-REE ore, disseminated arfvedsonite-phlogopite-muscovite-magnetite-REE ore, disseminated dolomite-magnetite-REE ore, disseminated and partly banded aegirine-REE ore, disseminated and partly banded diopside-phlogopite-REE ore, disseminated biotite-magnetite-REE ore. These deposits are replacement bodies hosted predominantly within a dolomite-calcite marble overlain by black shale, slate and schist located adjacent to abundant carbonatite dykes intruded within the same metasediments. Fluorite data includes 11 analyses for Bayan Obo all done by ICMPS, (Xu et al, 2012).

The fluorite-REE±Nb Rock Canyon Creek/Deep Purple deposit in British Columbia is similar to the Bayan Obo deposit in that it occurs as a strata-parallel replacement body within limestone and dolomite. However, unlike at Bayan Obo, there are no known occurrences of adjacent peralkaline or carbonatititc intrusions. Fluorite data includes two averaged LA-ICPMS analyses from breccia matrix, veins, and disseminations that occur with synchysite, parasite, barite, quartz, carbonate, pyrochlore, and Nb-rutile (Gagnon et al., 2003).

Mississippi Valley Type (MVT) deposits

Fluorite data included within this category comes from two well-known fluorite MVT deposits known for exquisite fluorite hand specimens, namely the mines of the South and North Pennine Orefields, England, (Bau et al., 2003) and the Berbes, La Collada, and Villabona fluorite districts of Asturias, Spain (Sánchez et al., 2010), as well as other MVT style fluorite deposits such as Jebel Stah in north-eastern Tunisia, (Souissi et al., 2010), and the Pb-F-Ba MVT deposits of the Hansonburg mining district, New Mexico (Putnam III et al., 1986; Hill et al., 2000). Three other fluorite deposits are included in this set for which categorizing these as a true MVTs may be disputable. These include an epigenetic carbonate replacement fluorite deposit in a thrust zone in Çelikhan, Adiyaman, Eastern Turkey, (Sasmaz et al., 2005a), the fluorite deposits of MVT or manto origin at La Encantada, Mexico (González-Partida et al., 2002; Levresse et al., 2006) and the F±Cu±Zn±Pb deposits of the Valle de Tena region of the Spanish West Pyrenees of possible manto-style origin, (Subías, Fernández-Nieto, 1995). Commodities at these deposits include the following: F, Pb, Ag from the South Pennine Orefield; F from Asturias, Spain; F-(Ba-Pb-Zn) from the Jebel Stah district, Tunisia; Pb-Zn-Ag from the Hansonburg district, NM; F and nearby Pb-Zn at Çelikhan, Adiyaman, Turkey, and F from the Portalet MVT/manto deposit of the Valle de Tena district, Spain.

The South Pennine Orefields are famous for their fluorite hand specimens, particularly the "Blue John" fluorite found within one of the districts. Historically however, districts of the South Pennines have been mined for fluorospar, fluorite hand specimens, galena, and possibly for silver during Roman times, (Jones, 2006). The South Pennine Orefield is located within the Derbyshire Dome in central England, hosted within platform carbonates interbedded with basic lavas and tuffs, chert and dolomite, underlain by Lower Paleozoic or Precambrain basement rocks, (Bau et al., 2003). Ore mineralization consists primarily of fluorite and galena, with lesser sphalerite, chalcopyrite, and pyrite as "rakes, scrins, flats, and pipes." Calcite is a common gangue mineral. The North Pennine Orefields differ from the South Pennines in that quartz is more abundant, REE geochemical patterns differ significantly, and Rb-Sr data and Sr and Nd isotopes suggest a different timing of mineralization. Sources of fluids for both districts are debated but the North Pennine Orefield is suggested to have an alkaline magmatic influence and source of fluorine while the source

of fluorine for the South Pennine Orefield is proposed from evaporated seawater and/or Namurian shales (Kendrick et al., 2002 from Bau et al., 2003). The districts within the South Pennine Orefield vary morphologically and minerallogically with formations occurring in the Carboniferous and others as episodes throughout the Permian (Ewbank et al., 1995; Ineson and Mitchel 1972; Dunham 1983 from Bau et al., 2003). Thirty-eight analyses on fluorite trace element geochemistry taken by ICP-MS are compiled within this study from the Treak Cliff Caverns, Treak Cliff Castelton, Dirtlow open-pit, Mitchell Bank, Lady Walsh Mine, and Smalldale & Pindale districts, while nine are compiled for the North Pennines from the Frazer's Hush mine, (Bau et al., 2003).

Fluorite data from Asturias, Spain comes from the Berbes, La Collada, and Villabona districts whereas of 2010, the most important active mines were located, (Sánchez et al., 2010). Mineralization within this deposit consists of fluorite, quartz, barite, calcite, dolomite and minor pyrite, marcasite, galena, and chalcopyrite. Silicification and local chloritization was followed by fluoritization with local coeval silicification, followed by silicification, carbonitization, with a final phase of barite and quartz mineralization. The Berbes district consists of ore vein mineralization in Variscan-folded Carboniferous limestones and stratabound bodies within silicified Permo-Triassic conglomeratic breccia that unconformably overlies the aforementioned limestone. Brecciation volume is greatest adjacent to faults and mineralization is contained within the breccia as replacements. Fluorite occurs as cm to meter thick veins and dissolution cavities as well as local clast replacement. Within La Collada, fluorite occurs as vein and stratabound bodies hosted within Permo-Triassic marls and sandstones. Fluorite deposits at Villabona are predominantly stratabound and fault controlled, hosted within silicified Permo-Triassic carbonates that overlie basement rocks of Devonian shales, sandstones, limestones, and local Carboniferous, coal-bearing basement. REE analyses from fluorite from this deposit include five analyses each from Berbes, La Collada, and Villabona totaling 15 representing the deposit taken by ICP-MS methods, (Sánchez et al., 2010). The authors concluded the chemical compositions of fluorites from the various deposits were heavily influenced by host rock compositions.

Fluorite from the Jebel Stah district within the Zaghouan F-(Ba-Pb-Zn) deposit in north-eastern Tunisia occur within stratabound and/or stratiform ore bodies and cross

cutting veins hosted within silicified and dolomitized Jurassic reef limestones. Ores at Jebel Stah consist of fluorite and calcite with minor sphalerite, galena, barite, celestite, malachite, azurite, siderite, ankerite, and quartz. Ore variability within these deposits appears to be resultant of differences in host rock composition and formation. Specifically, fluorite generations occurred first as replacement clusters in the dolomotized reef limestone of the Oust Formation and the Carixian fossiliferous phosphatic limestone layer, and as intrakarst, finely laminated deposits, consisting of microgranular fluorite, relict dolomite, calcite, and apatite, glauconite, and authigenic quartz with rare sphalerite, galena and pyrite. Next, fluorite recrystallized the earlier generation as macrogranular fluorite forming banded, stratabound deposits within the Carixian layer. Fluorite also mineralized open space fillings within extensional faults cutting the Liassic series and hanging wall marls with coeval replacement of carbonates. Final fluorite mineralization occurred as smaller open space fillings within solution cavities of the Carixian layer. Thirteen analyses taken by ICP-MS on fluorite for REE content are included from the Jebel Stah fluorite deposit, (Souissi et al., 2010).

The Hansonburg mining district including the Ora, Royal Flush, and MexTex Pb-Zn-Ag deposits consisting of qtz-fl-ba-cal-gn-sp mineralization (Hill et al., 2000) occurring in karsts along bedding irregularities of Pennsylvanian reef limestone adjacent to high-angle reverse faults have been described by Putnam III et al., 1983 as an MVT district. This is based on the grounds that deposits within the district are of consistent mineralization style (dolomitization and silicification followed by replacement by galena and barite, and layered galena, barite, fluorite, quartz mineralization with minor sphalerite, and late pyrite and chalcopyrite) and fluid inclusion data supports formation by low-moderate temperature (130-210° C) low-moderately saline (10-18 eq. wt% NaCl) fluids with chemistries similar to other MVT-style deposits. Five REE and trace element analyses on fluorite from these deposits taken by INAA were compiled from Hill et al., 2000.

The Çelikhan fluorite deposits of Adiyaman, Turkey occur as fracture fills and replacement bodies hosted within the Kalecik Limestone footwall of a thrust zone between these limestones and the Pinarbasi Formation hanging wall. Lithologies within this area found stratigraphically between these two formations include: marble, limestone, dolomitic limestone, mica-schist and calc schist. Many thrust zones exist within the greater Adiyaman

area but only the zone between the Pinarbasi formation and Kalecik limestone is host to fluorite deposits. This zone also contains Pb-Zn mineralization farther to the west. Fluorite deposition, which occurs as replacement pockets and disseminations in zones up to 5 m thick, and coeval alteration that precipitated quartz, carbonate, barite and kaolinite occurred as a single hydrothermal event, (Sasmaz et al., 2005a). The authors (Sasmaz et al., 2004), do not explicitly describe the Çelikhan fluorite deposit as a district of MVT mineralization, but do suggest the formation of these fluorite deposits were unrelated to magmatic activity. This combined with tectonic setting, as these deposits are hosted within thrust-zone limestone, and associated districts of Pb-Zn mineralization suggest the Çelikhan fluorite deposits may be of MVT style mineralization. Fifteen analyses for REE content in fluorite taken by ICP-MS are contained therein, (Sasmaz et al., 2004).

La Encantada mining district produces high-grade fluorite hosted in lower Cretaceous reef limestone capped by upper Cretaceous shales. These deposits consist of stratiform beds, veins and stockworks and fluorite contains petroleum-rich inclusions which suggest MVT-style mineralization, though the deposits are located proximal to rhyolitic domes which may suggest otherwise (González-Partida et al., 2002). Two ICP-MS analyses of REEs on samples of fluorite were compiled from Levresse et al., 2006 who suggested a possible manto-style formation model for the deposit.

Fluorite found in the Valle de Tena area, Huesca, Spanish Pyrenees mountains are included in three types of deposits that have been mined for lead, silver, and fluorite: F-(Cu) veins hosted by Devonian limestones at the Lanuza mine; Zn-F-(Pb) veins hosted in Devonian marbles at Tebarray; and fluorite pockets, bands, nodules, and veins found within Carboniferous limestones of the Portalet mines of possible manto-MVT-style mineralization. The vein deposits at Lanuza and Tebarray have been named by this author as vein deposits hosted in carbonate to be discussed later. Fluorite mineralization at Portalet is described by the authors, Subías, Fernández-Nieto, 1995, as analogous with MVT-style mineralization since textures contained within consist of breccias, zebra ores, nodules, paleokarst replacements, and steeply dipping veins. Fluorite mineralization is preceded by intense silicification however, and a deposit model that may be more befitting to Portalet is manto-style mineralization. Here, quartz and disseminated fluorite and donbassite (a Cl mineral?)

were deposited followed by coarse to very coarse quartz and rare pyrite associated with donbassite, followed finally by fluorite and sparry calcite with rare siderite, (Subías, Fernández-Nieto, 1995). No He isotope data quoted. Thirty-one samples of fluorite were analyzed by ICP-MS for REEs from the Portalet mine of the Valle de Tena district and compiled within this study.

Sedimentary Exhalative (SEDEX) deposits

Fluorite found within the stratabound to stratiform Pb-Zn deposits of the Nördliche Kalkalpen is described by Schneider et al., 1975 as occurring in three generations consisting of sedimentary to hydrothermal structures hosted within Mid-Triassic carbonate rocks. The fluorite within this region occurs within a possible carbonaceous back reef lagoonal facies that also contains other evidence of evaporites such as anhydrite and celestite along with sulfide ores and minor quartz, all mixed with carbonates (including dolomites) and some bituminous or argillaceous matter. Generation I fluorite represents "synsedimentary to diagenetic" fine grained fluorite that occurs in dark colored stratiform layers and lenses with bituminous and argillaceous matter and fine-grained sulfide ores. Fluorite in this generation "is concentrated in rhythmic and graded bedding" consisting of thin laminations, cross bedding, and slumping. Generation II fluorite appears to be in-situ recrystallized fluorite from Generation I leading to increased crystal size with rim patterns. Generation III fluorite is clear to white or light violet or brown in color and fills veins, vugs, and replacement bodies. The authors cited the evidence of sedimentary structures as well as the placement of fluorite REE analysis data on a Tb/La vs. Tb/Ca diagram to determine a sedimentary/diagenetic origin for these deposits, though by modern classification, the description of these deposits could qualify it as a SEDEX or an MVT deposit. Additionally, the Tb/La vs Tb/Ca diagram by Jacob et al., 1975 and Möller 1975 may not depict accurate data fields which will be analyzed within this thesis. 30 REE analyses on fluorite taken by instrumental activation analysis (INAA) employing Ge (Li) detectors were compiled from samples taken from 12 deposits in the Nördliche Kalkalpen district.

Iron Oxide Copper Gold (IOCG) deposits

Data from only one IOCG deposit, the Lala Fe-Cu-REE deposit from the Kangding region, Sichuan, China (Huang et al., 2014) was compiled within this study consisting of nine fluorite analyses on multiple generations of fluorite. Ores at this deposit include Cu, Mo, Co, REE, Au, and Ag contained within magnetite, chalcopyrite, pyrite, molybdenite, REE, native gold and silver, with potassic-feldspar, albite, quartz, fluorite, biotite, and calcite gangue minerals. Ore bodies are lentoid, stratabound, and are structurally controlled. Mineralization is proposed to have occurred in three events including marine volcanic eruption, metamorphic mineralization of metallic ores, and hydrothermal mineralization related to the intrusion of a gabbro. Fluorite mineralization is proposed to have occurred during the second stage of mineralization as intergrowths with chalcopyrite and molybdenite in veins and massive ores. Additionally, purple fluorite mineralized during hydrothermal veining with calcite, cutting ore bodies, (Huang et al., 2014; Li et al., 2002) The formation model proposed for the Lala deposit does not represent the typical CO_2, volatile, carbonate and REE-enriched, oxidized diatreme breccia models related to mantle plumes for IOCGs and therefore may not represent the desired REE geochemical character for this deposit type. Also, paragenetical distinctions were not made for the fluorite samples compiled from this publication, (Huang et al., 2014).

Skarn deposits

REE compositions of skarn fluorite were compiled from the El Pilote fluorite deposit, northern Mexico, (Levresse et al., 2006), the No. 19 skarn vein of the Tiepokeng-Wuchangping tin belt of the Bailashui deposit, Hunan, China, (Yuan et al., 2008), the fluorite-skarn of Perda Niedda, Sardinia, Italy (Castorina et al., 2008), and the fluorite deposits within epidote-exoskarn in the Büyükçal Tepe and the fluorite-sulfide bodies within garnet-epidote skarns of the Akçakislan alkaline pluton of the Akdagmadeni region in Yozgat, Central Turkey, (Sasmaz et al., 2005b).

Northern Mexico is famous for extensive fluorite mineralization that has historically been attributed to the formation of felsic granitic intrusions and volcanism. Recently,

however, MVT-style mineralization has been used to selectively contest these explanations with one such example, the La Encantada district. Within the La Encantada district however, fluorite mineralization also occurs in the well-defined El-Pilote rhyolitic-stock-related skarn, hosted within Aurora reef limestones. This deposit is inarguably a skarn, consisting of an andradite, wollastonite, calcite, fluorite endoskarn, a recrystallized calcite, fluorite, wollastonite/enstatite, andradite/grossular, spurrite, rankinite, albite, ankerite, ilvaite exoskarn, and a foliated manganiferous marble aureole. Retrograde fluorite veins cross-cut the deposit associated with propylitic alteration consisting of tremolite and sericite. Trace element analyses taken by ICP-MS on two fluorite samples from El Pilote are included within this compilation, (Levresse et al., 2006).

Located in the Furong ore field of the Hunan Province, China, the No. 19 skarn vein of the Tiepokeng-Wuchangping tin belt of the Bailushui deposit is controlled by a series of faults hosted within Permian Qixia Formation carbonate rocks adjacent to the Qitianling granitic pluton. This vein contains disseminated, banded, and massive ores of cassiterite with minor amounts of magnetite, chalcopyrite, galena, sphalerite, scheelite, and bismuthinite, with additional gangue minerals of tremolite, diopside, and quartz, (Yuan et al, 2008). Fluorite mineralized as disseminated and massive aggregates within skarn ores, and eight analyses of REE in fluorite by ICPMS were compiled from Yuan et al., 2008. This deposit shares many features with what could be described as a greisen deposit.

Sardinia, Italy is home to one of Europe's largest fluorite districts. These deposits include karst and lens deposits hosted in metasediments and vein deposits hosted within felsic volcanics. Fluorite appears to have been sourced from felsic volcanic rocks throughout the region and was remobilized by tectonic activity, including but not limited to, Variscan orogeny and granitic intrusions. Within this fluorite district exists a fluorite-skarn deposit hosted within Cambrian metalimestones. The Perda Niedda skarn deposit consists of fluorite, diopside, wollastonite, garnet, quartz, magnetite and lesser hematite, pyrite, galena, and sphalerite whose formation is related to intrusion of Variscan granite. One sample of fluorite analyzed for REE by ICP-MS analysis from the Perda Niedda skarn was compiled from Castorina et al., 2008.

The Akdagmadeni region of central Turkey is home to several fluorite and fluorite-bearing Pb-Zn-Ag-(Cu) deposits including the Tad Dere vein deposit, the epidote-skarn hosted Büyükçal Tepe, and the garnet-epidote skarns of the Akçakisla pluton. Of these, only the latter two can be classified as skarn deposits, while Tad Dere may be classified as a vein deposit hosted in carbonate rocks to be discussed later [or omit]. Epidote-exoskarn deposits of Büyükçal Tepe occur as massive or disseminated zones of fluorite including scheelite, hosted in marble, mica schist, and gneiss. The associated granitoid at Büyükçal Tepe is not specifically named by the authors but could consist of granite, quartz monzonite, quartz syenite, or syenite. Fluorite mineralization at Akçakisla consists of massive lumps within garnet-epidote exoskarn along with sphalerite, chalcopyrite, galena, and pyrite and as fracture fillings within endoskarn of an alkaline granitoid, (Sasmaz et al, 2005b).

Rare-metal pegmatites

REE data from analyses on fluorite from pegmatites includes the REE-F-Y-Nb-U pegmatites of the Pike's Peak granite, Colorado (Gagnon et al., 2003) and the skarn-contaminated barren pegmatites of the Vlastějovice area of the Bohemian Massif, Czech Republic, (Ackerman 2005) though rare-element LCT, and U-Th-(Ti-Zr-Nb-Ta) pegmatites are also found in this area.

Hosted within the anorogenic Pike's Peak granitic batholith of the South Platte District in Colorado are concentrically zoned, fluorite-bearing, REE-F-Y-Nb-U pegmatites. Fluorite occurs as primary/magmatic and hydrothermal phases. Averaged LA-ICPMS data on four phases of fluorite from the White Cloud and Oregon 3 pegmatites are included herein (Gagnon et al., 2003).

Pegmatites from the Vlastějovice area of the Bohemian Massif are more difficult to categorize as a singular deposit type as they consist of three varieties of pegmatitic intrusion that cut and are assuredly contaminated by skarn deposits. These pegmatites intrude skarn lenses found within metasedimentary gneiss that also contains lenses of, amphibolite, quartzite and eclogite (Koutek 1950 and Klečka et al., 1992 from Ackerman 2005). Barren pegmatites found within this region consist of plagioclase, microcline, quartz and accessory

allanite, titanite, and fluorite. Endocontact mineralization of barren pegmatites consists of garnet, Ca-hornblende, titanite, and fluorite, and lesser feldspar and quartz suggesting similar temperatures between pegmatite and skarn formation. One rare-element LCT pegmatite found within this region includes plagioclase, quartz, schorl, and lesser biotite, fluorite and endocontact graphic quartz and plagioclase, and k-spar with tourmaline. Accessory minerals to the LCT pegmatite include bavenite, danburite, datolite, pyrochlore, Bi-pyrochlore, magnetite, Mn-columbite (Čech 1985; Novák & Povondra 1995; Nová & Černý 1998). U-Th-(Ti-Zr-Nb-Ta) pegmatites consist of plagioclase, microcline, quartz and accessory uraninite, thorite, anatase, pyrochlore and sulfides (Rezek & Kryst 1985 from Ackerman 2005). It is unclear which pegmatites were sampled and analyzed in Ackerman 2005 by INAA, but the samples are divided by zonation which suggests the 13 samples compiled herein are from the barren variety.

Granite-related uranium deposits

Two granite-related uranium deposits were included in this compilation. These were the No. 302 uranium ore deposit of Guangdong, South China (Zhang et al., 2007), and mineralization at Gabbal Gattar, Egypt (Mahdy et al., 2014).

The No. 302 uranium ores of the Changjiang uranium ore field of Guangdong, South China consist of pitchblende and secondary U-minerals hosted within a brecciatied zone caused by pivotal tension faults mineralized near the contact of a medium grained, porphyritic two-mica granite and a fine to medium grained porphyritic biotite granite “due to alkali metasomatism,” (Zhang et al., 2007). Associated minerals include pitchblende, hematite, fluorite, and red, microcrystalline quartz. Eight analyses of REE in fluorite from the No. 302 uranium deposit taken by ICP-MS were compiled within this study, (Zhang et al., 2007).

Uranium mineralization at Gabbal Gattar, North Eastern Desert, Egypt occurs as hexavalent and tetravalent uranium minerals such as primary pitchblende and kasolite, and secondary uranophane and beta-uranophane. The formation of this deposit is interpreted as remobilization of fluids from late U-F-rich granite due to tectonically induced activity. This

allowed for alteration (hemitization, episyenitization [greisenization?], kaolinitaztion, fluoritization, chloritization, and silicifcation) of fracture zones within the granite and host conglomeratic-turbidite-siltstone units and deposition of uranium minerals and fluorite. Fluorite occurs within the unaltered granite as medium grained interstices to quartz, in the altered granite as trace interstices to silicates, and as vein fill in U-rich samples where it is anhedral and dark purple, and vein fill in U-poor samples where it is euhedral and zoned. In addition to U-mineralization associated with the Gabal Gattar granite are fracture controlled molybdenum-bismuth-silver ores that do not appear to contain or have a close association with fluorite mineralization. Only six LA-ICP-MS analyses of fluorite samples associated with secondary uranium mineralization were compiled within this study, (Mahdy et al., 2014).

Greisen deposits

REE geochemistry data from fluorite related to greisinization compiled within this study comes mainly from the works by Monecke et al., 2000 and 2002 studying REE fractionation according to tetrad effects caused by granitic fluid fractionation and mixing with host rock waters. Included within these studies are greisen deposits formed mostly in and around Hercynian Li-F granite cupolas including the Zinnwald tin deposits from the Erzgebirge region between Czech Republic and Germany, (Monecke et al., 2002), the tin-tungsten deposits of Ehrenfriedersdorf, also within the Erzgebirge region of Germany, (Monecke et al., 2000), the tungsten deposits of Qaraoba, Kazakhstan including a marble hosted ore field at Solnechoe (Monecke et al., 2002), the W-Mo-Be deposits at Aqshatau, Kazakhstan (Monecke et al., 2002), and the Nb-Zr-REE altered pegmatite deposits at Kent, Kazakhstan (Monecke et al., 2002).

The flat-lying to steeply dipping cassiterite-quartz veins at the Zinnwald deposit are medium to coarse grained, and occur within the endo- and exocontacts of a Li-F (albite) granite hosted within the Teplice rhyolite. Greisens are also topaz or mica dominant and contain variable amounts of topaz, zinnwaldite, and lepidolite. Three analyses for fluorite were compiled from the Zinnwald deposit taken by ICP-AES on crystal core and rim samples from a flat-lying endocontact vein within kaolinized and sericitized albite granite, and one

sample from a flat-lying vein in the exocontact within fluoritized Teplice rhyolite, (Monecke et al., 2002).

The Sn-W deposit of Ehrenfriedersdorf consists of greisens and greisen veins contained within the endo- and exocontacts of a Li-F granite hosted within gneiss, mica schist, and phyllite, that also contain lenses of skarn, amphibolite, and marble. Five fluorite samples were analyzed by Monecke et al., 2000 taken from different stages of greisen-vein evolution determined by cross cutting relationships. Fluorite samples were taken from tourmaline-beryl-cassiterite veinlets, cassiterite-bearing quartz veins of the endocontact, and cassiterite-bearing quartz veins of the exocontact. Ore veins also contain gilbertite, arsenopyrite, apatite, miscellaneous sulphides, and early wolframite. Three IPC-MS analyses of fluorite analyzed for REE content were compiled from the Ehrenfriedersdorf deposit from Monecke et al., 2000.

Fluorite samples taken from the Qaraoba tungsten deposit, Kazakhstan include core and rim samples that occurred in quartz-wolframite veins from the endocontacts of a Li-F granite. Part of this deposit, at Solnechnoe, is hosted within marble forming exocontact ore bodies of fluorite and quartz containing minor wolframite. Three REE analyses on fluorite taken by ICP-AES were compiled from the Qaraoba endocontact veins, and one analysis from the exocontact, marble hosted Solnechnoe ore field is included, (Monecke et al., 2002).

The W-Mo-Be orebodies at the Aqshatau deposit consist of quartz, quartz-topaz, and quartz-wolframite veins that formed within the endo- and exocontacts of a Li-F granite hosted within granitic, sedimentary, and volcanic rocks. Early fluorite formed within quartz-topaz greisen bodies containing wolframite, beryl, and sulfides, as well as within quartz-sericite-fluorite altered rocks and quartz-fluorite veins. Late fluorite occurs as overgrowths on early fluorite. Four analyses on fluorite for REE content, taken by ICP-AES were compiled from Monecke et al., 2002.

Not much information is provided within Monecke et al., 2002, on the Kent Nb-Zr-REE deposit other than it exists as an intensely altered pegmatite bodies in veins hosted within the endocontact of granite hosted within volcanic and sedimentary rocks. Barren and economic pegmatite bodies are associated with this deposit, and barren pegmatites can

contain optical fluorite. Four analyses of REE taken by ICP-AES on fluorite from Kent were compiled from Monecke et al., 2000.

Cryolite deposits

As of 2008, only two exploitable economic cryolite mines existed in the world, including the Pitinga mine in Amazon, Brazil, (Minuzzi et al., 2008) and the Ivigtut deposit in South Greenland, (Schönenberger et al., 2008). Cryolite mineralization at Pitinga appears to be magmatic to hydrothermal associated with the formation of an albite granite while mineralization at Ivigtut was caused by metasomatism of an A-type granite that formed immiscible fluorine- and silica-rich melts/fluids and subsequent mineralized bodies.

Cryolite mineralization at Ivigtut has been well studied (Pauly and Bailey, 1999, and Goodenough et al., 2000, in Schönenberger et al., 2008). It occurs within an A-type granitic stock interpreted as a mineralized body formed from a fluoride-rich component of an immiscible aluminofluoride-rich melt that formed from F-, CO_2-metasomatism of the host granite. The silicate portion of this melt formed a siderite-quartz layer at the base of the cryolite deposit which also consists of topaz and other fluorides such as fluorite, cryolithionite ($Na_3Li_3Al_2F_{12}$), chiolite, ralstonite, pachnolite, and prosopite, (Pauly and Bailey, 1999; Schönenberger et al., 2008). Two zones make up the cryolite deposit, represented by an upper fluorite-cryolite unit and a lower fluorite-topaz zone. Compiled within this study are 57 LA-ICP-MS analyses for REE on fluorite, (Schönenberger et al., 2008).

Cryolite mineralization at Pitinga occurs as a disseminated magmatic phase that was enriched by hydrothermal cryolite mineralization as well as a massive, hydrothermal phase within albite granite. The description of cryolite mineralization applicable to the massive phase is reminiscent of greisinization where “residual hydrothermal fluids from the albite granite ascended from lower parts of the body” to form massive cryolite “lenticular shaped deposits situated at the apical zone of the granite,” (Minuzzi et al., 2008). These massive cryolite cuppolas also consist of quartz, zircon, alkali feldspar, galena, xenotime, and gagarinite-(Y). Additionally, the Madeira granite of the Pitinga mine is a historic tin producer, and is the largest of Brazil. Granitic phases within this mine include the core albite granite

consisting of quartz, albite, alkali feldspar, cryolite, zircon, polythionite, riebeckite, pyrochlore, biotite, cassiterite, and magnetite, and the border albite granite consisting of quartz, k-spar, albite, fluorite, zircon, chlorite, cassiterite, hematite, and columbite. Six analyses on fluorite taken by ICP-MS for REE were compiled from the Pitinga mine without distinguishing between primary or secondary fluorite, (Minuzzi et al., 2008).

Intrusion-related molybdenum deposits

Two molybdenum deposits are included within this study: the Sweet Home mine in Colorado, (Lüders et al., 2009) related to late stage Climax-type molybdenum mineralization near Climax, Co, and the Tumen molybdenite-fluorite veins hosted in dolostone and schist associated with the Qinling Mo porphyry-skarn belt of central-eastern China, (Deng et al., 2008).

The Sweet Home mine located in the Mosquito Range of the Colorado Mineral Belt, has historically been mined for minor silver as well as rhodochrosite mineral specimens from early quartz-molybdenite-pyrite-topaz-muscovite-fluorite and later galena-sphalerite-tetrahedrite-bornite-fluorite-rhodochrosite veins, and hübernite pockets hosted by granodiorite, granitic gneiss, and migmatite of the Idaho Springs Formation and Tertiary monzonite porphyry±quartz dikes. Calcite, barite, and apatite are also present as the latest crystallites. Even though the Sweet Home mine is proximal to several gold-silver-lead-zinc deposits, its formation has been attributed to a final exsolution fluid phase from the highly differentiated, Climax-forming, Alma Batholith that mixed with meteoric waters driven by heat from the intrusion. Through fluid inclusion, trace element, and isotope analyses, early veins are interpreted as forming due to primarily magmatic waters while later mineralization consists of more meteoric derivation forming the main sulfide stage of the deposits. Alteration haloes around veins consists of quartz-sericite-pyrite and greisen-like muscovite-quartz-pyrite-fluorite assemblages, while regional scale propylitic alteration consists of chlorite-hematite-pyrite. Two fluorite samples from the early quartz-molybdenite-pyrite-topaz-muscovite-fluorite phase and ten samples from the later sulfide-rhodochrosite phase were analyzed by ICP-MS for REE content and compiled within this study, (Lüders et al., 2009).

Molybdenite mineralization at the Tumen deposit of Qinling, China is contained within stratigraphically controlled molybdenite-fluorite veins hosted within the transition zone between quartz-sericite schist and dolomite along a NW trending extensional fault zone. Mineralization also contains pyrite, calcite, quartz, with lesser sphalerite, galena, chalcopyrite, and minor muscovite and sericite with hydrothermal alteration that consists of silica, fluorite, carbonate and kaolinite. Vein mineralization is divided into four stages and may be related to syenitic dikes of nearly the same age. Vein mineralization is as follows: brecciated fluorite veins; fluorite±molybdenite±pyrite veins; calcite-pyrite±sphalerite±chalcopyrite veins; sulfide-barren carbonate veins. Sixteen fluorite samples from various stages of the Tumen vein mineralizations have been compiled within this study and analyzed for REE content by ICP-MS from Deng et al., 2014.

Hydrothermal/epithermal vein and replacement deposits

Vein and replacement deposits of hydrothermal/epithermal origin have been sorted according to host lithology with secondary classification assignations where applicable. Samples from these deposits have been analyzed by INAA, LA-ICP-MS, and ICP-MS methods. Publications from which REE data from fluorite sourced from hydrothermal/epithermal veins were compiled include: Castorina et al., 2008; Cheilletz et al., 2010; Hill et al., 2000; Gagnon et al., 2003; Sallet et al., 2005; Sasmaz et al., 2005b; Schwinn and Markl, 2005; Subías, Fernández-Nieto, 1995; Trinkler et al., 2005; and Xiang et al., 2010. The categorization of these deposits are outlined in **Error! Reference source not found.** including deposits hosted in carbonate, sedimentary, metamorphic and igneous rock. Secondary classifications also include, vein deposits associated with alkaline igneous silicate rock and one greisen deposit. First, these deposits will be summarized below according to host lithology classification, to then be further elaborated upon according to publication and region of occurrence.

Hydrothermal/epithermal vein deposits containing fluorite *hosted in carbonates* include F-Pb-Zn-Ag-(Cu) deposits at Tad Dere, hosted in marble, schist and gneiss (Sasmaz et al., 2005b), F-(Cu) deposits hosted in limestone at Lanuza, (Subías, Fernández-Nieto, 1995), Zn-F-(Pb) mineralization in marble at Tebarry, (Subías, Fernández-Nieto, 1995), F deposits at Yixian (Xiang et al., 2010), hosted in carbonate and sedimentary rock, F deposits at Santa

Lucia and Monreale, hosted in limestones, dolomitic limestones, and siliclastic metasedimentary rock in Sardinia, Italy (Sallet et al., 2005) and multiple deposits hosted in limestone in New Mexico containing Ag, Au, Pb, Zn, W, Cu, V, (Hill et al., 2000) including the Hanson, Chise, Gonzales, Yellowjacket, Marion, Hardin, Cox, Nakaye, Esperanza, Hiebert, Grants, and Ruby/Hayner deposits. Twelve REE analyses of fluorite taken by ICP-MS were compiled from Tad Dere, 12 from Lanuza, 11 from Tebarray, five from Yixian, two from, Sardinia, and twelve taken by INAA from New Mexico. Secondary classifications for veins in carbonate include secondary host classifications of metamorphic rocks for the deposits of Tebarray, Tad Dere, and Sardinia, and of igneous rocks for Pb and Cu deposits in New Mexico.

Deposits of hydrothermal/epithermal veins *hosted in igneous rocks* compiled within this study includes those of Sardinia, Italy; the Erzgebirge and Schwarzwald areas of Eastern Germany; St. Lawrence, Newfoundland, Canada; New Mexico, United States; and Santa Catarina, Brazil. Fluorospar veins, hosted within volcanic rocks and Variscan granites in Sardinia, Italy, including the Monte Grighini, Nuraghe Onigu, Silius, and Monte Genis deposits compose one of Europe's largest fluorospar districts (Sallet et al., 2005). Post-Variscan veins hosted within Variscan granites of Erzgebirge, Eastern Germany have been targeted for Ba-Sr, Bi-Co-Ni-As-Ag, Ge-Hg, Fe-Mn including the Beihilfe, Naundorf, Reiche Zeche Vater Abraham, Palmbaum Shaft, Brandbach Barite Adit, Armer Leute Bergfreund Shaft, Ehrenfriedersdorf, Dörfel, Schelma, and Pöhla-Tellerhäuser deposits (Trinkler et al., 2005). F; Ag-Cu-Bi; Pb-Zn; ±Co ±U ±Sb ±Fe deposits of the Schwarzwald area, Eastern Germany, hosted within Variscan granites includes the Friedenweiler, Ohlsback, Hesselback, Ödsbach, Sophia, Johann, Neuglück, Bleilersgrund, Ilse i. Kaltbrunn, Burgfelsen, König, Hilfe Gottes, Herzog Friedrich, Daniel Gallen-back, Neubergmännisch Glück, Schlechthalde, Southern Reinerzau valley, Hohberg, and Tennenbronn deposits (Schwinn and Markl, 2005). Veins hosted within granite and porphyry dikes of the St. Lawrence region, Newfoundland, Canada were producers of fluorite (Gagnon et al., 2003). Finally, Pb, Zn, W, Cu, Au, F deposits of New Mexico hosted in granite, granodiorite, andesite, rhyolite porphyry, and basalt (Hill et al., 2000), include the Lemitar, Independence, Greenleaf, Lucky, Gratten, Green Spar, Animas, Fluorite Group, Lone Star, Spar Hill, Goat Camp Spring, and Shrine deposits. Three analyses of REE concentrations in fluorite taken by ICP-MS analysis were compiled from Sardinia, Italy, 15 from Erzgebirge, Eastern Germany, one of which was secondarily classified as a sample

from a greisen deposit, 19 averaged LA-ICP-MS analyses were compiled from Schwarzwald, Germany, and three from St. Lawrence, Newfoundland. Additionally, 22 analyses taken by INAA were compiled from New Mexican deposits, 10 of which were secondarily classified as samples taken from deposits hosted in alkaline silicate igneous rocks, similar to the 31 analyses compiled from Santa Catarina, Brazil, as explained below.

Veins *hosted in alkaline igneous silicate rocks* were labeled first as "hydrothermal/epithermal veins in igneous rocks" with secondary deposit assignations of the alkaline variety. These deposits include fluorite-chalcedony veins hosted in alkaline, biotite-granite and biotite-hornblende, subalkaline-monzonitic granite at Santa Catarina, Brazil (Sallet et al., 2005); the Foster, Clum, and Sadler fluorospar deposits of New Mexico, hosted in monzonite porphyry, trachytic latite, and alkali granite, (Hill et al., 2000); and Th-REE deposits of the Capitan Mountains, New Mexico (Hill et al., 2000). From Santa Catarina, Brazil, 31 analyses taken by ICP-MS analysis were compiled, while three were compiled from New Mexican deposits, taken by INAA, and seven were compiled from the Capitan Mountains, New Mexico.

Veins *hosted in metamorphic rocks* includes those hosted in siliclastic metasediments, schists, and ortho- and paragneisses. These include the Arcu Istiddà, Punta Geranule, Castello Medusa, Bruncu Mannu, Bruncu Ventura, Bruncu Molentinu, Is Crabus, Su Zufuru, Is Murvonis, and Nuraghe Perdu Spada F deposits hosted in metasiliclastics and metavolcanites of Sardinia, Italy (Castorina et al., 2008), and the Pb-Cu-Ag-Bi; Pb±Zn±Ag; Fe-(Pb)-(Ag); Cu-As; Ag-Sb; and F deposits hosted in gneiss of the Schwarzwald area, Germany including the Friedrich-Christian, Drey, Barbara, Segen Gottes, Artenberg, Erzengel Gabriel, Laßgrund, Wenzel, Fortuna Gelbach, and Ludwigs Trost deposits (Scwhinn and Markl, 2005). F deposits hosted in limestone, schist, and siltstone of El Hamman, Morocco (Cheilletz et al., 2010) were also compiled under this classification, as well as the Long Lost Brother, Spruce Hill, and Bonita deposits hosted in gneiss of New Mexico (Hill et al., 2000). Compiled analyses of REE values reported from fluorite taken by ICP-MS analysis includes 10 from Sardinia, Italy, and three from El Hamman, Morocco, while those recorded by LA-ICP-MS includes ten analyses from Schwarzwald, Germany, and three analyses from New Mexico, recorded by INAA. Of

these, the samples compiled from El Hamman, were also secondarily classified as veins hosted in sedimentary rock.

Hydrothermal/epithermal vein deposits containing fluorite *hosted in sedimentary siliclastic rocks* compiled within this study includes one sample taken from an F-vein hosted in arkose at Monte Cardiga, Sardinia, Italy, (Castorina et al., 2008), and six samples taken from Ag-Cu±Bi and F veins hosted in sandstone and sedimentary rock of Schwarzwald, Germany (Schwinn and Markl, 2005). Data compiled representing veins in sedimentary rocks of the Schwarzwald area, Germany includes that from the Käfersteige, Heiligenwald, Dorothea, Wittenweiler, Zunsweier, and Clara deposits. Samples from Sardinia were analyzed for REE by ICP-MS analysis, while those from Germany were analyzed by LA-ICP-MS.

Additionally, secondary classifications according to host lithology for hydrothermal/epithermal vein deposits containing fluorite are as follows: three samples from deposits hosted in metamorphic rock were also classified as hosted in sedimentary rock from El Hammam, Morocco (Cheilletz et al., 2010); two samples of fluorite compiled from the Gonzalez West, and Marion deposits of New Mexico were classified under igneous hosts in addition to carbonate hosts; 11 samples of fluorite representing deposits at Tebarry, Spain (Subías, Fernández-Nieto, 1995), 12 samples of fluorite from the Tad Dere deposit of Akdagmadeni, Turkey, (Sasmaz et al., 2005b), and two fluorite samples from the Monreale and Santa Lucia deposits of Sardinia, Italy were compiled as veins hosted in carbonate rock with secondary classifications as veins in metamorphic hosts; one sample of fluorite from the Ehrenfriedersdorf deposit of the Erzgebirge, Germany compilation from Trinkler et al., 2005, was secondarily classified as a greisen deposit after vein in igneous host, though data from this deposit compiled from Monecke et al., 2000 were classified primarily as sourced from greisens; finally, vein deposits hosted in igneous rocks that were hosted by or sourced from alkaline igneous, silicate rocks were classified secondarily under the alkaline silicate igneous rock group, including the Santa Catarina, Garganta, and Jaguaruna, Segunda Linha Torrens, Canela Grande, Canela Pequana, and São Pedro deposits of Santa Catarina Brazil, (Sallet et al., 2005), and the deposits of Sadler, Foster, Clum, and the Capitan Mountains of New Mexico, (Hill et al., 2000).

Listed above are the summaries of vein deposits compiled according to host lithology, below are summarized descriptions of the deposit occurrences according to publication from which their representative data were drawn. Some of the deposits and regions covered in this compilation encompass geographically small areas such as the Yixian, El Hammam, St. Lawrence, and Santa Catarina districts, while other studies, such as those covering the more expansive Erzgebirge, Schwarzwald, Sardinia, or New Mexican regions include a wide variety of vein deposits hosted in various lithologies.

Here's a brief summary of proposed deposit formation or description by publication with details to follow. Fluorite formation in the fluorite-barite, post-Variscan hydrothermal veins of the Erzgebirge region of Eastern Germany, (Trinkler et al., 2005) sourced fluorine from Variscan granitoids. Vein deposits of the Santa Catarina district, Brazil are hosted in two granitic complexes with alkaline affinity, but are also hosted in metasediments and basaltic feeder dikes (Sallet et al., 2005). Vein deposition and fluorospar generation on the Italian island of Sardinia is attributed to fluid remobilization by tectonism and intrusion of Variscan granites, hosted in a variety of metasediments, and one skarn, with F sourced from metarhyolites and metarhyodacites, (Castorina et al., 2008). Fluorite±barite vein formation of the expansive Schwarzwald region, of Germany continued from late- to post-Variscan time, hosted in sedimentary, igneous, and metamorphic rocks (Schwinn and Markl, 2005). Fluorospar veins are sourced from, and are hosted within the St. Lawrence granitic pluton and related porphyry dikes of St. Lawrence, Newfoundland, (Gagnon et al., 2003). Fluorite samples taken from structurally controlled, hydrothermal/epithermal fl-qtz-chalcedony vein deposits of Yixian, Liaoning, China, are hosted in carbonates, with a proposed source of F from regional volcanics. Fluorite-calcite veins located in the El Hammam fault zone of Morocco are hosted in sedimentary and metasedimentary rocks. The origin of hydrothermal activity of the Valle de Tena region of the Spanish Pyrenees Mountains is unclear, but multiple remobilization events deposited veins around the vicinity of the Panticosa granodiorite that have been mined for base metals and F, (Subías, Fernández-Nieto, 1995). Finally, hydrothermal/epithermal vein formation across New Mexico was compiled by Hill et al., 2000, encompassing a wide array of veins containing fluorite hosted in various lithologies, containing varying degrees of economic materials.

Fluorite-rich, post-Variscan hydrothermal vein mineralization dominates the Erzgebirge NE-SW trending antiformal structure of the Saxothuringian Zone of the Variscan fold belt located along the border between Saxony, Eastern Germany and Czech Republic. These post-Variscan veins represent the last sequence of activity of the region and are known to contain anomalous concentrations of Ba-Sr, Bi-Co_Ni-As-Ag, Ge-Hg, Fe-Mn. Preceding this hydrothermal event was another, dubbed late-Variscan, consisting of veins that have been mined extensively for Ag, Pb-Zn-Cu. Before this, the area was subject to two main events of the granitic emplacement during the Variscan orogeny. During the early stages of the Variscan orogeny, rhyodacitic and rhyolitic lavas were extruded and lamprophyric dikes emplaced within gneiss, mica schist, phyllite, and slate. 15 samples of fluorite taken from barite-fluorite-quartz±sulfide, post-Variscan hydrothermal veins were analyzed for REE via ICP-MS, (Trinkler et al., 2005). Of these, the Beihilfe, Naundorf, Reiche Zeche Vater Abraham, Palmbaum Shaft, Brandbach Barite Adit, Armer Leute Bergfreund Shaft, Dörfel, Schelma, and Pöhla-Tellerhäuser deposits were classified as hydrothermal/epithermal veins in igneous hosts, while the Ehrenfriedersdorf vein deposit was classified first as a hydrothermal/epithermal vein deposit hosted in igneous rock, and second as a greisen deposit.

The Santa Catarina district mined for fluorite of Southern Brazil is related to the emplacement of two fluorite-bearing granitoids. The Pedras Grandes granites are coarse to medium grained leucoctratic biotite-hornblende subalkaline-monzonitic granite with accessory titanite, allanite, apatite and metallic oxides. The Tabuleiro granites consist of leucocratic, medium to fine grained, alkaline, biotite granite with accessory fluorite. Overlying the granites are Permo-Carboniferous, coal-bearing sedimentary rocks and Cretaceous basalt. Fluorite ores are contained in epithermal, post-Jurassic fluorite-chalcedony±barite±pyrite veins hosted primarily within the aforementioned granitic suites and also cut the Permo-Carboniferous sedimentary cover and diabasic feeder dikes to the Cretaceous basalt. Five fluorite samples from veins associated with the Tabuleiro granites, and 26 fluorite samples from veins associated with the Pedras Grandes granites analyzed by ICP-MS were compiled from Sallet et al., 2005.

The Italian island of Sardinia is home to one of Europe's largest fluorite districts where deposition was sourced from Ordovician volcanic rocks and was remobilized during multiple tectonic events including: the Variscan orogeny and coeveal granitic intrusions, Permian uplift of Sardinia, and Oligocene-Miocene volcanism. Early fluorite deposition occurs as small, thin, massive lenses within a Middle Ordovician meta-volcanic complex consisting of metarhyolite and metarhyodacite. Fluorite deposits on Sardinia have been divided into three groups (A-C) by Castorina et al., 2008, with the existence of a few outliers, but have been sorted by this author according to host lithology.

According to Castorina et al., 2008, Group A fluorite consists of karst and lens deposits containing fluorite-barite-calcite ±quartz ±pyrite ±galena ±sphalerite ±marcasite ±chalcopyrite hosted in Cambrian low-grade metalimestone and metasediments. Group B consists of veins and stockworks in Ordovician volcanic and metasedimentary rocks including metarkoses and metagreywackes and mineralization includes fluorite-barite-calcite-quartz ±dolomite ±sphalerite ±pyrite ±galena ±marcasite. Group C consists of fluorite-chalcedony ± quartz ± barite hydrothermal veins hosted in Cenozoic volcanic rocks, including the Monte Grighini, Monte Cardiga, and Nuraghe Onigu deposits, (Castorina et al., 2008). Deposits in Group A includes: Monreale, Su Zurfuru, Is Murvonis, Nuraghe Perdu Spada, and the skarn deposit of Perda Niedda. Group B includes: Arcu Istiddà, Punta Geranule, Castello Medusa, Silius, Bruncu Mannu, Bruncu Ventura, Monte Genis, Bruncu Molentinu, and Is Crabus deposits, (Castorina et al., 2008).

The F deposits of Sardinia, Italy studied by Castorina et al., 2008 were sorted accordingly by host lithology. These groups encompass deposits hosted in carbonate, sedimentary, igneous silicate, and metamorphic rocks. Hydrothermal/epithermal vein deposits hosted in carbonate include the Santa Lucia deposit hosted in limestones, dolomitic limestones and siliclastic metasedimentary rocks, the Monreale deposit hosted in metalimestones and metasiliclastics, and the Perda Niedda skarn [compiled under skarn deposits] hosted in metalimestone. The Monte Cardiga deposit is hosted in arkose. Hydrothermal/epithermal vein deposits hosted in silicate igneous rocks include the Monte Grighini deposit hosted in rhyolite, the Nuaghe Onigu veins hosted in rhyolitic and "basaltic" tuff, the Silius deposit hosted in metavolcanics and metasedimentary rocks, and the Monte

Genis body hosted in leucogranite. Sardinia has undergone extensive low-grade metamorphism so most of the deposits compiled from this region were hosted in metamorphic rocks. These include the Acru Istiddà, Punta Geranule, Castello Medusa, Su Zurfuru, Is Murvonis, and Nuraghe Perdu Spada deposits hosted in metasediments, and the Bruncu Mannu, Bruncu Ventura, Bruncu Molentinu, and Is Crabus deposits hosted in metasiliclastics and metavolcanics. 18 analyses of REE taken by ICP-MS of fluorite samples representing mines throughout Sardinia were compiled from Castorina et al., 2008. Three of these samples were from deposits hosted in carbonate rocks including the skarn deposit at Perda Niedda, one sample was from a sedimentary-hosted deposit, four samples were from vein deposits hosted in igneous rocks and ten samples were compiled from veins hosted in metamorphic rocks. 5-15 samples were taken at each location and mixed by the cited authors, to form a representative sample of each locality.

Late to post Variscan hydrothermal veins in the Schwarzwald area of Germany are plentiful (approx. 400), subparallel a regional graben, and show evidences of single to multiple episodes of remobilization. About half of these veins contain economic quantities of fluorite±barite or alternatively, fluorite is a major constituent of mineralization. The remaining half contain ores of Cu-Bi, or various amounts of Pb, Co, Ag, Zn, Sb, and U. The veins of this area are hosted in Variscan granites and ortho- and paragneisses and migmatites that locally contain lenses of peridotites, pyroxenites, eclogites, and amphibolites, as well as Triassic Buntsandstein sandstone and Muschelkak limestone. Thirty-five analyses on fluorite of multiple generations resulting from numerous episodes of remobilization taken by LA-ICP-MS analyses were compiled from Schwinn and Markl, 2005 from Variscan fluorite veins in Schwarzwald area Germany. Nine of these analyses were taken from fluorite hosted in metamorphic rocks (from the Friedrich-Christian, Drey, Barbara, Segen Gottes, Artenberg, Erzengel Gabriel, Laßgrund, Wenzel, Fortuna Gelbach, and Ludwigs Trost deposits), six from veins hosted in sedimentary rocks (from the Käfersteige, Heiligenwald, Dorothea, Wittenweiler, Zunsweier, and Clara deposits) and 19 were taken from vein deposits in igneous hosts (Ohlsback, Bleilersgrund, Burgfelsen, Schlechthalde, Tennenbronn, Friedenweiler, Hesselback, Ödsbach, Johann, Ilse i. Kaltbrunn, Daniel Gallen-back, Neubergmännisch Glück, Southern Reinerzau Valley, Sophia, Neuglück, and Hohberg deposits).

Vein-hosted fluorospar deposits in St. Lawrence, Newfoundland occur within the St. Lawrence granitic pluton and related porphyry dikes. These veins also extend from the granite into the host country rock, which is unnamed by Gagnon et al., 2003. Vein mineralogy consists primarily of fluorite as well as quartz, calcite, minor chalcopyrite, sphalerite, galena, and rare barite. 48 LA-ICP-MS analyses of REE in fluorite from the Grebe's Nest deposit, 12 from the Iron Springs deposit, and 13 from the Lawn Barite Vein were averaged to make three representative samples that were compiled from Gagnon et al., 2003.

The Yixian fluorite district of Liaoning, China is hosted within the western portion of the Liaoning platform depression consisting of Mid Jurassic and Early Cretaceous volcanic rocks of the Lanqi and Yixian formations, and the Mesoproterozoic Changcheng-Jixian System of carbonate and sedimentary rocks. Fluorite mineralization is fault controlled, occurring with quartz, chalcedony, calcite, and barite, and is hosted exclusively within carbonate rocks of the Changcheng-Jixian System. Xiang et al., 2010, propose that F was sourced from the Lanqi Formation, composed of basalt, andesite, and volcaniclasitcs that was subsequently deposited hydrothermally within faulted carbonate to produce the fluorite deposits at Yixian. Five analyses of REE contents in fluorite samples from multiple mines at Yixian, taken by ICP-MS analysis were compiled within this study from Xiang et al., 2010.

The El Hamman fluorite deposit near Meknès, Morocco consists of structurally controlled calcite-fluorite veins generated during a period of transtensional dextral shearing of the main El Hammam fault zone. Three phases of fluorite mineralization are hosted within Carboniferous schists and siltstones and Devonian marbles. These phases include: early massive calcite and fluorite; later banded fluorite, calcite, quartz and sulfides (pyrite, pyrrhotite, sphalerite, arsenopyrite, stannite, galena, bismuthinite); and late quartz, siderite-ankerite. One fluorite sample from phase one, and two samples from phase two were analyzed by ICP-MS for REE by Cheilletz et al., 2010 and compiled within this study.

Fluorite found in the Valle de Tena area, Huesca, Spanish Pyrenees mountains are included in three types of deposits that have been mined for lead, silver, and fluorite: F-(Cu) veins hosted by Devonian limestones at the Lanuza mine; Zn-F-(Pb) veins hosted in Devonian marbles at Tebarray; and fluorite pockets, bands, nodules, and veins found within

Carboniferous limestones of the Portalet mines of possible manto-MVT-style mineralization (discussed above). The vein deposits at Lanuza and Tebarray occur around the Panticosa granodiorite of the late Hercynian orogeny of Westphalian age (Rios et al., 1983 from (Subías, Fernández-Nieto, 1995)). These deposits have been named by this author as vein deposits hosted in carbonate. Fluorite at Lanuza is mainly microcrystalline and cuts calcite and rare dolomitic layers as well as Permian diabasic dikes. Mm to cm wide sulfide-quartz veins parallel the main fluorite vein in host limestone at Lanuza, with sulfide-quartz disseminations occurring in both the microcrystalline fluorite vein and limestones. The Tebarray vein deposits partially replace marbles and cut and alter diabase dikes. Mineralization occurs as two phases within veins, first as a dark sphalerite-galena-pyrite-chalcopyrite phase and an inner phase of light sphalerite-(Ag) galena-tetrahedrite-fluorite that is massive and micro to macrocrystalline. Two episodes of calc-alkaline volcanism also affected the area during late Hercynian transcurrent shearing (Bixel and Lucas, 1983, from (Subías, Fernández-Nieto, 1995)). Twelve samples of fluorite were analyzed by ICP-MS for REE from Lanuza, and 10 from Tebarray, (Subías, Fernández-Nieto, 1995).

Hill et al., 2000 compiled fluorite from occurrences across New Mexico. Most of these samples came from epithermal/hydrothermal vein deposits hosted in a variety of lithologies, with or without formations related to igneous activity/rocks. These have been mined for F, Cu, Ag, Pb, Zn, W, V, Th, or REE in various combinations and quantities, or are barren regarding any metallic commodity. Fluorite-containing deposits hosted in limestone include the Ag-Au vein deposits of Hanson and Chise, the Pb deposit of Gonzales, the Pb, Zn, Ag, Cu deposits of Yellowjack, Nakaye, Esperanza, and Ruby/Hayner, and the Pb, W, V deposits of Hardin and Cox. Barren or fluorospar deposits hosted in limestone include those of Hiebert, and Grants. Pb, Zn, W-containing veins of Lemitar, and Cu-containing veins of Independence are hosted in granite, Cu, Au deposits at Fluorite Group are hosted in basalt, and those at Lone Star are hosted in granodiorite. Veins at Steeple Rock are hosted in andesite and contain Cu, Au, Ag, but fluorite-vein deposits at Fluorite Ridge are hosted in granodiorite and andesite and may or may not have been exploited for fluorite. Deposits at Big Burro, hosted in rhyolite, granite, and gneiss contain no mentioned metallic commodities according to Hill et al., 2000, so it is assumed that these deposits are barren. Fluorite veins at Sadler are hosted in monzonite and may or may not have been exploited for fluorospar, and the same goes for the

Foster and Clum deposits hosted in trachytic latite. One rare earth deposit was included in Hill et al., 2000's compilation, this being the Capitan Mountains deposit of Th-REE-containing fluorite veins, hosted in alkali granite. More barren deposits included those hosted in granitic gneiss at the Spruce Hill and Bonita deposits. Samples form the Hansonburg MVT district was also compiled by Hill et al., 2000, which was discussed earlier in the MVT section of this summary. 12 samples of fluorite from veins hosted in carbonate, two of which have a secondary igneous affinity, 22 samples from veins hosted in igneous rocks, 10 of which have a secondary, alkaline affinity, and 3 samples from deposits hosted in metamorphic rocks were compiled from Hill et al., 2000, which had undergone REE, trace-element analysis by INAA methods.

References

1. Ackerman, L., 2005. Magmatic vs. hydrothermal origin of fluorites from Vlastějovice, Bohemian Massif; Journal of the Czech Geological Society, v. 50, (35-41).
2. Alvin, M. P., Dunphy, J. M., Groves, D. I., 2004. Nature and genesis of a carbonatite associated fluorite deposit at Speewah, East Kimberley region, Western Australia; Mineralogy and Petrology, v. 80, (127-153).
3. Bau, M., Romer, R. L., Lüders, V., Dulski, P., 2003. Tracing element sources of hydrothermal mineral deposits: REE and Y distribution and Sr-Nd-Pb isotopes in fluorite from MVT deposits in the Pennine Orefield, England; Mineralium Deposita, v. 38, (992-1008).
4. Bixel, F., Lucas, C., 1983. Magmatisme, tectonique et sedimentation dans les fossés stéphano-permiens des Pyrénées occidentales; Rev. Géol. Dyn. Géogr. Phys., v. 24, (329-342).
5. Bühn, B., Schneider, J., Dulski, P., Rankin, A. H., 2003. Fluid-rock interaction during progressive migration of carbonatitic fluids, derived from small-scale trace element and Sr, Pb isotope distribution in hydrothermal fluids; Geochimica et Cosmochimica Acta, v. 67, 23, (4577-4595).
6. Castorina, F., Masi, U., Padalino, G., Palomba, M., 2008. Trace-element and Sr-Nd isotopic evidence for the origin of the Sardinian fluorite mineralization (Italy); Applied Geochemistry, v. 23, (2906-2921).
7. Čech, F., 1985. Mineralogic žulových pegmatite české části Českého Masívu: MS unpublished D.Sc. Thesis, Charles University, Prague (250 pgs).
8. Cheilletz, A., Gasquet, D., Filali, F., Archibald, D.A., Nespolo, M., 2010. A late Triassic $^{40}Ar/^{39}Ar$ age for the El Hammam high-REE fluorite deposit (Morocco): mineralization related to the Central Atlantic Magmatic Province?; Mineralium Deposita, v. 45, (323-329).
9. Davis, J.C., 1973; 1986. Statistics and data analysis in geology, second edition. John Wiley & Sons, Inc., ISBN: 0-471-08079-9, (646 pgs).
10. Deng, X.-H., Chen, Y.-J., Yao, J.-M., Bagas, L., Tang, H.-S., 2014. Fluorite REE-Y (REY) geochemistry of the ca. 850 Ma Tumen molybdenite-fluorite deposit, eastern Qinling China: Constraints on ore genesis; Ore Geology Reviews, (1-12).
11. Doroshkevich, A.G., Viladkar, S.G., Ripp, G.S., Burtseva, M.V., 2009. Hydrothermal, REE mineralization in the Amba Dongar carbonatite complex, Gujarat, India: The Canadian Mineralogist, v. 47, (1105-1116).
12. Dunham, K.C., 1983. Ore genesis in the English Pennines: a fluorite subtype, In: Kisvarsanyi, G., Grant, S.K., Pratt, W.P., Koenig, J.W., (eds.), International conference on Mississippi Valley-type lead-zinc deposits, University of Missouri-Rolla, (86-112).

13. Ewbank, G., Manning, D.A.C., Abbott, G.D., 1993. The relationship between bitumens and mineralization in the South Pennine Orefield, central England; J Geol Soc Lond, v. 152, (751-765).
14. Gagnon, J. E., Samson, I. M., Fryer, B. J., Williams-Jones, A. E., 2003. Compositional heterogeneity in fluorite and the genesis of fluorite deposits: insights from LA-ICP-MS analysis; Canadian Mineralogist, v. 41, (365-382).
15. González-Partida, E., Carillo-Chávez, A., Grimmer, J.O., Pironon, J., 2002. Petroleum-rich fluid inclusions in fluorite, Purisima mine, Coahuila, Mexico; International Geology Review, v. 44, 8, (755-764).
16. Goodenough, K. M., Upton, B. G. J., Ellam, R. M., 2000. Geochemical evolution of the Ivigtut granite, South Greenland: a fluorine-rich "A-type" intrusion; Lithos, v. 51, (205-221).
17. Gwalani, L. G., Rogers, K. A., Demény, A., Groves, D. I., Ramsay, R., Beard, A., Downes, P. J., Eves, A., 2010. The Yungul carbonatite dykes associated with the epithermal fluorite deposit at Speewah, Kimberly, Australia: carbon and oxygen isotope constraints on their origin; Mineralogy Petrology, v. 98, (123-141).
18. Hill, G.T., Campbell, A.R., Kyle, P.R., 2000. Geochemistry of southwestern New Mexico fluorite occurrences implications for precious metals exploration in fluorite-bearing systems; Journal of Geochemical Exploration, v. 68, (1-20).
19. Huang, C., Wang, J., Li, Z., 2014. REE geochemistry of fluorite from the Lala IOCG Deposit and its geological implications, Kangdian Region, SW China; Acta Geologica Sinica (English Edition), v. 88, 2, (357-358).
20. Ineson, PR., Mitchel, J.G., 1972. Isotopic age determination on clay minerals from lavas and tuffs on the Derbyshire orefield; Geol Mag, v. 109, (501-512).
21. Jacob, K.H., Möller, P., Parekh, P.P., Schneider, H.-J., 1975. Fractionation of the rare-earth elements as a geochemical indicator of florospar genesis; dissertation D 83, Technische Universität Berlin, (98 pgs).
22. Jones, I., 2006. Old classics and new finds: Fluorite from the United Kingdom, in *No. 9 Fluorite - the Collector's Choice*; ed. Fisher, J., Jarnot, M., Neumeier, G., Pasto, A., Staebler, G., Wilson; publ. Lithographie, LLC, East Hampton, Connecticut, USA, 2006. pp. 28-37.
23. Kendrick, M. A., Burgess, R., Pattrick, R. A. D., Turner, G., 2002. Hydrothermal fluid origins in a fluorite-rich Mississippi Valley-type district: combined noble gas (He, Ar, Kr) and halogen (Cl, Br, I) analysis of fluid inclusions from the South Pennine Ore Field, United Kingdom; Economic Geology, v. 97, (435-451).
24. Klečka, M., Machart, J., Pivec, E., 1992. Locality No. 10: Křížovská hora quarry near Vlašim, a Pre-Variscan tourmaline-bearing orthogneiss (Blaník type); Field Trip Guidebook, Lepidolite 200, Nové Město na Moravě, (69-74).
25. Koutek, J., 1950. Ložisko magnetovce skarnového typu u Vlastějovic v Posázavi; Ropr. Čs. Akad. Věd, Ř. Mat. Prir, v. 60, (27 pgs).
26. Levresse, G., Tritlla, J., Villareal, J., Gonzalez-Partida, E., 2006. The "El Pilote" fluorite skarn; A crucial deposit in the understanding and interpretation of the origin and mobilization of F from northern Mexico deposits; Journal of Geochemical Exploration, v. 89 (205-209).
27. Li, Z., Hu R., Wang, J., Liu, J., Li, C-y., Liu, Y., Ye, L., 2002. Lala Fe-oxide-Cu –Au-U-REE ore deposit, Sichuan China: an example of superimposed mineralization; Mineralogy Petrology Geochemistry (in Chinese with English abstract), v. 21, (258-260).
28. Lüders, V., Romer, R. L., Gilg, H. A., Bodnar, R. J., Pettke, T., Misantoni, D., 2009. A geochemical study of the Sweet Home Mine, Colorado Mineral Belt, USA: hydrothermal fluid evolution above a hypothesized granite cupola; Mineralium Deposita, v. 44, (415-434).
29. Mahdy, N. M., Shalagy, M. H., Helmy, H. M., Osman, A. F., El Sawey, E. S. H., Zeid, E. K. A., 2014. Trace and REE element geochemistry of fluorite and its relation to uranium mineralizations, Gabal Gattar area, Northern Eastern Desert, Egypt; Arabian Journal of Geoscience, v. 7, (2573-2589).
30. Minuzzi, O. R. R., Bastos Neto, A. C., Formoso, M. L. L., Andrade, S., Janasi, V. A., Flores, J. A., 2008. Rare element and yttrium geochemistry applied to the genetic study of cryolite ore at the Pitinga Mine (Amazon, Brazil); Anais da Academia Brasileira de Ciências, v. 80, 4, (719-733).
31. Möller, P., Parekh, P.P., Schneider, H.-J., 1976. The application of Tb/Ca-Tb/La abundance ratios to problems of fluorspar genesis; Mineralium Deposita, v. 11, (111-116)

32. Monecke, T., Kempe, U., Monecke, J., Sala, M., Wolf, D., 2002. Tetrad effect in rare earth element distribution patterns: a method of quantification with application to rock and mineral samples from granite-related rare metal deposits; Geochimica et Cosmochimica Acta, v. 66, 7, (1185-1196).
33. Monecke, T., Monecke, J., Mönch, W., Kempe, U., 2000. Mathematical analysis of rare earth element patterns of fluorites from the Ehrenfriedersdorf tin deposit, Germany: evidence for a hydrothermal mixing process of lanthanides from two different sources; Mineralogy and Petrology, v. 70, (235-256).
34. Novák, M., Černý, P., 1998. Scandium in columbite-group minerals from LCT pegmatites in the Moldanubieum, Czech Republic; Krystalinikum, v. 23, (73-89)
35. Novák, M., Povondra, P., 1995. Elbaite pegmatites in the Moldanubieum: a new subtype of the rare-element class; Mineralogy and Petrology, v. 55, (159-176).
36. Palmer, D.A.S., 1994. Geology and geochemistry of the Amba Dongar carbonatite-hosted fluorite deposit, India: MSc Thesis, McGill University, Montreal, (150 pgs).
37. Pauly, H., Bailey, J. C., 1999. Genesis and evolution of the Ivigtut cryolite depost, SW Greenland; Medd. Grønl., Geosci., v. 37, (60).
38. Putnam III, B.R., Norman, D.I., Smith, R.W., 1983. Mississippi Valley-type lead-fluorite-barite deposits of the Hansonburg mining district, New Mexico: New Mexico Geological Society Fall Field Conference Guidebook, v. 34, (253-260).
39. Rezek, K., Kryst, P., 1985. Předběžná zpráva o výskytu nerostü U-Th, Ti-Zr a Nb-Ta v pegmatite na Holém vrchu u Vlastějovic; Miner. Geol., v. 30, (434).
40. Sallet, R., Moritz, R., Fontignie, D., 2005. The use of vein fluorite as a probe for paleofluid REE and Sr-Nd isotope geochemistry: The Santa Catarina Fluorite District, Southern Brazil; Chemical Geology, v. 223, (227-248).
41. Sánchez, V., Cardellach, E., Corbella, M., Vindel, E., Martín-Crespo, T., Boyce, A. J., 2010. Variability in fluid sources in the fluorite deposits from Asturias (N Spain): Further evidences from REE, radiogenic (Sr, Sm, Nd) and stable (S, C, O) isotope data; Ore Geology Reviews, v. 37, (87-100).
42. Sasmaz, A., Önal, A., Sagiroglu, A., Önal, M., Akgul, B., 2005a. Origin and nature of the mineralizing fluids of thrust zone fluorites in Çelikhan (Adiyaman, Eastern Turkey): a geochemical approach; Geochemical Journal, v. 39, (131-139).
43. Sasmaz, A., Yavuz, F., Sagiroglu, A., Akgul, B., 2005b. Geochemical patterns of the Akdagmadeni (Yozgat, Central Turkey) fluorite deposits and implications; Journal of Asian Earth Sciences, v. 24, (469-479).
44. Schneider, H.-J., Möller, P., Parekh, P.P., 1975. Rare earth elements distribution in fluorites and carbonate sediments of the East-Alpine Mid-Triassic sequences in the Nördliche Kalkalpen; Mineralium Deposita (Berlin), v. 10, (330-344).
45. Schönenberger, J., Köhler, J., Markl, G., 2008. REE systematics of fluorides, calcite, and siderite in peralkaline plutonic rocks from the Gardar Province, South Greenland; Chemical Geology, v. 247, (16-35).
46. Schwinn, G., Markl, G., 2005. REE systematics in hydrothermal fluorite; Chemical Geology, v. 216, (225-
47. Sørensen, H., 1997. The agpaitic rocks-an overview*: Mineralogical Magazine, v. 61, (485-498).
48. Souissi, F., Souissi, R., Dandurand, J.-L., 2010. The Mississippi Valley-Type fluorite ore at Jebel Stah (Zaghouan district, north-eastern Tunisia): Contribution of REE and Sr isotope geochemistries to the genetic model; Ore Geology Reviews, v. 37, (15-30).
49. Subías, I., Fernández-Nieto, C., 1995. Hydrothermal events in the Valle de Tena (Spanish Western Pyrenees) as evidenced by fluid inclusions and trace-element distribution from fluorite deposits: Chemical Geology, v. 124, (267-282).
50. Trnkler, M., Monecke, T., Thomas, R., 2005. Constraints on the genesis of yellow fluorite in hydrothermal barite-fluorite veins of the Erzgebirge, Eastern Germany: evidence from optical absorption spectroscopy, rare-earth-element data, and fluid-inclusion investigations; The Canadian Mineralogist, v. 43, (883-898).
51. Ventura Santos, R., Dardenne, M. A., De Oliveira, C. G., 1996. Rare earth elements geochemistry of fluorite from the Mato Preto carbonatite complex, southern Brazil; Revista Brasileira de Geociências, v. 26, 2, (81-86).
52. Viladkar, S.G., 1986. Fenitization at the Amba Dongar Carbonatite alkali complex, India: Gabriel, M., (ed.), Symposium New Mineral Raw Materials: Proceedings, (170-189).

53. Williams-Jones, A.E., Samson, I.M., Olivio, G.R., 2000. The genesis of hydrothermal-fluorite-REE deposits in the Gallinas Mountains, New Mexico; Economic Geology, v. 95, (327-342).
54. Xiang, S., Jun, D., Liqiang, Y., Qingfei, W., Zirong, Y., Qingjie, G., Changming, W., 2010. REE and Sr-Nd isotope geochemistry for Yixian Fluorite Deposit, Westerin Liaoning Province, China and its geological implications; Journal of Earth Science, v. 21, (227-235).
55. Xu, C., Taylor, R. N., Li, W., Kynicky, J., Chakhmouradian, A. R., Song, W., 2012. Fluorite geochemistry from REE deposits in the Panxi region and Bayan Obo China; Journal of Asian Earth Sciences, v. 57, (76-89).
56. Yuan, S., Peng, J., Hu, R., Bi, X., Qi, L., Li, Z., Li, X., Shuang, Y., 2008. Characteristics of rare-earth elements (REE), strontium and neodymium isotopes in hydrothermal fluorites from the Bailashui tin deposit in the Furong ore field, southern Hunan Province, China; Chinese Journal of Geochemistry, v. 27, (342-350).
57. Zhang, G., Hu, R., Bi, X., Feng, H., Shang, P., Tian, J., 2007. REE geochemical characteristics of the No. 302 uranium deposit in northern Guangdong, South China; Chinese Journal of Geochemistry, v. 26, 4, (425-433).

Appendix C.

Summaries of handsample deposits

Summaries from which handsamples were sourced are provided here. Information contained herein was sourced primarily from government databases, from Minfile for deposits located in BC, and the USGS websites for American deposits. These are listed in no particular order: Liard fluorospar prospect, Hastie Quarry, Barnett Mine, Rexspar fluorite-uranium prospect, Eaglet F-Mo-Sr prospect, Kipawa deposit, Eldor deposit, and Rock Candy fluorite-silica past producer.

Liard fluorospar prospect

The Liard fluorospar prospect is described in its Minfile listing (094M 002, GEM, GEM E, Liard fluorospar), (Meredith-Jones, 2007) as a prospect of carbonate-hosted fluorospar and barite located in northern British Columbia. Mineralization occurs as irregular replacement bodies and massive stratiform bodies within a disconformable contact between brecciated and thinly bedded fossiliferous limestone of the Middle Devonian Dunedin Formation. Most mineralization occurs as matrix replacement of limestone breccia including fluorite, witherite, rare barite, and associated quartz and calcite. Coarse-grained fluorite is dark purple and fine grained fluorite is purple to black. Witherite is massive, very fine grained, colored from white to black.

The primary mineralization environment estimated for this prospect is a barium-rich MVT deposit, with a secondary mineralization environment estimated as a hydrothermal/epithermal vein/replacement deposit hosted in carbonate rock. A skarn deposit could also be a possible assignation.

Hastie Quarry and Barnett Mine

Both the Hastie Quarry and Barnett Mine deposits are proximal to the Cave-In-Rock subdistrict of the Illinois-Kentucky Fluorite District, if not a part of it. Over seven million tons

of fluorite have been mined from Illinois-Kentucky fluorite district with secondary resources including sphalerite, barite, and galena, (Denny et al., 2015). It has recently been discovered that these deposits contain the rare-earth fluorocarbonate synchysite reported by these authors. This region has historically been named a fluorite-rich MVT district, otherwise a manto-style MVT district as several of the deposits form typical stratiform, replacement deposits, while others are more fault replacement and vein deposits. The large volume of fluorite within this region has been explained by the presence of the Hicks Dome, a topographically high region including igneous dikes, pipes, several stock-like bodies of peridotite, lamprophyre, and other bodies of intrusive and explosive breccia. Drill holes also reveal felsic syenites and peridotite within the dome. Three styles of mineralization exist including fissure-filling veins along graben-bounding faults, flat-lying, stratabound replacement and bedded ores, and explosion breccias cemented by fluorite and barite which include carbonatite suite elements (Plumlee et al., 1995).

Specifically, the Hastie Quarry deposit, otherwise known as Spar Mountain is listed as a fluorite, crushed stone, barite deposit in the USGS database (10169305), (Drs, 1993). This deposit is described as a hydrothermal replacement, tabular-shaped deposit hosted in carbonate.

The Barnett Mine, also previously described as Parkinson, West Vein Mine, and the Barnett Complex Mine is described by the USGS database (10169446) as a fluorite, lead, zinc, barium deposit, (Hartos, 1993). This deposit consists of hydrothermal breccia fill within a shear zone and irregular fissure vein.

The primary mineralization environments assigned for these two deposits are MVTs followed by secondary carbonatite-related or otherwise hydrothermal/epithermal vein/replacement deposits hosted in carbonate rocks.

Rexspar fluorite-uranium prospect

The Rexspar fluorite-uranium prospect is described in its Minfile listing (082M 021), (Jones, 2012a, b) as a uranium, thorium, fluorite, REE, lead, zinc, molybdenum, copper, and tungsten prospect hosted within metavolcanics of the Paleozoic Eagle Bay Formation.

Mineralization occurs primarily within greenschist grade trachyte in two zones, a U-rich zone and an F-rich zone (called Spar).

The U-rich zone is characterized by deuteric, serecitic, carbonate, silicic, and pyritic alteration hosted in greenschist grade trachytic to rhyolitic tuff and tuff breccia with intrusive porphyry. U and Th mineralization occurs only within the trachytic unit as uraninite, uranothorite, torbenite, metatorbenite, thorianite, and uranium thorite inclusions within fluorophlogopite which extensively replaces trachyte, as well as included in pyrite-fluorophlogopite matrix. Mineralization also includes monazite, bastnäesite, rutile, galena, sphalerite, molybdenite, chalcopyrite, and scheelite with associated pyrite, mica, feldspar, fluorite, calcite, celestite, siderite, dolomite, barite, and quartz. Mineralization likely occurred during late-stage formation of the trachytic unit due to deuteric, volatile rich fluids.

The Spar zone, or fluorite zone, likely formed syngenetically with the U-rich zone and consists of a concordant, tabular body within lithic tuff and tuff breccia of the trachytic unit. Mineralization of purple fluorite occurs as massive lenses, small irregular streaks parallel to foliation, hairline veinlets, and disseminations. Associated minerals include celestite, pyrite, feldspar, mica, and minor bastnäesite concentrated in massive fluorite lenses.

Selecting a primary-deposit type to describe the Rexspar deposit was a difficult task since its description did not easily fit any one category within the classification scheme determined for this project or it seemingly fits a poorly classified group. One possible primary deposit type that could be assigned is an IOCG deposit, though seemingly missing the “oxide” criteria, the deposit does contain carbonate alteration, fluorite, uranium, rare-earths and copper. A safe assignation could be a hydrothermal/epithermal vein/replacement deposit in igneous host rocks, while another less accurate description could be a granite-related uranium depots. No granites are presented in the description, but alkaline volcanic rocks are.

Eaglet F-Mo-Sr prospect

The Eaglet developed F-Mo-Sr prospect is described in its Minfile listing (093A 046), (Barlow, 2013) as a fluorospar, molybdenum, strontium, silver, zinc, lead deposit hosted within Early Mississippian Quesnel Lake granitic orthogneiss at its contact with Late

Proterozoic biotite-garnet metapelite of the Snowshoe Group within central BC. The orthogneiss is cut by irregular dikes of granite, aplite, and pegmatite, and drillcore indicates widespread potassic alteration. Sericitic and chloritic alteration is also present.

Mineralization includes fluorite, molybdenite, celestite, galena, sphalerite, and minor pyrochlore and pyrite with associated quartz, calcite, siderite, kaolinite, dickite, and allanite. Fine grained hematite and fluoroapophyllite, and possibly gypsum are also present. Fluorite mineralization "occurs as veinlets, scattered veins and pods, and disseminated grains." Molybdenite is present along "slickenside and gneissosity planes as groups of flakes several centimeters in size, in quartz veinlets, and as grains within crosscutting fluorite veinlets." High-grade fluorite and molybdenite zones do not overlap.

The Minfile record suggests this deposit-type is either a barite-fluorite vein deposit, or a porphyry-molybdenum deposit, possibly a Climax-type. The possible primary mineralization environment assigned to this deposit is intrusion-related molybdenum, with a secondary mineralization environment assignation as a hydrothermal/epithermal vein/replacement deposit hosted in igneous or metamorphic rocks.

Kipawa

The Kipawa syenite complex of western Quebec is described in Currie and Breemen (1996) as a concordant, folded sheet of peralkaline kataphorite-aegirine syenite with several lenses of biotite-aegirine nepheline syenite contained entirely within the Red Pine Chute gneiss of biotite-magnetite granitic gneiss. The basal Kikwissi gneiss hosts the Red Pine Chute gneiss in the following sequence: Kikwissi gneiss overlain by a thin unit of metasedimentary rocks including feldspathic quartzite, amphibolite, marble, and peraluminous magmatic gneiss, which is overlain by the Red Pine Chute gneiss cut by hornblende granite, with overlying quartzite. Eudialyte, agrellite and other rare minerals occur on the fringe of the folded Kipawa syenite complex, Since evidence for anatectic melting is prevalent, including some skarnification of marble, and original igneous structures scarce, the authors have attributed the deposition of rare minerals at this deposit as metosomatic in origin. Their understanding of the formation of the deposit is as follows:

> "A peralkaline complex was emplaced ~1240 Ma as a pluton, volcanic rocks, or as a combination of both. Emplacement probably accompanied development of the Sudbury dyke swarm and postdated more extensive orogenic magmatism. Any concentrations of rare minerals associated with emplacement have not survived later deformation and metamorphism. At ~995 Ma, ductile northwest-directed thrusting under amphibolite-facies metamorphic conditions juxtaposed a marble and calc-silicate unit with syenite along a surface of movement marked by mechanical mixing on a meter scale. This juxtaposition was followed by metasomatic reactions and anatectic melting in the presence of F-rich brines. These processes produced not only the spectacular rare minerals, but redistributed alkalis and trace elements on scales varying from a few meters to several kilometers." – Currie and Breeman, 1996.

In other words, this syenite complex could be composed of plutonic or volcanic peralkaline silicate igneous rocks that have been extensively metamorphosed and influenced metasomatism that produced skarn rocks. These primary and secondary mineralization environments can be assigned accordingly.

Eldor

The Eldor Carbonatite Complex is listed within the USGS mining data website with data sourced largely from Wright (1997) as a Precambrian rare earth element deposit hosted in an early Proterozoic sedimentary terrane in northern Quebec. Intrusions within the complex include syenite, calcite-, magnesio-, and ferro-carbonatite, glimmerite, and feldspathic breccia. Ore minerals include monazite, apatite, pyrochlore, fersmite, zircon, rutile, baddeleyite, uranium, and magnetite. Fenetization is present in many of the units, and the main intrusion consists of early stage calcite and dolomite carbonatite and late-stage veining calcite carbonatite. Pyrochlore mineralization is concentrated in glimmerite.

The primary mineralization environment assigned to this deposit is carbonatite-related. A secondary mineralization environment of peralkaline silicate igneous rock-related could be assigned as well, but this doesn't seem necessary.

Rock Candy fluorite-silica past-producer

The Minfile listing (082ESE070), (deGroot, 2014) for the Rock Candy past-producer describes this deposit as an epithermal fluorite, silica, copper, lead deposit hosted in igneous rocks in south central BC. Mineralization includes fluorite, chalcopyrite, galena, chalcocite,

and covellite with associated quartz, barite, calcite, kaolinite, chalcedony, and pyrite with argillic, chloritic, carbonatitic, and silicic alteration. Host rocks include fine-grained andesite, feldspar porphyry, dacite, trachyte, granite, syenite, and monazite.

Fluorite mineralization is hosted primarily in andesites as fine to medium grained, green to grey veins that also contain albite, oligoclase, and actinolite with minor magnetite and biotite. Fluorite veins containing chlorite, sericite, quartz, calcite, pyrite, and clay minerals pervasively alter green-grey fluorite veins to a pink color. Large fluorite veins 3-4 m wide contains massive, coarse-grained green fluorite with minor purple fluorite, and are cut by vuggy quartz veins, and vugs filled with kaolinite or lined with drusy barite, quartz, calcite, and fluorite.

It is suspected that the medium to coarse grained Coryell syenite veins occurring east of fluorite mineralization may be related to mineralization. This syenite contains large pink and green orthoclase.

The primary mineralization environment assigned to Rock Candy is a hydrothermal/epithermal vein/replacement deposit hosted in igneous rocks, and due to its possible formation relation to the syenite and that large fluorospar deposits have been recorded in association to carbonatitic formation (Okorusu, Namibia; Speewah, Australia; Bühn et al., 2003 and Alvin et al., 2004 respectively), the secondary mineralization environment assigned to this deposit is carbonatite-related.

References

1. Barlow, N., 2013. Eaglet; Minfile number: 093A 046., BC Geological Survey Ministry of Energy, Mines, and Natural Gas and Responsibility. http://minfile.gov.bc.ca/report.aspx?f=PDF&r=Minfile_Detail.rpt&minfilno=093A++046
2. Currie, K.L., Van Breemen, O., 1996. The origin of rare minerals in the Kipawa Syenite Complex, western Quebec; The Canadian Mineralogist, v. 34, (435-451).
3. deGroot, L, 2014. Rock Candy; Minfile number: 082ESE070., BC Geological Survey Ministry of Energy, Mines, and Natural Gas and Responsibility. http://minfile.gov.bc.ca/report.aspx?f=PDF&r=Minfile_Detail.rpt&minfilno=082ESE070
4. Denney, F.B., Guillemette, R.N., Lefticariu, L., 2015. Rare earth mineral cncentrations in ultramafic alkaline rocks and fluorite within the Illinois-Kentucky Fluorite District: Hicks Dome cryptoexplosive complex, southeast Illinois and northwest Kentucky (USA); Lasemi, Z., ed; Proceedings of the 47th Forum on the Geology of Industrial Minerals: Illinois State Geological Survey, Circular 587, (1-16).
5. Drs, 1993. Hastie Quarry and mill, plant in Hardin county in Illinois; USGS deposit ID: 10169305., U.S. Bureau of Mines. https://mrdata.usgs.gov/mrds/show-mrds.php?dep_id=10169305

6. Eldor carbonatite complex, carbonatite rare earth element deposit in Quebec, CA; USGS database, https://mrdata.usgs.gov/ree/show-ree.php?rec_id=24
7. Hartos, 1993. Barnett Mine past producer in Pope county Illinois; USGS deposit ID: 10169446., U.S. Bureau of Mines. https://mrdata.usgs.gov/mrds/show-mrds.php?dep_id=10169446
8. Jones, L, 2012b. Spar: Minfile number: 082M 007., BC Geological Survey Ministry of Energy, Mines, and Natural Gas and Responsibility. http://minfile.gov.bc.ca/report.aspx?f=PDF&r=Minfile_Detail.rpt&minfilno=082M++007
9. Jones, L., 2012a. Rexspar; Minfile number: 082M 021., BC Geological Survey Ministry of Energy, Mines, and Natural Gas and Responsibility. http://minfile.gov.bc.ca/report.aspx?f=PDF&r=Minfile_Detail.rpt&minfilno=082M++021
10. Meredith-Jones, S., 2007. Gem; Minfile number: 094M 002., BC Geological Survey Ministry of Energy, Mines, and Natural Gas and Responsibility. http://minfile.gov.bc.ca/report.aspx?f=PDF&r=Minfile_Detail.rpt&minfilno=094M++002
11. Plumlee, G.S., Goldhaber, M.B., Rowan, E.L., 1995. The potential role of magmatic gases in the genesis of Illinois-Kentucky Fluorospar deposits: Implications from chemical reaction path modeling; Society of Economic Geologists, Inc., Economic Geology, v. 90, (999-1011).
12. Wright, W.R., 1997. Mineralogy, petrology, petrogenesis, paragenesis and geochemistry of the Eldor carbonatite complex, Labrador Trough, Quebec, Canada; Master's Thesis University of Missouri-Rolla, (200 pgs).

Appendix D. Small-scale fluorite chemical variability

D.1. Introduction

The trace-element compositional variation in fluorite is inferred from optically heterogeneous fluorite as differently colored concentric/growth or sector zones. However, coloration in fluorite can be caused by a variety of factors such as growth rate, mineral inclusions, and lattice defects, and is not exclusively related to trace-element inclusion. Growth and sector zones observable by cathodoluminescence analyses, even in optically homogenous fluorite, is indicative of differing concentrations of trace-elements between these zones. In using the trace-element geochemistry of fluorite to infer genetic implications about formational environments, authors (Gagnon et al., 2003; Schwinn & Markl, 2005) using point-ablation (LA-ICP-MS) analytical methods have warned about chemical variability on the fluorite grain-scale while others (Vinokurov et al., 2014) cautioned against drawing deposit-wide formational conclusions from chemical analyses using single fluorite samples. These conditions may have been confirmed by the works of Beale et al., (2012), and Smolyanski et al., (2009) in which concentration differences of REE between temporally equivalent crystal sectors (|100| vs. |110| or |111|) were recorded. Mao et al., 2016b, however, determined that the chemical variability analyzed across a single fluorite crystal was less than that exhibited by all fluorite samples collected from the same deposit. Using compiled data, data on hand samples collected by FUS-ICP/MS analysis, and LA-ICP-MS analyses on a single fluorite crystal exhibiting differentially colored sector-zones, we will examine how trace-element chemical variability on the grain-scale and the sample-scale will affect the end goal of discriminating between different genetical fluorite varieties. Additionally, the REE-Y variability analyzed by FUS-ICP/MS of like-samples of different colors will also be examined.

D.2. Sample-scale

Sample-scale chemical variability in fluorite was tested by examining publication data where multiple analyses were reported for the same sample number, and FUS-ICP/MS

analytical data on fluorite hand samples separated by color. These data are compiled in Table D-1. Publications reporting multiple analyses of single samples include those on the Panxi Region carbonatite-related deposits, Daluxiang, Maoniuping, and Lizhuang (Xu et al., 2012), the Okorusu carbonatite-related deposit (Bühn et al., 2003), and the intrusion-related molybdenum deposit, Sweet Home Mine (Lüders et al., 2009). Hand samples from the BCGS collection included two where fluorite could be separated by color from the same possible paragenetical phases including purple and yellow fluorite from the Hastie Quarry (potential MVT) deposit, and purple and white fluorite from the Barnett Mine (potential MVT) deposit. REE analyses were normalized to carbonaceous chondrite (McDonough and Sun, 1995) for visual comparison and these patterns will be discussed herein, and values representing differences in visually observable patterns were quantified.

Table D-1 Data for sample-scale REE variability for reported fluorite analyses and analyzed fluorite including primary deposit type assignations, sample numbers, analysis counts per sample, variability of observed REE chondrite normalized patterns per sample, and analytical methods employed per publication.

Primary deposit type	Deposit	Sample	Count	Variability (REE chondrite-normalized patterns)	Analytical method
Carbonatite-related	Maoniuping Xu et al., 2012	ORE-2	3		ICP-MS
		ORE-4	6		
		ORE-6	2	La-Pr slope	
		MNP-135	2	La-Pr slope	
		MNP-150	2		
		MNP-151	2		
	Daluxiang Xu et al., 2012	DLX-23	3		ICP-MS
		DLX-24	4		
		DLX-27	2	Concentration	
		DLX-33	3	La-Pr slope	
	Lizhuang Xu et al., 2012	LZ-3	2		ICP-MS
		LZ-16	2		
		LZ-17	2		
	Okorusu Bühn et al., 2003	OK-1	14	Y anomaly gradient	ICP-MS
		OK-2	5	Y anomaly gradient, Concentration	
		OK-5	2		
Intrusion-related Mo	Sweet Home Mine Lüders et al., 2009	7	2		ICP-MS
		24	2	Ho-Lu slope	
		30	2	Ce, Pr, Nd	
MVT	Barnett Mine	28-12S-8E	2	Ce-Sm ratio, Eu anomaly magnitude	FUS-ICP/MS
	Hastie Quarry	3-12S-9E	2	Ce-Pr slope	FUS-ICP/MS

Overall, the REE chemical variability between multiple analyses of the same fluorite samples exhibited minor (less than one half order of magnitude) ranges in overall concentration (ΣREE-Y), while a few samples exhibited major differences approaching an order of magnitude including DLX-27 from Daluxiang, OK-1 from Okorusu, and 3-12S-9 from

Hastie Quarry, or reaching ranges of an order of magnitude of difference including OK-2 from Okurusu. This was measured visually by comparing chondrite-normalized spider diagrams and by calculating the effective ranges of total REE-Y concentration per sample. The ranges, calculated by finding the differences between logarithmic maximum and minimum values for total REE-Y content per sample analysis, are listed in Table D-2. The mean value of ranges for all 21 samples is 0.228, which is visually similar to samples 7 or 28-12S-8E seen in Figure D-1. The median value of ranges is 0.151.

Table D-2 Minimum and maximum values for ΣREE-Y of all analyses per sample as well as logarithmic transformations of these values and their differences representing ranges. Ranges of logarithmically transformed maximums and minimums of La/Pr ratios and calculations representing anomalous Y are also listed. Most ranges of ΣREE-Y are less than 0.5 except for DLX-27, 3-12S-9E, OK1, and OK2. Mean of values is 0.228 and median is 0.151. Most ranges of La/Pr are less than 0.3 except for DLX-33, ORE-6, 30, 28-12S-8E, and 3-12S-9E, and most values for Y anomalies are less than 0.3 except for OK1 and OK2. Mean of ranges for La/Pr is 0.157, and median is 0.096, and mean for anomalous Y ranges is 0.079, with a median of 0.028.

Sample	Min (ΣREE-Y)	Max (ΣREE-Y)	Log(Min)	Log(Max)	Range ΣREE-Y	La/Pr	Y anomaly
ORE-6	1720.4	1792.5	3.236	3.253	0.018	0.357	0.005
MNP-135	2275.7	2626.2	3.357	3.419	0.062	0.253	0.024
MNP-150	1420.7	1640.4	3.153	3.215	0.062	0.112	0.004
ORE-2	2025.5	2296.5	3.307	3.361	0.055	0.096	0.006
ORE-4	1370.7	2755.5	3.137	3.440	0.303	0.143	0.032
MNP-151	1457.2	1564.6	3.164	3.194	0.031	0.021	0.003
DLX-27	810.1	2752.0	2.909	3.440	0.531	0.034	0.099
DLX-33	1204.8	2616.6	3.081	3.418	0.337	0.434	0.022
DLX-23	1043.6	1075.2	3.019	3.032	0.013	0.069	0.034
DLX-24	920.7	1323.4	2.964	3.122	0.158	0.132	0.085
LZ-3	2575.4	2741.6	3.411	3.438	0.027	0.005	0.005
LZ-16	3165.2	4485.3	3.500	3.652	0.151	0.057	0.024
LZ-17	2341.7	2402.5	3.370	3.381	0.011	0.058	0.002
OK1	279.2	1179.1	2.446	3.072	0.626	0.083	0.390
OK2	126.7	1097.9	2.103	3.041	0.938	0.070	0.534
OK5	644.9	908.3	2.809	2.958	0.149	0.096	0.030
24	158.9	166.3	2.201	2.221	0.020	0.020	0.029
7	200.0	321.7	2.301	2.507	0.206	0.096	0.000
30	60.1	130.6	1.779	2.116	0.337	0.374	0.135
28-12S-8EP	11.9	21.1	1.074	1.325	0.251	0.313	0.106
3-12S-9EY	10.3	33.4	1.015	1.524	0.509	0.465	0.080
Mean					0.228	0.157	0.079
Median					0.151	0.096	0.028

-

Figure D-1 Chondrite-normalized (McDonough and Sun, 1995) REE-Y patterns for analyses on samples 7 from the Sweet Home Mine and 28-12S-8E from the Barrett Mine deposits visually depicting the average range of REE-Y sums from multiple analyses on single fluorite samples. Quantified REE-Y ranges are 0.206 and 0.251 respectively. The mean value for all REE-Y ranges for like samples is 0.228 and the figure visually represents a range showing the average amount of difference between multiple analyses of the same samples.

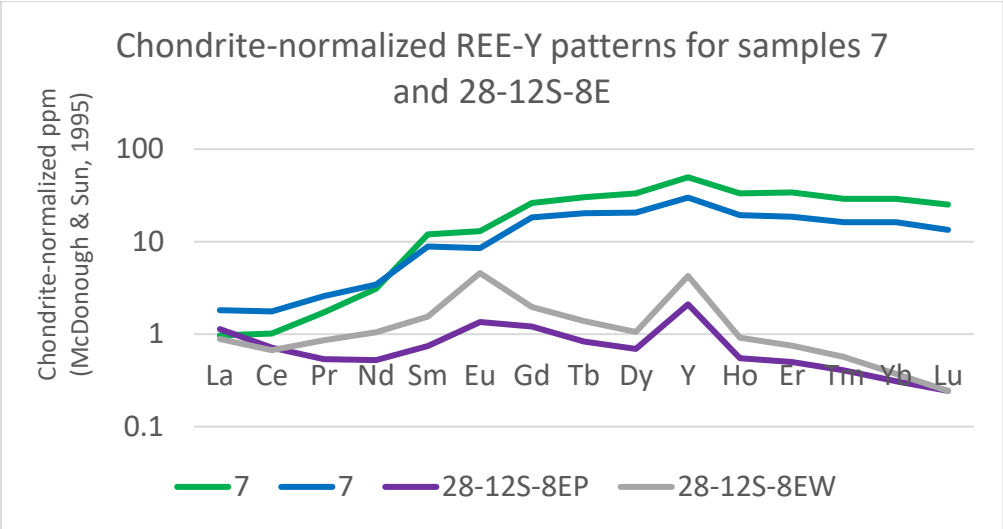

Even though the overall total REE concentrations varied per sample analysis, the overall REE patterns exhibited by analyses per sample were consistent with a few minor exceptions listed in Table D-1. These differences were primarily between LREE patterns between La and Pr, and the anomalous behavior of Y. These value ranges were quantified similarly to REE-Y as La/Pr and Y/((Dy+Ho)/2) and are displayed in Table D-2. The mean of ranges for La/Pr is 0.157 with a median of 0.096, and those for anomalous Y values are 0.0786 and 0.029 respectively. Observable differences in chondrite-normalized REE-Y spider diagram patterns listed in Table D-1 correspond with quantified differences listed in Table D-2, granting merit to this method of comparison. As indicated by the average values of ranges for both of these measures (La/Pr and anomalous Y), which were the only observable differences in chondrite-normalized REE-Y patterns between analyses of the same samples, the patterns observed per sample were generally consistent between analyses.

Patterns and concentrations exhibited between fluorite samples for the same deposit were variable due to sample representation. Each sample likely represents different formational conditions as they were likely sourced from different parts or phases of

paragenetical sequences of the deposits in question. Regardless, the overall patterns exhibited per sample were generally consistent while the overall ranges varied minimally on average. The chondrite-normalized REE-Y patterns exhibited by multiple analyses per sample were consistent regardless of variability between samples, as seen in the examples for the Lizhuang and Maoniuping deposits in Figure D-2 (with the exception of sample ORE-6 from Maoniuping). Pattern variability between samples was observed primarily for the behavior of LREE for all deposits analyzed listed in Table D-1.

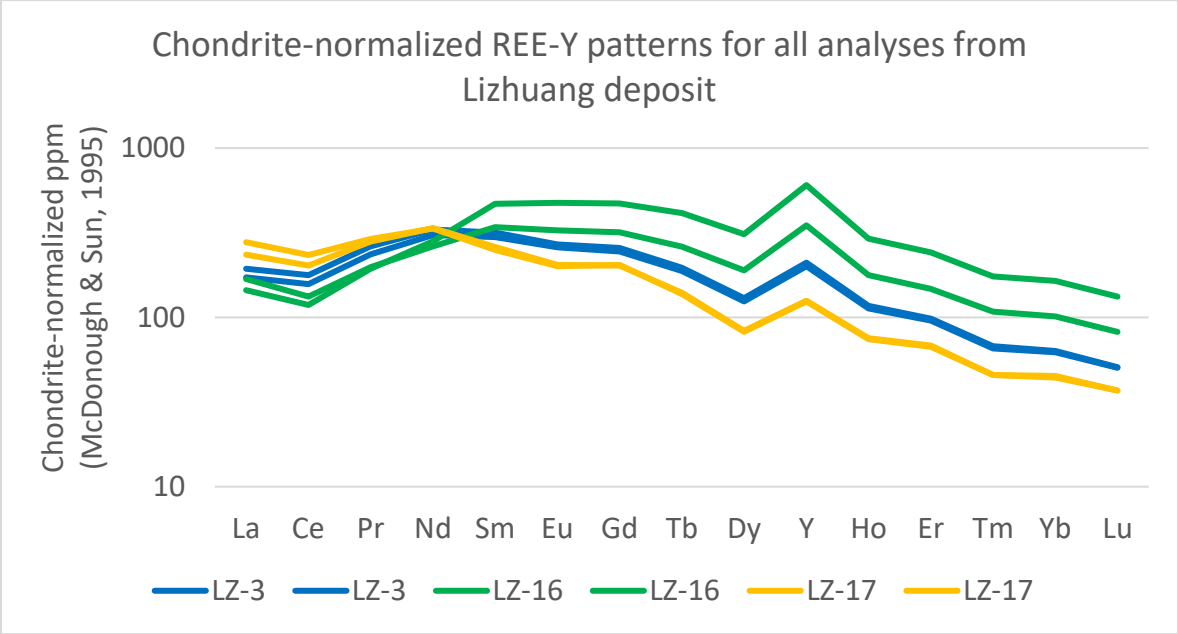

Figure D-2 Chondrite-normalized (McDonough and Sun, 1995) REE-Y patterns for all analyses per sample from the Lizhuang and Maoniuping deposits. Patterns per sample are consistent with minimal total REE-Y concentration variability. Patterns between samples are variable for LREE values.

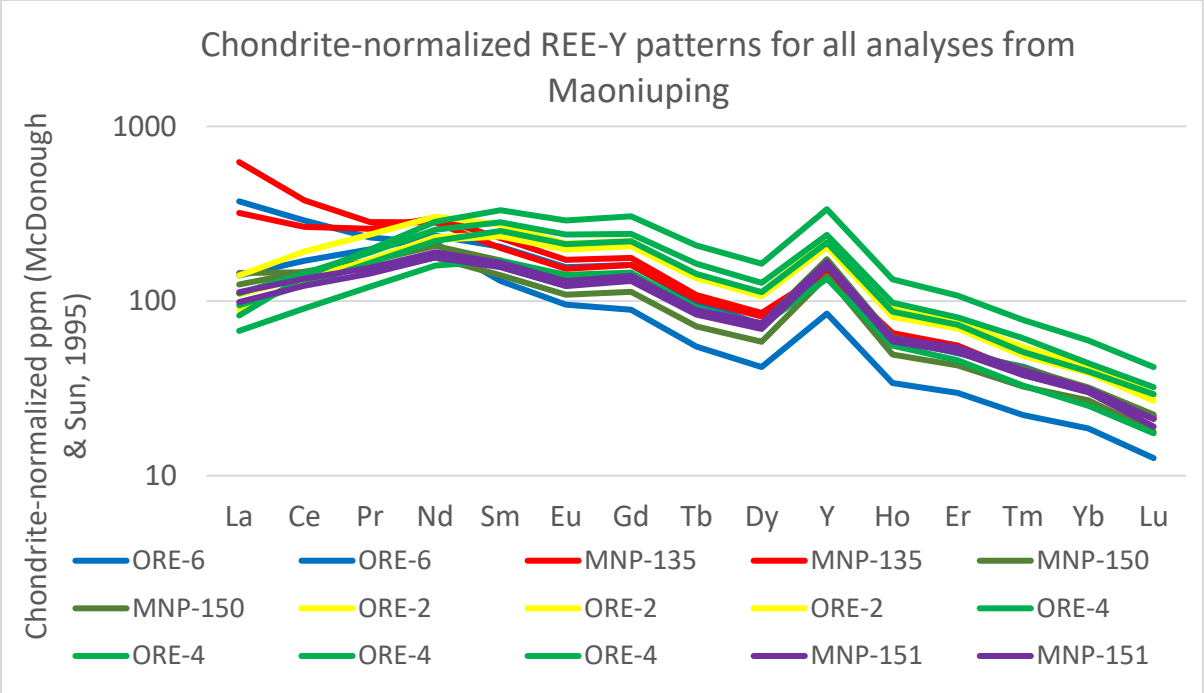

D.3. Grain-scale

Grain-scale chemical variability in fluorite was tested by examining publication data where multiple LA-ICP-MS analyses were reported for the same sample number, and by using LA-ICP-MS analytical data from a single fluorite crystal delimited by color. These data are compiled in Table D-3. Publications reporting multiple laser-ablation analyses from single crystal samples include those on the Motzfeldt and Ilímaussaq peralkaline silicate igneous deposits (Schönenberger et al., 2008). Additionally, laser ablation data was collected as a traverse across a single, optically heterogeneous crystal cleavage flake from the Hastie Quarry (potential MVT) deposit. REE-Y analyses were normalized to chondrite (McDonough and Sun, 1995) for visual comparison and these patterns will be discussed herein. Quantified values representing visually observable differences between LREE (La/Sm), MREE (Sm/Dy), and HREE (Dy/Lu) segments will also be discussed.

Table D-3 Data for grain-scale REE-Y variability of reported fluorite LA-ICP-MS analyses and analyzed fluorite including primary deposit type assignations, sample numbers, analysis counts per sample, variability of observed REE-Y chondrite normalized patterns per sample, and the ranges of logarithmically transformed ΣREE-Y values.

Primary deposit type	Deposit	Sample	Count	Variability (REE chondrite-normalized patterns)	Range ΣREE-Y
Peralkaline silicate igneous rock	Motzfeldt	JS88	3		0.1780
	Schönenberger et al., 2008	JS122	3		0.0224
		JS193	2		0.0154
		JS195	3		0.3196
		JS197	2		0.0281
		JS2	2	Concentration, LREE (La-Sm)	0.6737
		JS10	8	Concentration, HREE (Dy-Lu), LREE (La-Sm), anomalous Y	1.1124
		JS9A	9	Concentration, slight Y variation	1.3691
		JS6B	6	Concentration	0.9614
		JS4	4	Concentration	1.8703
		JS16	5	Concentration, HREE (Dy-Lu)	2.1186
		JS67	3	Concentration, LREE (La-Sm), HREE (Dy-Lu)	1.2771
		JS225	5		0.1888
		JS226	5	Concentration, LREE (La-Sm)	0.5164
		JS91A	3		0.0273
		JS86	4	Concentration, anomalous Y, Yb	1.2833
		JS168B	5		0.2941
		JS90	5		0.0811
		JS152A-B	3		0.4136
		JS34	9	Inconsistent, MREE (Sm-Dy)	0.7726
		JS183	7	Concentration, LREE (La-Sm), MREE (Sm-Dy)	0.5507
		JS110	3	Inconsistent	1.6860
		JS175	8	Concentration, LREE (La-Sm), HREE (Dy-Lu), anomalous Y	1.3646
		JS109	6	LREE (La-Sm)	0.3689
	Ilímaussaq	Ilm225	3		0.1255
	Schönenberger et al., 2008	Ilm260A	2		0.0641
		Ilm260B	2		0.0234
		Ilm259	3		0.0603

MVT	Hastie Quarry	XL30	15		0.2868
		Ilm325	5	LREE (La-Sm), MREE (Sm-Dy), HREE (Dy-Lu)	0.1320
		Ilm77	4		0.1036
		Ilm99	9	Concentration, LREE (La-Sm), Yb	0.8265
		3-12S-9E	22	Concentration	0.5081
Mean					0.5947
Median					0.3689

When comparing the REE chemical variability reported in analyses of single fluorite crystals and grains, we found that the ranges of overall ΣREE-Y concentrations were minimal (spanning less than 0.50 of an order of magnitude) for approximately half of the samples reported (15 out of 33). Nearly one-third of samples (10 out of 33) contained ΣREE-Y ranges nearly spanning an order of magnitude or greater (>0.80). The maximum range measured for logarithmically transformed ΣREE-Y values reported for single fluorite grains was 2.1186 for sample JS16 from the Motzfeldt peralkaline-silicate igneous deposit. The mean of ranges was 0.5947, with a median of 0.3689. Overall, ΣREE-Y concentration variability within fluorite measured on the grain-scale using LA-ICP-MS analytical techniques spans a range of values of approximately one-half of an order of magnitude.

Table D-4 Ranges of logarithmically transformed ratios representing LREE (La-Sm), MREE (Sm-Dy), and HREE (Dy-Lu) measured from single fluorite grains.

Sample	La/Sm	Sm/Dy	Dy/Lu
JS88	0.0082	0.0685	0.1542
JS122	0.0474	0.0375	0.0942
JS193	0.0416	0.0525	0.0078
JS195	0.0957	0.0655	0.2283
JS197	0.0355	0.0197	0.0085
JS2	0.4942	0.2472	0.1670
JS10	0.9255	0.5438	0.7099
JS9A	0.3297	0.1520	0.4970
JS6B	0.6211	0.2843	0.3718
JS4	0.1800	0.5959	0.7116
JS16	0.3487	0.5455	1.4567
JS67	0.8008	0.2632	0.4332
JS225	0.0457	0.0692	0.0580
JS226	1.6826	0.3863	0.3793
JS91A	0.0667	0.0366	0.0803
JS86	0.1333	0.4112	0.3742
JS168B	0.2446	0.1329	0.1281
JS90	0.0506	0.0815	0.0977
JS152A-B	0.1396	0.0072	0.1000
JS34	2.3347	1.9501	1.2111
JS183	1.5707	1.0269	0.3225
JS110	0.8739	0.9599	0.2869
JS175	1.2342	0.3540	0.7977
JS109	0.7937	0.2531	0.5804
Ilm225	0.0207	0.1090	0.2776
Ilm260A	0.0008	0.0398	0.0929
Ilm260B	0.0401	0.0548	0.0198
Ilm259	0.0787	0.0483	0.0052
XL30	0.1725	0.1404	0.2612
Ilm325	0.7146	0.6535	0.2727
Ilm77	0.9890	0.1878	0.3310
Ilm99	0.8692	0.1753	0.1903
3-12S-9EY	1.5037	0.2319	0.2700
3-12S-9EP	0.3424	0.3959	0.6320
Mean	0.5244	0.3112	0.3414
Median	0.2872	0.1815	0.2714

Overall, the chondrite-normalized (McDonough and Sun, 1995) patterns of REE-Y diagrams displayed relative visual consistency between multiple analyses on the same crystals/grains. Ranges of overall pattern components (LREE, MREE, HREE) quantified by calculating the differences between logarithmically-transformed ratios (La/Sm, Sm/Dy, Dy/Lu) were subject to stricter penalty since the overall ranges of ΣREE-Y spanned at least half an order of magnitude on average. Because the overall ranges between analyses per grain were great for at least half of all samples, small variations in REE segment patterns as visually observed, could result in a wide range of values for calculated ratios. This is true even if only one analysis pattern out of several crosses orders of magnitudes more than the rest like that for sample JS16 from the Motzfeldt deposit as seen in Figure D-3. Here the overall patterns appear relatively consistent, but the quantified ratio ranges are large at 0.3487, 0.5455, and 1.4567 for LREE, MREE, and HREE respectively. Even so, the vast majority of ranges for each REE-Y pattern segment were less than half of an order of magnitude, with only 11 samples containing a segment range nearing an order of magnitude (>0.8) or more. The mean and median values for LREE ranges are 0.5244 and 0.2872, with a close visual representation of the mean displayed in Figure D-4 between samples JS2 and JS6B with mean ranges of 0.4942 and 0.6211 respectively. Sample JS6B also exhibits a similar representation of the mean value (0.2843) for all MREE ranges which is 0.3112 with a median of 0.1815 as seen in Figure D-4. Finally, sample JS183 exhibits one of the highest values for LREE variability at 1.5707, but also displays a close-visual representation of the average HREE range for all samples at 0.3245 while the mean for all is 0.3414 with a median of 0.2714, seen in Figure D-5. Overall, the patterns displayed and ranges of ratios representing chondrite-normalized REE-Y pattern segments were consistent on the fluorite grain-scale.

Figure D-3 Chondrite-normalized REE-Y patterns for analyses of sample JS16 from Motzfeldt deposit. Patterns appear consistent, though quantified ranges of logarithmically transformed ratios representing LREE, MREE, HREE segments are large at 0.3487, 0.5455, and 1.4567, respectively.

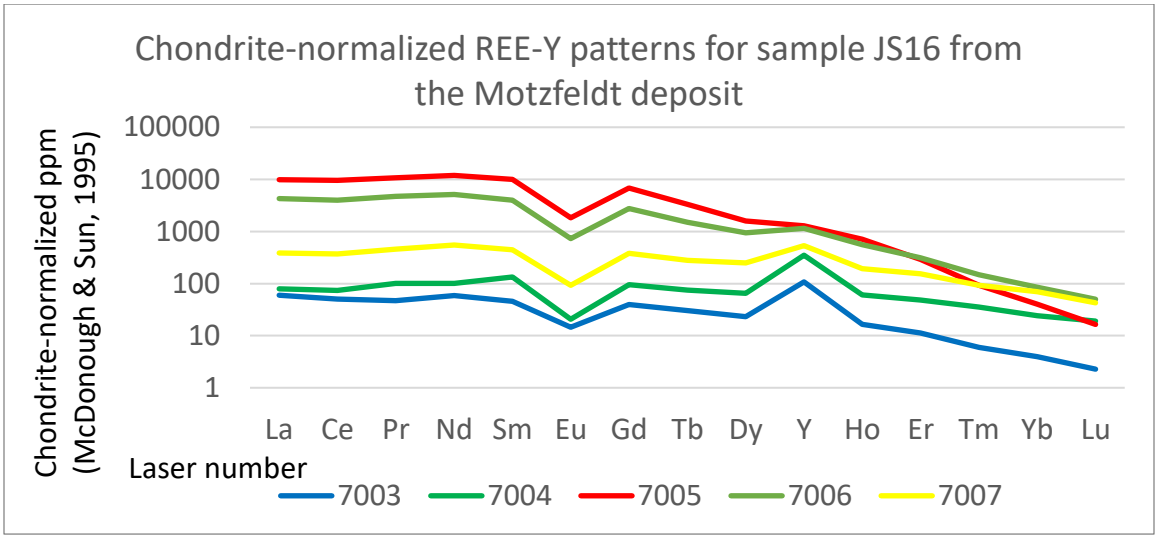

Figure D-4 Chondrite-normalized REE-Y patterns for all analyses of samples JS2 and JS6B from the Motzfeldt peralkaline-silicate igneous deposit. The mean of LREE variability represented by ranges of logarithmically transformed La/Sm ratios for all compiled and recorded point-analyses is 0.5244. The range of resultant La/Sm values for the sample JS2 is 0.4942 while the range for sample JS6B is 0.6211. These are the closest visual representations of the mean for LREE (La/Sm) variability of grain-scale analyses. The mean of ranges representing MREE variability (Sm/Dy) is 0.3112 while the range of values for sample JS6B is 0.2843 resulting in a close visual representation of the mean.

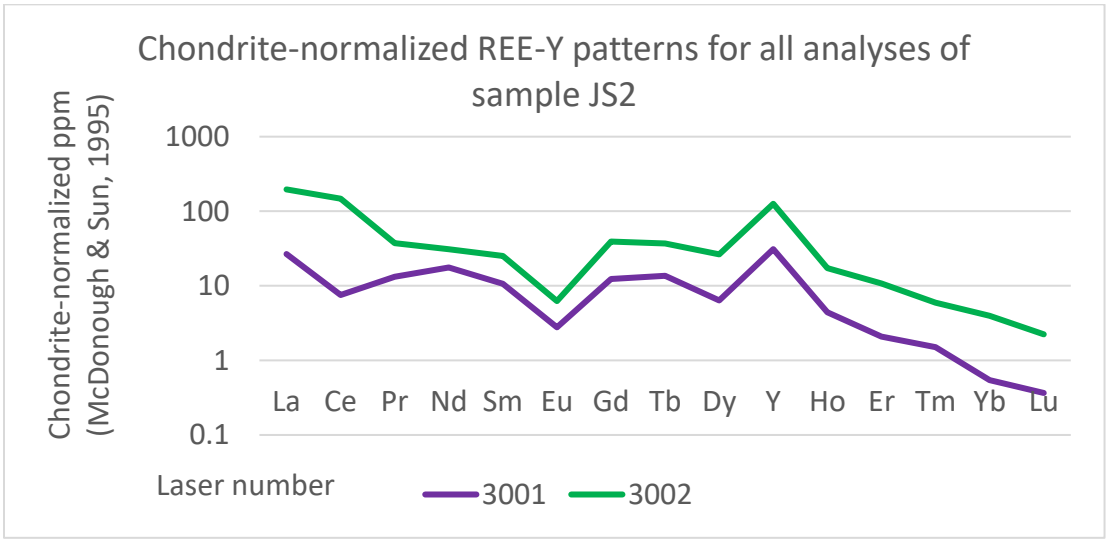

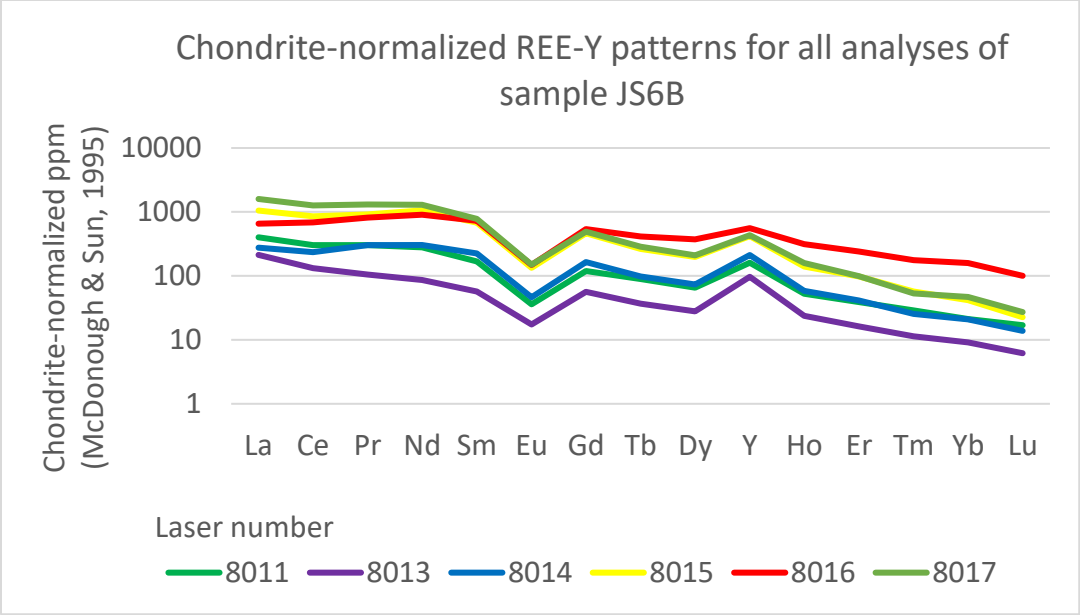

Figure D-5 Chondrite-normalized REE-Y patterns for all analyses of sample JS183 from the Motzfeldt peralkaline-silicate igneous deposit. The mean of HREE variability represented by ranges of logarithmically transformed Dy/Lu ratios for all compiled and recorded point-analyses is 0.3414 while the range for sample JS183 is 0.3245. Which is a close visual representation of the mean value.

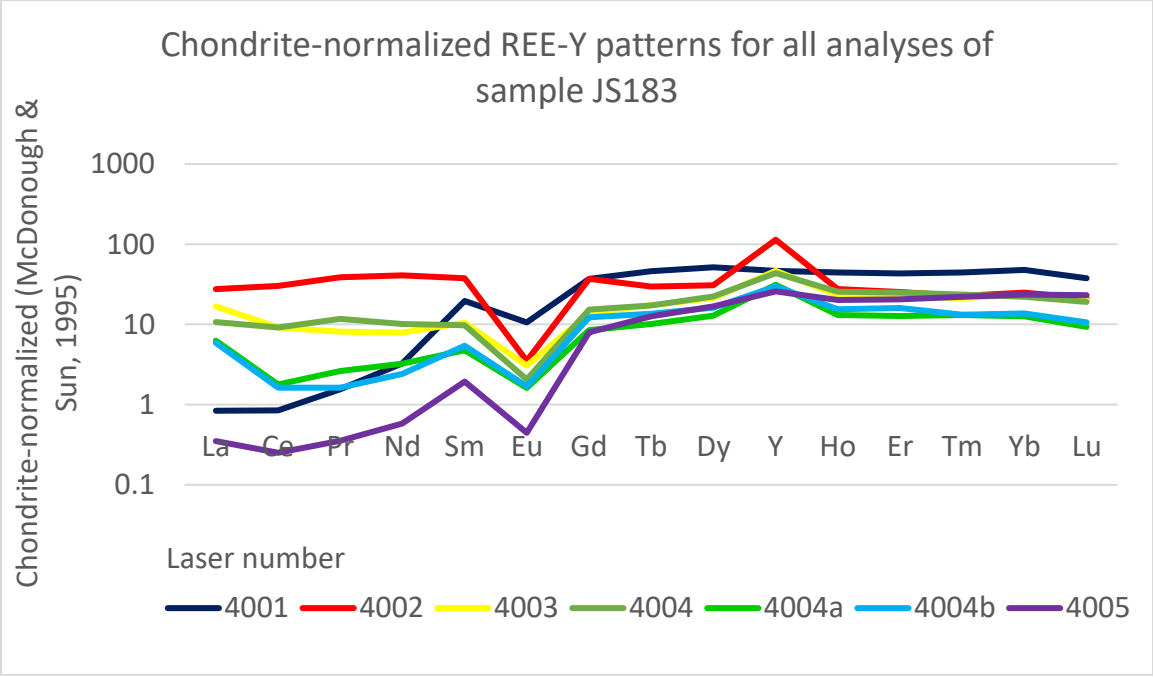

D.4. Color comparisons

The variability of REE-Y between color zones of the same fluorite samples and crystals was examined to assess possible correlation. A traverse of 22 LA-ICP-MS analyses were taken on a single fluorite cleavage chip across two zones of color, yellow and purple. This fluorite sample (3-12S-9E) was from the Hastie Quarry, probable MVT deposit, and displayed basal yellow fluorite growth zones that transitioned into purple in corners of cubes and on "top" cube edges. Additionally, samples 3-12S-9E and 28-12S-8E from the Hastie Quarry and Barnett Mine deposits were separated by color for FUS-ICP/MS analysis. The Hastie Quarry sample was split into yellow and purple portions, while the Barnett Mine sample was split into purple and white portions. Results of these analyses are displayed in Figure D-6 below.

Figure D-6 Chondrite-normalized (McDonough & Sun, 1995) REE-Y patterns for samples 3-12S-9E and 28-12S-8E from the Hastie Quarry and Barnett Mine deposits. Hastie Quarry deposit sample separated by yellow and purple fluorite, Barnett Mine sample separated by purple and white fluorite.

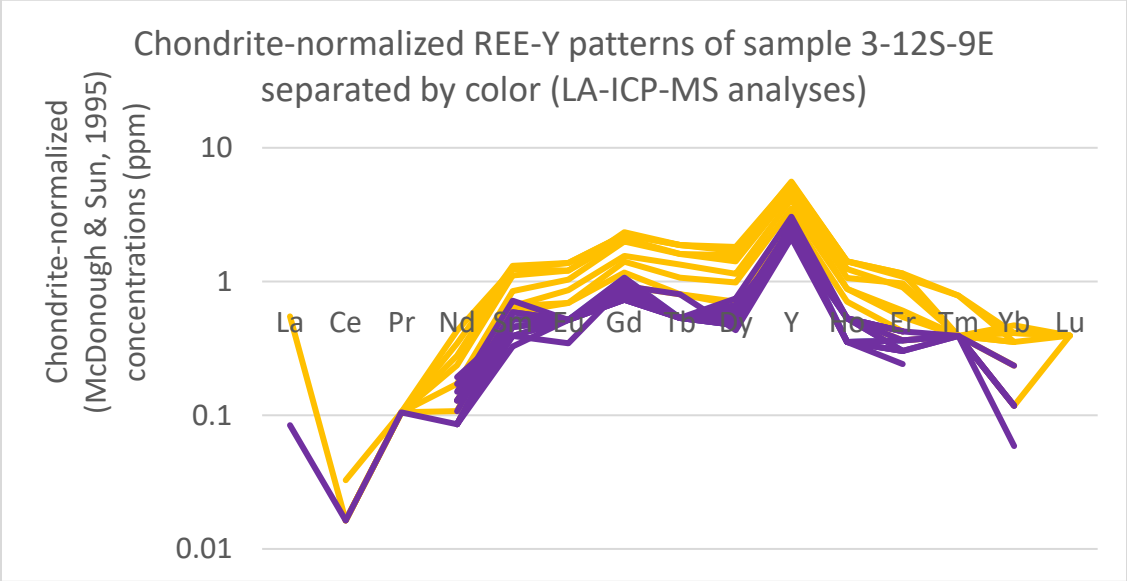

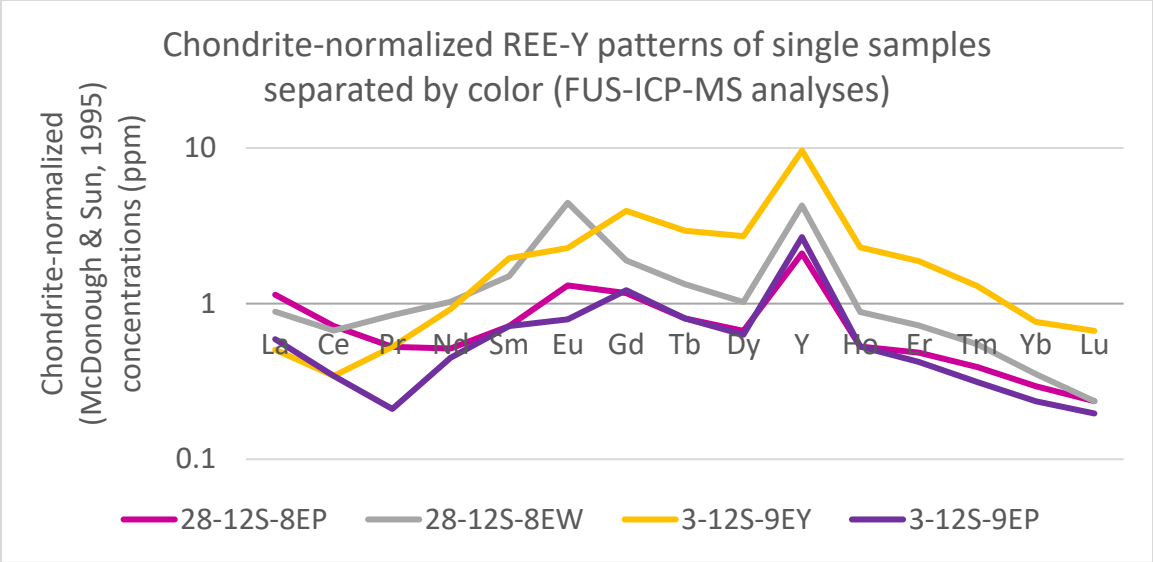

For analyses across yellow and purple, and purple and white fluorite for the Hastie Quarry and Barnett Mine deposits, chondrite-normalized REE-Y patterns display no major pattern differences between color groups. Overall concentrations vary according to fluorite color, generally showing less enriched purple fluorite opposed to white or yellow. However, overall concentrations span less than an order of magnitude. From this it can be determined that REE-Y systematics have little to no bearing on the coloration of fluorite for these samples.

D.5. Summary

The variability of REE-Y content of fluorite was examined on the sample- and grain-scales by comparing multiple analyses recorded for the same samples and grains/crystals from literature. These data were supplemented by test analyses performed in this study on fluorite of differing color from the same sample and likely paragenetical event, as well as the same crystal cleavage chip across color sectors. These data were compared visually, using carbonaceous chondrite-normalized (McDonough and Sun, 1995) spider diagrams, and quantitatively by comparing logarithmically transformed ranges of observed differences in overall concentration (REE-Y), anomalous Y, La/Pr ratios, and LREE (La/Sm), MREE

(Sm/Dy), and HREE (Dy/Lu) ratios. For measurements on both scales, it was clear that the overall concentration (REE-Y) could be quite variable, with ranges spanning orders of magnitude within the same sample or crystal but on average only spanning 0.228 and 0.5947 orders of magnitude respectively. Patterns on both scales were relatively consistent. These were first inspected visually, then elements were chosen to represent variability and so La/Pr ratios and Y anomalies were calculated on the sample-scale while La/Sm, Sm/Dy, and Dy/Lu ratios were calculated for the grain-scale. For each of these measurements, the average values for logarithmically transformed ranges were as follows: 0.157, 0.079, 0.5244, 0.3112, 0.3414.

From these measurements and observations, it can be concluded that overall, the variability of REE-Y concentration in fluorite is significant on the sample-scale, and especially on the grain-scale. However, chondrite-normalized patterns tend to be consistent on smaller-scale measurements of fluorite REE-Y content. Even though, the total concentration of REE-Y can span orders of magnitudes, the overall patterns are consistent and therefore, ratios representing segments of REE-Y patterns could offer a good measurement for comparison between fluorite samples. Additionally, on the fluorite grain-scale, measurements of LREE patterns were more variable on average than MREE and HREE patterns. This is perhaps due to the ease of LREE mobility in lower-temperature hydrothermal environments (Williams-Jones et al., 2009) or due to analytical traverses crossing crystal sectors with differing partitioning coefficients for LREE (Baele et al., 2012; Smolyanski et al., 2009; Bosze and Rakovan 2002). Finally, for samples analyzed within this study, variability in REE-Y concentrations could not be correlated to changes in fluorite coloration within the same samples.

D.6. References

1. Baele., J-M., Monin, L., Navez, J., André, L., 2012. Systematic REE partitioning in cubo-dodecahedral fluorite from Belgium revealed by cathodoluminescence spectral imaging and Laser Ablation-ICP-MS. 10th International Congress for Applied Mineralogy (ICAM), (23-30).
2. Bühn, B., Schneider, J., Dulski, P., Rankin, A. H., 2003. Fluid-rock interaction during progressive migration of carbonatitic fluids, derived from small-scale trace element and Sr, Pb isotope distribution in hydrothermal fluids; Geochimica et Cosmochimica Acta, v. 67, 23, (4577-4595).

3. Gagnon, J. E., Samson, I. M., Fryer, B. J., Williams-Jones, A. E., 2003. Compositional heterogeneity in fluorite and the genesis of fluorite deposits: insights from LA-ICP-MS analysis; Canadian Mineralogist, v. 41, (365-382).
4. Lüders, V., Romer, R. L., Gilg, H. A., Bodnar, R. J., Pettke, T., Misantoni, D., 2009. A geochemical study of the Sweet Home Mine, Colorado Mineral Belt, USA: hydrothermal fluid evolution above a hypothesized granite cupola; Mineralium Deposita, v. 44, (415-434).
5. Mao, M., Rukhlov, A.S., Rowins, S.M., Spence, J., Coogan, L.A., 2016b. Apatite trace element compositions: a robust tool for mineral exploration. Economic Geology, v. 111, (1187-1222).
6. McDonough, W.F., Sun, S.-s., 1995. The composition of the Earth; Chemical Geology, v. 120 (223-253).
7. Schönenberger, J., Köhler, J., Markl, G., 2008. REE systematics of fluorides, calcite, and siderite in peralkaline plutonic rocks from the Gardar Province, South Greenland; Chemical Geology, v. 247, (16-35).
8. Schwinn, G., Markl, G., 2005. REE systematics in hydrothermal fluorite; Chemical Geology, v. 216, (225-248).
9. Smolyanskii, P.L., Proskurnin, V.F., Bogomolov, E.S., 2009. Growth dissymmetrization of rare earth element distribution and the Sm-Nd isotope system in fluorite crystals of the Nordvik Deposit (Taymyr). Doklady Earth Sciences (Geochemistry), v. 424, No. 1, (86-89).
10. Vinokurov, S.F., Golubev, V.N.., Krylova, T.L., Prokof'ev, V.Yu., 2014. REE and fluid inclusions in zoned fluorites from Eastern Transbaikalia: distribution and geochemical significance. Geochemistry International, v. 52, no. 8, (654-669).
11. Williams-Jones, A.E., Migdisov, A.A., Samson, I.M., 2012. Hydrothermal mobilisation of the Rare Earth Elements – a tale of "ceria" and "yttria"; Elements, v. 8, (355-360).
12. Xu, C., Taylor, R. N., Li, W., Kynicky, J., Chakhmouradian, A. R., Song, W., 2012. Fluorite geochemistry from REE deposits in the Panxi region and Bayan Obo China; Journal of Asian Earth Sciences, v. 57, (76-89).

Appendix E. Compilation of REE data in fluorite

E.1. Data used to produce discrimination diagrams

McDonough & Sun (1995) chondrite values			0.237	0.613	0.093	0.457	0.148	0.056	0.199	0.036	0.246	1.57	0.055	0.16	0.025	0.161	0.025	-
-	Deposit name	Sample #	La	Ce	Pr	Nd	Sm	Eu	Gd	Tb	Dy	Y	Ho	Er	Tm	Yb	Lu	n = #
Peralkaline silicate igneous rock																		
Gardar Province	Motzfeldt	JS195	255	454	58.6	269	62.5	6.79	66.5	9.86	66.5	820	13.8	34.1	4.2	22.6	2.52	1
Schönenberger et al., 2008		JS193	209	353	47.1	212	51	4.14	56.7	9.18	59.3	774	11.9	32.4	3.67	20.6	2.26	1
LA-ICP-MS		JS10	3.63	1.74	0.8	3.37	1.66	0.2	3.79	0.65	3.88	93.3	0.58	1.16	0.11	0.47	0.05	1
(ppm)		JS9	1.24	3.4	0.73	3.34	2.06	0.39	2.42	0.65	4.04	34.5	0.7	1.77	0.23	2.08	0.19	2
Total (49 from 159)		JS6	214.25	426.2	65.89	314.75	62.21	4.71	54.75	5.82	29.12	416.5	5	9.205	0.8	4.52	0.41	1
		JS168	30.7	87.2	17.1	95.5	26.3	2.28	34.3	4.97	32.8	372	6.19	15	1.77	8.77	0.97	1
		JS152	18.4	57.5	13	84	30.4	3.09	43.5	6.65	42.6	795	8.48	20.7	2.22	12.4	1.24	1
		JS175	46.8	108	16.5	85.5	17	1.89	14.6	1.67	8.71	108	1.36	2.48	0.25	1	0.13	1
		JS109	13.4	33.3	4.97	20.4	4.94	1.83	3.81	0.48	2.68	10.7	0.28	0.75	0.06	0.26	0.02	2
		JS88A	170	358.5	60.6	310	67.2	4.89	66.05	7.36	43.5	434	6.91	14.9	1.37	6.37	0.54	1
		JS88C	135	288	48.9	242	54	3.12	50.9	6.17	32.3	377	5.24	11.6	1.2	5.41	0.55	2
		JS122A	187	387	60.75	314.5	65.9	4.65	65	7.49	42.85	491	7.53	16	1.53	7.05	0.69	1
		JS122B	179	373	60	322	68	5.07	63.2	7.65	41.2	471	6.96	14.9	1.32	6.16	0.66	2
		JS193	203	355	48.1	222	51.95	4.06	57.5	8.82	56.9	719.5	11.2	29.95	3.46	19.05	2.15	1

JS195C	218	400	56.4	256	63.5	4.63	63.3	9.25	58.1	718	11.8	28.9	3.69	21.2	2.31	2
JS195A	380	762.5	90.8	403.5	90.25	9.40	95.25	14.43	91.75	1032	17.9	43.35	4.87	24.9	2.64	2
JS197B	251.5	442	59.5	262.5	58.95	5.46	66	9.47	59.5	753	11.4	29.85	3.45	19.85	2.26	2
JS2	26.415	47.52	2.36	11.13	2.65	0.25	5.15	0.91	4.03	122.9	0.59	1.03	0.09	0.36	0.032	8
JS10	3.67	1.98	0.86	3.68	1.83	0.23	3.24	0.70	4.69	44.34	0.80	1.99	0.27	1.58	0.16	9
JS9A	5.113	13.71	2.59	13.74	10.61	2.14	16.96	3.90	26.40	140.8	4.18	9.62	1.18	6.59	0.60	6
JS6B	165.53	354.1	58.1	299.08	65.09	5.003	60.8	7.15	38.89	491.8	6.80	14.26	1.45	8.04	0.77	4
JS4	1294.4	2372	332	1558.3	303.8	19.16	244.8	22.12	94.3	795	12.42	19.59	1.41	5.04	0.43	5
JS16	696.02	1717	299.1	1621.4	430.1	30.24	399.4	37.68	141.7	1074	16.76	26.03	1.84	7.18	0.64	3
JS67	10.37	19.19	3.06	18.33	4.05	1.80	10.35	0.97	6.38	69.43	1.11	2.06	0.17	0.71	0.06	5
JS225	13.12	41.48	8.62	53	16.42	1.66	22.18	3.35	22.38	354.6	4.36	11.28	1.22	6.54	0.64	5
JS226	35.94	79.52	13.77	73.48	24.74	2.03	26.27	3.42	22.22	566.7	5.14	16.14	2.53	19.11	2.75	3
JS91A	5.79	18.3	3.84	24.1	7.74	0.91	11.07	1.75	12.1	181.6	2.51	6.33	0.76	4.17	0.44	1
JS38	1.69	1.92	0.31	1.91	1.36	0.17	3	0.53	4.23	103	0.918	2.57	0.29	2.06	0.24	4
JS86	3.92	8.64	1.08	5.8	3.14	0.38	6.15	1.01	5.95	117.4	1.04	2.26	0.25	1.32	0.14	5
JS168B	17.5	52.88	10.73	60.48	18.2	1.73	25.62	3.79	25.74	321.2	5.12	12.56	1.49	8.21	0.88	5
JS90	5.23	17.18	3.67	22.34	7.29	0.73	10.03	1.588	11.06	157.2	2.22	5.55	0.66	3.73	0.42	3
JS152A-B	12.57	39.13	8.35	52.9	18.13	1.85	25.03	3.85	25.3	429	5.11	12.68	1.39	7.66	0.79	6
JS34	166.17	0.461	0.19	267.48	55.8	4.61	8.73	1.45	7.98	4.65	2.81	0.23	4.3	0.81	5.08	7
JS183	2.32	4.66	0.86	4.47	1.89	0.19	3.75	0.76	6.05	75.8	1.32	3.77	0.57	3.86	0.5	3
JS110	15.89	31.7	4.49	14.67	3.26	0.61	4.25	0.62	3.55	23.61	0.62	1.55	0.17	0.87	0.1	8
JS175	14.93	33.16	5.27	26.93	9.52	1.74	11.62	1.66	8.66	70.78	1.30	2.41	0.23	1.04	0.11	6
JS109	9.26	22.84	3.37	13.7	3.54	1.22	2.62	0.41	2.20	10.64	0.3	0.59	0.07	0.29	0.02	1
Ilm325	1.63	1.59	0.26	1.09	0.24	0.03	0.35	0.07	0.05	35.32	0.12	0.33	0.031	0.17	0.02	3
Ilm259	118	234.5	36.8	195.5	41.9	3.99	45.5	5.73	33.05	398.5	6.36	13.55	1.48	7.49	0.8	1
Ilm133	183	282	42.3	217	48.5	4.42	55	6.89	45	415	9.1	21	2.12	10.3	1.08	1

	Ilímaussaq	XL30	259.93	515.33	85.89	424.47	88.8	8.31	87.83	10.22	57.48	651.4	10.31	22.1	2.26	10.44	1.03	5
		Ilm225	163	327	52.5	275	55.7	4.9	56.5	6.43	34.8	430	6.17	13	1.28	5.88	0.62	3
		Ilm259	120	243	36.9	200	47.2	4.63	52.6	7.42	39.5	423	7.47	18.1	1.85	9.03	0.96	3
		Ilm99	3.88	5.56	1.02	3.81	0.89	0.08	0.92	0.11	0.81	14.9	0.14	0.39	0.04	0.25	0.02	1
		Ilm77	0.01	0.01	0.01	0.03	0.04	0.01	0.07	0.01	0.09	16.7	0.02	0.06	0.01	0.03	0.01	1
		XL30	217	426	75.2	385	78.7	7.21	80.1	8.27	46.6	582	7.75	17.7	1.66	8.85	0.79	15
		Ilm225	124	237.5	35.35	190	40.45	3.555	42.5	4.88	29.8	392.5	5.54	13.8	1.44	7.74	0.84	1
		Ilm260A	134	261.5	42.15	210.5	45.1	3.9	46.5	5.46	31.35	404	5.71	12.85	1.37	7.12	0.71	2
		Ilm260B	137	259.5	39.55	195	41.6	3.975	49.45	6.37	37.4	409	6.89	16.05	1.66	8.11	0.83	2
Peralkaline…																		
Gallinas Mountains	Pinatosa	P1	73	68	5.9	26	4.4	1.2		0.8	4.8	179	1.3	4.2	0.6	3.4	0.4	9
Gagnon et al., 2003		P2	5510	4720	478	1350	140	32.6		14.7	65.8	676	14.1	41.1	6.3	38	4.2	11
LA-ICP-MS		P3	55100	45300	4760	13500	1070	264		95.7	613	2620	75.5	209	50.5	193	16.4	12
(µg/g)																		
Total (3 from 32)																		
Carbonatite-related			La	Ce	Pr	Nd	Sm	Eu	Gd	Tb	Dy	Y	Ho	Er	Tm	Yb	Lu	n = #
Panxi Region	Daluxiang	DLX-27	179	246	28.8	115	26	8.46	21.4	3.32	16.5	391	3.18	7.91	0.86	4.74	0.49	
Xu et al., 2012		DLX-27	45.2	66.3	7.86	39.2	9.63	2.11	7.73	1.21	5.72	112	1.19	3.05	0.29	1.69	0.2	
ICP-MS		DLX-30	77.4	139	15.8	66.3	12.3	3.67	10.9	1.5	6.2	115	1.32	3.63	0.35	2.14	0.26	
(ppm)		DLX-33	53.2	108	14.3	71.3	16.4	5.13	12.6	2.08	10.2	210	2.12	5.52	0.56	3.22	0.38	
Total (40)		DLX-33	30.7	81.8	12.4	69.5	16.9	5.26	12.1	2.14	10.7	227	2.23	5.92	0.6	3.47	0.41	
		DLX-23	34.2	74.9	10.8	57.9	13.5	4.25	10.2	1.77	8.79	180	1.85	4.89	0.5	2.92	0.34	
		DLX-23	33.1	76.9	11.2	58.5	13.9	4.41	10.8	1.84	9.33	190	1.94	5.34	0.54	3.09	0.37	
		DLX-23	28.9	75.5	10.7	56.7	13.3	4.26	10.4	1.79	9.29	204	1.92	5.2	0.54	3.25	0.39	

	DLX-24	33.2	84.3	12.6	67.6	15.6	4.97	11.7	2.01	9.91	290	2.12	5.68	0.61	3.38	0.41	
	DLX-24	36.3	87.5	12.7	69.5	15.9	4.9	11.7	2.02	10.1	242	2.14	5.67	0.59	3.45	0.41	
	DLX-24	33.3	87.7	13.6	72.7	17	5.31	12.5	2.23	11.4	314	2.42	6.37	0.67	3.89	0.46	
	DLX-24	31.1	67.9	9.37	49.8	11.1	3.5	8.73	1.47	7.47	183	1.56	4.17	0.43	2.55	0.3	
	DLX-33	166	273	24.7	112	25.2	8.14	20.6	3.23	15.43	328	3.08	7.72	0.75	4.11	0.48	
Maoniuping	ORE-6	88.2	177	21.5	98	19.3	5.37	17.7	1.98	10.3	133	1.85	4.77	0.55	3	0.31	
	MNP-135	148	231	26.3	129	29.8	8.6	32	3.69	20.1	237	3.49	8.85	0.93	4.92	0.54	
	ORE-5	43.1	97.9	16.6	100	36.1	12	43.7	5.41	29.8	379	5.28	12.5	1.42	7.64	0.78	
	MNP-96	61.2	133	19.5	113	38.7	12.7	47.4	5.88	32.6	431	5.74	14.7	1.71	8.09	0.85	
	MNP-127	36.9	99.3	15.4	85.2	18.8	5.13	18.5	2.09	11.6	175	2.16	5.56	0.67	3.75	0.41	
	MNP-132	47.4	105	14.9	80.6	20	5.73	21.5	2.6	14.1	194	2.58	6.51	0.79	4.31	0.44	
	MNP-135	75.7	163	24.1	137	34	9.71	35.1	3.9	21	232	3.57	8.89	0.96	4.87	0.52	
	MNP-150	34.3	89.6	14.1	81	20.8	6.12	22.5	2.58	14.4	218	2.7	6.85	0.8	4.34	0.44	
	ORE-2	21.3	80.5	16	106	35.7	11.5	42	5.08	27.7	350	4.92	12.2	1.35	6.8	0.72	
	ORE-2	25.9	83.8	15.6	102	34.7	11.1	41.1	4.87	27.1	343	4.81	12	1.34	6.56	0.7	
	ORE-2	33.2	118	22.3	139	40.6	12	44	4.9	26.2	320	4.43	11.1	1.2	6.26	0.66	
	ORE-4	26.2	88.4	17.6	117	41.8	13.5	48.3	5.9	31.2	376	5.33	12.9	1.51	7.09	0.79	
	ORE-4	22.4	75.9	15.3	101	37.3	11.9	43.8	5.16	27.6	340	4.75	11.7	1.26	6.36	0.72	
	ORE-4	19.6	84.7	18.3	130	48.9	16.3	60.9	7.51	40.3	527	7.26	17.2	1.92	9.56	1.03	
	ORE-4	16	55.6	11.2	73	25.2	7.94	28.9	3.32	17.8	211	3.04	7.32	0.81	4.05	0.43	
	ORE-6	33.2	104	18.4	108	30.3	8.8	32	3.57	18	233	3.33	8.02	1.04	5.01	0.53	
	MNP-69	19.2	74	14.9	102	40.1	13.4	51	6.62	37.3	477	6.78	16.4	1.85	9.59	0.99	
	MNP-150	29.5	90.1	15.7	94.5	25.3	7.46	28.1	3.29	18.2	272	3.39	8.35	1.02	5.15	0.55	
	MNP-151	26.6	82.4	14.4	86.8	24.5	7.3	27.7	3.2	18.4	262	3.35	8.66	0.99	5.06	0.52	
	MNP-151	23.4	75	13.3	81.2	23.1	6.85	25.9	3.02	17	248	3.21	8.15	0.93	4.83	0.47	
Lizhuang	LZ-3	46	109	24.4	151	46.8	15.2	51.1	7.08	31.9	331	6.38	15.7	1.67	10.2	1.25	

		LZ-3	40.8	96.5	21.9	140	44.2	14.6	48.8	6.8	30.6	315	6.18	15.3	1.62	10	1.24	
		LZ-6	63.4	128	27	166	50.1	15.8	53.5	7.11	30.7	308	6.19	15.5	1.66	10.4	1.28	
		LZ-16	40	81.3	18.4	120	50.4	18.4	63.2	9.46	46.6	549	9.71	23.6	2.67	16.3	2.02	
		LZ-16	34.3	72.6	18	129	69.4	26.7	93.7	14.9	76.3	949	15.9	38.7	4.32	26.4	3.26	
		LZ-17	65.9	143	26.9	153	37	11.3	40.6	4.96	20.2	195	4.06	10.7	1.13	7.1	0.91	
		LZ-17	55.7	124	26	154	38.6	11.5	40.2	5.05	20.5	197	4.12	10.9	1.13	7.26	0.91	
Carbonatite-related																		
Bayan Obo	Bayan Obo	BY-1	42.8	97.8	11	38.3	5	1.82	6.58	1.31	9.04	210	2.46	6.52	0.69	3	0.3	
Xu et al., 2012		BY-2	10.2	21.3	2.66	10.6	1.47	0.6	2.55	0.6	5.88	152	1.58	4.5	0.5	2.32	0.25	
ICP-MS		BY-4	170	38.8	41.6	132	10.8	2.37	8.8	1.16	6.93	140	2.04	6.19	0.64	3.22	0.32	
(ppm)		BY-11	22.6	34.4	4.06	15.9	3.2	1.45	6.02	1.56	13.9	217	3.93	10.1	1	4.56	0.43	
Total (11)		BY-12	84.2	116	11.7	38.4	4.16	1.18	4.91	0.95	7.92	202	2.54	7.36	0.78	3.45	0.29	
		BY-5	18.1	46.4	6.2	23.9	3.75	1.24	4.4	0.86	6.15	69.8	1.61	4.42	0.51	2.19	0.21	
		BY-6	181	406	59.5	200	18.6	3.66	11.4	1.43	4.93	28.1	0.97	2.39	0.14	0.59	0.03	
		BY-7	266	616	72.8	271	34.6	9.55	28.8	3.9	14.2	108	2.27	5.16	0.43	2.25	0.25	
		BY-8	214	369	37.5	127	14.7	3.31	12	1.47	6.37	68.1	1.28	3.18	0.29	1.34	0.12	
		BY-9	166	389	45.8	165	19.2	4.53	15.2	2.04	7.7	71.7	1.42	3.73	0.32	1.54	0.16	
		BY-10	461	1365	151	437	36.6	10.3	37.3	5.35	25.4	207	4.59	11.4	0.93	4.14	0.43	
Carbonatite-related																		
Yungul carbonatite complex	Speewah Fluorite	MA158a	2.88	5.12	0.67	3.76	1.62	1.02	4.63	0.73	4.42		0.79	1.8	0.19	1.02	0.11	
Alvin et al., 2003		MA158b	21.48	40.84	5.55	30.01	7.54	1.76	7.44	1.23	7.8		1.53	3.8	0.41	2.2	0.24	
ICP-MS		MA158c	2.18	3.99	0.64	4.14	2.56	1.9	7.37	1.2	7.31		1.28	2.98	0.33	1.5	0.17	
(ppm)		MA158d	11.51	18.85	2.45	13.32	3.91	1.08	5.25	0.8	4.59		0.86	2.16	0.23	1.23	0.13	
Total (7)		MA158e	18.29	31.85	4.18	21.37	5.69	1.55	6.71	1.07	6.61		1.3	3.2	0.36	1.88	0.21	
		MA158f	11.87	18.88	2.62	13.72	4.06	1.2	5.6	0.86	4.88		0.95	2.29	0.24	1.32	0.13	

		Replacement	40.8	89.9	10.2	44.4	15.1	4.1	22	3.6	21		3.6	8.3	0.9	3.8	0.4	
Carbonatite-related																		
Okorusu carbonatite complex	Okorusu	OK1-9	81	137	14	44	7.5	2.3	7.4	1.1	6.9	63	1.5	4.7	0.74	4.6	0.59	
Bühn et al., 2003		OK1-8	74	125	12	37	6	1.9	5.6	0.87	5.5	44	1.2	4	0.65	4.2	0.55	
ICP-MS		OK1-7	71	119	12	35	5.6	1.8	5.2	0.8	5.1	40	1.1	3.7	0.6	3.9	0.52	
(ppm)		OK1-6	60	100	9.6	28	4.7	1.4	4.2	0.67	4.5	32	1	3.4	0.56	3.8	0.51	
Total (22)		OK1-5	55	89	8.4	24	3.8	1.2	3.4	0.56	3.8	24	0.86	2.9	0.5	3.5	0.49	
		OK1-4	53	83	7.9	23	3.5	1.1	3.2	0.53	3.5	21	0.8	2.8	0.49	3.5	0.49	
		OK1-3	41	68	6.4	18	2.8	0.84	2.4	0.41	2.8	16	0.66	2.3	0.43	3.3	0.48	
		OK1-2	18	32	3.1	8.9	1.4	0.45	1.2	0.22	1.6	6.4	0.4	1.5	0.3	2.4	0.35	
		OK1-21	72	127	13	39	6.7	2.1	6.2	1	6.1	50	1.3	4.4	0.71	4.4	0.57	
		OK1-18	52	91	9	26	4.2	1.3	3.7	0.6	4	27	0.91	3.1	0.53	3.5	0.47	
		OK1-15	59	100	9.7	28	4.6	1.4	4.1	0.66	4.4	32	1	3.3	0.56	3.8	0.51	
		OK1-13	46	78	7.5	22	3.5	1.1	3.1	0.51	3.5	21	0.82	2.8	0.51	3.7	0.52	
		OK1-11	31	52	5.1	15	2.4	0.72	2	0.36	2.6	12	0.61	2.2	0.43	3.3	0.48	
		OK1-10	20	35	3.4	10	1.7	0.5	1.4	0.25	1.8	7.6	0.44	1.7	0.35	2.7	0.39	
		OK2-5	84	125	12	37	6.2	2	6.3	0.97	6.2	57	1.4	4.5	0.7	4.4	0.55	
		OK2-4	73	117	12	36	6.6	2.1	6.8	1	6.6	66	1.5	4.7	0.72	4.6	0.6	
		OK2-3	57	90	8.9	27	4.5	1.4	4.5	0.7	4.5	36	1	3.4	0.58	4	0.55	
		OK2-2	25	43	4.2	12	1.8	0.59	1.7	0.29	2.1	11	0.49	1.8	0.35	2.6	0.39	
		OK2-1	9.2	16	1.4	3.8	0.55	0.16	0.41	0.08	0.57	1.8	0.15	0.6	0.12	1	0.16	
		OK3	37	55	6.5	23	6	2.3	7.4	1.3	8.8	60	2	6.9	1.1	7.2	0.9	
		OK5-1	47	98	12	43	7.4	2.3	6.3	0.82	4.8	35	1.1	3.7	0.71	5.6	0.81	
		OK5-2	22	50	7	28	6.7	2.3	6.5	0.88	5.2	39	1.1	4	0.76	5.7	0.82	
Carbonatite-related																		

Arco de Ponta Grossa alkaline complex	Mato Preto	P81B	15113	18869		4416	453.1	94.3	241.1		81.5	3360	17.4	38.7		15.4	1.7	
Ventura Santos et al., 1996		29DB34	2881	3017		550.2	59.3	14.4	49.8		38.7	520	6.8	16.6		12	1.5	
ICP-MS		P30A	699	1178		411.8	67.5	17.3	43.8		27	440	4.8	12.3		9.6	1.2	
(ppm)		P34B	1670.1	2121		670.4	96.9	24.6	66.6		29.6	392	5.1	11.9		7.3	0.85	
Total (12)		P70B	761.8	1241		407.6	69	21.3	71.6		47.2	520	6.9	13.7		6.6	0.79	
		TH2	832.6	1573		707.8	121.3	32	70.7		33	840	6.3	15.9		9.7	1.09	
		GAL01	126.3	183.1		65.4	10.2	2.7	7.2		6.4	168	1.3	3.9		3.5	0.43	
		P34C	2122	2522		421.4	35.8	6.9	24.6		8.9	164	1.92	4.7		2.5	0.43	
		P71C	501.3	841.5		349.3	50.2	14.2	31.52		14.1	200	2.6	5.4		2.4	0.29	
		71DB60	55.1	79.8		32.4	6.8	2.5	9.1		13	280	2.7	7.8		7.9	1.02	
		P71D	3501	21.9		50.1	9.5	3	8.5		8.9	368	1.9	5.7		5.3	0.72	
		T1C	15.8	28.1		26.1	7.9	3.3	11.7		25.5	164	6.5	24.2		22.7	2.7	
Carbonatite-related																		
Gagnon et al., 2003	Deep Purple/ RCC	dis	25400	19200	1620	3660	117	27.5		7.8	22.5	211	4.5	12.5	2.3	17	2.4	19
LA-ICP-MS		vb	51.7	1620	17.7	83	31.7	16.1		13.6	111	469	23.9	65.8	10.4	64.1	8.7	44
(µg/g)																		
Total (2 from 63)																		
Carbonatite-related																		
Baroda	Amba Dongar	AD066Z	7	25		9	3.3	2.2		2.2		148				7.9	1.04	
Palmer & Williams-Jones, 1994		AD050B	5	17		9	2.2	1.4		1.1		90				3.5	0.46	
INAA		AD066XB	9	27		11	2.7	1.8		1.9		151				8.2	0.95	
(ppm)		AD066W	12	33		11	2.5	1.3		0.9		78				3	0.4	
Total (7)		AD008A	6	27		8	3.3	1.8		1.7		74				12.7	1.99	
		AD066XY	3	13		5	1.3	0.8		0.9		59				8.8	1.3	

		AD050C	5	22		9	3.7	2.7		2.8		185				11.9	1.66	
Mississippi Valley Type																		
			La	Ce	Pr	Nd	Sm	Eu	Gd	Tb	Dy	Y	Ho	Er	Tm	Yb	Lu	n = #
South Pennine orefield	Treak Cliff Caverns	TCC-1	1.2	1.35	0.32	1.57	0.45	0.12	0.88	0.17	1.1	23.9	0.26	0.75	0.09	0.44	0.05	
Bau et al., 2003		TCC-2	0.69	0.97	0.23	1.26	0.35	0.1	0.67	0.11	0.79	18.4	0.18	0.51	0.06	0.25	0.03	
ICP-MS		TCC-3	0.79	1.01	0.23	1.22	0.33	0.1	0.63	0.1	0.74	17.8	0.17	0.48	0.05	0.24	0.03	
(µg/g)		TCC-4	0.57	0.63	0.15	0.75	0.17	0.05	0.29	0.04	0.32	8.3	0.07	0.19	0.02	0.07	0.01	
Total (47)		TCC-5	0.79	0.95	0.24	1.29	0.33	0.07	0.57	0.08	0.6	14.3	0.14	0.37	0.04	0.15	0.02	
		TCC-6	0.84	1.2	0.33	1.75	0.58	0.15	1.13	0.19	1.33	27.3	0.31	0.88	0.1	0.45	0.05	
		TCC-7	0.8	1.2	0.31	1.67	0.49	0.13	0.93	0.15	1.04	20.9	0.24	0.66	0.07	0.35	0.04	
		TCC-8	0.91	1.37	0.36	1.96	0.63	0.18	1.28	0.22	1.53	30.6	0.36	1	0.12	0.54	0.07	
		TCC-9	0.98	1.43	0.36	1.97	0.62	0.17	1.26	0.21	1.51	30.3	0.34	1.01	0.11	0.54	0.07	
		CT-1a	0.51	0.53	0.12	0.59	0.12	0.04	0.22	0.03	0.2	5.38	0.04	0.11	0.01	0.04	0	
		CT-1b	1.24	1.81	0.44	2.35	0.62	0.16	1.14	0.19	1.32	27.3	0.31	0.9	0.1	0.48	0.06	
		CT-2a	0.54	0.89	0.23	1.42	0.57	0.18	1.33	0.23	1.71	35.6	0.4	1.15	0.13	0.61	0.07	
		CT-3b	0.91	1.36	0.35	1.94	0.6	0.17	1.18	0.2	1.42	29.1	0.34	0.97	0.11	0.54	0.06	
		CT-5	0.54	0.94	0.26	1.66	0.71	0.23	1.72	0.3	2.22	46.5	0.52	1.52	0.17	0.83	0.1	
		CT-21a	1.17	1.61	0.38	1.87	0.54	0.11	0.87	0.13	0.9	18.9	0.2	0.57	0.06	0.28	0.04	
		CT-10a	1.12	1.61	0.42	2.33	0.75	0.21	1.48	0.25	1.79	37.2	0.43	1.2	0.14	0.65	0.08	
		CT-10c	0.61	1.03	0.27	1.55	0.55	0.17	1.16	0.19	1.38	27.5	0.32	0.92	0.1	0.5	0.06	
	Dirtlow open-pit	DO-19a	0.82	1.2	0.33	1.68	0.45	0.14	0.87	0.14	1.03	18.4	0.23	0.65	0.07	0.39	0.05	
		DO-19b	0.76	0.95	0.27	1.26	0.39	0.14	0.82	0.12	0.88	17.1	0.2	0.53	0.06	0.28	0.04	
		DO-20	1.51	1.96	0.45	2.25	0.57	0.14	0.94	0.16	1.07	20.5	0.25	0.71	0.07	0.39	0.05	
		DO-4	0.33	0.43	0.08	0.46	0.2		0.47	0.07	0.5	12.4	0.11	0.28	0.03			
		DO-7	1.06	1.53	0.38	2	0.57	0.16	1	0.17	1.14	20.9	0.25	0.71	0.08	0.44		

North Pennine orefield	Lady Walsh Mine	DO-8	0.61	0.69	0.15	0.74	0.2	0.08	0.44	0.07	0.46	11.4	0.1	0.26	0.03	0.14	0.02	
		DO-9a	0.81	1.22	0.3	1.66	0.54	0.14	1.17	0.2	1.41	27.3	0.32	0.93	0.1	0.52	0.07	
		DO-9c	0.66	1.02	0.27	1.62	0.59	0.15	1.26	0.22	1.55	29.8	0.36	1.01	0.11	0.57	0.07	
		LW-12a	0.48	0.76	0.15	0.74	0.21	0.07	0.45	0.07	0.49	12.7	0.11	0.28	0.03	0.13	0.01	
		LW-12b	0.24	0.4	0.09	0.52	0.2	0.08	0.49	0.08	0.59	13.7	0.13	0.34	0.03	0.15	0.02	
		LW-12c	2.73	3.43	0.52	2.14	0.4	0.1	0.52	0.07	0.47	8.51	0.1	0.26	0.03	0.15	0.02	
		LW-13	1.74	2.28	0.35	1.33	0.26	0.08	0.39	0.06	0.37	7.15	0.08	0.2	0.02	0.1	0.01	
		LW-14	0.55	0.86	0.17	0.8	0.24	0.09	0.55	0.08	0.56	13.9	0.12	0.31	0.03	0.15	0.02	
		LW-17	0.4	0.68	0.13	0.64	0.18	0.07	0.46	0.08	0.5	13	0.11	0.29	0.03	0.13	0.01	
	Mitchell Bank	MB-31a	0.91	1.37	0.34	1.86	0.54	0.13	1.11	0.18	1.28	24.6	0.3	0.8	0.09	0.44	0.05	
		MB-31b	0.95	1.12	0.24	1.24	0.39		0.79	0.12	0.84	19.4	0.17	0.44	0.05	0.27		
		MB-32	0.97	1.65	0.38	2.17	0.91	0.25	1.96	0.35	2.49	44.1	0.57	1.64	0.2	0.99	0.12	
		MB-33	0.78	1.13	0.29	1.7	0.5	0.13	1.1	0.18	1.26	23.2	0.28	0.77	0.08	0.4	0.04	
		MB-34a	0.68	0.99	0.26	1.46	0.5	0.13	1.05	0.18	1.32	27.2	0.31	0.88	0.1	0.54	0.06	
		MB-34b	0.76	1	0.22	1.04	0.29	0.12	0.74	0.12	0.8	21.1	0.17	0.45	0.05	0.2	0.02	
	Smalldale	SD-6	0.71	0.8	0.14	0.63	0.16	0.06	0.32	0.04	0.25	6.62	0.05	0.12	0.01	0.04	0.01	
	Pindale	PD-18a	0.42	0.7	0.12	0.56	0.14	0.06	0.38	0.06	0.42	10.2	0.09	0.24	0.03	0.12	0.02	
	Frazer's Hush	FH-1	13.6	25.1	3.1	13.9	4.71	4.66	8.71	1.65	9.29	186	1.55	3.67	0.39	2.07	0.24	
		FH-2	10.1	19.1	2.44	11.4	4.52	5.95	10.3	1.92	10.8	227	1.84	4.11	0.39	1.82	0.21	
		FH-3	16.4	36.6	5.72	31.5	19.1	29.4	41.4	7.4	38	435	5.85	12.5	1.26	6.33	0.78	
		FH-4	9.24	17.2	2.28	11.6	5.56	8.03	13.6	2.63	14.6	272	2.44	5.41	0.51	2.45	0.27	
		FH-5	12.5	25.3	3.76	19.7	11.7	9.91	25.1	4.78	25.5	303	3.98	8.76	0.9	4.91	0.57	
		FH-6	40.9	68.9	9.37	45.8	22.7	53.4	44.3	7.62	37.2	285	5.53	11.8	1.18	6.4	0.81	
		FH-7	16	29.9	4.11	20.5	9.43	16	20.7	3.74	19.3	313	3.04	6.39	0.6	2.82	0.31	
		FH-8	55.7	115	16.8	83.1	36.2	39	58.9	9.91	47.7	403	6.91	15	1.56	8.87	1.09	

MVT																		
Asturias	Berbes	BE03-3	0.076	0.398	0.018	0.0167	0.136	0.009	0.051	0.010	0.042		0.01	0.023	0.005	0.011	0.002	
Sánchez et al., 2010		BE03-4	0.115	0.6368	0.053	0.05	0.542	0.022	0.121	0.020	0.14		0.02	0.054	0.005	0.02	0.002	
ICP-MS		BE03-36	0.115	0.796	0.088	0.0777	0.78	0.027	0.252	0.050	0.309		0.060	0.177	0.012	0.04	0.004	
(ppm)		BE05-7	0.038	0.398	0.026	0.0333	0.441	0.013	0.112	0.020	0.131		0.03	0.088	0.008	0.031	0.002	
Total (15)		BE05-20	0.038	0.3184	0.018	0.0389	0.915	0.118	0.419	0.08	0.501		0.100	0.288	0.025	0.1	0.009	
	La Collada	CO04-3	0.038	0.398	0.053	0.0444	0.610	0.024	0.168	0.030	0.22		0.04	0.123	0.008	0.031	0.003	
		CO04-3	0.115	0.796	0.168	0.2276	5.119	0.220	1.519	0.22	1.02		0.16	0.388	0.029	0.1	0.006	
		CO04-4	0.115	0.6368	0.150	0.222	5.56	0.258	1.92	0.290	1.47		0.25	0.584	0.047	0.189	0.012	
		CO04-6	0.076	0.4776	0.071	0.0666	0.915	0.062	0.349	0.07	0.449		0.090	0.242	0.022	0.079	0.006	
		CO04-10	0.153	0.6368	0.106	0.111	1.458	0.062	0.429	0.07	0.449		0.090	0.265	0.024	0.090	0.009	
	Villabona	VI04-7	1.222	5.0148	1.051	1.21	18.68	0.987	5.872	1.12	7.062		1.290	3.633	0.390	1.799	0.198	
		VI04-10	1.795	5.8904	1.077	1.1711	17.46	0.906	5.159	0.969	5.878		1.060	3.138	0.359	1.700	0.190	
		VI04-15	0.993	3.98	0.857	1.1211	19.59	1.08	6.151	1.180	7.418		1.369	3.956	0.460	2.250	0.25	
		VI04-19	0.879	3.5024	0.821	1.0601	18.75	0.979	5.839	1.07	6.852		1.270	3.403	0.376	1.87	0.201	
		VI04-19	1.108	4.0596	0.742	0.7881	9.153	0.460	2.521	0.44	2.509		0.47	1.314	0.139	0.640	0.074	
MVT																		
Zaghouan	Jebel Stah	L6-5	0.384	0.47	0.09	0.444	0.107	0.05	0.129	0.016	0.094		0.018	0.054	0.007	0.037	0.006	
Souissi et al., 2010		L6-30	0.35	0.42	0.08	0.39	0.1	0.05	0.13	0.02	0.11		0.02	0.06	0.01	0.05	0.01	
ICP-MS		L6-30Q	0.068	0.109	0.019	0.075	0.019	0.006	0.019	0.002	0.013		0.003	0.007	0.001	0.006	0.001	
(ppm)		L5-3	0.17	0.24	0.034	0.146	0.024	0.011	0.025	0.003	0.018		0.004	0.013	0.001		0.001	
Total (24)		DZ6-G	0.56	0.73	0.11	0.38	0.037	0.007	0.034	0.006	0.034		0.009	0.031	0.005	0.04	0.007	
		DZ6-J	0.21	0.3	0.06	0.28	0.061	0.015	0.075	0.011	0.066		0.015	0.047	0.007	0.055	0.01	
		DZ6-F	0.01	0.01	0.003	0.02	0.011	0.003	0.023	0.003	0.022		0.005	0.01	0.001	0.002	2E-04	
		JS1-6P	4.354	4.717	1.313	6.618	1.506	0.609	1.752	0.23	1.394		0.284	0.744	0.085	0.262	0.064	
		CC3-3	0.12	0.2	0.05	0.31	0.104	0.03	0.229	0.038	0.253		0.056	0.154	0.017	0.091	0.012	

		CC3-2	0.068	0.122	0.036	0.224	0.088	0.051	0.232	0.037	0.244		0.054	0.146	0.016		0.012	
		JS1-6F	0.076	0.144	0.04	0.237	0.08	0.042	0.197	0.03	0.197		0.043	0.114	0.012		0.009	
		L3-21D	0.15	0.22	0.03	0.13	0.028	0.008	0.044	0.007	0.045		0.011	0.033	0.004	0.022	0.003	
		L3-21F	0.149	0.256	0.048	0.237	0.057	0.016	0.106	0.015	0.1		0.022	0.06	0.006	0.031	0.004	
		L5-16	1.792	2.32	0.372	1.562	0.249	0.099	0.302	0.043	0.272		0.059	0.157	0.018		0.015	
		L5-15F	11.5	14.8	3.32	16.9	4.79	1.06	5.18	0.67	3.47		0.643	1.629	0.19	1.08	0.163	
		L5-15G	3.36	4.23	0.856	3.89	0.946	0.217	1.09	0.146	0.766		0.145	0.377	0.043	0.251	0.035	
		FZ-5N	1.41	1.95	0.27	0.95	0.15	0.043	0.202	0.032	0.218		0.049	0.134	0.016	0.093	0.013	
		FZ-5B	0.03	0.07	0.02	0.13	0.051	0.017	0.129	0.022	0.153		0.032	0.091	0.009	0.05	0.006	
		JS5-F	0.007	0.02	0.004	0.022	0.014	0.006	0.029	0.004	0.024		0.005	0.01	0.001	0.004	0.001	
		JS6-HF	0.004	0.012	0.004	0.023	0.012	0.004	0.032	0.004	0.019		0.004	0.008	0.001	0.006	0.001	
		JS5-C	0.154	0.73	0.218	1.37	0.54	0.138	0.62	0.091	0.491		0.09	0.23	0.028	0.17	0.022	
		JS6-HC	0.458	1.83	0.61	4.06	2.14	0.64	2.92	0.486	2.59		0.46	1.13	0.129	0.789	0.109	
		L4-2	0.008	0.017	0.003	0.024	0.01	0.005	0.021	0.003	0.014		0.003	0.006	0.0004	0.003	0.00004	
		JS3-5	0.01	0.01	0.003	0.02	0.015	0.005	0.035	0.004	0.024		0.005	0.01	0.001	0.006	0.001	
MVT																		
Adiyaman	Çelikhan	ÇK2	4.8	7	0.49	3	0.6	0.15	1.39	0.16	1.26		0.18	0.6	0.09	0.46	0.04	
Sasmaz et al., 2004		ÇK3	1.9	5	0.3	2	0.6	0.2	1.53	0.29	1.57		0.26	0.8	0.14	0.63	0.05	
ICP-MS		ÇA3	6.4	10	0.25	4	0.8	0.2	0.96	0.14	1.4		0.14	0.8	0.08	0.5	0.04	
(ppm)		ÇD2	8.6	11	0.41	3	0.5	0.2	1.08	0.15	1.18		0.34	0.8	0.07	0.3	0.05	
Total (15)		ÇD3	4.7	5	0.56	4	0.9	0.3	1.4	0.16	1.2		0.31	0.8	0.1	0.46	0.04	
		ÇD5	8	11.3	1.35	4.7	0.6	0.08	0.43	0.07	0.5		0.11	0.3	0.05	0.25	0.02	
		ÇD6	6	8.4	0.98	3.7	0.5	0.09	0.39	0.07	0.52		0.1	0.3	0.05	0.23	0.02	
		DT1	12	12	0.88	3	1	0.3	1.25	0.15	0.86		0.17	0.4	0.06	0.6	0.03	
		DT2	12	16	1.05	7	1	0.2	1.94	0.15	1.11		0.27	0.8	0.09	0.46	0.04	
		DT3	9	10	0.73	11	0.9	0.3	1.35	0.12	0.95		0.23	0.6	0.08	0.38	0.04	

		DT7	2.1	3.9	0.48	2.3	0.6	0.13	0.86	0.12	0.83		0.18	0.5	0.05	0.28	0.03	
		DT8	1	2	0.38	2.2	0.6	0.14	0.99	0.15	1.17		0.25	0.7	0.08	0.49	0.05	
		DT9	1.6	2.8	0.43	1.9	0.4	0.11	0.72	0.11	0.86		0.18	0.5	0.06	0.35	0.04	
		DT10	1.2	2.3	0.37	1.9	0.5	0.12	0.82	0.13	0.96		0.21	0.6	0.08	0.4	0.05	
		DT11	1.2	2.3	0.39	2	0.5	0.12	0.82	0.13	0.96		0.21	0.6	0.07	0.41	0.04	
MVT																		
La Encantada	La Encantada	Fluorite 1	0.857	1.615	0.207	0.819	0.155	0.039	0.124	0.017	0.094	0.037	0.017		0.045		0.029	
Levresse et al., 2006		Fluorite 2	0.05	0.122	0.021	0.097	0.039		0.059	0.011	0.085	1.081	0.018	0.048		0.04	0.006	
ICP-MS (µg/g) Total (2)																		
MVT																		
Valle de Tena	Portalet	B-11	0.4	0.2	0.01	0.53	0.23	0.05	0.26	0.05	0.31		0.05	0.19		0.13	0.02	
Subías & Fernández-Nieto, 1995		B-13	0.12	0.31	0.06	1.1	0.05	0.04	0.24	0.04	0.19		0.04	0.06		0.07	0.03	
ICP-MS, NAA		B-14	0.4	0.28	0.06	0.32	0.02	0.04	0.24	0.05	0.32		0.06	0.14		0.07	0.02	
(ppm)		B-17	1.8	1.81	0.31	1.07	0.13	0.03	0.21	0.03	0.16		0.04	0.09		0.07	0.02	
Total (30)		B-18	0.3	0.18	0.06	0.34	0.02	0.02	0.11	0.02	0.09		0.02	0.06		0.03	0.02	
		B-31	0.88	0.81	0.3	2.5	0.02	0.09	0.65	0.09	0.35		0.1	0.47		0.09	0.05	
		F-1.1	0.53	1.43	0.17	0.9	0.13	0.07	0.3	0.05	0.3		0.06	0.24		0.09	0.02	
		F-30	0.42	0.95	0.22	1.15	1.57	0.61	4.44	0.8	5.33	38	0.99	2.87		1.87	0.25	
		F-31	0.22	0.55	0.16	0.75	0.28	0.15	1.43	0.24	1.45	4	0.29	0.61		0.37	0.06	
		F-33	0.33	0.34	0.17	0.25	0.19	0.11	1.19	0.19	1.08		0.24	0.24		0.28	0.06	
		F-35	0.63	0.99	0.19	0.71	0.66	0.4	4.31	0.75	4.79	46	0.88	2.22		1.07	0.13	
		F-36	19.03	43.05	5.44	21.6	4.81	2.31	5.21	0.79	4.22		0.68	1.71		1.18	0.17	
		F-36.1	0.69	0.84	0.26	0.71	0.38	0.16	1.52	0.24	1.33	4	0.27	0.45		0.29	0.05	
		FA-2	2	3.46	1	5.07	3.55	1.2	7.21	1.23	7.73	60	1.42	3.53		2.33	0.31	

		FA-3	1.26	3.75	1.24	6.6	3.73	1.23	7.13	1.24	7.92	56	1.46	3.68		2.41	0.31	
		FA-5	1.64	3.85	1.06	4.95	2.59	0.79	4.47	0.72	4.24	20	0.77	1.93		1.29	0.18	
		FA-8	0.75	1.25	0.4	1.84	1.17	0.31	1.86	0.27	1.37		0.28	0.51		0.38	0.07	
		FA-10	2.56	6.74	1.96	11.98	4.37	1.09	5.74	0.91	5.23	42	0.99	2.74		1.63	0.2	
		FA-19	0.65	0.93	0.23	0.23	0.55	0.14	0.94	0.13	0.57		0.14	0.18		0.18	0.04	
		BF-5	0.7	0.86	0.13	1	0.68	0.25	1.62	0.29	1.88		0.35	0.91		0.42	0.06	
		BF-6	0.6	0.75	0.09	0.9	0.59	0.2	1.4	0.25	1.61	24	0.29	0.8		0.35	0.04	
		BF-7	0.6	0.78	0.08	0.5	0.31	0.11	0.71	0.12	0.75	8	0.13	0.37		0.14	0.01	
		BF-8	0.4	0.67	0.08	1	0.56	0.21	1.38	0.24	1.57	24	0.28	0.78		0.38	0.05	
		BF-9	0.3	0.53	0.1	1	0.74	0.27	1.95	0.36	2.43	28	0.45	1.24		0.56	0.07	
		BF-10	0.4	0.55	0.27	1.6	1.04	0.47	1.5	0.24	1.36	20	0.24	0.69		0.43	0.05	
		F-10	0.34	1.09	0.23	1.01	1.82	0.93	8.45	1.51	10.07	84	1.81	3.63		1.8	0.25	
		F-16	0.94	2.64	0.53	2.13	2.8	1.29	13.57	2.53	17.47	132	3.09	7.61		3.63	0.43	
		F-22	0.31	1.08	0.15	1.32	0.82	0.51	5.19	0.86	5.22	52	0.92	1.71		0.97	0.14	
		F-22B	0.23	1.17	0.21	1.64	0.5	0.35	3.77	0.62	3.67	32	0.69	0.67		0.7	0.12	
		F-23	0.13	1.12	0.18	0.94	0.48	0.21	2.11	0.35	2.07	12	0.4	0.54		0.4	0.07	
MVT																		
Hansonburg	Ora	39	1.7	4.6		4	2.3	0.96		1.15		146				1.28	0.12	
Hill et al., 2000		40	1.3	2.9		2	0.7	0.24		0.29		67				0.47	0.05	
INAA		41	0.9	1.5		1	0.3	0.12		0.17		51				0.29	0.02	
(ppm)	Royal Flush	42	6	10.7		3	0.9	0.17		0.17		12				0.44	0.06	
Total (43)	MexTex	43	1.5	3.1		2	0.4	0.11		0.15		38				0.37	0.04	
SEDEX			La	Ce	Pr	Nd	Sm	Eu	Gd	Tb	Dy	Y	Ho	Er	Tm	Yb	Lu	n = #
Nördliche Kalkalpen	Tschirgant-Silberstube	214/EO	0.33	0.66			0.1	0.04		0.05						0.076	0.04	

Schneider et al., 1975		214/ER	0.32	0.58			0.09	0.037		0.05						0.056	0.005	
INAA		214/GO	0.66	1.32			0.15	0.071		0.08						0.106	0.003	
(?)		214/GR	0.59	1.11			0.2	0.071		0.084						0.074	0.006	
Total (33)		214/HO	0.96	1.93			0.19	0.059		0.07						0.058	0.006	
		214/HR	0.93	1.72			0.16	0.053		0.054						0.079	0.007	
	Tschirgant-Wasteleshütte	218/IO	0.38	0.63				0.018		0.016						0.055	0.004	
		218/IR	0.22	0.33				0.022		0.029						0.013		
	Tschirgant-Gipfelbaue	221/KO	0.67	1.8			0.05	0.035		0.006						0.06		
		221/LR		0.52				0.018		0.021						0.051		
		221/Lx	0.22	0.25			0.05	0.02		0.02						0.01		
	Gaflein-Mitte	317/MO	0.4	0.52						0.048						0.047		
		317/MR	0.28	0.23				0.036		0.002						0.032		
		317/YO	0.48	0.37				0.008		0.003						0.009	0.001	
	Gassenalpe	506/XO	0.67	0.7			0.11	0.007		0.02						0.061	0.009	
		506/XR	0.43	0.58			0.06	0.019		0.03						0.082	0.007	
	Ferchensee-wand	510/RO	0.69	1.36				0.02		0.006						0.061	0.009	
		510/RR	0.9	1.8				0.018		0.01						0.088	0.007	
		510/WO	0.63	0.86			0.08	0.013		0.023						0.025	0.004	
		510/WR	0.42	0.66			0.05	0.013		0.016						0.03	0.006	
		510/Wx	0.04	0.11			0.01	0.008		0.009						0.005	0.001	
	Lafatsch-Reps	612/NO	0.73	1.91			0.17	0.037		0.02						0.083	0.005	
		612/NR	0.83	1.52			0.13	0.033		0.047						0.09	0.007	
	Hohe Warte	403/Ux1	2.5	4.7			0.76	0.23		0.16						0.19	0.02	
		403/Ux2	0.9	1.86			0.34	0.12		0.11						0.21	0.013	

	Lech-Knappenboden/Arlberg	101/AR	0.5				0.18											
		101/BR	0.49	0.78			0.16	0.048		0.047						0.052		
	Blaue Grotte Laggers-Tschirgant	208/DR	0.61	1.01			0.16	0.059		0.1						0.11		
		208/CR	0.55	0.88			0.17	0.049		0.11						0.078	0.009	
		208/VO	4.3	4.75			0.92	0.18		0.04						0.41	0.007	
	Marienberg-Dreikönigszeche	412/PR	0.41	0.81				0.005		0.004						0.02	0.003	
	Kleiner Lafatscher	610/SR	0.2	0.37			0.06	0.02		0.02						0.05	0.003	
	Vomperlock	614/TR	0.15	0.23			0.02	0.006		0.01						0.01	0.001	
IOCG			La	Ce	Pr	Nd	Sm	Eu	Gd	Tb	Dy	Y	Ho	Er	Tm	Yb	Lu	n = #
Kangding	Lala	LO-88-2	827.68	1252.5	103.1	405.59	56.38	13.241	54.54	7.596	34.95		7.007	19.59	2.236	11.10	1.0	
Huang et al., 2014		LO-6	684.95	1054.0	95.88	356.83	68.13	17.301	70.05	9.653	51.03		10.94	31.63	4.169	22.12	2.250	
?		LO-85	371.33	577.8	53.45	216.22	39.28	22.226	44.64	6.837	42.47		9.679	27.99	3.815	18.82	2.004	
(?)		LO-74	375.12	651.17	57.33	251.11	49.1	11.455	55.65	8.232	49.66		12.46	36.92	5.069	25.67	2.426	
Total (9)		LO-20	292.79	481.09	51.61	224.49	46.04	12.644	71.06	10.7	61.29		14.42	41.72	5.766	29.5	2.913	
		LD-7-2	336.52	588.13	64.35	279.92	56.63	10.278	66.4	9.825	56.11		12.33	34.62	4.516	22.03	2.012	
		L-25	116.68	236.78	29.28	131.79	33.92	6.815	40.44	6.605	40.51		9.028	23.35	2.519	11.32	1.082	
		LD-7-1	11.566	20.624	2.014	7.472	1.454	0.8352	1.624	0.295	1.91		0.469	1.374	0.156	0.731	0.094	
		Op-77	15.476	28.091	2.86	10.881	2.081	1.2238	2.466	0.404	2.64		0.685	1.903	0.232	1.088	0.127	
Skarn			La	Ce	Pr	Nd	Sm	Eu	Gd	Tb	Dy	Y	Ho	Er	Tm	Yb	Lu	n = #
La Encantada	El Pilote	Fluorite 1	0.857	1.615	0.207	0.819	0.155	0.039	0.124	0.017	0.094	0.037	0.017		0.045		0.029	
Levresse et al., 2006		Fluorite 2	0.05	0.122	0.021	0.097	0.039		0.059	0.011	0.085	1.081	0.018	0.048		0.04	0.006	

ICP-MS (μg/g) Total (2)																		
Skarn																		
	No. 19 skarn vein	FRB-7	1.58	2.64	0.289	1.09	0.212	0.025	0.233	0.034	13	2.67	0.043	0.149	0.02	0.135	0.019	
Tiepokeng-Wuchangping tin belt		FRB-8	0.265	0.411	0.055	0.222	0.046	0.004	0.038	0.009	17.5	1.3	0.01	0.035	0.005	0.025	0.003	
Yuan et al., 2008		FRB-9	1.7	3.35	0.42	1.71	0.348	0.03	0.348	0.054	14.2	3.58	0.063	0.207	0.029	0.176	0.022	
ICP-MS		FRB-10	1	2.04	0.252	0.991	0.199	0.012	0.204	0.028	346	1.58	0.031	0.098	0.013	0.088	0.012	
(μg/g)		FRB-10-1	1.08	2.21	0.302	1.29	0.244	0.013	0.24	0.04		2.85	0.045	0.152	0.021	0.121	0.018	
Total (8)		FRB-11	0.163	0.245	0.03	0.119	0.03	0.005	0.015	0.005		0.66	0.006	0.026	0.003	0.019	0.004	
		FRB-12-1	0.984	1.85	0.247	1.01	0.228	0.013	0.215	0.038		2.83	0.046	0.135	0.019	0.13	0.017	
		FRB-12-2	0.827	1.64	0.224	0.973	0.222	0.012	0.211	0.032		2.45	0.043	0.127	0.017	0.104	0.016	
Skarn																		
Akdagmadeni	Akçakisla	AK01	264	174	96	62	33	69	17	1.5			11	11.5	11.3	11.9	11.6	
Sasmaz et al, 2005		AK02	248	163.5	97	67	39	30	22	1.98			14	13.1	12.6	12.9	12	
ICP-MS		AK03	300	208	120	82	39	28	20.5	1.63			10.5	9.9	9.3	9	8.3	
(ppm)	Büyükçal Tepe	AK04	4332	2394	1316	784	473	630	330	3.31			287	290	292	276	250	
Total (12)		BT51	23	30		6	0.5	0.2		1.8							1.4	
		BT52	22	33		11	0.7	0.2		0.1							1.4	
		BT53	64	59		10	0.3	0.4		0.4							1.2	
		BT54	56	70		3	1.2	0.2		0.2							0.1	
		BT55	54	77		15	1.2	0.1		0.1							1.6	
		BT56	54	75		15	1.2	0.1		0.1							1.7	
		BT.06	26.2	36.8	3.4	3.6	0.2	0.1	0.2	0.2	0.5		0.2	0.5	0.1	0.7	0.1	
		BT.05	47.8	67.8	4.5	8.7	0.9	0.2	0.4	0.4	0.5		0.3	0.5	0.1	0.9	0.3	
Skarn																		

Sardinia	Perda Niedda	F16	4.23	10.06	1.7	8.99	6.22	0.67	10.16	1.95	11.74	104.2	2.05	5.48	0.84	5.77	0.84	
Castorina et al., 2008																		
ICP-MS																		
(ppm)																		
Total (1)																		
Skarn																		
	Solnechnoe	SN 309b		7.74	1.03	4.29	1.36	0.29	1.32	0.27	1.74	7.07	0.3	0.92	0.17	1.39	0.17	
Herzynian rare metal province																		
Monecke et al., 2002																		
ICP-AES																		
(ppm)																		
Total (1)																		
Rare-metal pegmatite			La	Ce	Pr	Nd	Sm	Eu	Gd	Tb	Dy	Y	Ho	Er	Tm	Yb	Lu	n = #
South Platte	White Cloud, Oregon 4		141	232	42.9	253	139	16.6		90.5		8320	206	675	97.4	820	114	4
Gagnon et al., 2003			719	851	157	499	202	5.5		32		2330	54.9	203	22.2	370	49.6	7
LA-ICP-MS			104	116	22.5	103	42	3.9		21.7		993	48.8	165	8.5	208	28.4	6
(µg/g)			220	370	66	398	218	22.8		123		9770	247	796	144	998	139	9
Total (4 from 26)																		
Rare-metal pegmatite																		
Bohemian Massif	Vlastějovice	1	1.1	3.28		3.9	2.08	0.24	4.33	1.21			3.46			9.91	1.65	
Ackerman, 2005		2	4.28	6.77		3.8	1.37	0.14	2.21	0.53			1.26			4.3	0.73	
INAA		3	16.8	17.8		14.2	4.09	0.35	3.88	0.72			1.37		0.51	3.89	0.6	
(ppm)		4	20.6	32.86		20.6	4.95	0.41	3.94	0.77			1.2			3.86	0.54	
Total (13)		5	58.9	147.9		65.9	13.39	1.02	9.52	1.31			1.37			4.15	0.56	

		6	84.7	273.2		69.6	13.97	1	10.98	1.56			1.76			6.05	0.85	
		7	15.9	13.08		13.9	2.95	0.29	2.76	0.81			1.76			7.19	1.12	
		8	28.9	39.75		22	4.2	0.35	3.07	0.75			1.39			5.24	0.76	
		9	10.5	12.16		8.5	2.13	0.23	3	0.75			1.82		0.77	6.7	1.11	
		10	49.9	126.3		38.1	7.28	0.52	6.09	0.99			1.71		0.88	5.54	0.91	
		11	1.44	2.01		1.49	0.2	0.13	0.11	0.03						0.02	0.01	
		12	2.49	3.48		1.47	0.36	0.33	0.35	0.05						0.05	0	
		13	1.57	1.95		0.77	0.22	0.13	0.25	0.02						0.02	0	
Granite-related U			La	Ce	Pr	Nd	Sm	Eu	Gd	Tb	Dy	Y	Ho	Er	Tm	Yb	Lu	n = #
Changjiang U orefield	No. 302 uranium vein	3-02	7.5	9	1.23	5.2	0.62	0.08	0.99	0.12			0.13	0.41	0.08	0.37	0.08	
Zhang et al., 2007		3-28	9.5	17	2.1	9.8	2.2	0.23	2.2	0.41			0.62	1.57	0.34	2	0.36	
ICP-MS		3-21	13	15	1.9	9.8	2.5	0.2	2.7	0.53			0.76	2.4	0.31	1.9	0.33	
(ppm)		3-50	20	20	3.3	11.2	2.1	0.21	2.2	0.43			0.65	2	0.35	2.3	0.33	
Total (8)		1-45	13	16	2.2	8.5	2.6	0.28	2.3	0.47			0.92	3.2	0.42	2.9	0.39	
		2-43	7.6	13	1.9	7.7	2.2	0.28	2	0.56			1.09	3.6	0.58	3.4	0.65	
		2-29	24	46	6.3	26	8.8	1.23	7.2	2.05			3.9	13	2	13	2.1	
		1-28	19	35	5.5	23	7.2	0.89	6.3	1.67			3.2	9.6	1.4	11	1.68	
Granite-related U																		
Gabbal Gattar	Gabbal Gattar	WDZ1c										12.1						
Mahdy et al., 2014		WDZ1r		1.85	0.67	4.14	2.63		2.62		2.63	15.39	0.38	1.6		2.37		
LA-ICP-MS		WDZ2r	0.09	49	0.15	1.07	0.84		1.31	0.23	2.1	19.6	0.34	1.19	0.27	2.58	0.35	
(ppm)		WDZ2r	1.43	1.93	0.36	1.72	0.85		1.42	0.24	1.91	31.72	0.45	1.44	0.21	1.48	0.24	
Total (7)		AU1	6.95	16.15	2.64	16.23	5.4		6.41	0.99	6.97	81.66	1.54	4.72	0.81	7.11	1.22	
		AU2	10.98	16.3	1.96	8.47	1.95	0.44	3.11	0.55	3.76	78.71	0.9	2.4	0.26	1.9	0.23	

		AU3	12.97	20.2	2.84	11.15	3.24	0.45	4.55	0.96	6.35	152.2	1.43	3.59	0.43	2.64	0.31	
Greisen			La	Ce	Pr	Nd	Sm	Eu	Gd	Tb	Dy	Y	Ho	Er	Tm	Yb	Lu	n = #
Hercynian tin province	Zinnwald tin deposit	315/2g	115	316	38.6	131	61.7	0.67	67.2	17.2	151	374	34.3	105	25.5	188	25.4	
Monecke et al., 2002		315/2v	21.8		11	39.3	9.94	0.23	6.74	1.6	18.5	152	4.49	17.8	4.47	30.5	4.46	
ICP-AES		379	14.2	32.2	3.53	15.3	4.68	0.67	5.83	1.11	8.31	60.6	1.47	6.3		8.02	1.24	
(?)																		
Total (3)																		
Greisen																		
Hercynian tin province	Ehrenfrieder sdorf	ED-1b	27.1	53.6	6.63	28.3	9.84	6.1	19.3	5.01	37.1		7.77	22.6	2.83	17.1	2.08	
Monecke et al., 2000		ED-1c	9.28	18.3	2.25	8.55	2.54	3.21	3.94	1.05	7.83		1.59	4.73	0.65	4.32	0.54	
ICP-MS		ED-1a	2.63	7.75	0.53	1.59	0.39	0.45	0.4	0.1	0.72		0.15	0.5	0.075	0.6	0.08	
(ppm)																		
Total (3)																		
Greisen																		
	Qaraoba	KO 1g	1.7	7.05	1.17	5.42	2.29	0.03	2.89	0.51	3.56	160	0.82	3.08	0.58	5.24	0.82	
Herzynian rare metal province		KO 40a		4.37	0.87	5.7	5.79	0.58	6.63	1.5	11.3	135	2.34	9.16	2.08	21.5	3.7	
Monecke et al., 2002		KO 40b		8	1.27	5.61	2.34	0.07	2.74	0.59	4.83	109	1.11	4.2	0.8	6.96	1.09	
ICP-AES	Aqshatau	AC 2		34.3	3.74	15.4	6.24	1.06	13.3	3.45	31.8	274	8.2	33.8	6.9	60.2	11.6	
(?)		AC 16038g		7.42	0.64	2.26	0.39	0.06	0.63	0.11	0.9	60	0.27	1.15	0.22	2.08	0.45	
Total (12)		AC 16038r		4.72	0.61	3.31	3.34	2.32	14.1	3.7	32	721	8.51	33.7	6.18	56.1	10.5	
		AC 16404v		1.86	0.21	0.36	0.35	0.24	1.43	0.4	3.48	24.8	0.8	2.96	0.6	5.42	1.02	
	Kent	KN 1a		1.48	0.33	2.06	1.36	0.08	2.89	0.59	5.28	307	1.52	5.88	0.91	6.9	1.05	
		KN 2a	25	42.7	4.9	17.7	4.67	0.6	5.61	0.93	6.96	169	1.67	5.96	1	8.08	1.4	

		KN 3	29.3	91.6	10.8	31.5	12.8	0.4	10.3	2.67	19.6	80.1	3.8	13.3	2.35	17.8	2.77	
		KN 6	750	1151	106	283	53.3	1.47	48.6	10.26	74.2	384	16.3	58.1	9.83	76.9	11.1	
Cryolite			La	Ce	Pr	Nd	Sm	Eu	Gd	Tb	Dy	Y	Ho	Er	Tm	Yb	Lu	n = #
Gardar Province	Ivigtut	9051	0.622	1.53	0.121	0.472	0.12	0.03	0.088	0.042	0.269	0.147	0.035	0.101	0.023	0.103	0.017	
Schönenberger et al., 2008		9052	0.815	1.71	0.201	0.67	0.39	0.02	0.205	0.054	0.202	0.17	0.046	0.102	0.024	0.082	0.02	
LA-ICP-MS		9053	0.493	1.69	0.257	0.919	0.446	0.045	0.354	0.092	0.633	0.43	0.072	0.199	0.028	0.242	0.034	
(ppm)		9054	0.298	1.73	0.432	1.96	2.57	0.133	2.34	0.638	4.28	1.3	0.492	1.09	0.18	1.07	0.083	
Total (23)		5014	0.022	0.02	0.01	0.03	0.035	0.01	0.04	0.01	0.03	0.013	0.01	0.019	0.01	0.03	0.01	
		5015	0.081	0.14	0.014	0.056	0.035	0.009	0.042	0.014	0.247	0.211	0.078	0.19	0.028	0.18	0.027	
		5016	0.035	0.04	0.006	0.054	0.04	0.01	0.088	0.044	0.633	0.671	0.17	0.592	0.09	0.396	0.046	
		5017	0.009	0.01	0.01	0.03	0.03	0.12	0.04	0.01	0.048	0.055	0.01	0.02	0.012	0.03	0.01	
		5021	2.37	9.39	1.57	7.18	4.12	0.179	3.45	0.971	7.36	9.1	1.11	3.1	0.517	2.98	0.278	
		5022	5.42	22.4	3.62	11.5	4.84	0.159	4.23	1.23	9.33	16.4	1.59	4.53	0.736	4.7	0.437	
		5023	0.442	1.48	0.186	0.544	0.23	0.01	0.215	0.067	0.496	1	0.098	0.344	0.041	0.25	0.018	
		5024	5.47	28.8	5.36	20	9.99	0.35	8.87	2.86	24	36.1	4.21	12.1	1.71	11.3	0.932	
		5025	0.775	8.59	3.48	21.9	26.9	1.02	28.8	9.79	79.5	128	14.4	39.4	6.09	36	3.09	
		5027	6.98	33.7	5.96	22.3	9.6	0.315	7.31	2.24	20	43.8	4.17	12.9	2.02	12.1	1.05	
		5028	2.06	10.2	1.92	6.77	4.58	0.1	4.14	1.41	12.7	15.2	1.96	6.6	0.846	4.85	0.406	
		5029	0.571	2.72	0.436	2.15	1.07	0.022	0.814	0.254	0.989	2.67	0.222	0.631	0.125	0.695	0.076	
		5031	7.65	39.4	6.74	22.7	7.62	0.243	5.23	1.57	12.1	17.5	2.11	5.95	0.886	5.82	0.431	
		5032	0.852	8.95	2.98	17.1	18.3	0.772	18.3	6.3	46.4	74	7.78	23.6	3.7	22.9	1.85	
		5033	13	79.4	16.8	73.8	44.8	1.42	41.3	13.6	115	249	22.6	69.2	10.3	67.6	6.04	
		5034	4.06	22.8	4.14	14.6	6.66	0.2	5.63	1.89	17	31.4	3.04	9.47	1.49	9.16	0.805	
		5035	0.518	1.38	0.187	0.584	0.342	0.013	0.387	0.095	0.654	2.4	0.16	0.483	0.087	0.538	0.057	

		5036	9.61	27.9	3.65	12.1	5.03	0.164	3.94	1.1	6.85	12.2	1.16	3.76	0.555	3.69	0.384	
		5042	4.74	22.4	4.06	13.1	7.57	0.3	7.17	2.21	19.8	29.8	3.34	8.16	1.47	9.56	0.933	
Cryolite																		
Pitinga	Pitinga	PMR-7A	171.17	561.31	82.67	290.29	123.5	2.31		35.17	245.3	1435.8	45.24	117.0	19.78		15.14	
Minuzzi et al., 2008		PMR-10	125.76	471.41	68.88	234.83	93.44	1.63		31.49	254.1	1209.8	55.33	152.0	23.83		14.1	
ICP-MS		PMR-2	67.84	155.95	35.28	110.4	63.43	1.38	48.98	16.64	102.1	186.7	18.31	41.39	5.74	27.25	3.71	
(ppm)		PMR-7	13.84	49.69	6.74	19.45	9.78	0.18		2.87	24.83	217.9	6.54	24.69	5.6		6.22	
Total (6)		PMR-9	9.72	33.16	5.01	11.55	7.93	0.15		2.49	18.53	196.4	4.08	12.13	2.23		1.94	
		VF-1	2.26	6.4	0.77	3.15	1	0.03	2.06	0.39	3.22	34.81	1.06	3.14	0.51	4.29	0.39	
Intrusion-related Mo			La	Ce	Pr	Nd	Sm	Eu	Gd	Tb	Dy	Y	Ho	Er	Tm	Yb	Lu	n = #
Mosquito Range	Sweet Home Mine	1	7.73	19.6	3.89	27.8	18.8	7.18	39.4	8.2	56	294	11.4	31.4	4.3	26.5	3.66	
Lüders et al., 2009		18	3.93	10.5	2.26	16.9	12.7	5.06	26.8	5.68	38.2	209	7.84	21.8	2.9	18.1	2.47	
ICP-MS		24	0.21	0.62	0.16	1.42	1.76	0.73	4.35	0.75	4.28	30.1	0.78	2.01	0.26	1.61	0.2	
(ppm)		25	0.78	1.68	0.32	2.02	1.09	0.56	2.37	0.44	3.13	41.9	0.67	1.94	0.26	1.81	0.23	
Total (12)		6	0.56	1.19	0.2	1.35	1.18	0.62	3.74	0.69	4.4	39.6	0.88	2.28	0.28	1.76	0.22	
		7	0.23	0.62	0.16	1.42	1.77	0.73	5.21	1.09	8.16	78	1.82	5.44	0.72	4.68	0.62	
		7	0.43	1.08	0.24	1.57	1.31	0.48	3.65	0.73	5.09	47	1.06	2.98	0.4	2.61	0.33	
		24	0.22	0.67	0.16	1.35	1.13	0.44	2.55	0.48	3.6	30.1	0.82	2.44	0.38	2.67	0.36	
		10	0.16	0.28	0.07	0.52	0.48	0.23	1.57	0.33	2.76	27.4	0.65	2	0.28	1.92	0.27	
		11	0.52	1.64	0.38	2.64	1.56	0.68	3.89	0.72	5.12	57.8	1.1	2.96	0.37	2.39	0.31	
		30	0.18	0.22	0.03	0.21	0.17	0.09	0.66	0.14	1.17	22.3	0.26	0.86	0.14	1.12	0.16	
		30	0.38	0.83	0.15	0.97	0.67	0.31	2.13	0.42	3.12	42.5	0.66	1.84	0.24	1.6	0.21	
Intrusion-related Mo																		
Qinling	Tumen	TM-14	3.56	7.91	0.95	3.06	0.6	0.18	0.63	0.1	0.62	3.7	0.11	0.28	0.04	0.22	0.03	

Deng et al., 2014		TM-15	6.32	11.7	1.38	4.67	0.79	0.26	0.92	0.15	0.85	9.23	0.16	0.39	0.05	0.26	0.04	
ICP-MS		TM-18-1	3.69	9.57	1.29	4.6	0.92	0.29	0.8	0.13	0.69	4.27	0.13	0.3	0.04	0.22	0.03	
(ppm)		TM-19	3.34	6.3	0.72	2.01	0.33	0.18	0.36	0.05	0.26	2.29	0.05	0.12	0.02	0.09	0.01	
Total (17)		TM-03	3.66	7.79	1.16	4.6	1.01	0.28	1.18	0.19	1.1	10.5	0.21	0.51	0.06	0.36	0.05	
		TM-05	4.28	8.13	1.11	4.62	1.03	0.33	1.26	0.22	1.36	15.6	0.28	0.71	0.09	0.49	0.06	
		TM-08	2.48	5.35	0.88	3.64	0.83	0.26	1.02	0.17	1.08	11.4	0.21	0.53	0.07	0.35	0.05	
		TM-11	3.75	7.71	1.26	5.31	1.16	0.34	1.31	0.22	1.31	13.7	0.26	0.61	0.07	0.39	0.05	
		TM-12	4.12	8.3	1.36	5.61	1.27	0.32	1.65	0.26	1.51	15.2	0.28	0.7	0.08	0.43	0.06	
		TM-13	3.23	6.09	0.87	3.19	0.65	0.16	0.81	0.14	0.88	11.2	0.18	0.47	0.06	0.34	0.05	
		TM-18-2	3.22	8.13	1.32	5.99	1.55	0.67	1.88	0.32	2.02	13.2	0.38	0.93	0.12	0.62	0.08	
		TM-20	2.96	6.47	1.01	4.82	1.56	0.7	2.35	0.45	2.87	23.6	0.58	1.51	0.2	1.09	0.13	
		TM-06	11.3	18.1	1.95	6.12	0.96	0.22	1.09	0.18	1.17	13.6	0.24	0.6	0.08	0.44	0.06	
		TM-07	15.5	27.8	3.73	14.5	2.81	0.67	3.03	0.5	3.01	26.2	0.59	1.5	0.2	1.1	0.14	
		TM-09	11.3	19.5	2.13	7.53	1.56	0.59	2.09	0.36	2.35	25.8	0.49	1.27	0.17	0.97	0.12	
		TM-10	15.1	21.5	2.19	6.75	1.09	0.28	1.55	0.27	1.75	25.5	0.36	0.93	0.12	0.66	0.08	
		GSR3-RVR	56	105	13.2	54	10.2	3.2	8.5	1.2	5.6	22	0.88	2	0.28	1.5	0.19	
Hydrothermal/epithermal vein/replacement deposits in carbonate																		
			La	Ce	Pr	Nd	Sm	Eu	Gd	Tb	Dy	Y	Ho	Er	Tm	Yb	Lu	n = #
Huesca	Lanuza mine	L-1A	24	53		32	6.9	4.9		1.1						2.89	0.48	
Subías & Fernández-Nieto, 1995			28.6	56	6.71	24.48	4.18	1.2	3.93	0.6	3.2		0.56	1.43		1.05	0.12	
ICP-MS		L-2C	4.03	8.26	0.83	3.8	0.91	0.45	1.59	0.22	1.07		0.18	0.41		0.11	0.03	
(ppm)		L-2	3.9	7		5	1	0.5		0.5						0.08	0.1	
Total (23)		L-1C	3.89	6.56	0.86	4.3	1.14	0.72	2.28	0.32	1.49		0.23	0.52		0.21	0.03	
		L-5C	0.99	2.15	0.25	1.1	0.15	0.12	0.58	0.11	0.71		0.13	0.33		0.08	0.02	
		L-9	35.82	53.41	5.68	19.5	3.58	1.19	3.48	0.52	2.79		0.49	1.25		1.29	0.2	

		L-12C	8.55	14.75	1.38	5.2	0.78	0.47	1.09	0.16	0.76		0.13	0.27		0.13	0.03	
		L-13C	9.43	16.23	1.91	7.6	1.44	0.6	1.58	0.24	1.31		0.22	0.61		0.38	0.05	
		L-14	2.64	3.99	0.42	2.1	0.37	0.16	0.71	0.11	0.57		0.1	0.27		0.09	0.01	
		L-15C	2.63	3.82	0.52	1.9	0.1	0.11	0.59	0.08	0.39		0.05	0.2		0.06	0.02	
		L-16	2.61	4.84	0.67	3.5	1.08	1	2.16	0.3	1.36		0.2	0.45		0.12	0.02	
	Tebarray	T-13	19.62	39.66	5.5	27.1	3.46	1.09	2.43	0.26	0.45		0.1	0.07		0.05	0.03	
		T-13B	24	45.96	6.16	29.9	4.32	1.32	2.67	0.28	0.45		0.07	0.06		0.04	0.01	
		T-22	11.1	16.18	1.64	5.9	0.87	0.66	0.64	0.09	0.41		0.07	0.19		0.12	0.02	
		T-24	0.9	1.48	0.22	1.1	0.32	0.12	0.46	0.08	0.46		0.1	0.23		0.12	0.01	
		T-41	0.5	0.56	0.19	0.6	0.15	0.08	0.36	0.06	0.34		0.07	0.18		0.08	0.02	
		T-41V	2.69	2.92	0.64	1.79	0.36	0.12	0.63	0.11	0.67		0.13	0.37		0.19	0.03	
		T-44	0.48	0.58	0.15	0.66	0.29	0.08	0.44	0.08	0.49		0.09	0.24		0.1	0.01	
		T-63	2.36	2.6	0.21	1.12	0.32	0.2	0.33	0.06	0.36		0.06	0.19		0.1	0.01	
		T-65	1.55	1.62	0.46	2	0.6	0.57	0.7	0.11	0.64		0.11	0.3		0.15	0.02	
		T-69	0.46	1.15	0.42	1.52	0.38	0.5	0.8	0.12	0.7		0.14	0.06		0.14	0.03	
		B-V	0.49	0.73	0.3	1.9	0.07	0.1	1.03	0.19	1.26		0.27	0.03		0.26	0.06	
...in carbonate																		
Akdagmadeni	Tad Dere	TD61	9.4	12		6	0.6	0.2		0.18							0.3	
Sasmaz et al, 2005		TD62	19	16		3	0.8	0.4		0.11							0.7	
ICP-MS		TD63	8	7		5	0.6	0.2		0.15							0.3	
(ppm)		TD64	15	14		5	0.6	0.2		0.09	0.65						0.4	
Total (12)		TD65	13	13		4	0.6	0.2		0.14	1.02						0.3	
		TD66	14	10	0.84	5	0.72	0.18	1.27	0.09	0.78		0.18	0.59	0.07	0.41	0.05	
		TD67	17	16	1.28	7	1.17	0.26	1.78	0.14	2		0.26	0.8	0.11	0.66	0.07	
		TD68	17	21	1.16	6	0.89	0.14	1.43	0.11	0.46		0.19	0.61	0.08	0.48	0.05	
		TD69	15	14	0.94	5	1.16	0.35	1.96	0.14			0.24	0.71	0.12	0.66	0.08	

		TD70	14	11	0.7	4	0.53	0.15	1.01	0.06			0.11	0.43	0.04	0.24	0.03	
		TD71	8.8	8		3	0.4	0.15		0.13								
		TD72	18	18		6	0.6	0.3		0.22								
...in carbonate																		
Yixian F deposit	Saobaotun	SBT-9	0.6	2.3	1.2	2.5	1.1	0.4	1.1	0.3	1.1	7.8	0.3	0.5	0.2	0.5	0.1	
Xiang et al., 2010		ZSBT-4	0.1	0.7	0.6	1.1	0.8	0.4	1.1	0.3	1.2	12.9	0.3	0.5	0.1	0.3	0.1	
ICP-MS	Liulongtai	YJG-3	0.3	1.5	0.7	2.6	1.9	0.7	1.9	0.5	2.3	14.4	0.5	1.2	0.2	1	0.2	
(?)	Laohudong	LHD-3	0.1	1.7	0.7	2.4	1.1	0.5	1.3	0.3	1.7	12.8	0.3	0.9	0.2	0.8	0.1	
Total (5)	Toadoahexiang	XS-3	2.1	6	1.2	4.4	1.4	0.6	1.3	0.3	1.3	8.9	0.2	0.6	0.1	0.5	0.1	
...in carbonate																		
Sardinia	Monreale	F8	1.13	2.64	0.35	1.48	0.58	0.23	0.73	0.15	0.97	5.82	0.2	0.62	0.09	0.7	0.12	
Castorina et al., 2008	Santa Lucia	F14	3.85	9.03	1.54	8.39	6.13	1.51	11.96	2.16	12.2	200.46	2.08	4.55	0.47	2.06	0.24	
ICP-MS																		
(ppm)																		
Total (2)																		
...in carbonate																		
New Mexico	Hanson	1	33.4	42		34	11.6	2.99		3.3		317				13.92	1.79	
Hill et al., 2000	Chise	5	17.9	23.3		9	2.1	0.67		0.35		26				0.97	0.12	
INAA	Gonzales west	8	3.8	9.4		5	1.5	0.26		0.4		125				1.37	0.16	
(?)	Yellowjacket	10	1.5	2			0.4	0.1		0.09		23				0.28	0.04	
Total (12)	Marion	13	0.6	1.3		1	0.2	0.05		0.05		13				0.13	0.02	
	Hardin	14	1.1	1.8		1	0.3	0.04		0.03		12				0.04		
	Cox	15	0.4	0.8			0.1	0.02		0.03		8				0.03		
	Nakaye	16	15.7	16.7		8	1.5	0.39		0.34		40				1.65	0.24	
	Esperanza	17	9.7	20.8		9	2.3	0.5		0.56		35				1.33	0.16	
	Hiebert	18	1	2.5		2	0.9	0.3		0.31		44				0.65	0.08	

	Grants	19	2.6	4.7		4	1.7	0.43		0.33		26				0.53	0.06	
	Ruby/Hayner	20	3.9	5.5		3	0.7	0.2		0.09		10				0.13	0.01	
Hydrothermal/epithermal vein/replacement deposits in igneous																		
			La	Ce	Pr	Nd	Sm	Eu	Gd	Tb	Dy	Y	Ho	Er	Tm	Yb	Lu	n = #
Santa Catarina	Santa Catarina	T623B	1074	2125		1680	528	7.66	657		861		236	711		805	131	
Sallet et al., 2005		T623A	783	1896		1589	553	2.54	596.1		621		150	383		364	58.2	
ICP-MS		T611A	1525	3142		2926	896	2.99	834.4		699		165	418		378	59.4	
(ppm)		T616	624	1511		956	290	1.83	356.8		513		133.2	369		408	62.5	
Total (31)		T7	377	1281		1069	527	1.03	519		742		186	511		625	110	
	Garganta	GN31	6.33	12.9		9.2	3.01	0.4	4.11		5.02		1.05	2.86		1.99	0.24	
		GN320	3.1	6.9		5.43	3.57	0.65	7.14		12.2		2.35	6.2		4.51	0.47	
		GN321	3.93	8.68		6.71	5.7	1.41	10.7		19		3.71	10.2		9.27	1.06	
		GN322	3.52	8.57		6.53	5.37	1.4	10.9		20.3		4.05	11.3		10.5	1.2	
		GN323	8.21	18.1		11.8	5.73	1.44	9		13.6		2.56	6.99		6.72	0.8	
		GN324	6.75	14.9		10.9	6.02	1.68	11		17.8		3.5	9.84		9.03	1.09	
		GN33	4.84	10.4		7.97	5.87	1.74	12.2		21.2		4.16	11.3		8.96	0.97	
		GN34	6.28	13.7		10.1	6.27	1.79	12		19.4		3.64	9.52		7.36	0.8	
		GN35	13.8	21.5		13.6	5.06	1.37	7.71		9.06		1.74	4.39		2.47	0.28	
		GN37	5.3	11.3		9.09	7.08	2.32	14.1		26.6		5.3	15.1		13.4	1.49	
		GN38	4.26	4.35		2.86	1.45	0.4	2.15		3.79		0.67	1.67		1.17	0.14	
		GN36	9.81	21.5		14.1	6.3	1.67	10.4		17.3		3.48	9.54		7.32	0.81	
		GN71	9.49	19.4		14.5	5.81	1.39	9.4		12.7		2.68	7.67		6.24	0.78	
	Jaguaruna	J1	3.76	9.32		8.2	5.94	1.44	11		15.8		2.94	7.79		7	0.85	
		J2	2.57	5.32		4.95	5.32	0.59	13.1		21.9		3.99	9.97		7.98	0.94	
	Segunda Linha Torrens	SCN82	1.16	3.67		3.47	2.18	0.7								5.02	0.63	

		SC86	2.6	8		5	2.33	0.7								4.2	0.55	
		SC86-3	2.15	19.2		2.86	1.54	0.8	2.36		3.73			2.15		1.56	0.19	
	Canela Grande	CG86	3.4	9		6	2.04	0.59								2.69	0.43	
		CGX	1.6	6		4	1.86	0.57								3.65	0.47	
	Canela Pequena	CP40A	1.4	6		4	2.4	0.96								4.4	0.56	
		CP40B	1.5	5		4	2.5	0.9								4.75	0.6	
		CP70	2.37	23		4.51	2.67	1.7	4.24		6.36			2.9		2.21	0.25	
		CP48	4.62	24.6		11.5	5.9	2.16	8.49		12			4.97		4.46	0.5	
	São Pedro	MSP1	1.2	5		3	2.82	0.25	7.41		12.5		2.33	6.13		4.11	0.62	
		MSP2	1	5		2	2.44	0.26	8.07		14.9		2.8	7.21		5.03	0.75	
...in igneous																		
Sardinia	Monte Grighini	F4	17.51	30.93	4.4	18.37	5.55	2.24	9.44	2.06	14.45	122.13	3.07	8.59	1.3	8.01	1.2	
Castorina et al., 2008	Nuraghe Onigu	F6	12.23	16.6	2.1	7.65	1.39	0.37	2.01	0.32	2.09	20.58	0.49	1.58	0.26	1.68	0.31	
ICP-MS	Monte Genis	F11	6.73	15.27	2.47	13.23	6.22	1.31	12.69	2.12	12.81	244.81	2.38	5.11	0.43	1.44	0.16	
(ppm)																		
Total (3)																		
...in igneous																		
Schwarzwald	Friedenweiler	GS 86-3	1.91	5.17	0.93	5.59	3.15	2.5	6.82	1.36	9.64		1.85	5.16	0.66	3.89	0.47	
Schwinn & Markl, 2005	Ohlsback	GS151FL-1	1.49	2.71	0.37	1.83	0.54	0.83	1.13	0.22	1.61		0.34	0.91	0.11	0.55	0.06	
LA-ICP-MS	Hesselback	GS151FL-4	0.11	0.24	0.05	0.41	0.24	0.54	0.71	0.14	1.01		0.21	0.58	0.06	0.32	0.04	
(ppm)	Ödsbach	GS151FL-5	0.19	0.48	0.09	0.61	0.36	0.62	0.91	0.17	1.28		0.26	0.73	0.08	0.39	0.04	
Total (19)	Sophia	GS 194A-1	0.42	0.96	0.15	0.78	0.35	0.34	0.96	0.23	1.84		0.43	1.17	0.15	0.81	0.1	
	Johann	GS 194A-2	0.53	1.43	0.24	1.46	0.77	0.83	2.15	0.5	4.04		0.85	2.35	0.29	1.51	0.17	
	Neuglück	GS 194A-3	0.46	1.35	0.27	1.63	1.1	1.2	3.1	0.75	6.04		1.32	3.79	0.51	2.66	0.31	
	Bleilersgrund	GS 194A-4	0.69	2.23	0.42	2.81	1.84	2.08	5.04	1.19	9.96		2.22	6.53	0.85	5.09	0.58	

	Ilse i. Kaltbrunn	GS 194A-5	0.8	2.63	0.55	3.42	2.35	2.81	6.56	1.6	13.74		2.95	9	1.19	7.19	0.87	
	Burgfelsen	WJB2-2	0.57	1.99	0.53	4.68	6.08	2.57	16.6	2.93	17.27		2.78	5.22	0.51	2.26	0.24	
	König	WJB2-3	1.64	4.7	1.09	8.81	8.43	3.6	20.78	3.36	19.65		3	5.7	0.55	2.4	0.25	
	Hilfe Gottes	WJB2-4	1.6	4.62	1.08	8.37	8.16	3.46	20.08	3.26	19.56		3.02	5.6	0.56	2.37	0.24	
	Herzog Friedrich	WJB2-5	0.73	1.83	0.4	3.08	2.99	1.34	7.66	1.35	7.9		1.25	2.26	0.23	0.97	0.1	
	Daniel Gallen-back	WJB2-6	0.42	0.88	0.16	1.02	0.75	0.29	1.9	0.3	1.86		0.3	0.52	0.05	0.22	0.02	
	Neubergmännisch Glück	WJB2-7	1.26	3.74	0.91	7.25	7.65	3.18	19.03	3.23	18.76		2.94	5.41	0.52	2.3	0.23	
	Schlechthalde	WJB2-8	0.96	2.95	0.73	6.24	7.05	2.86	18.79	3.07	18.26		2.91	5.23	0.52	2.15	0.22	
	Southern Reinerzau valley	GS 71FI-1	3.06	7.16	1.24	7.12	2.55	1.25	4.1	0.76	5.43		1.23	3.71	0.49	3.07	0.39	
	Hohberg	GS 194B-4	1.07	2.31	0.3	1.53	0.37	0.61	0.83	0.16	1.3		0.29	0.88	0.1	0.44	0.05	
	Tennenbronn	GS 194B-5	1.64	3.1	0.42	1.93	0.38	0.44	0.48	0.08	0.63		0.15	0.43	0.05	0.26	0.03	
...in igneous																		
Erzgebirge	Beihilfe mine	BH-1	16.4	39.8	6.2	30.7	15	8.68	25.9	5.1	28	337	4.73	12.1	1.57	10.1	1.21	
Trinkler et al., 2005	Naundorf granite quarry	NBO-06	14.2	25.7	3.48	16	9.22	7.49	18.4	3.57	20.8	271	3.67	9.23	1.16	6.36	0.74	
ICP-MS	Reiche Zeche mine	R-374	16.6	35.5	5.04	26	11.1	6	18.3	2	14.8	196	2.6	6.4	0.92	4.85	0.61	
(ppm)	Grießbach	G-37aU	5.41	17.2	3.07	18.3	10.2	4.55	17.7	2.95	15.2	185	2.58	6.23	0.66	3.85	0.44	
Total (15)	Vater Abraham shaft	AH-1	6.79	26.2	5.36	32	17.5	5.25	22.1	3.11	13	157	1.85	3.96	0.43	2.44	0.28	
	Vater Abraham shaft	AH-4	5.77	20.3	4.2	25.7	15.6	4.37	25.6	3.38	14.9	210	2.18	4.74	0.54	2.73	0.34	
	Palmbaum shaft	CWF-15g	1.33	4.48	0.96	6.99	7.22	2.51	15.5	2.87	14.4	173	2.14	4.88	0.55	2.92	0.33	
	Brandbach - Barite adit	CWF-18	12.2	32.8	5.55	29.8	12.8	3.28	18.7	3.23	16.2	173	2.5	5.65	0.62	3.27	0.37	
	Armer Leute Bergfreund shaft	F-228	14.3	39.6	6.59	33.5	16.7	4.54	24.4	4.64	22.4	195	3.34	7.76	0.91	5.53	0.64	

	Armer Leute Bergfreund shaft	F-285	2.92	12.6	2.98	20.8	18.3	4.07	26.6	3.76	15.4	130	2.13	4.92	0.54	3.06	0.35	
	Ehrenfrieder sdorf Sn mine	ED-F01	1.12	4.86	1.23	9.43	8.72	1.97	13.6	1.77	7.91	89.9	1.14	2.54	0.3	1.64	0.19	
	Dörfel gneiss quarry	DF-03	6.59	16.9	2.85	15.1	8.65	2.34	17.3	3.16	18.2	213	3.26	7.81	0.92	4.88	0.61	
	Schelma - Shaft 38	HS-05	4.09	9.92	1.64	10.2	9.19	4.5	22	2.86	13.7	177	2.16	4.2	0.42	1.8	0.19	
	Pöhla-Tellerhäuser U mine	R-449	4.02	14.6	2.85	17.3	10.7	3.03	20.1	3.3	16.7	176	2.53	5.84	0.7	4.18	0.5	
	Pöhla-Tellerhäuser U mine	TE-101	2.51	9.5	2.15	14.2	12.5	3.36	25.1	3.84	17.4	154	2.45	5.07	0.58	3.07	0.38	
...in igneous																		
St. Lawrence	Grebe's Nest		21.6	30.9	2.7	44	13.7	2		1.4	26.5	2060	2	16.1	0.6	11	0.5	48
Gagnon et al., 2003	Iron Springs		9.7	15.9	2.8	13.2	7.7	0.5		5	36.6	3570	9.3	24.4	3.5	19.1	2.4	12
LA-ICP-MS	Lawn Barite		25.6	60.9	9.4	48.6	23	3.2		7.9	60	1120	12.9	35.8	4.4	23.4	2.2	13
(µg/g)																		
Total (3)																		
...in igneous																		
New Mexico	Capitan Mountains	CPU-1	9.2	25.5		17	6.7	0.65		1.88		744				14.2	2.6	
Hill et al., 2000		FN	16.4	48.3		36	14.9	0.89		4.48						27.04	3.91	
INAA		CM239	17.2	43.7		24	6.7	0.65		1.88						14.2	2.11	
(ppm)		KS-1	11.4	35.5		28	11.4	1.05		3.79						22.67	3.32	
Total (21)		W3-4	14.3	40.4		35	12.5	0.83		3.59						20.87	3.04	
		W3-6	19.5	54.2		37	11.3	0.77		2.9						16.29	2.43	
		McCory	14.7	40		30	13.3	1.1		4.37						22.93	3	
	Independence	12	16.6	36.1		14	4.2	1.35		1.05		82				4.86	0.68	
	Greenleaf	24	7.2	16.2		10	3.1	1.29		0.9		103				2.03	0.23	
	Sadler	25	3.6	8.1		5	1	0.31		0.24		33				0.61	0.07	
	Lucky	26	6.3	13.1		6	1.8	0.68		0.39		36				0.9	0.09	

	Gratten	27	9.6	9.3		9	2.2	0.77		0.58		68				1.94	0.24	
	Green Spar	28	5.6	7		8	2.4	0.9		0.98		122				3.52	0.45	
	Animas	29	18.1	42.3		23	9	2.58		2.46		138				3.4	0.38	
	Fluorite Group	30	23.3	43.4		23	5.1	1.81		0.68		32				0.95	0.11	
	Lone Star	31	22.9	46.6		27	10.2	5.8		2.42		114				3.61	0.45	
	Spar Hill	32	12.6	27.4		16	6.1	2.23		2.21		234				10.86	1.59	
	Shrine	33	5.7	11.9		7	3.7	1.33		1.1		51				3.76	0.48	
	Foster	35	18.8	35.5		13	1.5	0.71		0.08		3				0.03	0.01	
	Clum	36	17.8	29.3		11	3.3	1.83		0.89		60				1.5	0.17	
	Goat Camp Spring	37	6.2	13.5		7	1.7	0.68		0.4		52				0.58	0.05	
...in igneous																		
Sardinia	Arcu Istiddà	F1	32.79	68.64	5.18	18.56	4.21	1.6	4.42	0.63	4.13	126.5	0.93	2.53	0.29	1.33	0.15	
Castorina et al., 2008	Punta Geranule	F2	18.29	37.09	5.02	21.15	5.89	2.69	8.52	1.49	9.69	91.49	2.09	6	0.76	4.53	0.68	
ICP-MS	Castello Medusa	F3	16.82	33.98	4.6	19.92	6.48	3.76	10.87	2.22	15.90	137.9	3.33	9.67	1.33	8.08	1.17	
(ppm)	Monte Grighini	F4	17.51	30.93	4.4	18.37	5.55	2.24	9.44	2.06	14.45	122.1	3.07	8.59	1.3	8.01	1.2	
Total (18)	Monte Cardiga	F5	5.12	10.31	1.4	5.91	5.02	2.88	2.02	0.33	1.98	14.08	0.39	0.97	0.12	0.65	0.09	
	Nuraghe Onigu	F6	12.23	16.6	2.1	7.65	1.39	0.37	2.01	0.32	2.09	20.58	0.49	1.58	0.26	1.68	0.31	
	Silius	F7	3.28	8.64	1.35	6.64	2.63	1.73	5.71	1.06	6.82	184.5	1.37	3.32	0.34	1.55	0.19	
	Monreale	F8	1.13	2.64	0.35	1.48	0.58	0.23	0.73	0.15	0.97	5.82	0.2	0.62	0.09	0.7	0.12	
	Bruncu Mannu	F9	3.79	10.3	1.86	10.31	4.93	2.17	8.1	1.31	7.49	120.8	1.36	3.12	0.32	1.56	0.2	
	Bruncu Ventura	F10	2.56	6.87	1.32	7.99	4.03	0.64	7.79	1.11	5.88	94.74	0.99	1.99	0.18	0.69	0.09	
	Monte Genis	F11	6.73	15.27	2.47	13.23	6.22	1.31	12.69	2.12	12.81	244.8	2.38	5.11	0.43	1.44	0.16	
	Bruncu Molentinu	F12	6.96	14.64	2.34	12.6	6.76	1.77	15.05	2.72	17.15	354.4	3.45	8.64	1	5.3	0.68	
	Is Crabus	F13	12.79	44.16	9.36	54.03	21.44	6.5	26.83	3.84	21.55	241.2	4.1	10.28	1.09	5.18	0.7	
	Santa Lucia	F14	3.85	9.03	1.54	8.39	6.13	1.51	11.96	2.16	12.20	200.5	2.08	4.55	0.47	2.06	0.24	

	Su Zurfuru	F15	3.93	6.28	0.91	3.36	0.81	0.33	1	0.18	1.06	8.03	0.2	0.55	0.09	0.51	0.07	
	Perda Niedda	F16	4.23	10.06	1.7	8.99	6.22	0.67	10.16	1.95	11.74	104.2	2.05	5.48	0.84	5.77	0.84	
	Is Murvonis	F17	0.99	1.78	0.23	0.91	0.26	0.11	0.36	0.06	0.29	4.2	0.06	0.15	0.02	0.12	0.02	
	Nuraghe Perdu Spada	F18	10.35	21.01	2.91	12.23	3.72	1.43	5.49	0.95	5.77	41.23	1.12	2.89	0.37	2.19	0.32	
Hydrothermal/epithermal vein/replacement deposits in metamorphic																		
El Hammam	El Hammam	ELH 05-01	211	230	20.9	72.7	13.9	6.9	12.4	1.6	7.8	71.8	1.2	2.3		0.7	0.1	
Cheilletz et al., 2010		ELH 06-07a	260	194	15.8	55.4	11	10.3	15	1.9	10	218	1.7	3.5		0.8	0.1	
ICP-MS		ELH 06-07b	369	244	17.4	56.7	9.8	9.4	14.5	1.9	10.2	192	1.8	3.4		0.7	0.1	
(ppm)																		
Total (3)																		
...in metamorphic																		
Sardinia	Arcu Istiddà	F1	32.79	68.64	5.18	18.56	4.21	1.6	4.42	0.63	4.13	126.5	0.93	2.53	0.29	1.33	0.15	
Castorina et al., 2008	Punta Geranule	F2	18.29	37.09	5.02	21.15	5.89	2.69	8.52	1.49	9.69	91.49	2.09	6	0.76	4.53	0.68	
ICP-MS	Castello Medusa	F3	16.82	33.98	4.6	19.92	6.48	3.76	10.87	2.22	15.9	137.9	3.33	9.67	1.33	8.08	1.17	
(ppm)	Silius	F7	3.28	8.64	1.35	6.64	2.63	1.73	5.71	1.06	6.82	184.5	1.37	3.32	0.34	1.55	0.19	
Total (11)	Bruncu Mannu	F9	3.79	10.3	1.86	10.31	4.93	2.17	8.1	1.31	7.49	120.6	1.36	3.12	0.32	1.56	0.2	
	Bruncu Ventura	F10	2.56	6.87	1.32	7.99	4.03	0.64	7.79	1.11	5.88	94.74	0.99	1.99	0.18	0.69	0.09	
	Bruncu Molentinu	F12	6.96	14.64	2.34	12.6	6.76	1.77	15.05	2.72	17.15	354.4	3.45	8.64	1	5.3	0.68	
	Is Crabus	F13	12.79	44.16	9.36	54.03	21.44	6.5	26.83	3.84	21.55	241.2	4.1	10.28	1.09	5.18	0.7	
	Su Zurfuru	F15	3.93	6.28	0.91	3.36	0.81	0.33	1	0.18	1.06	8.03	0.2	0.55	0.09	0.51	0.07	
	Is Murvonis	F17	0.99	1.78	0.23	0.91	0.26	0.11	0.36	0.06	0.29	4.2	0.06	0.15	0.02	0.12	0.02	
	Nuraghe Perdu Spada	F18	10.35	21.01	2.91	12.23	3.72	1.43	5.49	0.95	5.77	41.23	1.12	2.89	0.37	2.19	0.32	
...in metamorphic																		
Schwarzwald Schwinn & Markl, 2005	Friedrich-Christian	GS151FL-9	0.57	1.51	0.27	1.83	1.15	1.21	3.15	0.64	4.69		0.91	2.76	0.31	1.57	0.17	
	Drey	GS 71FI-2	3.06	7.96	1.32	7.46	2.78	1.37	4.47	0.78	5.71		1.22	3.79	0.49	2.96	0.39	

LA-ICP-MS	Barbara	GS 71FI-3	10.31	15.92	1.85	7.8	1.05	0.17	0.65	0.09	0.47		0.12	0.37	0.04	0.25		
(ppm)	Segen Gottes	GS 71FI-4	2.29	4.78	0.62	3.39	0.67	0.16	1.07	0.17	1.36		0.34	1.08	0.13	0.65	0.08	
Total (10)	Artenberg quarry	GS 71FI-5	8.02	18.31	2.65	12.2	1.94	0.51	2.19	0.35	2.57		0.59	1.85	0.22	1.24	0.15	
	Erzengel Gabriel	GS 71FI-6	10.31	23.08	3.27	14.24	2.61	0.75	2.75	0.4	2.9		0.61	1.88	0.22	1.21	0.16	
	Laßgrund	GS 71FI-7	3.06	7.16	1.15	5.76	1.28	0.62	1.82	0.34	2.76		0.64	2.17	0.29	1.92	0.26	
	Wenzel	GS 194B-1	1.34	4.22	0.77	4.71	3.53	5.93	11.31	2.86	23.83		5.11	15.81	2.17	13.7	1.79	
	Fortuna Gelbach	GS 194B-2	2.87	8.76	1.48	8.31	3.87	4.14	8.84	2.08	17.6		3.94	12.51	1.76	10.98	1.38	
	Ludwigs Trost	GS 194B-3	0.42	1.19	0.2	1.15	0.54	0.62	1.17	0.27	2.12		0.49	1.45	0.18	0.99	0.11	
...in metamorphic																		
New Mexico	Long Lost Brother	34		4	11		7	5.1	2.07		3.12		265				15.72	
Hill et al., 2000	Spruce Hill	50		12.3	32.7		30	19.7	3.52		7.92		967				24.16	
INAA	Bonita	51		16	38.7		40	22.6	5.61		7.05		1147				31	
(ppm)																		
Total (3)																		
Hydrothermal/epithermal vein/replacement deposits in sedimentary																		
Sardinia			La	Ce	Pr	Nd	Sm	Eu	Gd	Tb	Dy	Y	Ho	Er	Tm	Yb	Lu	n = #
Castorina et al., 2008	Monte Cardiga	F5	5.12	10.31	1.4	5.91	5.02	2.88	2.02	0.33	1.98	14.08	0.39	0.97	0.12	0.65	0.09	
ICP-MS																		
(ppm)																		
Total (11)																		
...in sedimentary																		
Schwarzwald	Käfersteige	GS 86-1	1.99	5.57	1.02	6.14	3.72	3.43	8.33	1.67	11.65		2.34	5.98	0.75	4.33	0.53	
Schwinn & Markl, 2005	Heiligenwald	GS 86-2	1.91	5.09	0.93	5.7	3.34	2.64	7.26	1.47	10.38		2.04	5.54	0.69	4.15	0.52	
LA-ICP-MS	Dorothea	GS 86-4	1.83	5.01	0.92	5.39	3.16	2.52	6.71	1.35	9.6		1.9	5.37	0.69	4.04	0.49	
(ppm)	Wittenweiler	GS 86-5	1.87	5.09	0.92	5.53	3.15	2.58	6.77	1.32	9.42		1.82	5.3	0.68	3.81	0.46	

Total (6)	Zunsweier	GS 86-6	1.83	5.17	0.9	5.49	3.23	2.65	6.74	1.32	9.38		1.81	5.25	0.66	3.84	0.46	
	Clara	GS151FL-8	0.11	0.32	0.07	0.54	0.35	0.68	1.05	0.2	1.48		0.31	0.84	0.1	0.47	0.05	
New Mexico	Gonzales east	7	1.9	3.2		2	0.4	0.05		0.07		17				0.19	0.02	
Hill et al., 2000 INAA (ppm) Total (1)																		

Table E-1. Compiled REE-Y data used to produce discrimination diagrams categorized by primary mineralization environments. Included are publication sources, deposit names, regions, sample numbers, analytical methods, and units of measurements.

E.2. Test analyses on hand samples

Table E-2. REE-Y test analyses taken by FUS-MS on fluorite hand samples sorted by assigned primary mineralization environments. Included are deposit names, secondary mineralization environment assignations, and sample numbers.

Detection limit (FUS-MS)			0.05	0.05	0.01	0.05	0.01	0.005	0.01	0.01	0.01	0.5	0.01	0.01	0.005	0.01	0.002
Deposit Name	Secondary type	Sample #	La	Ce	Pr	Nd	Sm	Eu	Gd	Tb	Dy	Y	Ho	Er	Tm	Yb	Lu
Mississippi Valley type																	
Liard fluorospar	vein in carbonate	Liard-1	0.64	0.85	0.15	0.92	0.33	< 0.005	0.71	0.12	0.79	25.1	0.18	0.51	0.054	0.29	0.04
Hastie Quarry	carbonatite-related	3-12-9EP	0.12	0.21	0.05	0.43	0.3	0.132	0.81	0.11	0.69	15.1	0.13	0.31	0.033	0.13	0.017
		3-12-9EY	0.14	0.21	0.02	0.21	0.11	0.046	0.25	0.03	0.16	4.2	0.03	0.07	0.008	0.04	0.005
Barnett Mine	carbonatite-related	28-12S-8EW	0.27	0.44	0.05	0.24	0.11	0.076	0.24	0.03	0.17	3.3	0.03	0.08	0.01	0.05	0.006
		28-12S-8EP	0.21	0.41	0.08	0.48	0.23	0.258	0.39	0.05	0.26	6.7	0.05	0.12	0.014	0.06	0.006
IOCG																	
Rexspar	replacement in igneous	REXSPAR-82-C	399	537	48.1	169	31.3	9.06	33	4.4	25.4	396	4.97	13.7	1.75	9.27	1.27
Intrusion-related Mo																	
Eaglet	replacement in igneous	EAGLET-7	3.72	12.6	2.4	14.1	4.3	1.47	5.61	0.77	3.96	70.8	0.77	2.03	0.262	1.45	0.208
		EAGLET-9	4.16	11.2	1.59	6.98	1.64	0.458	2.36	0.35	2.11	40.2	0.46	1.53	0.224	1.18	0.148
Peralkaline silicate igneous rock																	
Kipawa	skarn	KIPAWA	59.9	118	15.4	62.8	12.9	1.61	14.6	2.33	14.8	285	3.3	10.1	1.33	7.32	0.847
Carbonatite-related																	
Eldor	peralkaline	ELDOR-2	1.12	2.83	0.41	2.2	1.21	0.657	3.5	0.74	5.42	226	1.24	3.53	0.429	2.55	0.356
Hydrothermal/epithermal vein/replacement in igneous host																	
Rock Candy	carbonatite-related	RC-1	11.4	19	2.39	10.6	2.76	1.36	3.25	0.54	3.5	36.7	0.71	1.93	0.238	1.39	0.2

Table E-3. LA-ICP-MS analytical traverse across single cleaved fluorite chip displaying late-stage color change from yellow to purple. Laser numbers starting with Y indicate analyses on yellow portion of fluorite chip, and those starting with P indicate purple.

LA-ICP-MS (ppm)															
Hastie Quarry sample 3-12-9E															
Laser #	La	Ce	Pr	Nd	Sm	Eu	Gd	Tb	Dy	Y	Ho	Er	Tm	Yb	Lu
Y1		0.02	0.01	0.2	0.19	0.07	0.48	0.07	0.44	8.77	0.08	0.19	0.01	0.08	0.01
Y2	0.13	0.01	0.01	0.16	0.2	0.08	0.46	0.07	0.46	8.62	0.08	0.18	0.02	0.06	0.01
Y3		0.01	0.01	0.13	0.19	0.08	0.46	0.07	0.43	8.47	0.08	0.19	0.02	0.07	0.01
Y4		0.01	0.01	0.11	0.17	0.07	0.43	0.06	0.4	7.99	0.07	0.15	0.01	0.07	0.01
Y5		0.01		0.08	0.13	0.06	0.41	0.06	0.36	7.34	0.06	0.16	0.01	0.06	
Y6			0.01	0.05	0.1	0.05	0.32	0.05	0.29	6.48	0.05	0.09	0.01	0.06	
Y7		0.01	0.01	0.08	0.1	0.04	0.29	0.04	0.25	5.54	0.05	0.1	0.01	0.04	
Y8		0.01		0.04	0.09	0.04	0.24	0.03	0.18	4.77	0.04	0.07		0.02	0.01
Y9				0.06	0.1	0.03	0.19	0.03	0.17	4.03	0.03	0.06	0.01	0.02	
P1	0.02	0.01		0.06	0.06	0.03	0.2	0.02	0.19	4.79	0.03	0.07	0.01	0.02	
P2		0.01		0.08	0.07	0.03	0.17	0.02	0.14	3.68	0.02	0.05	0.01	0.04	
P3		0.01		0.06	0.09	0.03	0.15	0.02	0.15	4.07	0.02	0.06	0.01	0.01	
P4		0.01		0.04	0.08	0.03	0.22	0.02	0.12	4	0.02	0.06		0.02	
P5				0.06	0.06	0.03	0.19	0.02	0.15	4	0.03	0.05	0.01	0.02	
P6		0.01		0.07	0.11	0.03	0.15	0.02	0.14	3.56	0.03	0.05		0.02	
P7		0.01		0.04	0.06	0.02	0.19	0.02	0.17	3.37	0.03	0.06	0.01	0.02	
P8		0.01		0.04	0.08	0.03	0.16	0.02	0.12	3.61	0.02	0.05		0.01	
P9		0.01		0.04	0.05	0.03	0.19	0.03	0.11	3.33	0.02	0.06		0.02	
P10		0.01		0.04	0.07	0.03	0.18	0.02	0.13	3.61	0.02	0.05		0.02	
P11		0.01	0.01	0.04	0.08	0.03	0.22	0.02	0.12	4	0.02	0.04		0.01	
P12		0.01		0.05	0.09	0.03	0.15	0.02	0.12	4.25	0.03	0.07		0.02	
P13		0.01		0.09	0.07	0.03	0.2	0.02	0.16	3.29	0.03	0.07		0.02	